NTNU

Norwegian University of
Science and Technology

Traffic induced vibrations of cable-supported bridges

Rolf Christensen Andersen

Eirik Røhme Aunemo

Civil and Environmental Engineering
Submission date: June 2016
Supervisor: Ole Andre Øiseth, KT
Co-supervisor: Gunnstein Frøseth, KT

Norwegian University of Science and Technology
Department of Structural Engineering

Department of Structural Engineering
Faculty of Engineering Science and Technology
NTNU- Norwegian University of Science and Technology

ACCESSIBILITY

OPEN

MASTER THESIS 2016

SUBJECT AREA:	DATE:	NO. OF PAGES:
Structural dynamics	10.06.2016	172 (12 + 118 + 42)

TITLE:

Traffic induced vibrations of cable-supported bridges

Vibrasjoner av slanke brukonstruksjoner utsatt for trafikklaster

BY:

Rolf Christensen Andersen and
Eirik Røhme Aunemo

PROBLEM DESCRIPTION:

Loads from heavy traffic may sometimes cause unpleasant vibrations in single components or bigger parts of the structure of the bridge. Vibrations of such kind will also be present at all instrumentation of bridge structures which are kept open for traffic in the measurement period. In such cases it is desirable to have basic knowledge about the characteristics of these vibrations, to ensure they can be differentiated from movement caused by other types of loads.

RESPONSIBLE TEACHER: Associate professor Ole Øiseth

SUPERVISOR(S): Associate professor Ole Øiseth,
PhD-Candidate Gunnstein Frøseth
PhD-Candidate Aksel Fenerci

CARRIED OUT AT: Department of Structural Engineering

The picture on the front page is found on the website of the Norwegian Public Roads Department [40]

Institutt for konstruksjonsteknikk

FAKULTET FOR INGENIØRVITENSKAP OG TEKNOLOGI
NTNU – Norges teknisk-naturvitenskapelige universitet

MASTEROPPGAVE 2016

for

Rolf Andersen og Eirik Aunemo

Vibrasjoner av slanke brukonstruksjoner utsatt for trafikklaster

Traffic induced vibrations of cable-supported bridges

Last fra tung trafikk kan i enkelte tilfeller forårsake ubehagelige vibrasjoner av enkeltkomponenter eller større deler av brokonstruksjoner. Slike vibrasjoner vil også være tilstede ved all instrumentering av brukonstruksjoner som holdes åpne for trafikk i måleperioden. I slike tilfeller er det ønskelig med grunnleggende kunnskap om disse vibrasjonenes karakteristikk slik at disse kan skilles fra bevegelse som er forårsaket av andre typer laster.

Oppgaven bør inneholde følgende temaer.

- Beskrivelse av de ulike modellene som finnes for å beskrive interaksjon mellom bro og kjøretøy.
- Etablering av en modell av en valgt brukonstruksjon i programmet Abaqus eller Matlab.
- Beregning av trafikkinduserte vibrasjoner for den valgte konstruksjonen
- Sammenlikning av predikert og målt respons for den valgte brokonstruksjonen.

Studentene velger selv hva de ønsker å legge vekt på

Besvarelsen organiseres i henhold til gjeldende retningslinjer.

Veileder(e): Ole Andre Øiseth, Gunnstein Frøseth

NTNU, 25.01.2015

Ole Andre Øiseth
faglærer

Sammendrag

Vindlaster og laster fra jordskjelv vil ofte være de dominerende og avgjørende faktorene i prosjektering av slanke brukonstruksjoner. Imidlertid kan også trafikklaster være en kilde til betydelige vibrasjoner. Trafikkinduserte vibrasjoner kan eksitere andre frekvenser i brua enn vindlastene, og hvis disse frekvensene og bruas resonans-frekvenser samsvarer, kan trafikklastene bli kritiske. Det er derfor ønskelig å oppnå grunnleggende kunnskaper angående trafikkinduserte vibrasjoner og deres egenskaper.

I denne oppgaven har det blitt identifisert og foreslått metoder for å undersøke trafikkindusert respons på bruer. Det har blitt utledet og vurdert numeriske metoder for å analysere måledata fra eksisterende brukonstruksjoner, med formålet å identifisere trafikk på bruer, og responsen fra nevnte trafikk. For å simulere effekten av trafikklaster på bruer har det i tillegg blitt etablert og undersøkt en elementmetode-modell. Et studie på Hardangerbrua ble utført for å teste ut og verifisere metodene. Måledata fra akselerometre langs brua ble brukt i den numeriske analysen, og trafikklogging utført på brua ga informasjon angående den faktiske trafikksituasjonen på Hardangerbrua for et tidsintervall.

Undersøkelsene viser at tungtrafikk kan identifiseres ved å se på responsen fra akselerasjoner. Når tungtrafikk er tilstede på brua vil frekvensen på svingningene i akselerasjonsresponsen øke merkbart. Undersøkelsene tyder på at trafikk fra personbiler ikke påvirker akselerasjonsresponsen i nevneverdig grad.

Kryss-kovarians har ikke blitt vurdert som fordelaktig for å identifisere trafikklaster, da akselerasjonsresponsen ser ut til å bestå av flere faktorer enn bare trafikk. Tilstedeværelsen av effekter som vind gir responsen en kompleksitet som fører til at resultatene fra kryss-kovarians ikke er av tilfredsstillende art.

Ved å undersøke spektraltettheten av måledataene ble det funnet at tungtrafikk i all hovedsak eksiterer egenfrekvenser under én hertz, men også noen høyfrekvente egenmoder. Siden vind for det meste også gir respons under én hertz, viste det seg vanskelig å filtrere vekk vindindusert respons. Dette indikerer en høy grad av interaksjon mellom vindlaster og trafikklaster, og anses som signifikant og noe som bør tas hensyn til i fremtidige analyser.

Ved å integrere de målte akselerasjonene ble forskyvninger funnet. Resultatene fra denne metoden ga gode resultater, med unntak av en ikke-eksisterende egenfrekvens som oppstår og eksiteres med høy amplitude, noe som gir en viss usikkerhet for resultatene. Videre studier bør utføres på dette feltet.

Elementmetode-modellen for en last i bevegelse ga resultater som tyder på at denne kan brukes til å estimere trafikkindusert respons på bruer. Estimatet er konservativt, og måledataene gir tidvis svært mye lavere respons enn Abaqus-modellen. Dette anses å være i sammenheng med de høye vindhastighetene som opptrådte ved den undersøkte tidsserien, da responsen fra vindlastene antas å gi brua en stivere oppførsel.

Abstract

When considering cable-supported bridges, forces from wind and earthquakes often governs design. Heavy vehicles can also excite considerable vibrations on long and slender bridges, and may excite other frequencies in the bridge than the wind. If those frequencies are close to the resonance frequencies of the bridge, this response will be critical. As such, it is of interest to accumulate knowledge considering characteristics of traffic induced vibrations on slender bridges.

In this thesis, methods for examining the traffic induced response on cable-supported bridges have been proposed. In order to identify traffic on bridges, and the response invoked by said traffic, numerical methods of analysing recorded data from existing bridge structures have been derived and reviewed, and a finite element analysis for simulating the effect of traffic loading on bridges has been established and investigated. A case study on the Hardanger Bridge was carried out as a means of verifying the methods. Recordings from accelerometers along the bridge was used in the analysis, and a traffic logging at the site provided information regarding the actual traffic situation at the bridge for a time series.

It was found that heavy vehicles can be identified from the vertical acceleration response, as the frequency of the oscillations in the acceleration response increases significantly. The presence of passenger cars on the bridge does not seem to affect the acceleration response noticeably. The use of cross-covariance as a means of identifying moving loads and their characteristics, proved unsuccessful. Other factors than traffic seems to contribute to the acceleration response, and as such the cross-covariance did not provide satisfactory results due to the complexity of the response.

The power spectra of the recorded data revealed that heavy traffic excites eigenfrequencies mostly below one hertz, but also some higher eigenfrequencies. The attempts of filtering away wind induced response, which is in general present below one hertz in the frequency spectra, proved unsuccessful as most of the traffic induced response happens in the same frequency spectra as the wind. Because of this, the wind-traffic interaction on bridges appear to be significant, and should be considered in analyses.

Integration of the recorded accelerations was shown to give good results as a means of obtaining displacements, with the exception of a non-existing eigenfrequency appearing and getting excited with a high amplitude, providing some uncertainty regarding the results. As such further study on the subject is recommended.

The findings suggests that a finite element moving load model, consisting of a moving force representing each axle of the vehicle, may be used to conservatively estimate the response of a bridge. The recorded data gives a smaller response than the Abaqus model, but the car loggings used for the recorded data were done during times of high wind velocities, which is assumed to provide a stiffer response of the bridge. Further study on the wind-traffic interaction, is recommended.

Preface

This master thesis has been carried out during the spring of 2016, and concludes the authors 5 years Master's Degree Programme in Civil and Environmental Engineering. The thesis has been carried out at the Department of Structural Engineering at the Norwegian University of Science and Technology (NTNU). The master thesis has been supervised by Associate Professor Ole Øiseth, and PhD candidates Gunnstein Thomas Frøseth and Aksel Fenerci.

A study on methods for analyzing the effect of traffic induced vibrations of cable-supported bridges, finalized by a case study of the Hardanger Bridge, is presented in the thesis. The dynamic effects of traffic induced vibrations on bridges is relatively uncharted territory, and this master thesis will thus aim to shine some light onto which methods may be used in analyses of traffic loading on cable-supported bridges.

The authors would like to thank our supervisor Ole Øiseth for his guidance during the study. His knowledge of the field has been of big help. In addition, the numerical routines he provided for the integration of accelerations has been of great value for the thesis. We would also like thank our co-supervisors Gunnstein Thomas Frøseth and Aksel Fenerci for valuable discussions and guidance during our work. Their knowledge and assistance has been appreciated, and has helped guiding us in the right direction.

Daniel Cantero Lauer and his masters students are also owed a big thank you for the car loggings performed at the Hardanger Bridge, as the data has been of utmost importance in the thesis.

Finally, praise goes out to our girlfriends for sticking out with us through this semester and keeping us sane even when the results tried their best to do otherwise. Their support has been invaluable, and we are forever grateful.

Trondheim, June 10, 2016

Rolf Christensen Andersen *Eirik Røhme Aunemo*

Contents

1 Introduction

In today's society, the limits of engineering capability are pushed further than before. Bridges are getting longer and more slender. An example of this is the fjord crossing which are a part of the project *Coastal Highway Route E*39 by the Norwegian Public Roads Administration. Many of these crossing will demand state of the art solutions. Because of this, it is vital to acquire precise knowledge of the response these bridges are subjected to from different types of loading.

In this thesis, the traffic induced response on cable-supported bridges will be investigated. The research on the dynamic effects of traffic induced vibrations on cable-supported bridges is not a well traversed field of study, and hence it is of interest to accumulate knowledge considering the characteristics of these vibrations.

In this thesis there will be carried out a study on ways to examine the response from traffic induced vibrations using recorded data, as well as calculating the response from traffic on a cable-supported bridge using a finite element analysis. In a case study on the Hardanger Bridge, which is the longest cable-supported bridge in Norway with a span of 1310 metres, the proposed methods for investigation of traffic induced vibrations on cable-supported bridges are examined . The results from the case study will, along with theory and experience from previous studies, be the foundation upon which the methods will be evaluated

1.1 Problem description

When considering cable-supported bridges, wind and earthquake induced forces is often governing factors in design, but heavy vehicles on long and slender bridges can also be the source of considerable vibrations. These vibrations can excite other frequencies in the bridge than the wind, and thus be critical if those frequencies are close to the resonance frequencies of the bridge. As such, it is of interest to gain knowledge regarding the characteristics of these vibrations.

1.2 Scope of work

The focus of this master thesis is to analyse traffic induced vibrations excited on cable-supported bridges. In order to gather information on the traffic induced response, the first step was to derive methods for separating the traffic induced response from other forces influencing the bridge. Also methods to identify the characteristics of the traffic induced response were investigated. In this thesis, the response is separated into wind induced and traffic induced response. Other forces such as waves and earthquakes are not considered, partly to limit the scope of the thesis, and partly because no time series containing wave or earthquake loading on a bridge were available for the thesis.

The methods for investigating the traffic induced response is carried out in Matlab. The methods addresses both the response in time domain and the frequency domain. As a means of simulating the response from traffic induced vibrations, a finite element model in Abaqus will also be established.

The proposed methods for the investigation of traffic induced vibrations on cable-supported bridges are examined in a case study on the Hardanger Bridge. The results from the case study will, along with theory and experience from previous studies, be the foundation upon which the methods will be evaluated.

All the Matlab scripts referred to in the thesis can be found in the digital appendix.

1.3 Structure of the report

Section 2 All the basic theory needed for the master thesis is outlined. The section is divided into subsections considering the theory behind dynamic systems, signal processing and stochastic processes. Not all of the theory presented will be directly utilized, but will serve as a valuable foundation for the work in the thesis.

Section 3 Various ways for modelling the moving load are presented and evaluated. The analytical solution for the chosen moving load model is derived, and a finite element moving load model is established and validated with respect to the analytical solution.

Section 4 The methods and techniques seen as expedient for analyzing recorded data from a cable-supported bridge in order to examine traffic induced response are derived and explained. Important assumptions and sources of error are presented.

Section 5 The methods presented in the two previous sections are implemented onto The Hardanger Bridge. Noteworthy features and assumptions regarding the case study are delved upon, and the response is analysed. Important aspects for the implementation of the moving load model onto an existing bridge model are addressed. Results are presented, and the response from the finite element model is compared to the recorded data. To investigate what criteria affects the finite element model, a parameter study of the moving load on the Hardanger Bridge model is conducted.

Section 6 The findings from the case study are discussed and evaluated with regards to theory and prior studies. The compliance between the results and the theory is examined, and comparisons between results are drawn. Finally, the findings from the different methods are reviewed with regard to further use and application.

Section 7 An overview of the conclusions drawn are presented, and suggestions regarding possible further work on the subject are given.

2 Theory

In this section, relevant theory and principles for this master thesis will be accounted for. The theory focuses mainly on principles from structural dynamics and procedures for signal processing.

2.1 Dynamic systems

A dynamic system can consist of multiple degrees of freedom. It is assumed that the readers of the thesis possess basic knowledge of structural dynamics, and as such the single degree of freedom system (SDOF) will not be accounted for. Important concepts and terminology regarding the multi degree of freedom system (MDOF) will be presented, as well as essential theory regarding different types of analysis and the damping in dynamic systems.

2.1.1 Multi Degree of Freedom System

In this section, the multi degree of freedom system will be discussed for the undamped case. Damping will be accounted for in Section 2.1.2. When a system has more than one degree of freedom (DOF), it is called a multi degree of freedom system (MDOF). When working with MDOF's, the influence on the degrees of freedom $r_{i\neq j}$ from the actions on the degree of freedom r_j must be considered. The interaction between degrees of freedom is taken into account by the mass matrix $\boldsymbol{M}$ and stiffness matrix $\boldsymbol{K}$ of the system. If both the mass matrix and stiffness matrix of a system are diagonal, then there is no interaction between the degrees of freedom in the system.

The mass matrix can either be constructed as a lumped mass matrix or a consistent mass matrix. The consistent mass matrix and the stiffness matrix of a system is defined by respectively Equation (2.1) and Equation (2.2). $\boldsymbol{a_j}$ is the connectivity matrix between the elemental DOF's $\boldsymbol{d_j}$ and the degrees of freedom of the system $\boldsymbol{u}$, $\boldsymbol{d_j} = \boldsymbol{a_j u}$, ρ is the density of the material, $\boldsymbol{N_j}$ is the interpolation functions between the displacement field of the element $\boldsymbol{w_j}$ and the elemental DOF's, $\boldsymbol{w_j} = \boldsymbol{N_j d_j}$, the constitutive matrix $\boldsymbol{E}$ gives the relation between the stress field $\boldsymbol{\sigma}$ and the strain field $\boldsymbol{\epsilon}$, $\boldsymbol{\sigma} = \boldsymbol{E\epsilon}$, and $\boldsymbol{B} = \boldsymbol{\partial N}$ is known as the strain-displacement matrix, $\boldsymbol{\epsilon} = \boldsymbol{\partial w} = \boldsymbol{\partial N d} = \boldsymbol{Bd}$. The load vector of the system, $\boldsymbol{F}$, is given by equation (2.3), where $\boldsymbol{P_B}$, $\boldsymbol{P_T}$ and $\boldsymbol{p_c}$ represents the body forces, the traction forces and the concentrated forces working on the element, respectively.

$$\boldsymbol{M} = \sum_{j=1}^{J} \boldsymbol{a_j^T m_j a_j} = \sum_{j=1}^{J} \boldsymbol{a_j} \int_{V_j} \rho \boldsymbol{N_j^T N_j} dV \boldsymbol{a_j} \tag{2.1}$$

$$\boldsymbol{K} = \sum_{j=1}^{J} \boldsymbol{a_j^T k_j a_j} = \sum_{j=1}^{J} \boldsymbol{a_j} \int_{V_j} \boldsymbol{B_j^T E_j B_j} dV \boldsymbol{a_j} \tag{2.2}$$

$$\boldsymbol{F} = \sum_{j=1}^{J} \boldsymbol{a}_j^T \boldsymbol{p}_j = \sum_{j=1}^{J} \boldsymbol{a}_j \left(\int_{V_j} \boldsymbol{N}_j^T \boldsymbol{P}_{\boldsymbol{B},j} dV + \int_{S_j} \boldsymbol{N}_j^T \boldsymbol{P}_{\boldsymbol{T},j} dS + \boldsymbol{p}_c \right) \tag{2.3}$$

The consistent mass matrix distributes the mass along the element, as opposed to the lumped mass matrix which creates a diagonal matrix by accumulating the mass of the element into point masses. The consistent mass matrix is real, and thus the complex conjugate of the matrix is equal to the matrix, $\overline{\boldsymbol{M}} = \boldsymbol{M}$. The consistent mass matrix is symmetric, $\boldsymbol{M}^{\boldsymbol{T}} = \boldsymbol{M}$, and for any non-trivial vector $\boldsymbol{x}$ it is positive definite, $\boldsymbol{x}^{\boldsymbol{T}} \boldsymbol{M} \boldsymbol{x} > 0$. The consistent mass matrix is a more realistic representation of the mass of a system than the lumped mass matrix, and is usually the preferred way of constructing the mass matrix. When conducting hand calculations or explicit time integration, a lumped mass matrix may be considered favourable, as extracting the consistent mass matrix can be considered time demanding and computationally expensive. Considering that the lumped mass matrix is a diagonal matrix, it may as such become singular $\boldsymbol{M} \boldsymbol{x} = \boldsymbol{0}$ or semidefinite $\boldsymbol{M} \boldsymbol{x} \geq \boldsymbol{0}$ if there are degrees of freedom not associated with any inertia [7]. Thus the lumped mass matrix is only positive definite $\boldsymbol{M} \boldsymbol{x} > \boldsymbol{0}$ if the proper precautions are taken and all degrees of freedom are assigned with inertia. In the continuation of the thesis it is assumed proper care is taken in the construction of the mass matrix, and as such that it is positive definite.

In the continuation of the thesis, it is assumed the material is elastic and real, and as such that the constitutive matrix $\boldsymbol{E}_j$ is real. If $\boldsymbol{E}_j$ is real and symmetric, the stiffness matrix $\boldsymbol{K}$ is real and symmetric. As the work needed to deform an elastic body has to be positive [38], the constitutive matrix $\boldsymbol{E}_j$ is positive definite. Hence most structures, as long as the stiffness matrix is not singular, $\boldsymbol{K} \boldsymbol{x} = \boldsymbol{0}$, have a positive definite stiffness matrix. In this thesis, it is assumed that proper care is taken when constructing the system equations, such that rigid body motions are prohibited and mechanisms will not take place. Thus, the stiffness matrix is positive definite.

If the system is undamped, Equation (2.4) gives the equation of motion for the system.

$$\boldsymbol{M} \ddot{\boldsymbol{u}} + \boldsymbol{K} \boldsymbol{u} = \boldsymbol{F} \tag{2.4}$$

The homogeneous, undamped, free vibrating system has a general solution on the form $\boldsymbol{u} = \phi e^{-\omega t}$. Inserting the general solution into the homogeneous equation of motion, and introducing the eigenvalue $\lambda_n = \omega_n^2$ of eigenmode n and its corresponding eigenvector ϕ_n, yields the linear eigenvalue problem in Equation (2.5).

$$(\boldsymbol{K} - \lambda_n \boldsymbol{M}) \phi_n = \boldsymbol{0} \tag{2.5}$$

As established, $\boldsymbol{M}$ and $\boldsymbol{K}$ are real. Meirovitch [28] states that a real matrix yields a real eigenvalue λ, and thus the basis for the eigenvector ϕ is real. Because both property matrices $\boldsymbol{M}$ and $\boldsymbol{K}$ are positive definite, the eigenvalues λ_n are positive. Hence, by premultiplying Equation (2.5) by ϕ_n^T and solving for λ_n, Equation (2.6) is obtained.

$$\lambda_n = \frac{\phi_n^T \boldsymbol{K} \phi_n}{\phi_n^T \boldsymbol{M} \phi_n} > 0 \tag{2.6}$$

Considering $\lambda_n = \omega_n^2 > 0$, the non-decaying harmonic response function for the undamped free vibrating system is given on the form $u_n = \phi_n \left(C_{1n} cos(\omega_n t) + C_{2n} sin(\omega_n t)\right)$.

Only the direction, and not the magnitude, of the eigenvector is defined by the eigenvalue problem. To define the magnitude of the eigenvector, a method called *mass normalization* is used, which yields the relations $\phi_n^T \boldsymbol{M} \phi_n = 1$ and $\phi_n^T \boldsymbol{K} \phi_n = \lambda_n$. Considering that the property matrices are real and symmetric, the eigenvectors are orthogonal with respect to $\boldsymbol{M}$ and $\boldsymbol{K}$. This gives the relations in Equation (2.7) and Equation (2.8).

$$\phi_m^T \boldsymbol{M} \phi_n = \begin{cases} 1 & \text{for } m = n \\ 0 & \text{for } m \neq n \end{cases} \tag{2.7}$$

$$\phi_m^T \boldsymbol{K} \phi_n = \begin{cases} \lambda_n & \text{for } m = n \\ 0 & \text{for } m \neq n \end{cases} \tag{2.8}$$

The complete solution of the dynamic MDOF system is found from the superpositioning of the homogeneous solution and the particular solution of the system, and utilizes the orthogonality properties of the eigenvectors. As the system consists of N degrees of freedom, the complete solution is obtained by transforming the coupled MDOF system into a set of N SDOF systems, which yields N uncoupled equations of motion that can easily be solved.

$$\boldsymbol{u} \approx \sum_{n=1}^{N} \phi_n y_n \tag{2.9}$$

2.1.2 Damping in dynamic systems

The damping of a dynamic system can be described either by viscous or by non-viscous damping. The classical theory used to describe dynamic systems uses viscous damping. Cunha [8] states that although bridges may inhibit complex damping mechanisms, viscous damping is deemed to be sufficient to reproduce the bridge response accurately. This can be explained by the fact that the practical difference between non-viscous and viscous damping is negligible because of the relatively low damping values associated with bridges [11]. Thus the need to investigate the effects of a non-viscous damping model is not considered relevant for this thesis, and the rest of this thesis will be limited to the use of viscous a damping model. Equation (2.10) gives the equation of motion of a viscously damped dynamic system.

$$\boldsymbol{M\ddot{u} + C\dot{u} + Ku = F} \tag{2.10}$$

When modelling the response of a structure, the damping ratios ξ_n are often approximated based on empiricism from similar structures. The damping properties of a MDOF system is categorized as either classical damping or non-classical damping. The system is classically damped if the damping matrix $\boldsymbol{C}$ is diagonalized through the modal transformation $\boldsymbol{u} = \boldsymbol{\Phi y}$, such that $\boldsymbol{\Phi^T C \Phi}$ is a diagonal matrix. Hence, the MDOF system can be categorized as a set of uncoupled SDOF systems.

For a MDOF system the equation of motion for mode n in nodal coordinates is given by $\ddot{y}_n + 2\xi_n\omega_n\dot{y} + \omega_n^2 y_n = P_{\theta n}$, where $P_{\theta n} = \phi_n^T P_n$ is the modal load vector. At system level the diagonal matrices $\tilde{\boldsymbol{C}} = \begin{bmatrix} 2\xi_1\omega_1 & 2\xi_2\omega_2 & ... & 2\xi_N\omega_N \end{bmatrix}$ and $\boldsymbol{\Lambda} = \begin{bmatrix} \omega_1^2 & \omega_2^2 & ... & \omega_N^2 \end{bmatrix}$ needs to be introduced ot obtain the equation of motion for the system $\boldsymbol{\ddot{y} + \tilde{C}\dot{y} + \Lambda y = P_\Phi}$.

Direct damping

The direct method for constructing the viscous damping matrix is given in Equation (2.11), and provides precise control of the damping ratio in each mode. The method requires that the damping ratios are specified in all modes of vibration such that a dense damping matrix $\boldsymbol{C}$ is created. The eigenvalue problem has to be solved in order to obtain the elements in $\tilde{\boldsymbol{C}}$ and $\boldsymbol{\Phi}$, which leads to reduced efficiency of several numerical integration methods.

$$\boldsymbol{C = M\Phi\tilde{C}\Phi^T M} \tag{2.11}$$

Caughey damping

A less computationally expensive way to construct the damping matrix is the classical damping method Caughey damping. The damping matrix is constructed on the form $\boldsymbol{C} = \sum_b a_b \boldsymbol{M}(\boldsymbol{M^{-1}K})^b$, where a_b is an arbitrary constant and b is any integer $-\infty < b < \infty$. The eigenfrequencies retain the orthogonality properties described in Section 2.1.1, and the

damping matrix becomes diagonal by modal transformation. As each line in the equation of motion $\ddot{\boldsymbol{y}} + \boldsymbol{\Phi}^{\boldsymbol{T}}\boldsymbol{C}\boldsymbol{\Phi}\dot{\boldsymbol{y}} + \boldsymbol{\Lambda}\boldsymbol{y} = \boldsymbol{P}_{\boldsymbol{\Phi}}$ will become uncoupled, $\ddot{y}_n + \sum_b a_b \omega_n^{2b} \dot{y} + \omega_n^2 y_n = P_{\Theta n}$, the damping ratio described by the Caughey series can be given as $\xi_n = \frac{1}{2}\sum_b a_b \omega_n^{2b-1}$.

The use of Caughey damping is computationally efficient if $\boldsymbol{C}$ is constructed with care, such that the values of b does not lead to the damping matrix becoming a dense matrix. It is essential that no values of b is chosen in a way that leads to negative damping ratios ξ_n, as this will make the solution diverge. The advantage of the general Caughey damping matrix is that the solving of the eigenvalue problem is not necessary for specifying the values of the damping matrix, and that it with few parameters specifies the damping ratio with good precision within a chosen frequency range.

Rayleigh damping

Rayleigh damping is Caughey damping with $b = [0, 1]$, yielding the constants $\alpha = a_0$ and $\beta = a_1$, and is widely used in dynamic analysis due to its simplicity and precision. By enforcing Rayleigh damping, the damping matrix will be proportional to the mass- and stiffness matrix.

$$\boldsymbol{C} = \alpha \boldsymbol{M} + \beta \boldsymbol{K} \tag{2.12}$$

The constants α and β are computed using the damping ratios ξ_r and ξ_p in the modes with respective eigenfrequencies ω_r and ω_p. As the modal damping ratios for a structure are seldom known, and usually guessed based on data from similar structures, there is some uncertainty regarding the initial damping ratios. Thus, the modal damping ratios ξ_r and ξ_p are often chosen equal to each other, $\xi_r = \xi_p = \xi_0$. By choosing the first frequency equal to the lowest natural frequency, $\omega_p = \omega_1$, and the second frequency as an arbitrary higher frequency component of the loading, a specified damping ratio for the first mode, which usually is the most dominant in the total response, is obtained [5]. Thus, the damping ratios of the structure will have values close to the specified damping ratio ξ_0 for the modes within the specified range of frequencies, whereas the modes with higher frequencies will be damped heavily and contribute less. The equations for the Rayleigh damping ratio ξ_n and the constants α and β are given in Equations (2.13), (2.14a) and (2.14b):

$$\xi_n = \frac{1}{2}\left(\frac{\alpha}{\omega_n} + \beta\omega_n\right) \tag{2.13}$$

$$\alpha = 2\omega_r\omega_p \frac{\omega_p\xi_r - \omega_r\xi_p}{\omega_p^2 - \omega_r^2} \tag{2.14a}$$

$$\beta = 2\frac{\omega_p\xi_p - \omega_r\xi_r}{\omega_p^2 - \omega_r^2} \tag{2.14b}$$

Figure 2.1 displays a typical plot of Rayleigh damping rations. Rayleigh damping is preferred by many because of its simplicity, but care still needs to be taken when computing the damping ratios. If the range of frequencies is to small, too many modes will be damped out, whereas a too large range of frequencies may lead to an unphysically low damping ratio for some nodes. The minimum damping ratio should be $\xi_{min} = \frac{2\sqrt{\gamma}\xi_0}{1+\gamma}$ in mode $\omega_{min} = \sqrt{\gamma}\omega_p$, where $\gamma = \frac{\omega_r}{\omega_p}$ is the ratio between the highest and the lowest specified frequency. The first modes of a system will retain low damping compared to the higher modes. Hence, if the natural frequencies of the system are close to ω_{min}, it is recommended to stay critical when considering the response of a system with Rayleigh damping.

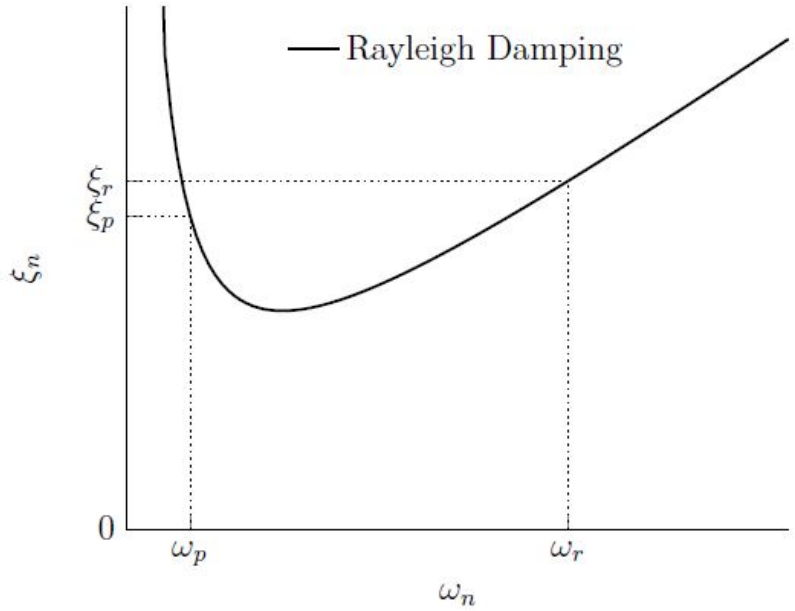

Figure 2.1: The typical shape of the damping ratio when using Rayleigh damping. The figure is found in Frøseth's master thesis [12]

One of the main advantages of Rayleigh damping is that the damping matrix has the same geometric properties as the mass matrix and the stiffness matrix, whereas the direct damping matrix is necessarily a dense matrix. This is influential for the computational efficiency of numerical integration schemes such as the Newmark method. Abaqus, the finite element program used for modelling in this thesis, uses the Hilbert-Hughes-Taylor α (HHT-α) method as its default implicit time integration scheme [37]. The HHT-α method is an extension of the Newmark method, and utilizes the inversion of the effective stiffness matrix, where $\boldsymbol{K^{eff}} = h_1\boldsymbol{M} + h_2\boldsymbol{C} + h_3\boldsymbol{K}$. Thus, if $\boldsymbol{C}$ is a dense matrix, $\boldsymbol{K^{eff}}$ will also be a dense matrix, which requires a lot of computational capacity and memory to invert. By utilizing Rayleigh damping, the damping matrix remains sparse as long as the mass- and stiffness matrices also are sparse, which is very favourable when considering computational efficiency in numerical integration schemes.

Non-classical damping

In most systems, the natural frequencies, and thus damping ratios, depend on the damping matrices of the system in addition to the mass and stiffness matrix [13]. Hence, the complex eigenvalues of the system needs to be procured in order to extract the damping ratio of the individual modes. If this is the case, the system is *non-classically damped*. If this is the case, $\boldsymbol{\Phi^T C \Phi}$ is not a diagonal matrix. Hence, the standard eigenvalue problem will be on the form of Equations (2.15) and (2.16), where $\boldsymbol{r}(t) = 2\bar{\boldsymbol{r}}_r e^{-\xi\omega_n t} cos(\omega_d t) - 2\bar{\boldsymbol{r}}_i e^{-\xi\omega_n t} sin(\omega_d t)$ is the decaying free vibration response of the damped system, and $\boldsymbol{\lambda}$ is the eigenvalues of the system. Due to their relation, solving one of the standard eigenvalue problems implies the solution of the other.

$$\begin{bmatrix} \boldsymbol{0}_{NxN} & \boldsymbol{I}_N \\ -\boldsymbol{M^{-1}K} & -\boldsymbol{M^{-1}C} \end{bmatrix} \begin{Bmatrix} \bar{\boldsymbol{r}} \\ \boldsymbol{\lambda}\bar{\boldsymbol{r}} \end{Bmatrix} = \boldsymbol{\lambda} \begin{Bmatrix} \bar{\boldsymbol{r}} \\ \boldsymbol{\lambda}\bar{\boldsymbol{r}} \end{Bmatrix} \tag{2.15}$$

$$\begin{bmatrix} \boldsymbol{0}_{NxN} & \boldsymbol{I}_N \\ -\boldsymbol{M^{-1}K} & -\boldsymbol{M^{-1}C} \end{bmatrix} \begin{Bmatrix} \bar{\boldsymbol{r}^*} \\ \boldsymbol{\lambda}\bar{\boldsymbol{r}^*} \end{Bmatrix} = \boldsymbol{\lambda}^* \begin{Bmatrix} \bar{\boldsymbol{r}^*} \\ \boldsymbol{\lambda}^*\bar{\boldsymbol{r}^*} \end{Bmatrix} \tag{2.16}$$

The quadratic eigenvalue problem

The relation $\boldsymbol{u} = \phi e^{-\omega t}$ is obtained from the general solution of the homogeneous free vibrating system. By introducing it into the second order differential equation (**??**), the quadratic eigenvalue problem is obtained.

$$\left(-\omega_n^2 \boldsymbol{M} + i\omega \boldsymbol{C} + \boldsymbol{K}\right) = \boldsymbol{0} \tag{2.17}$$

As opposed to the linear eigenvalue problem in Equation (2.5), the solving of the quadratic eigenvalue problem yields an eigenvalue λ with a real and an imaginary part, $Re|\lambda| = -\xi\omega_n$ and $Im|\lambda| = \omega_d = \omega_n\sqrt{1-\xi^2}$. This gives the relation $\lambda\lambda^* = \omega_n^2$. By utilizing the relation of the absolute value of the eigenvalue, $\lambda\lambda^* = |\lambda|^2$, the expression for the eigenvalue becomes $|\lambda| = \omega_n$. The expression for the imaginary part yields the relation $|\lambda| = \sqrt{Re|\lambda|^2 + Im|\lambda|^2}$ when substituting in the above relations. By using these relations, the expression for the damping ratio of a mode can be obtained by Equation (2.18).

$$\xi = \frac{-Re|\lambda|}{|\lambda|} = \frac{-Re|\lambda|}{\sqrt{Re|\lambda|^2 + Im|\lambda|^2}} \tag{2.18}$$

Remarks

The non-classical damping matrix is dependent on having experimental data of the structure in question. When experimental data is not available, the use of a non-classical damping matrix will be computationally expensive relative to the alternative, which is the direct method and the Caughey damping series with its special case Rayleigh damping. The Rayleigh damping is deemed to provide sufficient control over the damping ratios, and is superior to the alternatives when considering computational effieciency. Thus, due to the discussion done in this section, Rayleigh damping will be used to construct damping matrices in the continuation of the thesis.

The solution of the quadratic eigenvalue problem will be used in the thesis to determine the modal damping ratios of the finite element model by utilizing the complex eigenmodes of the system.

2.1.3 Solution methods

If the load situation on a system is not dependent on time, a static solution method can be applied. However, if the loading is time dependent, the response of the system will also be time dependent, and a dynamic solution method needs to be applied. The dynamic response of the system will depend the natural frequencies of the system and the loading frequency. If the loading frequency coincides with a natural frequency, the dynamic response will increase greatly due to resonance. If the loading frequency is low, less than approximately a quarter of the lowest natural frequency of the system [25], the dynamic effects will be small, and a quasistatic analysis may be used to calculate the response. As the moving load problem is a time dependent load situation, a dynamic analysis will be applied in this thesis.

The response history of a dynamic system can be computed using *direct integration*. Direct integration differs from modal analysis, as the dynamic equations remain the same during the step-by-step integration in time. In a nonlinear analysis, the stiffness matrix may change during the analysis, and thus it is advantageous to write the equation of motion at time step n as equation (2.19), where $\boldsymbol{R}_n^{int} = \boldsymbol{K}_n \boldsymbol{D}_n$ and $\boldsymbol{D}$ is a matrix containing the elemental degrees of freedom.

$$\boldsymbol{M}\ddot{\boldsymbol{D}}_n + \boldsymbol{C}\dot{\boldsymbol{D}}_n + \boldsymbol{R}_n^{int} = \boldsymbol{R}_n^{ext} \tag{2.19}$$

When using direct integration methods to discretize in the time domain, some assumptions are made. It is assumed that the mass matrix is positive definite, and that the stiffness matrix is at least positive semidefinite [6]. This allows for rigid body motions and massless mechanisms in the structure. Utilizing direct integration, the response in time step *n+1* is calculated using either an *explicit* method, see Equation (2.20), or an *implicit* method, see Equation (2.21).

$$\boldsymbol{D}_{n+1} = f\left(\boldsymbol{D}_n, \dot{\boldsymbol{D}}_n, \ddot{\boldsymbol{D}}_n, \boldsymbol{D}_{n-1}, \dot{\boldsymbol{D}}_{n-1}, ...\right) \tag{2.20}$$

$$\boldsymbol{D}_{n+1} = f\left(\boldsymbol{D}_n, \dot{\boldsymbol{D}}_n, \ddot{\boldsymbol{D}}_n, \dot{\boldsymbol{D}}_{n+1}, \ddot{\boldsymbol{D}}_{n+1}, ...\right) \tag{2.21}$$

Explicit integration utilizes the equilibrium conditions at previous steps to compute the next step without solving an equation system, whereas implicit integration requires the solving of a nonlinear algebraic equation based on the equation of motion at step *n+1* to predict the response.

The explicit method is computationally inexpensive since no equations solving is necessary, and convergence will not be an issue due to equilibrium iterations not being needed. The problem with explicit integration is that it is only conditionally stable, and thus requires very small time steps. Because of this, the explicit method is ideal for high speed dynamic problems over short time periods, and also for problems with discontinuous nonlinearities such as contact problems and buckling [25].

The implicit method requires the solution of nonlinear equations at each time step, and also demands convergence at each time increment using equilibrium equations. Because of this, the computation of each time increment will be computationally expensive. Implicit integration has the advantage of being conditionally stable, such that the time increments does not need to be small, and thus the simulation can be done with fewer time increments. The implicit method is considered well suited for problems with long time periods, as well as problems where the nonlinearities are somewhat smooth, such as plasticy problems [25].

The moving load problem in this masters thesis is simulating a vehicle driving across a long bridge, and as such the time period will be large. To limit the scale of this thesis, road surface roughness is not considered, which leads to discontinuous nonlinearities not being present. Thus, an implicit method will be most beneficial for the solving of the moving load problem, and will be implemented in the continuation of the thesis.

2.2 Signal processing

2.2.1 Fourier transform

The *Fourier transform* is a numerical method for creating a frequency domain representation of a signal in time domain. Considering a continuous function representing a signal *f(t)*,the analytical solution for the Fourier transform can be defined as [20]:

$$\hat{f}(\omega) = \frac{1}{2\pi}\int_{-\infty}^{\infty} f(t)e^{-i\omega t}dt \tag{2.22}$$

The Fourier transform is reversible, where its inverse is known as the *Fourier integral* and is defined as [20]:

$$f(t) = \int_{-\infty}^{\infty} \hat{f}(\omega)e^{i\omega t}d\omega \tag{2.23}$$

Discrete Fourier transform

The *discrete Fourier transform* (DFT) is an alternative method used to produce a Fourier transform. The DFT is used for discrete time signals with a finite sequence of data.

Considering a discrete time signal $\boldsymbol{f}$ and a time vector $\boldsymbol{t}$ with N function values at equally spaced data,

$$\boldsymbol{f} = [f_0 \ \cdots \ f_{N-1}]^T \tag{2.24}$$

$$\boldsymbol{t} = [t_0 \ \cdots \ t_{N-1}]^T \tag{2.25}$$

the corresponding DFT for frequency-component n is given by:

$$\hat{f}_n = \sum_{k=0}^{N-1} f_k e^{-2\pi i \frac{nk}{N}}, \quad n = 0, \ \cdots, N-1 \tag{2.26}$$

Here $\hat{f}_n$ represents the frequency spectrum of the signal. In vector notation the discrete Fourier transform is written as:

$$\hat{\boldsymbol{f}} = \boldsymbol{F}_N \boldsymbol{f} \tag{2.27}$$

where $\boldsymbol{F}_N$ represents the *Fourier matrix*

$$\boldsymbol{F}_N = \begin{bmatrix} e^{-2\pi i \frac{0\cdot 0}{N}} & e^{-2\pi i \frac{0\cdot 1}{N}} & \cdots & e^{-2\pi i \frac{0\cdot (N-1)}{N}} \\ e^{-2\pi i \frac{1\cdot 0}{N}} & e^{-2\pi i \frac{1\cdot 1}{N}} & \cdots & e^{-2\pi i \frac{1\cdot (N-1)}{N}} \\ \vdots & \vdots & \ddots & \vdots \\ e^{-2\pi i \frac{(N-1)\cdot 0}{N}} & e^{-2\pi i \frac{(N-1)\cdot 1}{N}} & \cdots & e^{-2\pi i \frac{(N-1)\cdot (N-1)}{N}} \end{bmatrix} \tag{2.28}$$

Fast Fourier transform

By using Equation (2.26) to compute a DFT for a signal, $O(N^2)$ operations are required [20], which for large data implies that the method is computationally expensive. An often used remedy to improve the computational time of the DFT is to introduce the algorithm *fast Fourier transform* (FFT). This algorithm computes the discrete Fourier transform by factorizing the Fourier matrix $\boldsymbol{F}_N$, and breaking it down into smaller problems. According to Smith [35], the FFT also produces a more precise result due to fewer calculations, which results in less round-off error. By introducing the FFT, the number of operations can be reduced to $O(N)log_2(N)$.

2.2.2 Window functions

When applying FFT to a signal, discontinuities between samples may often occur in the measured signal, as shown in Figure 2.4. These discontinuities are known as *spectral leakage*. Spectral leakage can be considered as a result of signals with frequencies not included in the basis set of frequencies [16]. These frequencies are seen as non-periodic in the window where the signal is observed.

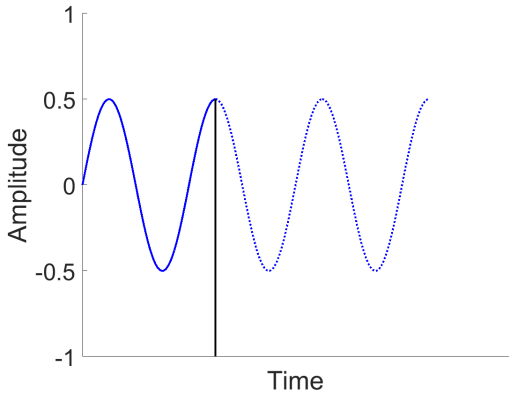

(a) Sampled segment for a sine wave

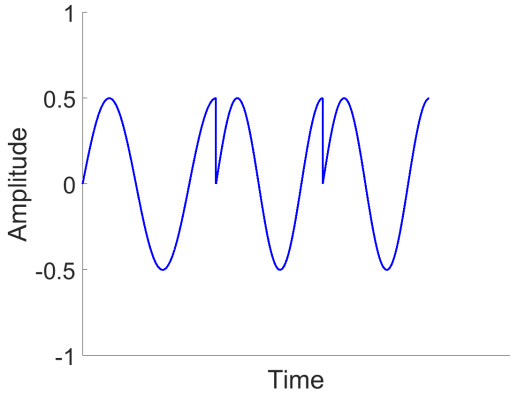

(b) Effects from spectral leakage due to periodic expansion

Figure 2.2: The FFT of a sine wave with no window function applied. The figure is based on illustrations from the master thesis by Kvåle [21]

The effects due to spectral leakage can be accounted for by introducing *window functions*. As stated by Harris [16], windows are used as weighting functions applied to data in order to reduce the magnitude of the discontinuities at the segments boundaries. A few window functions are illustrated in Figure 2.3.

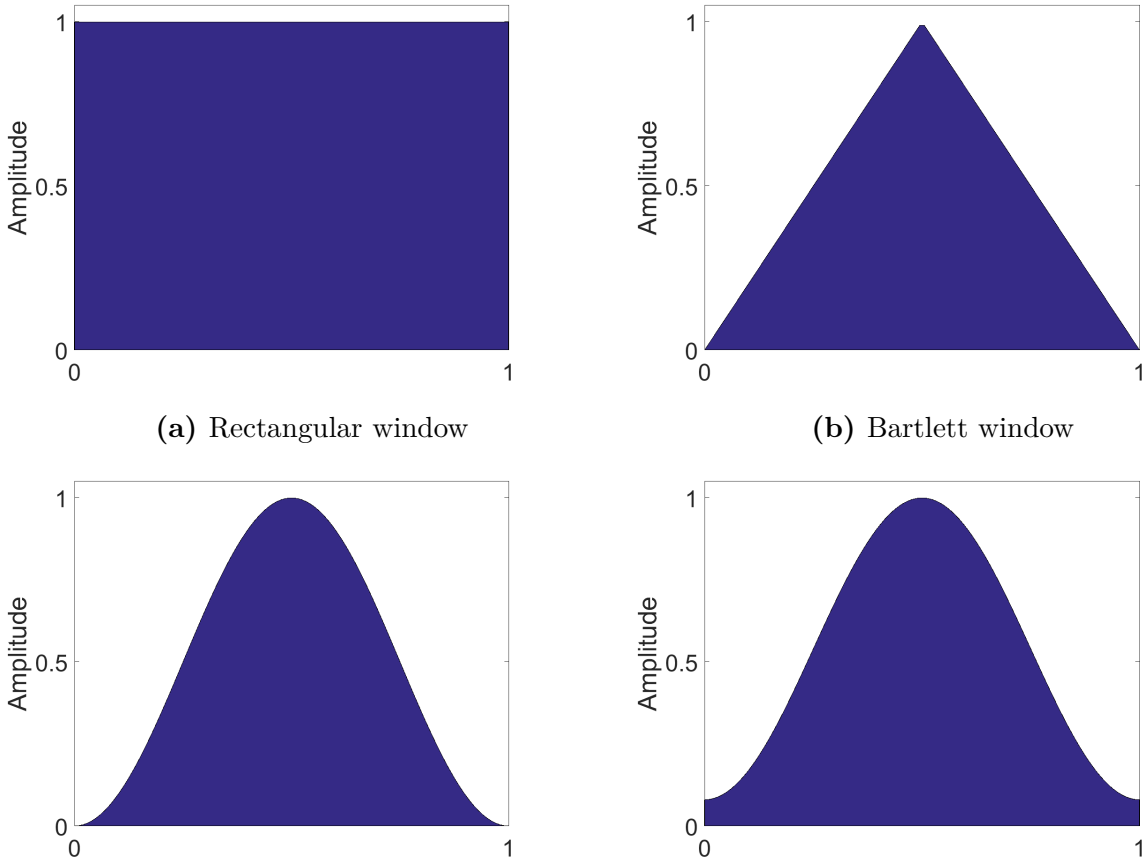

(a) Rectangular window

(b) Bartlett window

(c) Hanning window

(d) Hamming window

Figure 2.3: Illustrations of window functions. The figures are based on illustrations from the master thesis by Mork et al [29]

Window functions have small values near the boundaries for each segment, and thus reduces the amplitudes of the discontinuities at the boundaries. In Figure 2.4a, a Hanning window is applied to the same sine wave as in Figure 2.2, which results in a periodic expansion with no discontinuities.

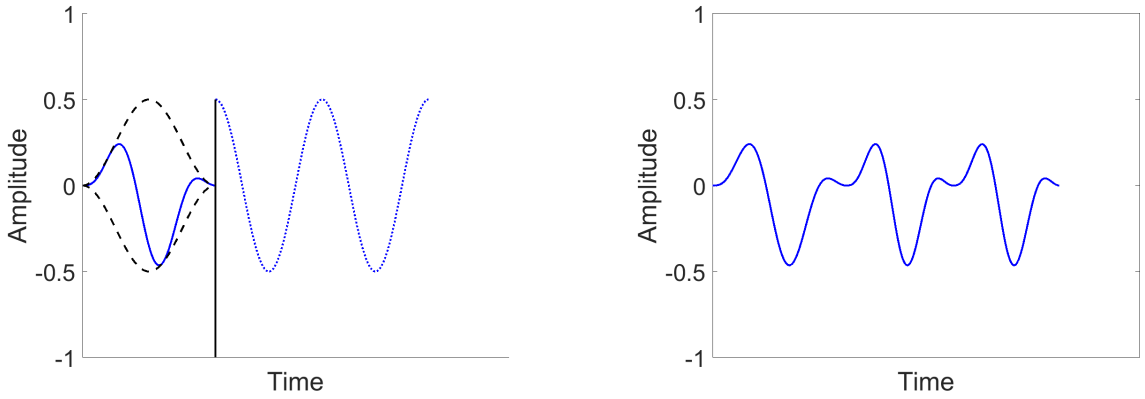

(a) Window function applied to sampled segment

(b) Periodic expansion of sine wave by windowing

Figure 2.4: A Hanning window function applied to the FFT. This figure is similar to illustrations from the master thesis by Kvåle [21]

2.2.3 Welch's method

When applying window functions and FFT to a signal, some parts of every segment is ignored due to small amplitudes near the boundaries [16]. By making the segments overlap, loss of data may be avoided.

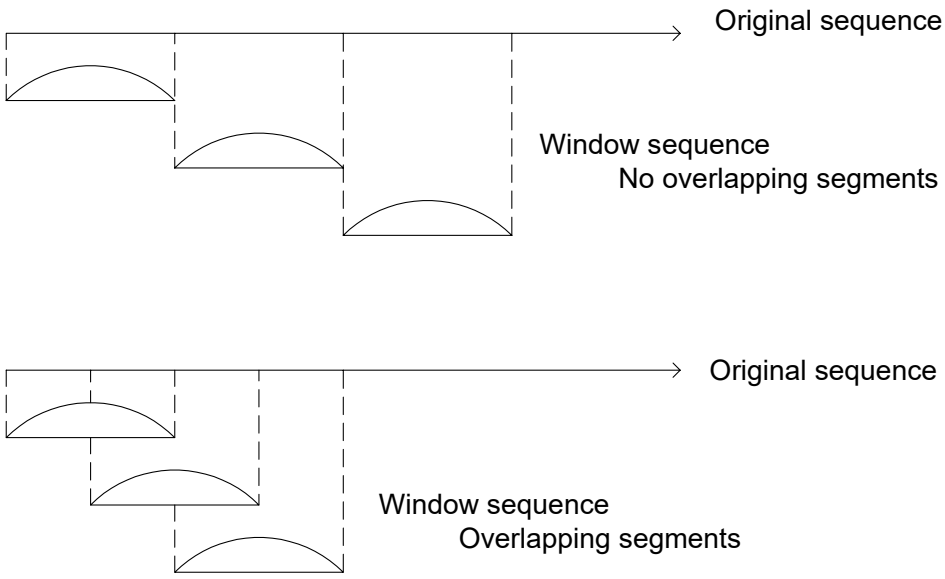

Figure 2.5: Overlapping and non-overlapping segments. This figure is based on illustrations from the article by Welch [44]

The *Welch's method* is a method that applies the FFT to estimate the power spectral density of a signal [44]. This method introduces overlapping data segments of the original signal, where each segment is windowed. Between the successive segments Welch introduces a 50 % overlap, as shown in Figure 2.5. The segments are furthermore averaged in order to decrease the variance of the power spectral density estimation [36]. The Welch's method is illustrated in Figure 2.8 for a sine function with an estimation of the power spectral density.

As shown in Figure 2.7, applying the Welch's method with a Hanning window, as can be seen in Figure 2.3c, will reduce the spread and amplitude in a FFT estimation. The Welch's method results in a lower variance for the power spectral density estimation, which can be observed by comparing the estimated FFT in Figure 2.6 and Figure 2.7.

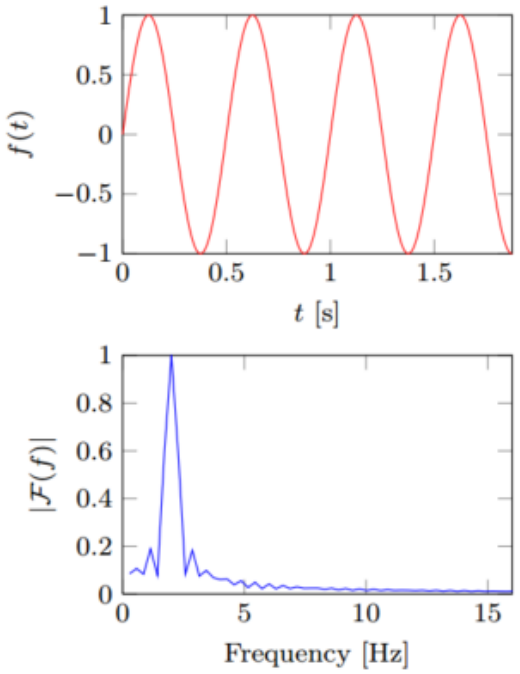

Figure 2.6: Without use of window function

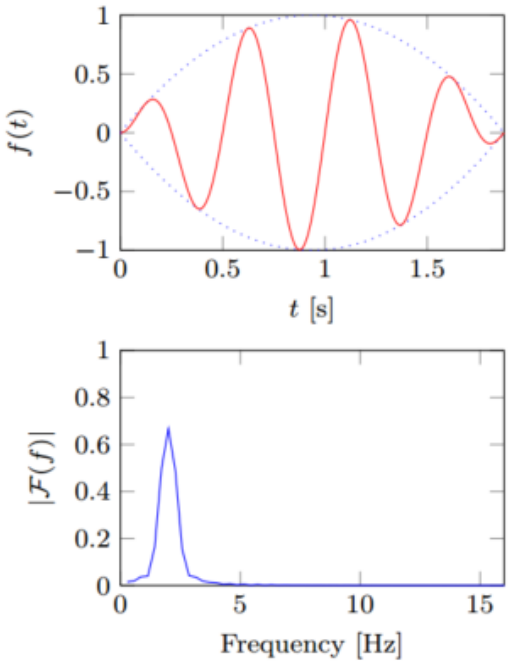

Figure 2.7: Use of Welch's window function

Figure 2.8: Illustration of a FFT for a harmonic motion [21]

2.2.4 Digital filtering

A digital filter is a numeric tool used in signal processing to remove unwanted parts of a signal, like random noise. The filter extracts the useful parts of a digital signal, leaving some frequencies unchanged and removing other frequencies.

In signal processing, digital filters are divided into two primary types: *finite impulse response* (FIR) and *infinite impulse response* (IIR). A FIR-filter is implemented by convolution, which implies that each sample of the output is a result of adding together the weighted samples of the input [35]. An IIR-filter is a recursive filter, which is an extension of filtering through

convolution. Recursion implies that some values of the output, which have previously been calculated, is re-used as an input.

In order to filter out certain frequencies, the four most common filtering methods used are: *low-passing*, *high-passing*, *band-passing* and *band-rejecting* [35]. Illustrations of these filtering methods are presented in Figure 2.9. As shown in this figure, the *passband* refers to frequencies that are passed through the filter, while the *stopband* refers to the frequencies that are removed by the filter. In the application of a digital filter to a signal, the filter should be designed in a way that effectively removes unwanted frequencies from the signal. As stated by Smith [35], a filter should have a steep *transition band* in order to separate closely spaced frequencies effectively.

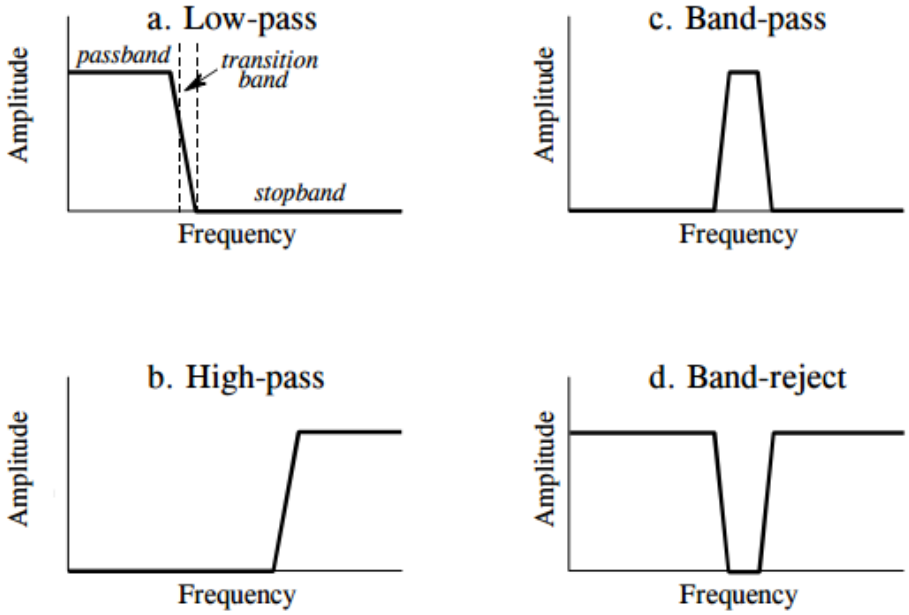

Figure 2.9: Filtering methods [35]

When choosing between the FIR-filter and the IIR-filter, two important issues should be considered: performance and speed [35]. As stated by Smith [35], the FIR-filter requires more computational time than the IIR-filter, but provides a higher performance. The shape of the frequency response for a FIR-filter can easily be defined by the user, where the IIR-filter cannot be as easily customized. In order to effectively separate closely spaced frequencies, a filter should have a steep transition band. Therefore, even though it comes at an expense of longer computational time, a FIR-filter is a preferable filter when a steep transition band is required, as the IIR-filter is less suited to separate closely spaced frequencies.

2.2.5 Numerical integration

Several numerical integration methods can be used in order to approximate the integrand for a signal. One common method is known as the *trapezoidal rule*. By considering a function $f(t)$ representing a signal with n equally spaced sample points, the approximate integral for this signal, J, is using the trapezoidal rule given by the function [20]:

$$J = \int_a^b f(t)dt \approx h\left[\frac{1}{2}f(t_1^*) + f(t_2^*) + \cdots + \frac{1}{2}f(t_n^*)\right] \tag{2.29}$$

where a and b represents the endpoints of t for the function $f(t)$, and $h = (b-a)/n$. In order to approximate a numerically integrated function of $f(t)$, *cumulative integration* may be used. This procedure calculates the integral for the entire signal and estimates a discrete sequence for the integrand. Cumulative integration is often used in numerical software like Matlab. In Matlab, the cumulative integration for a discrete signal may be calculated using the built-in function *cumtrapz*, which represents the *cumulative trapezoidal numerical integration* [26].

2.3 Stochastic processes

2.3.1 Random variables

In order to describe the concept of stochastic processes, some basic elements from statistical theory will be presented. The quantity $X(t)$, which consists of random variables over an interval t in a given time interval, is called a *stochastic process* [30]. In order to describe the behaviour of a random variable *X(t)*, the probability density function (PDF) is introduced. The PDF is a function *f(x)* that gives the probability of a random variable being equal to a given value.

In the following section, some important statistical measurements are accounted for. The estimates are presented considering a continuous random variable *X(t)*, in accordance with Walpole et al. [43].

Expected value

The *expected value*, also known as the *mean value* of a random variable *X(t)*, is given by

$$\mu_x = E[X] = \int_{-\infty}^{\infty} x f(x) dx \tag{2.30}$$

where E represents the expectation operator.

Variance

The *variance* of a random variable *X(t)* is given by

$$\sigma_x^2 = E[(X - \mu_x)^2] = \int_{-\infty}^{\infty} (x - \mu_x)^2 f(x) dx \tag{2.31}$$

where σ_x represents the *standard deviation* for $X(t)$.

Covariance

Considering two random variables, *X(t)* and *Y(t)*, the covariance is defined as:

$$\sigma_{xy} = E[(X - \mu_x)(Y - \mu_y)] = \int_{-\infty}^{\infty} \int_{-\infty}^{\infty} (x - \mu_x)(y - \mu_y) f(x, y) dx dy \tag{2.32}$$

where $f(x, y)$ represents the *joint probability distribution* between the variables x and y. The covariance of two random variables $X(t)$ and $Y(t)$ is defined as a measure of their correlation strength [43].

2.3.2 Cross-covariance

As stated by Naess [30], a stochastic process $X(t)$ is considered *stationary* if the expected value $E[X(t)]$ and the *autocorrelation* $E[X(t)X(t+\tau)]$ are independent of the time t. The variable τ represents a phase shift for the expected value $X(t)$ in time.

Considering two random, stationary processes $X(t)$ and $Y(t)$, the cross-covariance is defined as [30]:

$$C_{xy}(\tau) = E[(X(t) - \mu_x)(Y(t+\tau) - \mu_y)] \tag{2.33}$$

Autocovariance

For the special case of the cross-covariance considering only one random process, $X(t)$ is known as the *autocovariance* and is defined as [30]:

$$C_x(\tau) = E[(X(t) - \mu_x)(X(t+\tau) - \mu_x)] \tag{2.34}$$

2.3.3 Variance spectrum

Considering two random, stationary processes $X(t)$ and $Y(t)$, the Fourier transform of the cross-covariance C_{xy} produces the *covariance spectrum*, or *cross power spectral density* (CPSD)

$$S_{xy}(\omega) = \frac{1}{2\pi}\int_{-\infty}^{\infty} C_{xy}(\tau)e^{-i\omega\tau}d\tau \tag{2.35}$$

As for the special case of autocovariance, the Fourier transform of C_x gives the *auto-spectral density*, or *power spectral density* (PSD)

$$S_x(\omega) = \frac{1}{2\pi}\int_{-\infty}^{\infty} C_x(\tau)e^{-i\omega\tau}d\tau \tag{2.36}$$

The power spectral density for the stationary process $X(t)$, $S_x(\omega)$, represents the frequency content of the process. From this representation, it can be determined which frequencies are included in the signal. Thus, calculation of the power spectral density is an important tool used to determine the eigenfrequencies of a signal.

2.3.4 Response spectrum

Naess [30] states that the response will become stationary if the load is modelled as a stationary process. The variance spectrum of the response, *the response spectrum*, can be expressed in terms of the variance spectrum of the load, *the load spectrum*. This relationship is defined as [30]:

$$S_x(\omega) = |H_{fx}(\omega)|^2 S_f(\omega) \tag{2.37}$$

where $S_x(\omega)$ and $S_f(\omega)$ represents the response spectrum and the load spectrum respectively. From this relationship, the response spectrum may be determined from the variance spectrum of the loading through the *transfer function* $H_{fx}(\omega)$.

By assuming that the random, stationary process $X(t)$ is differentiable, Naess [30] proves that derivation of this process results in the following expressions:

$$\dot{X}(t) = H_{X\dot{X}}(\omega)X(t) \tag{2.38}$$
$$\ddot{X}(t) = H_{X\ddot{X}}(\omega)X(t) \tag{2.39}$$

where H represents the transfer function for the process $X(t)$ and its derivative. Considering that $X(t)$ may be expressed as a harmonic function, $X(t) = e^{i\omega t}$, the transfer function is defined as [30]:

$$H_{X\dot{X}}(\omega) = i\omega \tag{2.40}$$
$$H_{X\ddot{X}}(\omega) = -\omega^2 \tag{2.41}$$

By inserting the expressions from Equations (2.40) and (2.41) into Equation 2.37, the response spectrum for the process $X(t)$ can be estimated to:

$$S_X(\omega) = \frac{1}{\omega^2} S_{\dot{X}}(\omega) \tag{2.42}$$
$$S_X(\omega) = \frac{1}{\omega^4} S_{\ddot{X}}(\omega) \tag{2.43}$$

Alternatively, the estimation of the response spectrum for the process $X(t)$ can be written as:

$$S_X(f) = \frac{1}{(2\pi f)^2} S_{\dot{X}}(f) \tag{2.44}$$
$$S_X(f) = \frac{1}{(2\pi f)^4} S_{\ddot{X}}(f) \tag{2.45}$$

3 Moving Load model

In this section, the methods for modelling a moving load will be investigated. The analytical solution of the moving load problem will be derived and compared with a finite element model in Abaqus.

3.1 Load models

There are multiple ways of modelling traffic loading on a bridge structure. For preliminary studies of dynamic response on simple bridge models, Karoumi [19] showed that a simplified numerical model based on the superposition principle and the finite difference method may be used. However, when studying more realistic bridge models where more complex problems like nonlinear geometric effects and non-uniform cross sections may influence the response, a finite element approach will be more fitting [19]. Multiple methods for a finite element approach of the moving load have previously been investigated, and a brief comparison of these will be conducted in this thesis. For a more in-depth analysis of the previous research on the moving load, it is recommended to take a look at Karoumi's doctorate thesis [19].

When conducting a finite element analysis of the moving load problem, the vehicle is generally modelled as either a moving force, a moving mass or a sprung mass model with two degrees of freedom. Figure 3.1 shows a visual interpretation of the different models. Other ways of modelling the moving load also exists, among other as a harmonic variable force or a rigid body [11], but these models are not considered very relevant for the problem investigated in this thesis.

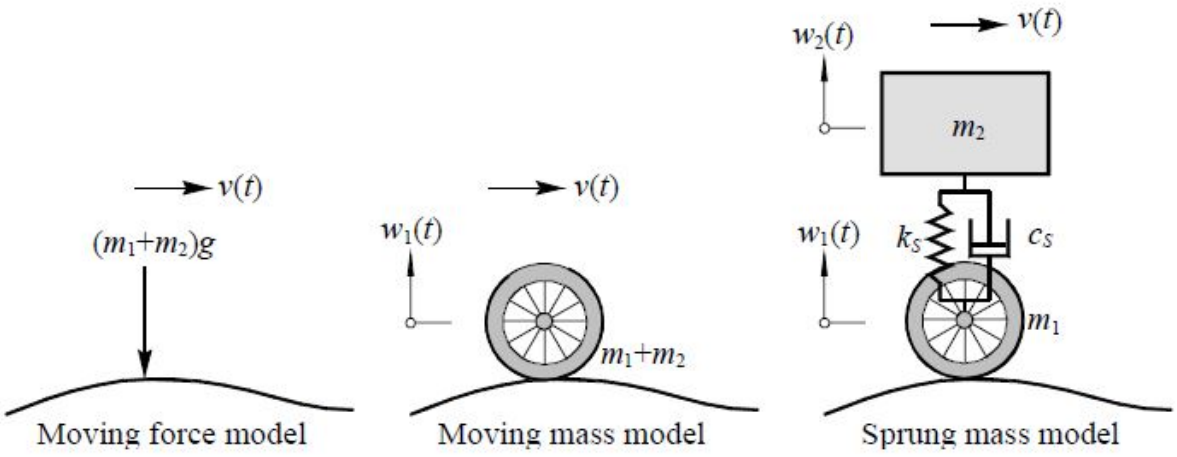

Figure 3.1: Representations of a vehicle in the moving load analysis. The figure is found in Karoumi's doctorate thesis [19]

The simplest way to model the vehicle is as a force with constant magnitude moving at a constant speed. This model is usually sufficient given a vehicle with much smaller inertia forces than the dead weight of the bridge, as the inertia forces thus can be neglected. The moving force model is, according to Frýba [11], a simplification which is valid for bridges with spans larger than 30 metres and considerably higher self weight than the weight of the vehicle. The model does not consider bridge-vehicle interaction. Factors that can cause interaction between the bridge and the vehicle because of bridge deformations are according to Karoumi [19] high vehicle speed, flexible bridge structure, stiff vehicle suspension systems and large surface irregularities. As the effects of interaction between the bridge and the moving vehicle is neglected for the moving force model, the model is only applicable when the vehicle response is not of interest [46].

By modelling the moving load as a mass travelling across the bridge, rather than as a constant force, the inertia effects from the mass of the car will be included in the analysis. This model should be considered when the inertia of the vehicle no longer can be considered small. When the mass of the vehicle is small compared to the mass of the bridge and the velocity is low, the difference between the moving force model and the moving mass model is negligible [12]. The moving force model has the disadvantage of only being applicable for vehicles moving at relatively low speeds on smooth road surfaces, as it does not consider the bouncing action of the moving mass relative to the bridge. For a road with significant surface irregularities, or for vehicles moving at high speeds, the bridge-vehicle interaction may influence the response significantly [27]. When analyzing vehicles travelling over bridges with poor road conditions, it may be necessary to account for the effect of the separation and re-contact of the moving vehicle and the bridge. For these cases, the bouncing action of the vehicle will play a decisive role [46].

The moving mass problem can be modified to account for bridge-vehicle interaction by adding a spring and a viscous damper to the model, and thus accounting for the effect of the suspension systems. As Figure 3.1 illustrates, the sprung mass model is comprised of two nodes, one related to the mass m_1 and the other related to the mass m_2. Considering that the moving force model and the moving mass model consists of only one node, the sprung mass model will be more complex and more computationally expensive. Studies have shown that the moving force model and the moving mass model are limiting cases of the sprung mass model [12]. For the limiting case, the moving mass model and the sprung mass model are equivalent in terms of beam displacement, but not for beam stresses. For small values of spring stiffness, the two cases are equivalent [31].

None of the above methods consider the effects on the vehicle from interaction between axles. This effect can be accounted for by coupling of the sprung mass models representing each axle and the coupling between bogies. In cases where it is relevant, like for railway trains or large trucks, also the coupling of multiple axles connected to each bogie should be considered. By representing the car body as a rigid body resting on bogies, each supported by one or multiple wheelsets, the models can account for a variety of motions depending on the number of DOF's assigned to the model. An example of a vehicle-bridge interaction model can be seen in Figure 3.2.

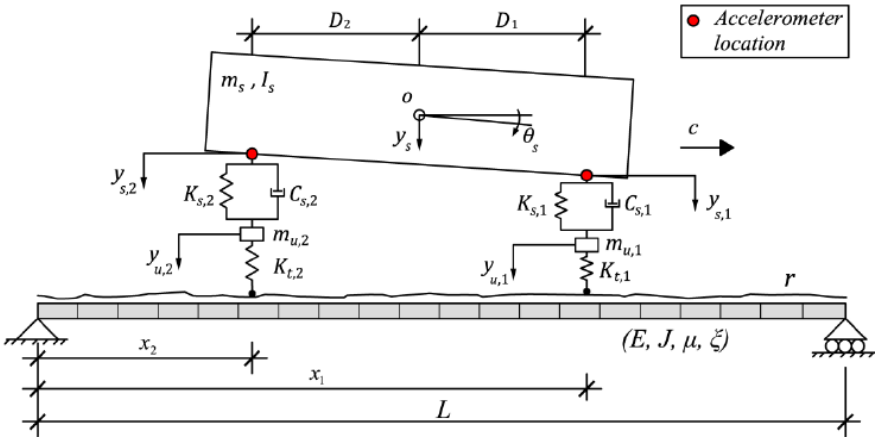

Figure 3.2: Vehicle-bridge interaction model [27]

The vehicle-bridge interaction model is accounting for many of the effects and responses which will happen when a bridge is suspected to traffic. Hence, it will create a more realistic approach to simulating the situation. It may however lead to computational difficulties. A bridge suspected to a series of vehicles appearing as a random flow, and thus an iteration process of searching for a large number of contact forces or contact points in a step-by-step time-history analysis, may lead to divergence or slow convergence. Comparative studies show that when considering the dynamics of the bridge, and not the dynamics of the vehicles, the sprung mass model and the more complex vehicle-bridge interaction models provides results which does not differ much [24].

This thesis focuses on the dynamics of bridges, and the response in the vehicles is not considered. Thus, the vehicle-bridge interaction model is not considered to be worth the extra computational requirements, considering the results found by Liu [24]. As the mass of the vehicle must be considered very small compared to the mass of the bridge, the maximal allowed mass of a trailer in Norway is 50 tonnes [32] and the weight of a cable supported bridge is expected to be several hundredfold larger than that, the inertia effect from the mass of the vehicle will be very small. As such, the difference between the moving mass model and the moving force model will be negligible [12]. The moving load model in this thesis is constructed for use on bridge models without modelled surface irregularities, and for relatively smooth road profiles the moving force can be used to predict the bridge response in an accurate way [14]. Hence, the moving force model will be used to model the moving vehicle in the finite element analysis in this thesis. The modelling choices made for this thesis is in good correlation with the findings of Karoumi [19], as he writes that when the main purpose is to study the dynamic response of bridges, very detailed vehicle models are unnecessary and generally not advantageous.

3.2 Analytical solution

Figure 3.3a shows a simply supported beam exposed to a concentrated force moving at a constant speed v_P. The beam is of length L, with mass per unit length m and bending stiffness EI. It has a constant cross sectional area, and is made from a uniform homogeneous and isotropic material which behaves linearly elastic. In the continuation of the derivation of the analytical solution for the moving load problem, it is assumed Navier's hypothesis is valid for the beam, which implies the length of the beam is large compared to its height and width. Hence, due to the validity of Navier's hypothesis, the plane sections of the beam will remain plane, and also remain perpendicular to the neutral axis.

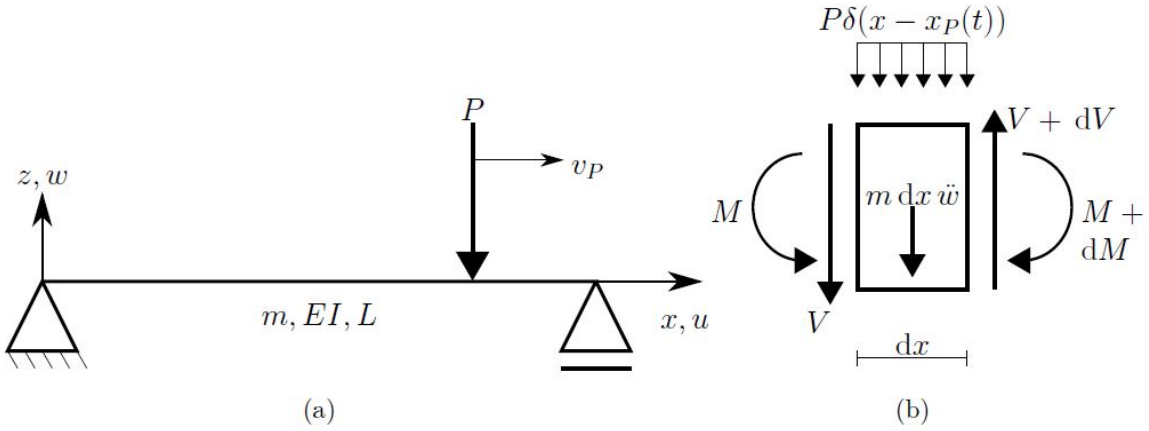

Figure 3.3: The properties and definitions utilized in the derivation of the analytical solution of the moving load problem. The figure is found in Frøseth's masters thesis [12]

In accordance with Figure 3.3a, the position of the concentrated force working on the beam is denoted x_P. It is described through the coordinate x, which follows the direction of the length axis of the beam and has its origin at the left end of the beam. The position of the load varies with the time t, and has its initial position at $x_P(t = 0) = x_{P_0}$. This yields Equation (3.1).

$$x_P(t) = x_{P_0} + v_P t \tag{3.1}$$

The introduction of the Dirac delta function (δ function), see Equation (3.2), allows for representing the moving load as a spatially distributed load.

$$\delta(x - x_P(t)) = \frac{1}{2\pi} \int_{-\infty}^{\infty} e^{i \cdot p \cdot (x - x_P(t))} dp \tag{3.2}$$

By neglecting the inertia associated with angular accelerations, an infinitesimal element with external distributed loading $P \cdot \delta(x - x_P(t))$ will have an internal moment M, an internal shear force V, and a lateral inertia force $m\ dx\ \ddot{w}$, as shown in Figure 3.3b. It is assumed that

$w(x,t) = \phi(x)y(t)$. Vertical force equilibrium yields $dV - m\ dx\ \ddot{w} - \delta(x - x_P(t))dx = 0$. The relation $\frac{dM}{dx} = V$ can be obtained by taking the moment equilibrium about the center of the element and neglecting higher order terms like $dVdx$. From Navier's hypothesis, the relation $M = -EI\frac{d^2w}{dx^2}$ can be obtained. The governing differential equation (3.3) is thus procured by inserting these relations into the vertical force equilibrium equation, and rewriting $\frac{d^2w}{dt^2}$ as $\ddot{w}$ and $\frac{d^4w}{dx^4}$ as w''''.

$$m\ddot{w} + EIw'''' = -P \cdot \delta(x - x_P(t)) \tag{3.3}$$

By embedding the relation $w(x,t) = \phi(x)y(t)$ into the homogeneous version of the differential Equation (3.3), $m\ddot{w} + EIw'''' = 0$, gives the following equation:

$$\frac{EI\phi''''(x)}{m\phi(x)} = -\frac{\ddot{y}(t)}{y(t)} \tag{3.4}$$

On the left hand side of the equals sign, the rewritten form of the differential equation (3.4) is only dependent on the variable x, and on the right hand side it only depends on the variable t. Thus, if the above equation is satisfied, both sides of the equals sign must be equal to the same constant. This constant, λ, represents the eigenvalues of the continuous system. For the continuous system, as will be shown in this chapter, there exists an infinite number of eigenvalues, which all satisfy Equations (3.5) and (3.6).

$$\ddot{y}_n(t) + \lambda_n y_n(t) = 0 \tag{3.5}$$

$$\phi_n''''(x) - \lambda_n t\frac{m}{EI}\phi_n(x) = 0 \tag{3.6}$$

The general solution of Equation (3.5) is $y_n = A_n e^{-\omega_n t}$, where ω_n represents the natural frequencies of the system. By inserting the general solution into Equation (3.5), the relation $\omega_n = \sqrt{\lambda_n}$ can be procured from Equation (3.5). As can be seen from the above relation, a negative eigenvalue, $\lambda_n < 0$ leads to an exponential growth of $y(t)$. Thus, the homogeneous solution of $w(x,t)$ will diverge. A behaviour like this is deemed as unphysical, and hence warrants positive eigenvalues $\lambda_n > 0$.

Equation (3.6) has a general solution which can be written on the form $\phi_n = B_n e^{\alpha_n x}$, which when inserted into Equation (3.6) yields the constant $\alpha_n = \lambda_n\frac{m}{EI}$. Thus, by defining ${\gamma_n}^4 = \lambda_n\frac{m}{EI}$, the relation in Equation (3.7) can be obtained. The solutions of Equation (3.7) are $\alpha_n = \pm\gamma_n$ and $\alpha_n = \pm i\gamma_n$. Utilizing Euler's formula and hyperbolic identities, the general solution of Equation (3.6) can hence be written in the form of Equation (3.8).

$${\alpha_n}^4 - {\gamma_n}^4 = ({\alpha_n}^2 + {\gamma_n}^2)({\alpha_n}^2 - {\gamma_n}^2) = 0 \tag{3.7}$$

$$\phi_n(x) = C_{1n}cos(\gamma_n x) + C_{2n}sin(\gamma_n x) + C_{3n}cosh(\gamma_n x) + C_{4n}sinh(\gamma_n x) \tag{3.8}$$

The boundary conditions $w(0,t) = 0,\ w(L,t) = 0,\ w''(0,t) = 0$ and $w''(L,t) = 0$ are governing for the SSB. The introduction of these boundary conditions into Equation (3.8) gives the solutions $C_{1n} = 0,\ C_{2n}sin(\gamma_n L) = 0,\ C_{3n} = 0$ and $C_{4n}sinh(\gamma_n L) = 0$. Considering that $sinh(\gamma_n L)$ never equals zero, C_{4n} needs to be zero. If the equation is to have a non-trivial solution, the relation $sin(\gamma_n L) = 0$ is by necessity true. This yields $\gamma_n = \frac{n\pi}{L}$. Inserting this back into Equation (3.8) gives Equation (3.9), which describes the nth vibration mode of a simply supported beam.

$$\phi_n(x) = C_n sin(\frac{n\pi x}{L}) \tag{3.9}$$

The constant C_n is the magnitude of the mode shape. Multiplying $\phi_n(x)$ in Equation (3.6) with an arbitrary constant also satisfies Equation (3.6). Thus C_n is arbitrary.

Inserting the displacement from the nth vibration mode, $w_n(x,t) = \phi_n(x)y_n(t)$, into Equation (3.3), and then multiplying both sides by $\phi_n(x)$ and integrating over the length of the beam, yields the equation of motion for the nth vibration mode, see Equation (3.10)

$$\int_0^L m[\phi_n(x)]^2 dx \cdot \ddot{y}_n(t) + \int_0^L EI\phi_n(x)\phi_n''''(x)dx \cdot y_n(t) = -\int_0^L P\phi_n(x) \cdot \delta(x - x_P(t))dx \tag{3.10}$$

The system is then subjected to *mass normalization*, thus choosing the modal mass to be equal to unity, $\int_0^L m|\phi_n(x)|^2 dx = 1$. This yields Equation (3.11) which is the nth mass normalized vibration mode.

$$\phi_n(x) = \sqrt{\frac{2}{mL}} sin(\frac{n\pi x}{L}) \tag{3.11}$$

The fundamental property of the δ function is $\int_0^L P\phi_n(x) \cdot \delta(x - x_P(t))dx = P\phi_n(x_P(t))$. Utilizing this relation, and combining Equations (3.1), (3.10) and (3.11), the equation of motion for the nth vibration mode with mass normalized mode shapes is obtained, see Equation (3.12)

$$\ddot{y}_n(t) + \frac{n^4\pi^4 EI}{mL^4} y_n(t) = -P\sqrt{\frac{2}{mL}} sin\left(\frac{n\pi v_p t}{L} + \frac{n\pi x p_0}{L}\right) \tag{3.12}$$

The homogeneous version of Equation (3.12) can be written on the form of Equation (3.5). By utilizing this and recalling the previously established relation $\omega_n = \sqrt{\lambda_n}$, the natural frequency of the system for mode n can be given as $\omega_n^2 = \lambda_n = \frac{n^4\pi^4 EI}{mL^4}$.

The equation of motion (3.12) does not consider damping. The total energy dissipation from the system can be considered proportional to the modal velocity if classical viscous damping is assumed. Thus, the homogeneous form of the equation of motion takes the form $m\ddot{y}_n(t) + c\dot{y}_n(t) + ky_n(t) = 0$. By introducing the well known relation $\omega_n^2 = \frac{k}{m}$, the modal damping ratio $\xi_n = \frac{c}{c_{cr}} = \frac{c}{2m\omega_n}$ can be used to obtain the rewritten form of the homogeneous equation of motion seen in Equation (3.13).

$$\ddot{y}_n(t) + 2\xi_n\omega_n\dot{y}_n(t) + \omega_n^2 y_n(t) = 0 \tag{3.13}$$

The introduction of damping into Equation (3.12) thus yields Equation (3.14).

$$\ddot{y}_n(t) + 2\xi_n\omega_n\dot{y}_n(t) + \omega_n^2 y_n(t) = -P\sqrt{\frac{2}{mL}}sin(\frac{n\pi v_p t}{L} + \frac{n\pi x p_0}{L}) \tag{3.14}$$

It is assumed that the simply supported beam in question is underdamped, $\xi < 1$, considering how the majority of engineering structures are underdamped structures [10]. The assumption that the beam is initially at rest, $y_n(0) = 0$ and $\dot{y}_n(0) = 0$, and that the load initiates at the left end of the beam, $x_P(0) = 0$, leads to the analytical solution for the modal coordinate y_n given by Equation (3.15).

$$\begin{aligned} y_n(t) =& \frac{P\sqrt{2mL}L^3}{n^4\pi^4 EI}\frac{1}{(1-\beta_n^2)^2 + (2\xi_n\beta_n)^2}\Bigg\{2\xi_n\beta_n cos(\omega t) - (1-\beta_n^2)sin(\omega t) \\ &+ e^{-\xi_n\omega_n t}\left[\frac{\beta_n}{\sqrt{1-\xi_n^2}}(1-\beta_n^2-2\xi_n^2)sin(\omega_{dn}t) - 2\xi_n\beta_n cos(\omega_{dn}t)\right]\Bigg\} \end{aligned} \tag{3.15}$$

The load frequency of the system is $\omega = \frac{n\pi v_p}{L}$, $\omega_n = \left(\frac{n\pi}{L}\right)^2\sqrt{\frac{EI}{m}}$ is the natural frequency, $\omega_{dn} = \omega_n\sqrt{1-\xi_n^2}$ is the damped natural frequency, $\beta_n = \frac{\omega}{\omega_n}$ represents the frequency ratio and $\xi_n = \frac{c}{2m\omega_n}$ is the damping ratio.

To obtain the displacement field for the SSB, $w(x,t)$, Equation (3.11) and Equation (3.15) are inserted into the equation for the nth vibration mode, gives as $w_n(x,t) = \phi_n(x)y_n(t)$. By summarizing all the modes, Equation (3.16) is obtained. Equation (3.16) only describes the displacement field for when the load is on the beam, $0 \leq x_P \leq L$.

$$\begin{aligned} w(x,t) =& \frac{2PL^3}{\pi^4 EI}\sum_{n=1}^{\infty}\frac{sin(\frac{n\pi x}{L})}{n^4[(1-\beta_n^2)^2 + (2\xi_n\beta_n)^2]}\Bigg\{2\xi_n\beta_n cos(\omega t) - (1-\beta_n^2)sin(\omega t) \\ &+ e^{-\xi_n\omega_n t}\left[\frac{\beta_n}{\sqrt{1-\xi_n^2}}(1-\beta_n^2-2\xi_n^2)sin(\omega_{dn}t) - 2\xi_n\beta_n cos(\omega_{dn}t)\right]\Bigg\} \end{aligned} \tag{3.16}$$

The theory behind solving the moving problem analytically has here been limited to the case of a moving load on a simply supported beam, as this is the simplest case. The theory behind the solution will also be applicable for more complex cases.

3.3 Nonlinear Finite Element Analysis Solution

In Abaqus, it is not possible to assign movement and speed to a concentrated force. In order to replicate the moving load, discretization and a load distribution model needs to be introduced. In the moving load problem, two different methods can be used to distribute the loads acting on the elements. Either by using the consistent load formulation, or by the means of load lumping. The load lumping method utilizes linear weighing functions to distribute the forces acting between nodes into statically equivalent nodal loads [6]. Load lumping is a simple and computationally inexpensive alternative for distributing moving loads, but can only approximate the solution. The consistent load formulation gives the exact solution to the mathematical problem, but at the expense of being complex and computationally expensive [22]. The solution obtained from the use of load lumping converges as the size of the elements get small enough, and thus proves to be a good method for computing moving concentrated loads [45]. Due to its simplicity and it being less computationally expensive than the consistent load formulation, as well as the results showing good accuracy of solving moving load problems [23], this thesis will use the lumped load formulation when modelling the moving load.

In a nonlinear system, the variables defining the system may vary with the time and loading, e.g. when a beam experiences bending its stiffness may increase. As such, the response of the system may not be directly proportional to the loading. The nonlinear finite element analysis (NFEA) moving load model in Abaqus consists of n beam elements, each defined by two nodes. Thus the model of the beam has *n+1* nodes. By assigning a concentrated force to each node, the model gets *n+1* equally spaced point loads. The moving load is replicated by activating each point load consecutively, and at the same time deactivating the prior point load. By assigning each point load an amplitude which goes from zero towards one when the previous load goes to zero, and fades to zero when the next load is activated, the moving load model will converge towards the analytical solution of the moving load when the spacing between the point loads included is small.

For a force starting in a position x_0 to the left hand side of the beam, the amplitude is equal to one at time $t_i = t_0 + T\frac{i-1}{n}$ for the point load $p_i = p(x_i)$ in node i, where $T = \frac{L}{v_p}$ is the steptime and $t_0 = \frac{x_0 T}{L}$ is the time between the starting position of the load and when it reaches the beam. The amplitude is equal to zero for point loads $p(x \neq x_i)$ at time t_i.

The moving load model is created for a simply supported beam, as the analytical solution of the moving load problem for a single moving load on a simply supported beam is derived in Section 3.2. The beam has a rectangular cross section with a constant cross sectional area. By comparing the analytical solution and the solution from the NFEA model for the simply supported beam, the validity of the moving load model can be confirmed. When the model is validated, it can later be implemented onto more complex structures, like Abaqus models of cable-supported bridges.

The analytical solution considers a damped system onto which Rayleigh damping has been applied. Choosing $\omega_p = \omega_1$ and $\omega_r = \omega_{10}$ yields the constants $\alpha = 0.0146$ and $\beta = 0.0067$. The minimum damping ratio is $\xi_{min} = \frac{2\sqrt{\gamma}\xi_0}{1+\gamma} = 0.099$ when using $\xi_0 = 0.05$, see Section 2.1.1. The Rayleigh damping for the system is shown in Figure 3.4, with a minimum damping ratio $\xi_{min} = 1.0\ \% > 0.99\ \%$. The stapled lines marks the range between ω_p and ω_r. Taking this into account, a damping ratio of $\xi_0 = 5\ \%$ is chosen as suitable for the beam.

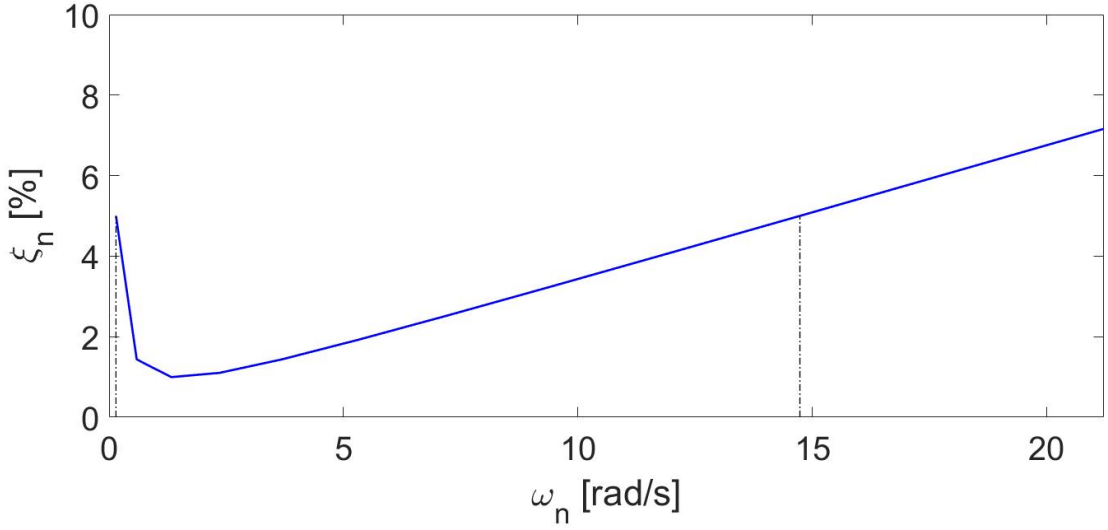

Figure 3.4: The Rayleigh damping for a simply supported beam with the characteristics given in Figure 3.5

Figures 3.5 and 3.6 shows the deflection at the midspan of a SSB when using the analytical solution and when using the finite element analysis with different element sizes.

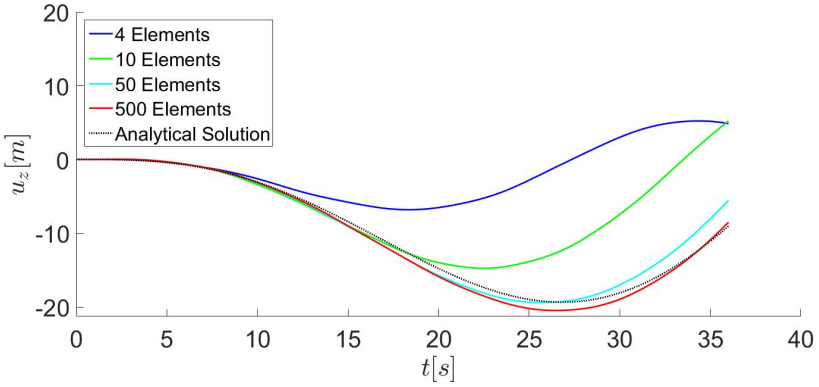

$Length$	100 m
$Width$	0.1 m
$Heigth$	0.1 m
E	$2.1 * 10^{11}$ N/m^2
ρ	7850 kg/m^3
α	0.0146
β	0.0067
F_{car}	1 kN
v_{car}	10 km/h

Figure 3.5: Comparison of the NFEA solution and the analytical solution for the displacement at midspan for a moving load on a simply supported beam

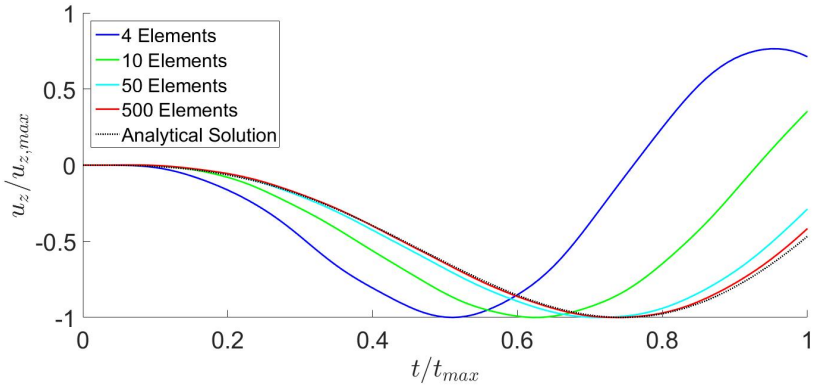

$Length$	100 m
$Width$	0.1 m
$Heigth$	0.1 m
E	$2.1 * 10^{11}$ N/m^2
ρ	7850 kg/m^3
α	0.0146
β	0.0067
F_{car}	1 kN
v_{car}	10 km/h

Figure 3.6: Comparison of the NFEA solution and the analytical solution for the relative displacement at midspan for a moving load on a simply supported beam

The results in Figures 3.5 and 3.6 shows that the NFEA solution resembles the analytical solution when the beam is discretized into many elements. The beam is very slender, and thus a very fine mesh is needed to achieve convergence. The results in Figure 3.5 shows the deflection at midspan for the undamped case of the simply supported beam acted upon by a moving load. When the load enters and moves across the beam, it may instigate a dynamic amplification of the static load due to oscillations. Introducing damping into the structure may therefore be influential in a moving load model, as it reduces oscillations over time. Rayleigh damping, with an initial damping ratio $\xi_0 = 5$ %, is used in accordance with the conditions for the analytical solution presented in Figure 3.5. As can be seen in Appendix B.1.1, Figure B.1 and Figure B.2 shows that it is hard to tell if introducing damping improves the behaviour of the beam when the mesh is course, but Figure B.3 shows that damping gives a behaviour closer to the analytical solution when the mesh is fine.

As seen in the displacement plots for the midspan of the beam in Figures 3.7 and 3.8, and also in Figures B.4 and B.5 in Appendix B.1.1, showing the same situation but with real displacements, when the beam is divided into enough elements, the moving load solution converges towards a solution very close to the analytical solution.

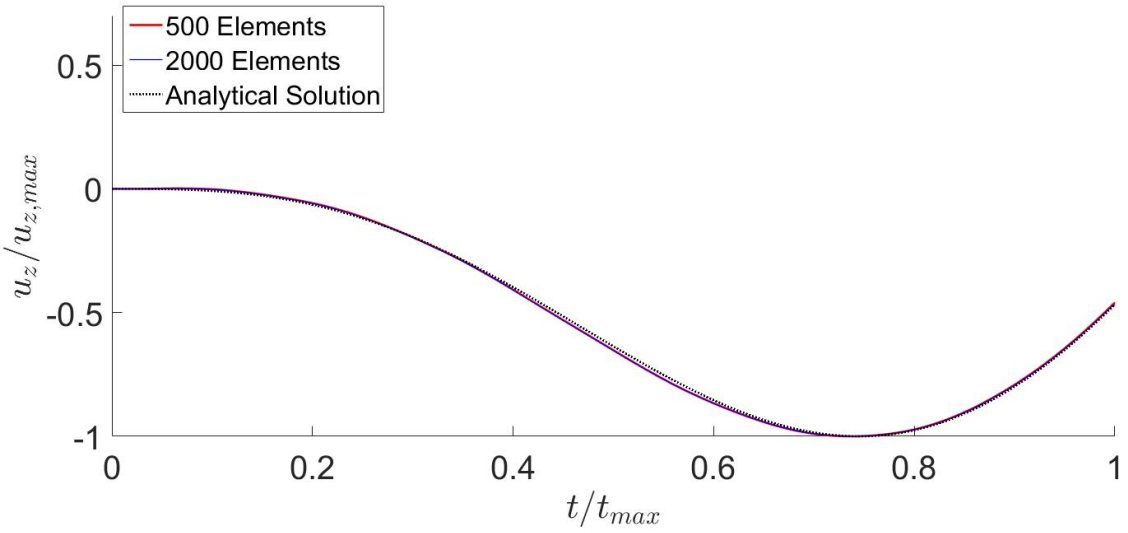

Figure 3.7: The relative displacement at midspan for a simply supported beam with Rayleigh damping of $\xi_0 = 5$ %, discretized into 500 and 2000 elements

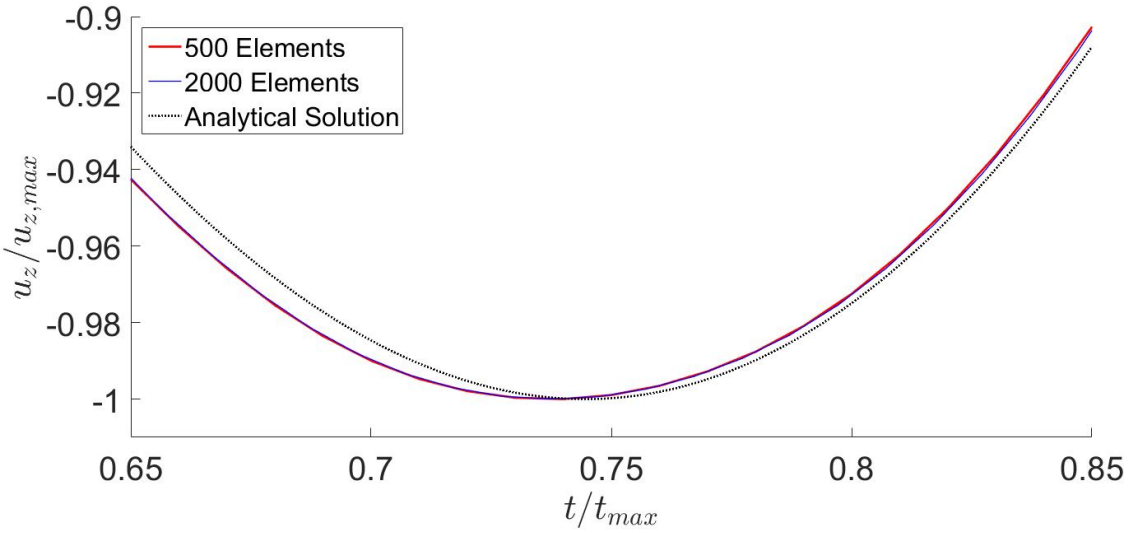

Figure 3.8: Zoomed in section at maximum relative deflection at midspan for the simply supported beam with Rayleigh damping of $\xi_0 = 5$ %, discretized into 500 and 2000 elements

As can be seen in Appendix B.1.1, damping influences the deflection of the simply supported beam subjected to a moving load. Although the deviation between the damped and the undamped case is small, it is significant, and damping should hence be introduced into the finite element model when examining a damped structure. Thus, Rayleigh damping will be implemented for the material in the continuation of the formulation of the moving load model. The results from Figure B.4 shows that the moving load model in Abaqus converges towards the analytical solution when the beam is discretized into many elements and damping is considered. The results from the simulations also show that the beam displays too stiff behaviour when a course mesh is applied. This might be because the rotational effects from the travelling load are not properly represented when the spacing between nodes becomes to big. As Abaqus can not represent a load on the element between nodes, just in the nodes, the moving load model will be a "jumping load" model when the mesh is course. To account for these effects, moments are enforced in the nodes the load travels between, see Figure 3.9. The magnitude of the moments will vary with the position of the moving load, with a maximum of $M(\frac{x}{L} = 2) = \frac{PL}{2}$ when the load is in the middle of the element. This will give some deflection at the position of the load, even when it is not in a node, and as such give a more physical behaviour when the element length is large. A comparison between the analytical solution and the finite element solution with and without enforced moments in margin nodes is shown in Figures B.8 to B.10 in Appendix B.1.2. The simulation is conducted with the same conditions as shown in Figure 3.5.

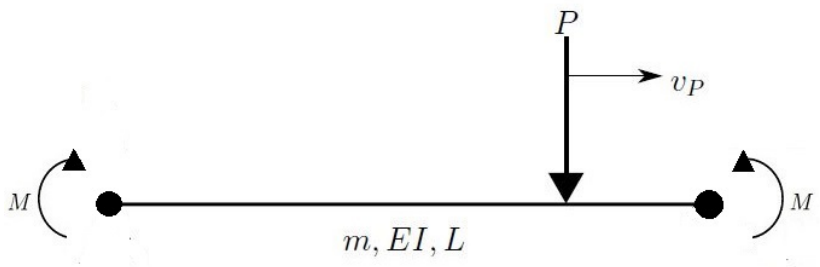

Figure 3.9: The moving load model with enforced moments in the nodes bounding the load

As the plots in Appendix B.1.2 show, the model with enforced moments give results closer to the analytical solution when the element is divided into few elements. The modelling of the beam with enforced moments at the nodes between the travelling load gives the same results as the model without enforced moments when the mesh of the beam is fine. This is due to the enforced moments, $M = P \cdot x$, getting so small they are negligible when the distance between the nodes, and thus the distance between the load and the node x, gets very small. The finite element solution converges towards the analytical solution for a very fine mesh, as can be seen in Figure B.11 in Appendix B.1.2. Hence, when taking the results from the simulations on the simply supported beam into account, enforced moments in the bounding nodes for the moving load will be included in the formulation of the moving load model in the continuation of this thesis. The results also suggests that if a moving load model displays the same behaviour with and without enforced moments in the boundary nodes, the response converges towards the analytical solution.

The FE model of the moving load, as well as the analytical solution for the moving load, is based on Euler-Bernoulli beam elements, see Figure 3.10. 2D Euler-Bernoulli beam elements in Abaqus are named B23-elements, and can be obtained my modelling the part as a wire.

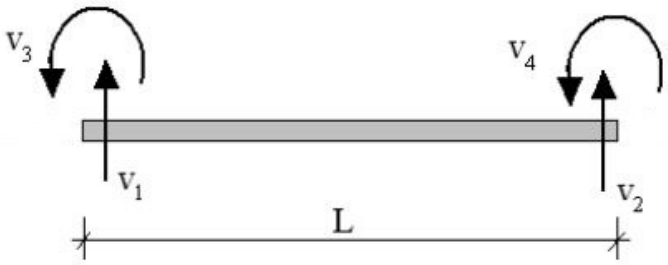

Figure 3.10: Euler-Bernoulli beam element

The SSB model is built in the same script in Matlab used for formulating the moving load on the beam. This ensures the possibility of modifying the properties of the beam according to the relevant specifications. The Matlab script takes in input info on the material properties and the dimensions of the beam. By specifying how many elements the beam should be divided into, the script meshes the beam and creates nodes between the elements.

The script allows for multiple moving loads, to simulate the effect of multiple cars moving across the beam, and also allows for each car to have more than one axle. By creating and assigning a separate amplitude for each of the point loads in the node, it is ensured that when an axle reaches an arbitrary position on the beam, the point load in the corresponding node has an amplitude of one, and the amplitude of the point loads in all the nodes where there is no axle is zero. All of the simulation takes place in one single time step.

For further investigation of the implementation in Abaqus of the moving load across a simply supported beam, the input file, as well as the full Matlab script for creating the input file, is included in the digital appendix.

4 Numerical methods for data processing

In this section the numerical methods and calculations used to separate wind- and traffic induced vibrations will be presented. Each numerical method is based on scripts produced in MATLAB. The first two methods are based on analyses of the response in time domain to identify vibrations caused by traffic. The next two methods considers analyses for the frequency content for wind- and traffic induced vibrations, and the attempt to separate these responses. The final method is based on numerical integration to estimate deformations due to traffic induced vibrations.

4.1 Main assumptions

Before presenting the numerical methods used in this thesis, some assumptions must be taken into account. These assumptions, and their validity, will later be assessed in the case study.

One important aspect to consider in the numerical analysis is the frequency domain for both the traffic- and wind induced vibrations. Brownjohn et al. [3] claims that data from wind induced response in the frequency domain of 0 - 1 hertz corresponds to the useful range of the response for the bridge deck and towers. It is therefore assumed that this is representative for the numerical analysis in the case study. Heavy vehicles applies most of its dynamic loadings in the frequency domain of 1.5 - 4 hertz [15]. This does not necessarily mean that the frequencies excited by vehicles does coincide with the frequencies excited on a system. This leaves an uncertainty regarding which frequencies are excited from wind and which are from vehicles, and the investigation of this will be an important part the case study.

In the analysis only the vertical accelerations will be accounted for. For the measurements and the observations of the vertical acceleration response for a bridge, it is assumed that heavy vehicles will produce larger accelerations than wind. As stated by Green [15], the dynamic loading from heavy vehicles applies loadings in a higher frequency range than wind. This assumption will be used as a basis for the scripts elaborated upon in Section 4.2.1 and Section 4.2.2.

4.2 Analysis of response in time domain

4.2.1 Identification of traffic induced vibrations

Identification of response caused by traffic induced vibrations on bridges is often carried out by analysing the recorded acceleration response of the bridge. This method is implemented in the script *trafficAcceleration*. The acceleration response is recorded by accelerometers distributed along the bridge.

To validate which parts of a recorded acceleration response is caused by traffic induced vibrations, a logging of the traffic for a time period can be used. This log provides a dependable input which may be used in comparing the response recorded from the bridge with the type of loading passing the bridge at each accelerometer. The log should consist of the time for entering and exiting for every vehicle passing the bridge. To distinguish between heavy vehicles and passenger cars, as these may instigate very different response, each logged vehicle should be distinguished based on the size of the vehicle. The log is also an important tool for the other numerical methods, in order to evaluate which parts of the acceleration response that is caused by traffic induced vibrations. For further examining on how a traffic log may look, the complete log used in the case study can be found in Appendix A.2.

When comparing the acceleration response and the traffic log, the recording devices on the bridge and the digital clock used for the logging are needs to be synchronized with respect to time. It is of interest that the accelerations in the response due to heavy vehicles and private cars are easily identified based on the observations in the log. This is achieved by implementing the subroutine *setDate* in the script *trafficAcceleration*, which analyses the recording and produces a time vector with the same length as the recorded accelerations in real time. By introducing the subroutine *setDate*, it becomes easier to observe how the presence of traffic coincides with the acceleration response.

4.2.2 Analysis of moving traffic

Using the script *trafficAcceleration* to analyse the acceleration response, only the magnitude and oscillation frequency of the response is analysed. This alone may not be sufficient to validate that a moving vehicle is observed. By analysing the acceleration response for two sections along the bridge, the coherence in time domain of the sections can be calculated. Assuming that the acceleration response from a heavy vehicle is the dominant response for a limited time period, it might be possible to calculate the time a vehicle spends moving between two accelerometers on the bridge.

By calculating the cross-covariance for the acceleration response recorded at each section, the time lag of the response can be determined. The time lag is assumed to correspond to the time for a vehicle moving between two sections containing accelerometers. This method is implemented in the script *trafficCrossCovariance*. The calculation of the cross-covariance, and the corresponding time lag for the acceleration responses, is carried out by implementation of the built-in Matlab function *xcov* in the script.

4.3 Analysis of response in frequency domain

4.3.1 Power spectral density estimate of response

The two previously described scripts, *trafficAcceleration* and *trafficCrossCovariance*, analyses the acceleration response in time domain. These scripts analyse how the response due to traffic might be identified, but they can not be used in order to separate the responses from wind and traffic. Thus, it is necessary to analyse and separate which eigenmodes that are excited due to response from wind and traffic. This is carried out by analysing the frequency content of the acceleration response. The analysis of this numerical method is implemented in the script *trafficSpecter*.

In order to analyse the frequency domain of the acceleration response, a discrete Fourier transform of the response must be carried out. The use of Welch's method provides an effective estimate of the power spectral density for a signal using fast Fourier transform. The power spectral density may be effectively calculated by introducing the built-in Matlab function *pwelch* in the script *trafficSpecter*. The function *pwelch* produces an estimation of the power spectral density from a discrete data signal using the Welch's method. For this script, the Welch method is chosen to consist of segments with 50 % overlap, and the *Hamming window* is chosen as the windowing function.

When estimating the power spectral densities for the acceleration response, there might be initial offsets in the recordings. These offsets appear as non-zero averages in the recordings, and might also appear as linear trends over time [17]. The effects due to the offsets results in large amplitudes for the first frequency in the power spectrum. The application of the least-square method to the recorded response, and removing these trends from the response, the undesired effects in the power spectrum can be removed. In Matlab, the function *detrend* calculates the least-square fit of a straight line for a data vector, and subtracts the trend from the data. Thus, by implementing *detrend* to the acceleration before performing the Welch method in the script *trafficSpecter*, the effects from the offset will be removed.

Combined with the script *trafficAcceleration* and the traffic log, the power spectral density estimations may be analysed with respect to the occurrences of vehicles crossing the bridge. The script *trafficSpecter* considers cases of the response where heavy vehicles and passenger cars dominate, identified using *trafficAcceleration*. Cases with low wind speeds as well as cases with high wind speeds are considered.

The script *trafficSpecter* is also useful for identifying eigenfrequencies from the acceleration response. The eigenfrequencies appear as peaks in the power spectral density estimates.

4.3.2 Response filtering

In order to analyse the responses due to traffic induced vibrations, the response caused by wind should be separated from the acceleration response. The frequency domain for wind induced response is assumed to occur in the range 0 - 1 hertz, while the dynamic loadings from heavy vehicles is assumed to be applied mostly in the range of 1.5 - 4 hertz [3, 15]. Considering these assumptions, and by applying digital filters to the acceleration response, the induced responses from wind and heavy vehicles might be separated. This procedure is implemented in the script *trafficFilter*.

The design of the digital filter is carried out by implementing the built-in Matlab function *designfilt* into the script. In order to separate the acceleration responses into wind induced and traffic induced vibrations, two digital filters are designed using the function *designfilt*. One high-pass filter, and one low-pass filter. A filter should have a steep transition band to be able to effectively separate closely spaced frequencies [35]. Thus, the design for the filters is carried out by using convolution through a FIR-filter. The filtering with the respective filters is carried out by applying the built-in Matlab function *filtfilt* to the acceleration response.

4.4 Numerical integration of response

For an analysis of the responses from a bridge, the output from the recording devices is, in most cases, given by accelerations from the bridge deck and pylons. When directly comparing the acceleration responses of the bridge and the FE model, it might be difficult to observe the similarities for these two responses. In order to evaluate the accuracy of the responses from the simulation, an analysis of the displacements might prove more useful. By comparing the displacements rather than the acceleration responses, the trends and the magnitude of the responses are more easily observed. As such, a numerical integration of the recorded accelerations might be a useful method in comparing the responses from the bridge with the FE model. This method is implemented in the script *calcDisplacement*.

In the script *calcDisplacement*, acceleration response is subjected to numerical integration by the use of the subroutine *acc2disp*. The routine is provided by NTNU, and estimates displacements from the acceleration response by utilizing *cumulative trapezoidal numerical integration* through the built-in Matlab function *cumtrapz*. In the estimation of displacements, the integrated response is high-pass filtered in order to remove the static response. It should be mentioned that the calculated displacements from the subroutine *acc2disp* does not give an exact representation of the real displacements. Hence, in order to evaluate the validity of the numerical integration, it is necessary to analyse the frequency content for the estimated displacements. The analysis is carried out by comparing the power spectral densities from the integrated displacements with the power spectral densities for the displacements, calculated using the acceleration response and a transfer function.

5 Case Study of the Hardanger Bridge

Figure 5.1: Overview of the Hardanger Bridge. The picture is obtained from the websites of the Norwegian Public Roads Administration [40]

In order to investigate the methods presented for examining the response from traffic induced vibrations on cable-supported bridges, a case study will be performed on the Hardanger Bridge. The case study is going to investigate if traffic on the bridge may be identified, and what information regarding the response of the traffic loading it is possible to acquire. The case study will also examine a finite element modelling of moving loads as a means of estimating the response from traffic.

To carry out the case study, some assumptions had to be made, and there are some sources of insecurity present:

- To limit the scope of the thesis, only vertical accelerations will be considered. Thus, some effects of the traffic load may not be identified. As traffic induced forces mostly works in the vertical direction, it is deemed reasonable to examine only the vertical response.
- The Hardanger Bridge has 16 accelerometers along the bridge deck. In general, only two sections of the bridge containing sensors has been investigated in the case study.
- To limit the scope of the thesis, solely the response from traffic induced vibrations is investigated in the case study. Thus, effects from interaction between wind and traffic is neglected.
- The logged vehicles has been assigned a constant speed based on the time they spent driving across the bridge and the length of the bridge. No data regarding the actual velocities of the vehicles exists. As such, the velocities are regarded as constant in the calculations.

5.1 The Hardanger Bridge

The Hardanger Bridge is the longest suspension bridge in Norway, with a main span of 1310 metres and a total length of 1380 metres. The pylons at the ends stand 200 metres high, and the sailing height beneath the bridge is 55 metres [2]. With one lane in each direction of traffic, as well as accommodated walkway and bicycle path, the Hardanger Bridge goes from Bu to Vallavik, and replaces the ferry-connection between Bruravik in the municipality of Ulvik and Brimnes in municipality of Eidfjord. The project, with a cost of 2,3 billions NOK [2], is a part of Riksvei 7 which is one of the main thoroughfares between Oslo and Bergen. The bridge was opened the 17th of August 2013, and is supposed to serve the following functions:

- Better communication in the inner Hardanger
- Better regional transportation between Odda and Voss, and between Bergen and Hardanger towards Hallingdal
- Offer a better service for the traffic with ferry free connection east-west and north-south

In addition to the bridge itself, the project also considers the means of approaching the bridge, including 2.4 kilometres of tunnels, 800 metres of new roads and 900 metres of walkway and a bicycle lane. To give the trafficants an early view of the bridge and the fjord crossing, the tunnel opening at Vallavik is 23 metres high, and at Bu it is 15 metres high, making the tunnel one of a kind in the world [2].

Figure 5.2: Illustration of the Hardanger Bridge. The illustration is found on the websites of the Norwegian Public Roads Administration [40]

5.1.1 Structure

The Hardanger Bridge is a slender structure. The 1380 metres long bridge deck consists of a hollow girder with a cross section of eighteen times three metres [39]. The bridge is suspended through cables anchored into mountains on both sides of the bridge. The suspension cables are supported at the top of the pylons on each side of the bridge, and is extended continuously between the pylons. The bridge deck is connected to the cables by the means of vertical hangers.

The Hardanger Bridge is despite its slender architecture a massive construction. There has been used a total of 22400 cubic metres of concrete and 3800 tonnes of reinforcements when including the tunnels [2], and there is 15500 cubic metres of concrete in the pylons and their foundations alone. Both B35 and B45 concrete has been used in the construction [41]. Consider that normal concrete has an approximate density of 2400 kg/m^3 [9], and add the 15000 tonnes of steel construction [2], and this yields the total weight of the bridge as approximately 53000 tonnes. When including the tunnels the weight becomes 73000 tonnes.

The structure of the bridge is described in detail in Appendix A.1.1

5.1.2 Recording devices

In order to record the response of the Hardanger Bridge, a monitoring system is installed on the bridge, which is shown in Figure 5.3. This system consists of several recorders, marked as *Data loggers* in Figure 5.3, where each recorder is connected to three components: a digital sensor, a GPS-antenna and a wifi-antenna. The recorders are connected by an Ethernet connection using the wifi-antennas, and the data from each recorder is adjusted with respect to time through the GPS-antenna [18]. The monitoring system also consists of a main data logger which is connected to all recorders on the bridge. The main data logger saves the recording data and transfers it to NTNU for analysis.

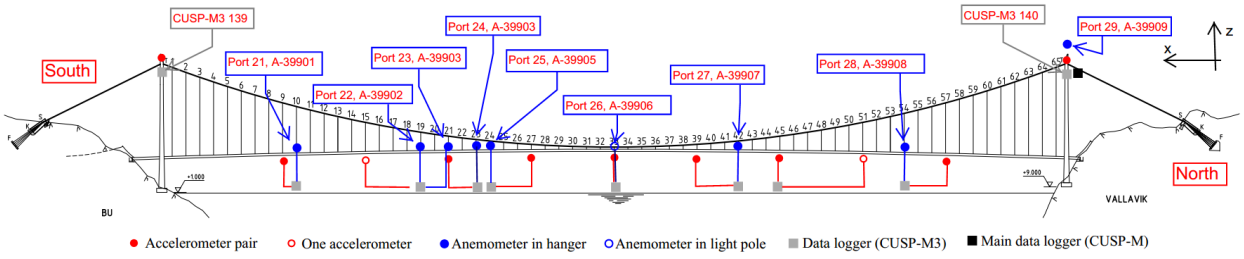

Figure 5.3: Positions of digital sensors and recorders on the Hardanger Bridge. The figure is obtained from the Norwegian Public Roads Administration.

On the Hardanger Bridge there are a total of ten recorders, of which eight are positioned along the main span of the bridge and one on top of each pylon. The recorders along the bridge are fastened inside the girder. Each recorder is connected to digital sensors, in the

form of accelerometers and anemometers measuring respectively accelerations and velocities. Information of the location of each recording device is given in Appendix A.1.2.

Accelerometers

As shown in Figure 5.3, 20 accelerometers are installed on the Hardanger Bridge. A total of 16 accelerometers are placed along the bridge's main span, while the remaining four accelerometers are installed pairwise on top of each pylon. On the main span of the bridge, the accelerometers are installed pairwise, with the exception of two sections, as can be seen in Figure 5.3 and Figure 5.4.

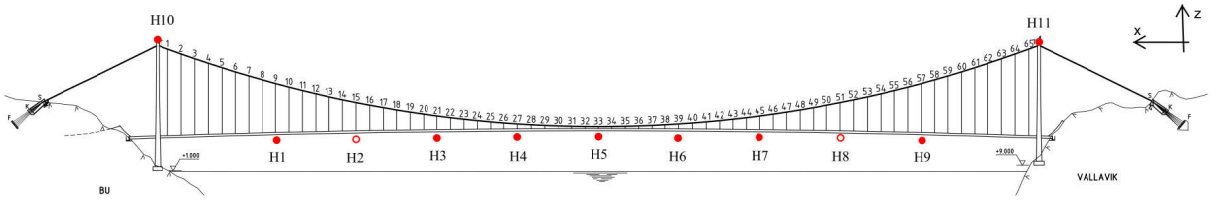

Figure 5.4: Placements of accelerometers along the Hardanger Bridge. The figure is obtained from the Norwegian Public Roads Administration.

The accelerometers along the main span of the bridge are equally spaced by 120 metres in the longitudinal direction, with the exception of the sensors near the midspan. These are positioned seven metres north with respect to the midspan, and thus will be positioned 127 metres and 113 metres relative to the nearest accelerometers.

The accelerometers are attached to the bulkheads beneath the bridge deck, as illustrated in Figure 5.5. Each accelerometer is oriented such that its axes are aligned to coincide with the axes of the bridge. Thus, each accelerometer measures accelerations in the x-, y- and z-direction related directly to the bridge's orientation. For the sections of the bridge with pairwise accelerometers, the torsional accelerations along the longitudinal direction of the bridge can be calculated.

In this case study, mainly two sections of the Hardanger Bridge containing accelerometers will be analysed. The reason for analysing just two of the sections on the bridge, is partly to limit the scope of the thesis, but also due to the assumption that two sections positioned at different locations of the bridge will provide a representative behaviour for the response of the bridge. In this case study, the response from section H5 and section H7 will mostly be used in the analysis. The position of these sections can be seen in Figure 5.4. Section H5 has been chosen because it is positioned near to the midspan of the bridge, where it is assumed that the largest deformations will take place. Not all of the eigenmodes of the bridge can be observed at the midspan, due to asymmetric motion in some of the eigenmodes. Therefore, it is deemed necessary to analyse the response in more than just one section, and for this study, the accelerometer in section H7 is used in the analysis.

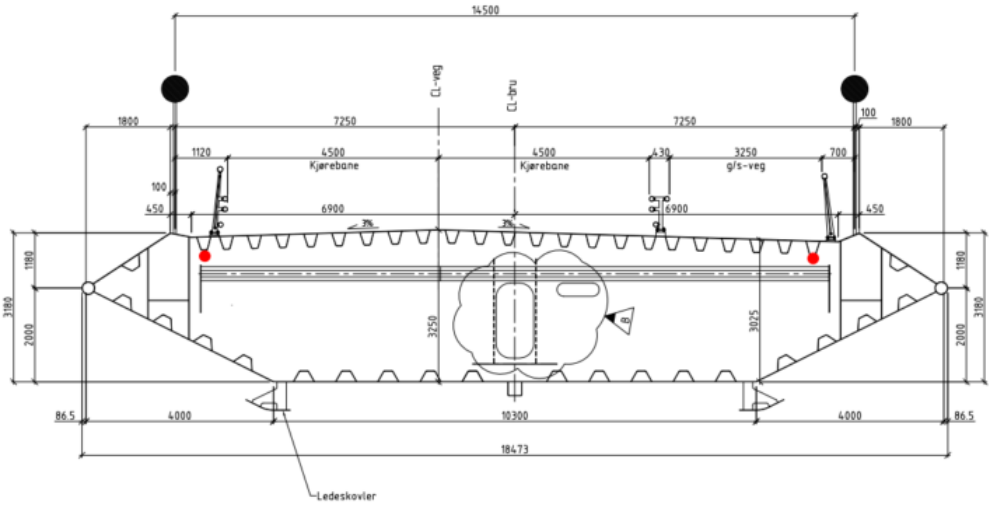

Figure 5.5: Cross-section of the Hardanger Bridge, showing the positions of the accelerometers. The figure is obtained from the Norwegian Public Roads Administration.

Anemometers

The anemometers on the bridge records the horizontal and vertical wind velocities, including the wind angle with respect to the bridge's orientation. There are in total nine anemometers, where eight are positioned along the main bridge span, and one is on top of the northernmost pylon, see Figure 5.6. The anemometers along the bridge span are mounted on hangers eight metres above the bridge deck. As stated by Øiseth [18], the anemometers are distributed in a way that makes it possible to analyse the coherence and the inhomogeneity of the wind field. In order to analyse the wind field close to the selected accelerometers in section H5 and H7, the anemometers A6 and A7 are chosen for this case study, see Figure 5.6.

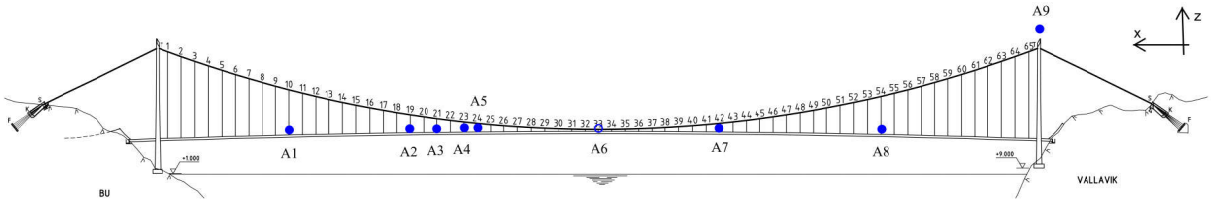

Figure 5.6: Placements of anemometers along the Hardanger Bridge. The figure is obtained from the Norwegian Public Roads Administration.

5.1.3 Finite element model

In this case study, a simulation of the traffic loading was done on a model of the Hardanger Bridge, which was built in the finite element program Abaqus. To limit the scope of the thesis, the Abaqus model was not built by the authors, but provided by the Norwegian Public Roads Administration. This section will describe the geometry of the Abaqus model, while the implementation of traffic load and damping will be described in Section 5.2.

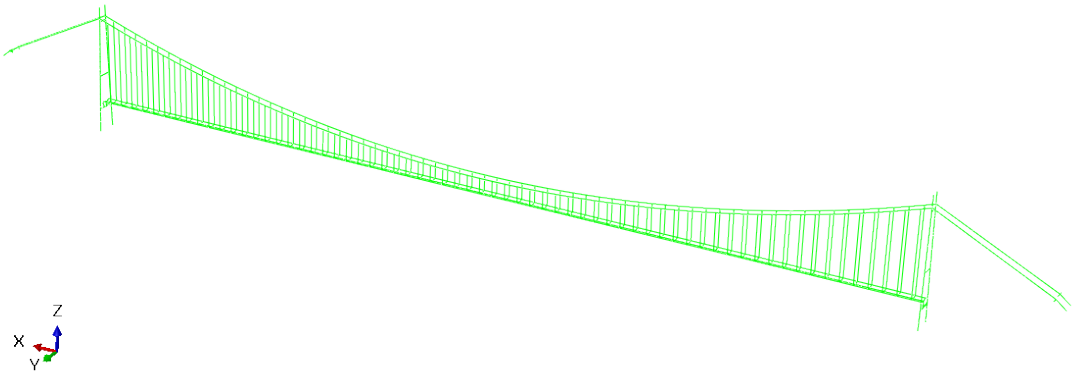

Figure 5.7: The finite element model of the Hardanger Bridge in Abaqus

The model consists of four main parts: The bridge deck, the pylons, the suspension cables and the hangers. These are modelled separately, and then connected to form a complete model at the end of the build. As described in Appendix A.1.1, the bridge deck is resting on the transverse girders at the pylons. In the FEA model, the side spans are not modelled, as the forces from the bridge deck are taken by the transverse girder.

The bridge is modelled using Timoshenko beam elements, with the exception of the splay saddles at the anchorage of the side cables, which are modelled using truss elements (T3D2). Truss elements has no bending stiffness and thus take only tensile and compression loads. The bridge deck and the transverse girders on the pylon at the Vallavik side are constructed with B32 elements, which corresponds to three-noded Timoshenko beam elements with quadratic interpolation. The rest of the beam elements are B31 elements with two nodes and linear interpolation. The elements of the bridge deck are two metres long, with the exception of the ends of the bridge, which consists of one and a half metres long elements. Timoshenko elements are shear deformable. Because of their higher order, they are usually superior to Euler-Bernoulli beam elements in predicting the transient response of a beam. Even so, as the beam gets slender, Euler-Bernoulli beam theory is approximated for the Timoshenko beam elements. This is because the deviation between the models gets small, and the lower order of the classical beam theory used for Euler-Bernoulli elements is more computationally efficient.

The material of the bridge has an linearly elastic behaviour, but the stiffness of the bridge will not be linear. The deformation of the suspension cables will be large compared to strain, and the bending stiffness of the cables are negligible. Thus, the largest contribution to the stiffness of the bridge will be the non-linear axial stiffness of the suspension cables. This effect is accounted for in Abaqus by switching on the option *nlgeom*, which accounts for non-linear geometry in the model.

In the model, the cables are initially modelled unstressed. The model is later subjected to several steps which includes the removal and reapplying of the hangers, applying correct loading from hanger forces and gravity to the cables and the bridge deck, and taking the asphalt into account. As a result of these steps, the bridge experiences large deflections. To fix this, the cables are suspended by applying thermal strain, which makes the cables contract, and the bridge gets pulled into the known initial state.

To account for the inertia effect from extruding parts like the bulkheads and the guide vanes on the bridge deck, lumped masses are added to the bridge deck in the model. There is also added a lumped mass to each hanger to account for the mass of the hanger clamps. The actual connection of the hangers to the bridge deck in the model is done as seen in Figure 5.8. The elements used in the connection are dummy elements, which means that they are not a part of the actual structure. Thus, they are modelled with high stiffness and low mass, as it is desirable that these elements neither gets deformed nor contribute to the mass matrix.

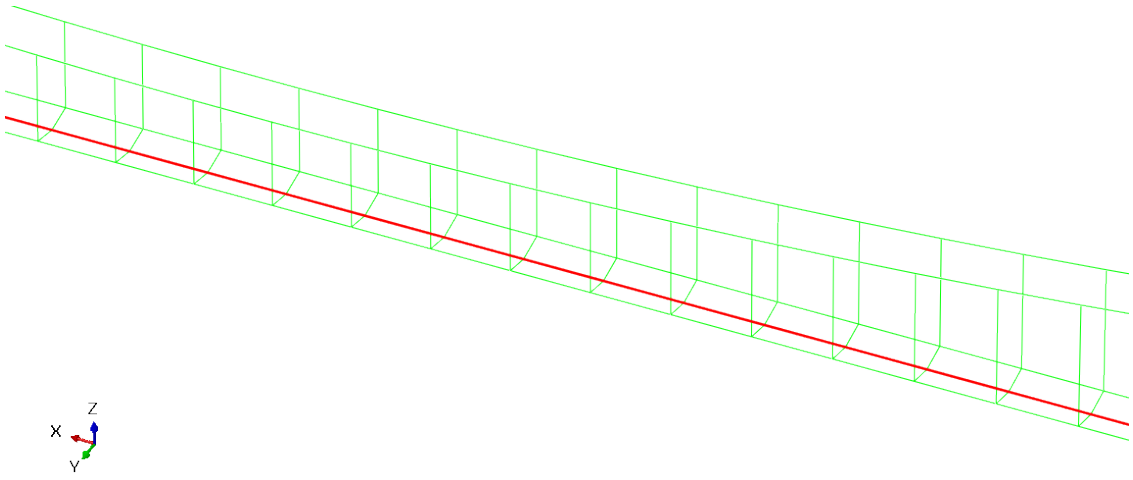

Figure 5.8: The connection between the bridge deck and the hangers in the Abaqus model.

Eigenvalues

By implementing the *frequency* step into the finite element model before any external loads are subjected to the bridge, Abaqus will estimate solutions of the eigenvalue problem $\det(\boldsymbol{K} - \omega^2 \boldsymbol{M}) = 0$ in order to extract eigenmodes, generalized mass and eigenfrequencies. The extraction of the eigenfrequencies is useful to validate the filtering method of the data from the sensors, as the most excited frequencies from the bridge should be similar to the eigenfrequencies from the model. These modes can be extracted from the spectral density of the measured data, see Section 2.3.3.

To extract the complex eigenmodes needed to find the damping of each mode in the Abaqus model, a *complex frequency* step also needs to be executed. As this step is done in order to extract the frequency response of the damped system, it is implemented after Rayleigh damping is introduced for the whole bridge. The complex frequency step solves the damped equation of motion of the system, see Section 2.1.2. From Abaqus, the real and the imaginary part of λ can be extracted, and thus the damping ratio of the mode can be found. The theory behind the complex eigenvalue problem is more closely examined in Section 2.1.2

5.2 Implementation of moving load model

In order to perform a finite element analysis of the traffic loading on the Hardanger Bridge, the moving load simulation developed in Section 3.3 will be implemented onto the Abaqus model of the Hardanger Bridge described in Section 5.1.3.

As the case study is performed on an existing Abaqus model, some changes are done to the script for the moving load across a simply supported beam. Firstly, the part of the script which creates the SSB is removed. It is replaced with the command *oldjob = 'old_job_name'* in the Abaqus command line, where 'old_job_name' is the name of the Abaqus job file (.odb file) for the construction of the bridge model. In addition, the line **Restart, read* is added to the input file for the moving load job, to start the moving load step in succession to the last step in the Hardanger Bridge model. This is necessary because the application of e.g. pylons and gravitational loading to the bridge model is done in steps succeeding the creation of the bridge deck and cables, see Section 5.1.3.

The Hardanger Bridge is 1310 metres long, and the speed limit at the bridge is 80 kilometres per hour. Thus, a vehicle will use approximately one minute driving across the bridge. The large time step makes an explicit integration scheme not suitable for the dynamic analysis, as it requires very small time increments to achieve convergence. Thus, implicit integration is implemented for the analysis, see Section 2.1.3.

The moving load model is constructed for use on two node Euler-Bernoulli elements, as described in Section 3.3. The FE model of the Hardanger Bridge is built using mainly three node Timoshenko elements, see Section 5.1.3. As such, the implementation of the moving load model onto the bridge model distributes loads only in the end nodes of the three node elements, not the midnodes.

In accordance with the findings from Section 3.3, moments in bounding nodes for the moving load, as well as damping in the structure, was implemented into the moving load model for the Hardanger Bridge. The damping in the bridge was achieved by implementing Rayleigh damping. As explained in Section 2.1.2, the Rayleigh damping is based on a guess of the damping ratio for two eigenmodes of the structure, ξ_0. As no information regarding the actual damping of the bridge was known, an initial guess of $\xi_0 = 5$ % was made. Choosing $\omega_p = \omega_1 = 0.3145$ and $\omega_r = \omega_{20} = 2.5619$, the minimum allowed damping ratio thus is $\xi_{min} = \frac{2\sqrt{\gamma}\xi_0}{1+\gamma} = 0.0312$ when using $\xi_0 = 0.05$, see Section 2.1.2. The minimum damping ratio of the system is $\xi_{\omega_{min}} = 0.0312$ at $\omega_{min} = 0.8976$, which gives damping ratios $\xi_{Rayleigh} \geq \xi_{min}$ for the system, see Figure 5.9.Hence, an initial damping ratio of $\xi_0 = 5\%$ is chosen as suitable for the beam. The Rayleigh damping ratio $\xi_0 = 5$ % for the Hardanger Bridge structure yields the constants $\alpha = 2\omega_r\omega_p\frac{\omega_p\xi_r - \omega_r\xi_p}{\omega_p^2 - \omega_r^2} = 0.0280$ and $\beta = 2\frac{\omega_p\xi_p - \omega_r\xi_r}{\omega_p^2 - \omega_r^2} = 0.0348$.

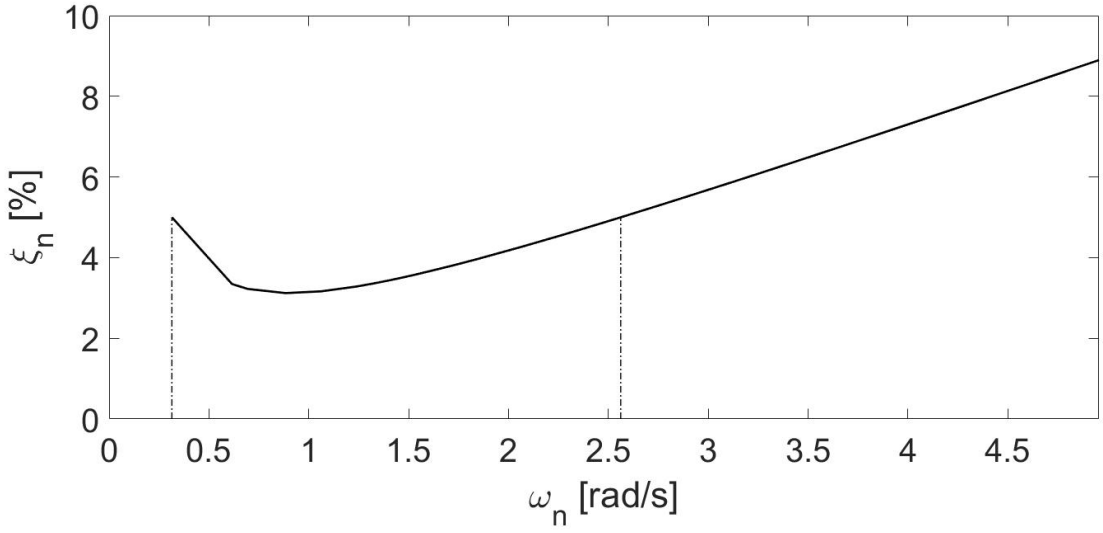

Figure 5.9: The Rayleigh damping for the Abaqus model of the Hardanger Bridge with $\xi_0 = 5$ %. The stapled lines marks the applied range between ω_p and ω_r

The traffic logging done at the Hardanger Bridge, see Appendix A.2, shows a case of a truck moving across the bridge without any other traffic. The trailer enters the bridge at the Bu side at 09:00:18 and leaves the bridge on the Vallavik side at 09:01:34. This will be the base case for the finite element modelling of the moving load problem on the Hardanger Bridge. Thus, the standard case of the moving load is a single force of 200 kilonewtons moving at 62 kilometres per hour, representing a semi-trailer weighing approximately 20 tonnes [34, 42] moving across the bridge in 76 seconds, in accordance with the traffic log.

To investigate which restrictions influences the response, a parameter test was conducted for the following criteria:

- Modelling with and without enforced moments in the nodes margin the moving load
- The weight of the car
- The speed of the car
- The number of axles on the car
- Static or dynamic analysis
- The boundary conditions of the connection between the bridge deck and the pylons
- The inclusion of damping in the bridge model

The weight, speed and axles on the car were managed in the text file describing the car input. The analysis type, the boundary conditions and the inclusion of enforced moments where all employed directly in the input file for the moving load. Finally, the damping was computed in a Matlab file, and included in the input file for the build of the Hardanger Bridge model. All of the above mentioned scripts and files can be found in the digital appendix.

5.3 Results from numerical analysis in MATLAB

In this section, the results from the numerical methods described in Section 4 implemented on the Hardanger Bridge will be presented. The analyses has been carried out on the recorded vertical acceleration responses. A traffic log recorded on the Hardanger Bridge on the 31st of April 2016, for the time period of 30 minutes from 08:45 to 09:15, forms the basis of the analyses. Due to the response from the bridge being recorded for two separate time series, 08:30-09:00 and 09:00-09:30, most of the figures in this section are chosen to be separated at 09:00.

5.3.1 Wind conditions

When analysing the vertical acceleration response of the Hardanger Bridge, the response due to wind induced vibrations should be taken into account. In order to assess the extent of the response due to the wind induced vibrations, the wind conditions for the case study are presented in Figure 5.10 - 5.15. The wind conditions has been recorded by the anemometers corresponding to the relevant accelerometers in this case study

As can be seen in Figure 5.10 and 5.13, the horizontal wind during the chosen time period displays velocities mostly between 5 and 10 metres per second. Together with the vertical wind shown in Figure 5.11 and 5.14, the result indicates that the wind induced response on the Hardanger Bridge during this time period is not negligible. The wind induced response might therefore influence the vertical acceleration response from the traffic induced vibrations. In Figure 5.12 and 5.15, the direction for the horizontal wind is shown. As can be observed from these figures, the recorded wind for this time period occur mostly with an angle of 90 degrees with respect to the Hardanger Bridge. This wind direction indicates that the horizontal wind acts perpendicular to the main span of the bridge. By comparing the measured wind data for each anemometer in Figure 5.10 - 5.15, observations of the results shows that the recordings of wind data differ for each anemometer.

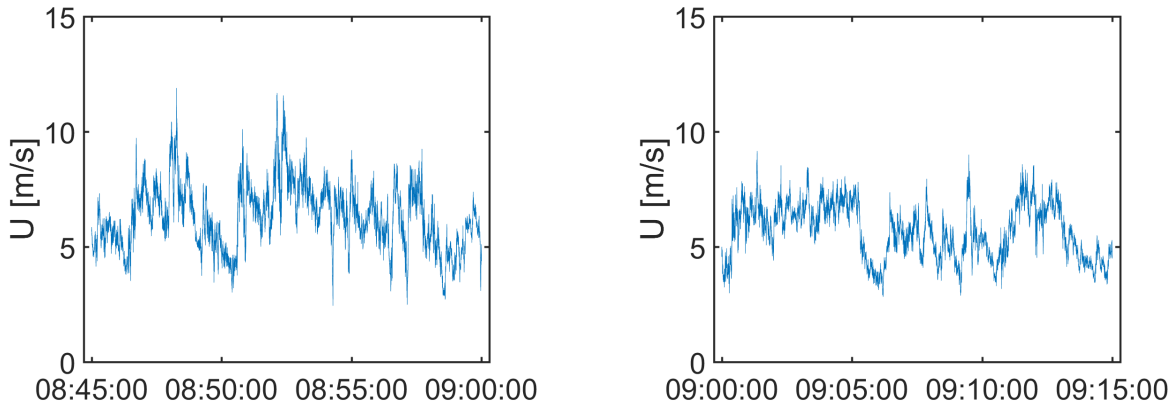

Figure 5.10: Horizontal wind velocity, sensor A6

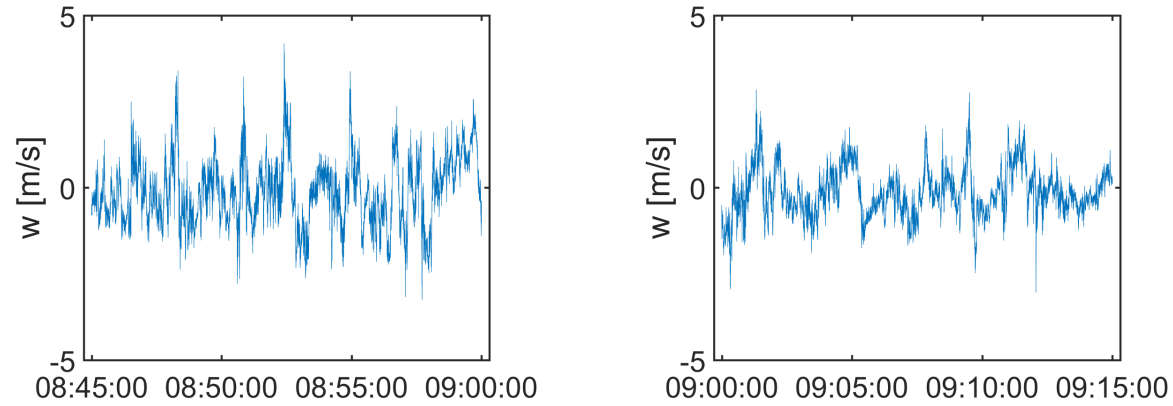

Figure 5.11: Vertical wind velocity, sensor A6

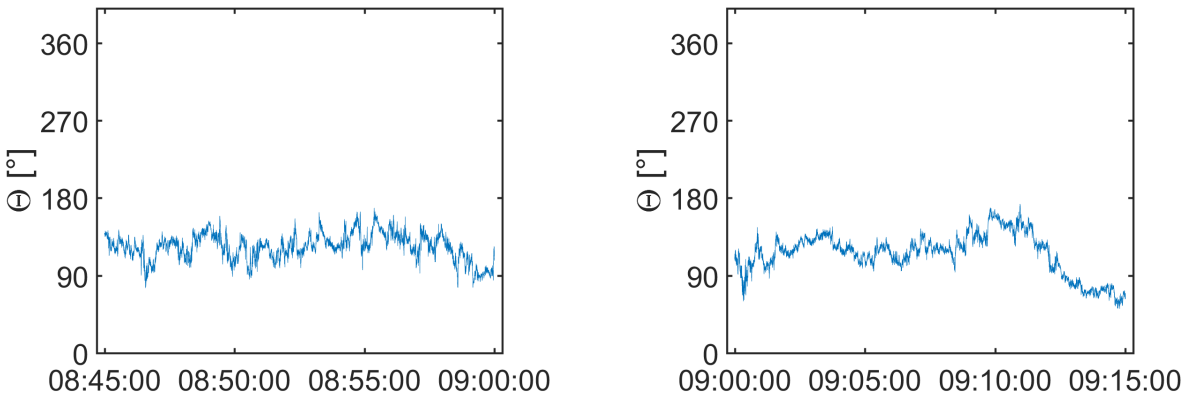

Figure 5.12: Angle for horizontal wind, sensor A6

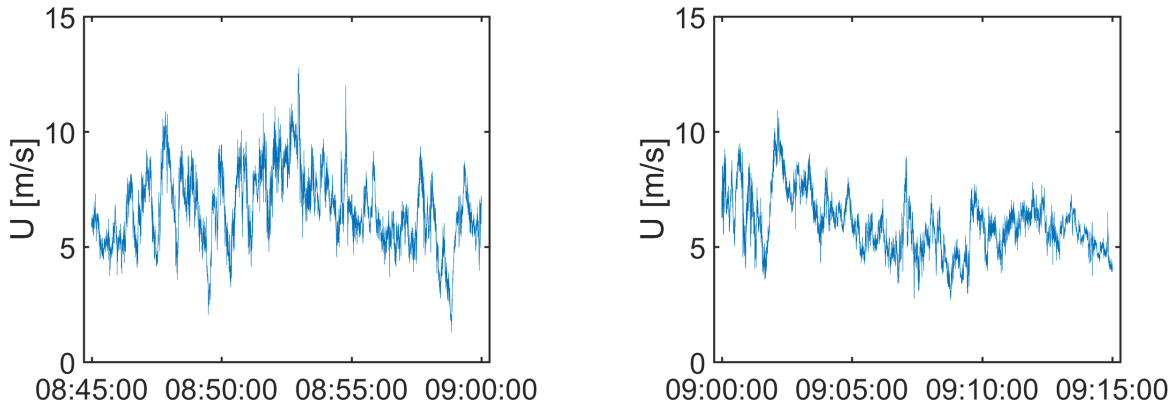

Figure 5.13: Horizontal wind velocity, sensor A7

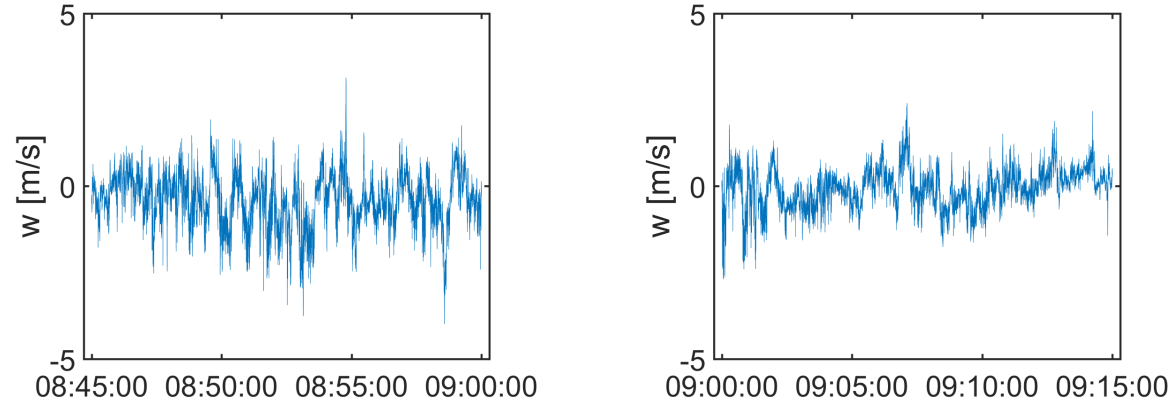

Figure 5.14: Vertical wind velocity, sensor A7

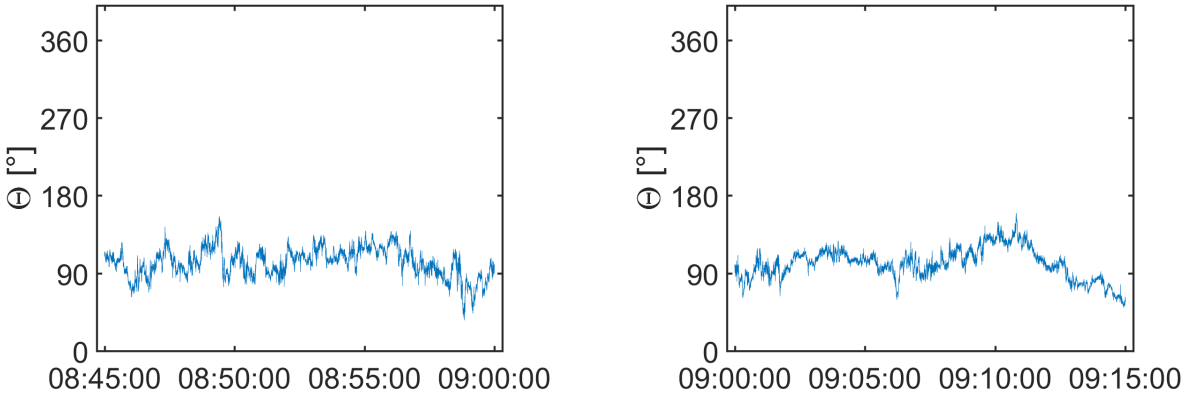

Figure 5.15: Angle for horizontal wind, sensor A7

5.3.2 Identification of traffic induced loading

An analysis of the vertical acceleration response is carried out for sections H5 and H7 using the script *trafficAcceleration*. By running the script, the output is given as the vertical acceleration response displayed in Figure 5.16 and Figure 5.17:

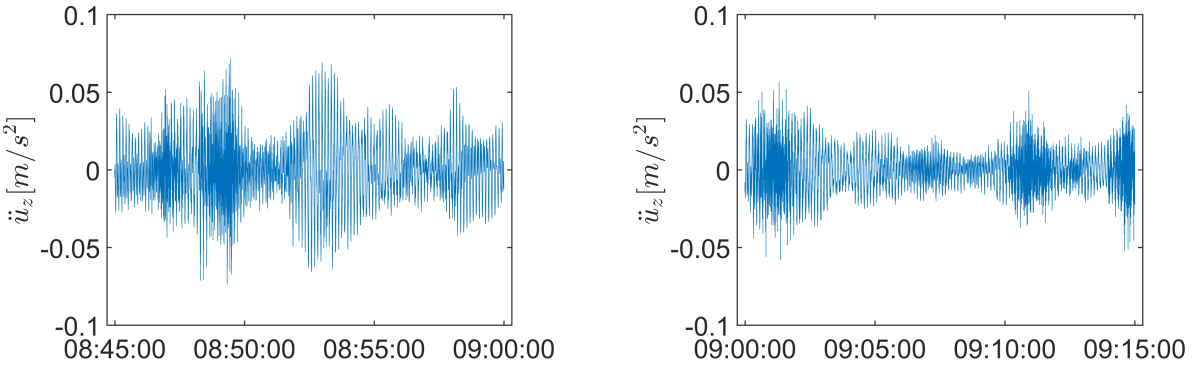

(a) 08:45 - 09:00 **(b)** 09:00 - 09:15

Figure 5.16: Vertical acceleration response, Section H5

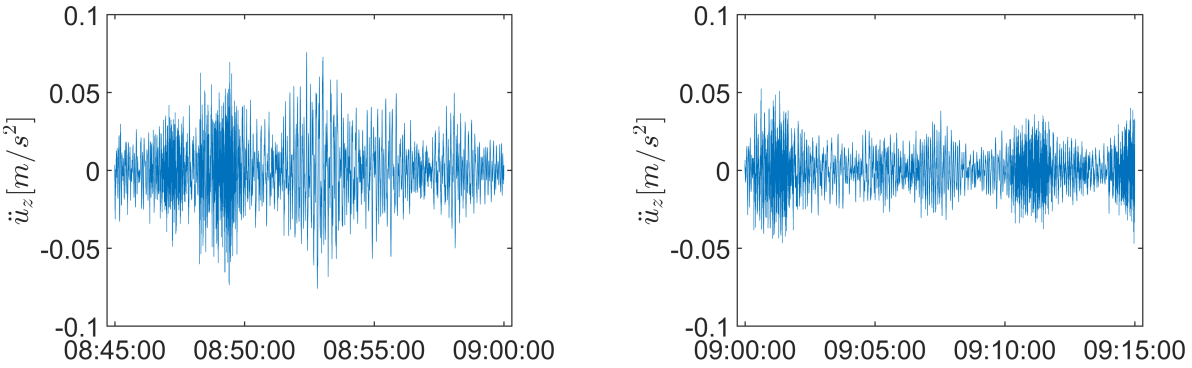

(a) 08:45 - 09:00 **(b)** 09:00 - 09:15

Figure 5.17: Vertical acceleration response, Section H7

In order to identify the acceleration response caused by traffic induced vibrations, the figure for the vertical acceleration response is compared with the traffic log in Appendix A.2. As given in the traffic log, a total of four trucks were observed in the current time interval from 08:45 to 09:15. The dimensions for these trucks are illustrated in Figure 5.22. In this analysis, three time intervals of one minute each, for both sections, has been analysed for time periods where a truck has been observed entering the Hardanger Bridge. These acceleration responses are shown in Figures 5.18, 5.19 and 5.20.

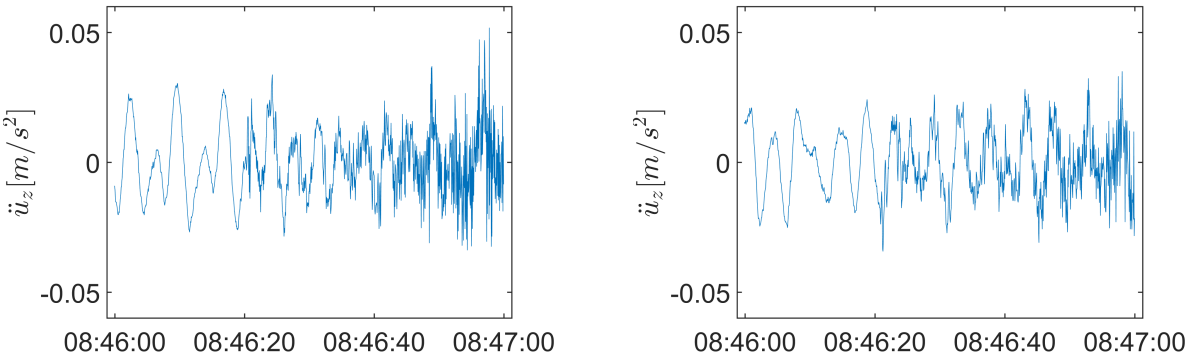

(a) Section H5 **(b)** Section H7

Figure 5.18: Vertical acceleration response of truck entering the bridge
Time: 08:46:19

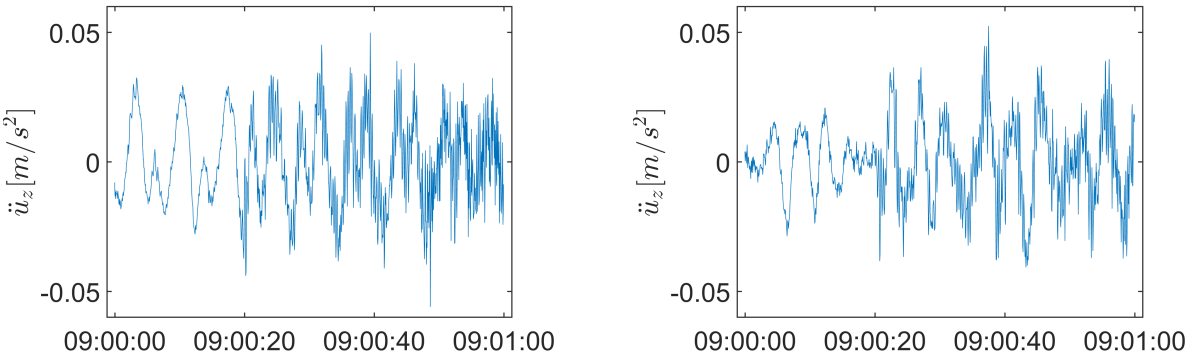

(a) Section H5 **(b)** Section H7

Figure 5.19: Vertical acceleration response of truck entering the bridge
Time: 09:00:18

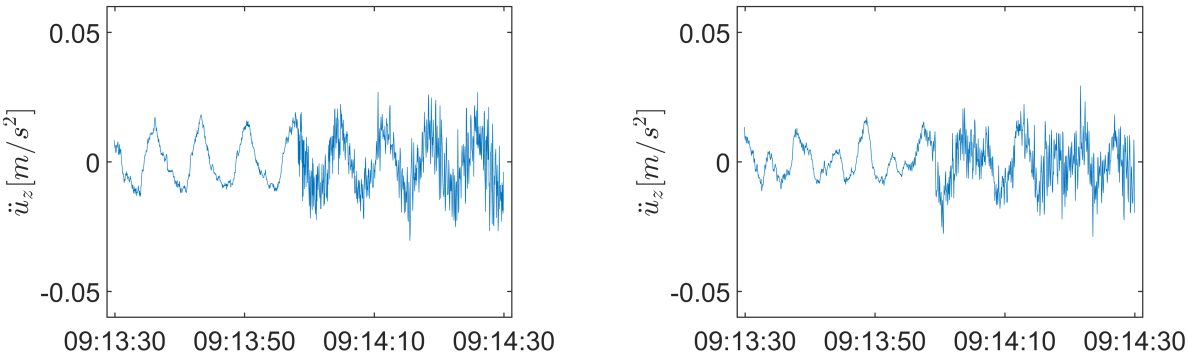

(a) Section H5 **(b)** Section H7

Figure 5.20: Vertical acceleration response of truck entering the bridge
Time: 09:13:56

As shown in Figures 5.18-5.20, the vertical acceleration responses begin to oscillate with larger frequencies for both sections close to the time of the observations of trucks on the Hardanger Bridge. One important observation from the acceleration response is that the oscillations due to the traffic induced vibrations appear to begin close to the time when the vehicles enters the bridge. This will be further investigated in Section 5.3.3.

In the time period before the respective trucks enters the bridge, the vertical acceleration response appears to have a constant behaviour. Although, in the time between 08:50 and 08:55, it can be observed from Figure 5.16a and 5.17a that the vertical acceleration response increases short time after a truck has passed the bridge. In Figure 5.21, this time interval is shown in detail.

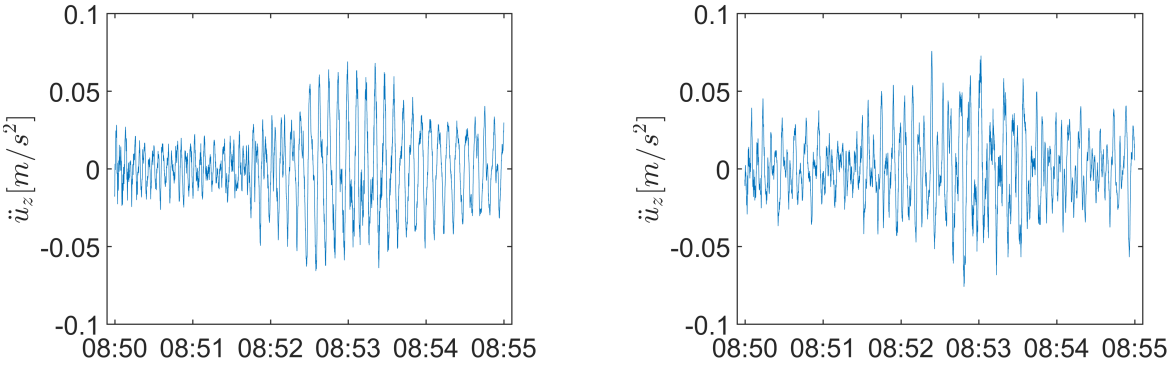

(a) Section H5 **(b)** Section H7

Figure 5.21: Vertical acceleration response from 08:50 - 08:55

In the time interval where the vertical acceleration response increases, shortly after 08:52, four cars are observed moving in the same direction in the traffic log. Presumably, the occurrence of these cars passing the bridge almost at the same time might explain the increase of vertical acceleration response in this time interval. The wind velocities for this time interval, shown in Section 5.3.1, display horizontal wind velocities close to 10 metres per second. These large wind velocities indicate that the increase in acceleration response could be a result of the wind condition. Thus, it remains unclear what could be the direct cause for this increase in vertical acceleration response.

(a) 08:46:19 **(b)** 08:48:14

(c) 09:00:18 **(d)** 09:13:56

Figure 5.22: Observations of trucks on the Hardanger Bridge. Time in subcaption refers to time of entering for the specific vehicle

(a) 08:52:39 **(b)** 08:52:57

Figure 5.23: Observations of passenger cars on the Hardanger Bridge. Time in subcaption refers to time of entering for the specific vehicle

5.3.3 Analysis of moving traffic

The script *trafficCrossCovariance* carried out analyses for sections H5 and H7 of the cross-covariance and the corresponding time lag. The analysis of the vertical acceleration response was done for one minute-intervals for time periods where trucks have been observed entering the Hardanger Bridge. The intervals analysed in the preceding section is chosen for analysis using this method. Only the cross-covariance of the vertical acceleration response is considered, and not the auto-covariance for analysing the time lag for the response between the two sections. The output for the script *trafficCrossCovariance* is given in Figure 5.24, 5.25, and 5.26:

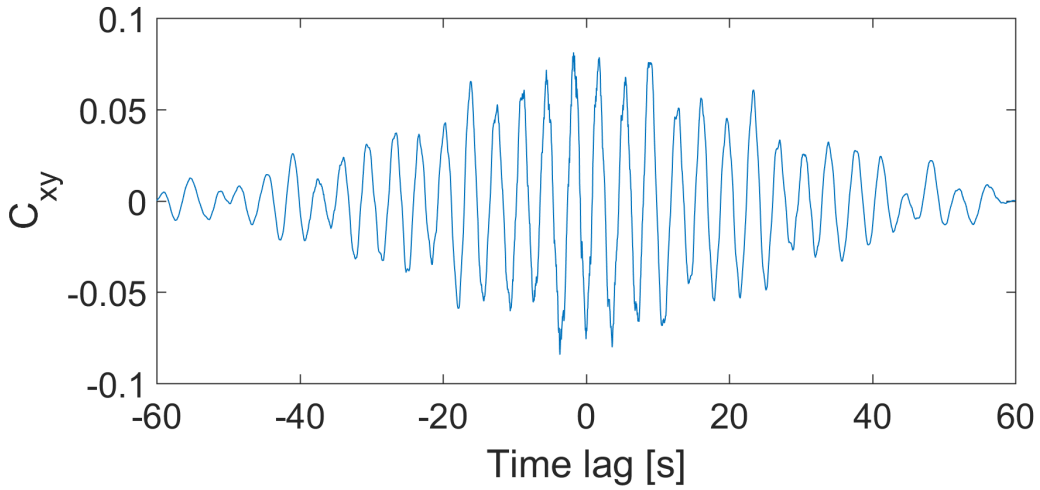

Figure 5.24: Cross-covariance for acceleration response between section H5 and H7
Time: 08:46 - 08:47

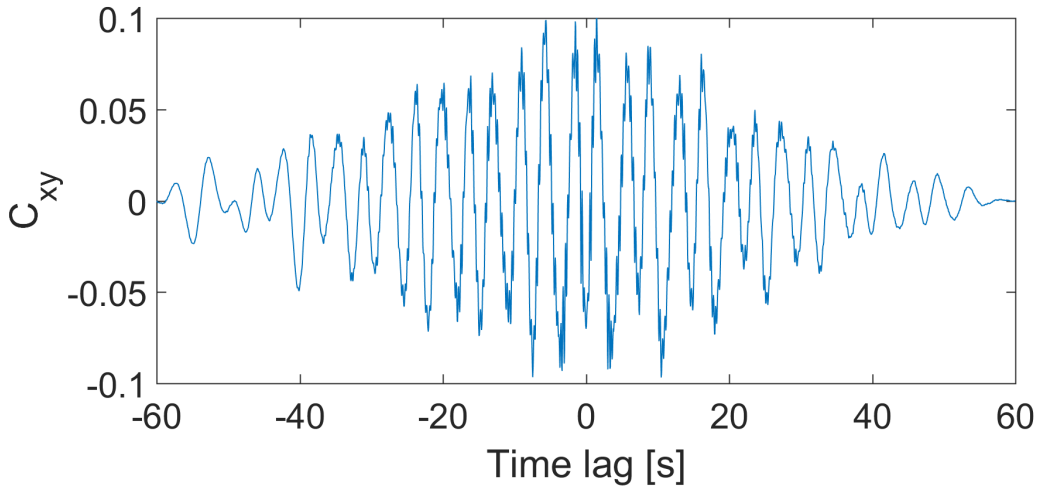

Figure 5.25: Cross-covariance for acceleration response between section H5 and H7
Time: 09:00 - 09:01

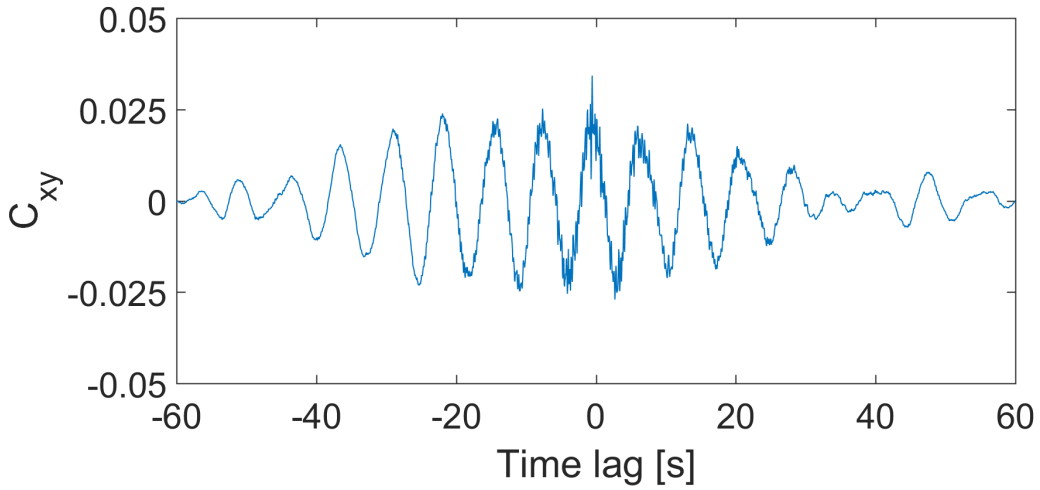

Figure 5.26: Cross-covariance for acceleration response between section H5 and H7
Time: 09:13:30 - 09:14:30

From Figures 5.24 - 5.26, the output of the cross-covariance shows large amplitudes close to time lags equal to zero. It is difficult to distinguish between these peaks. Thus, it is difficult to determine a time lag from the acceleration response due to the trucks for the chosen time intervals. As previously mentioned for the preceding method, the oscillations due to the traffic induced vibrations was observed in the acceleration response close to the time of entering. The time acquired from the traffic log for a vehicle entering the bridge does not coincide with the observations of faster oscillations for the sections H5 and H7 shown in Figure 5.18, 5.19 and 5.20. This could indicate vibrations with larger velocities than the vehicle itself. These vibrations may possibly be the cause for the difficulty in analysing the cross-covariance of the acceleration response and the corresponding time lag. This will be discussed further in Section 6.

5.3.4 Power spectral density

By using the script *trafficSpecter*, the power spectral density for the vertical acceleration response has been estimated at sections H5 and H7 for intervals of 5 minutes. Due to the limited traffic logging of 30 minutes, time intervals of 5 minutes is chosen, and will provide a total of six plots of the power spectral density for each section.

Table 5.1: Logging of vehicles in the given time intervals

Time period	Number of cars	Number of trucks
08.45-08.50	4	2
08.50-08.55	5	0
08.55-09.00	4	0
09.00-09.05	4	1
09.05-09.10	7	0
09.10-09.15	11	2

Table 5.1 shows a summary for the traffic logging, and states the number of observed vehicles entering the Hardanger Bridge at given time intervals. From the traffic log in Appendix A.2 for the last time interval, a camper van is observed entering the bridge. Since a camper van is heavier than a passenger car, it is assumed that the camper van may excite motions with larger frequencies than a car. Based on this assumption, the camper van is registered as a truck in Table 5.1. The analysis of the power spectral density is mainly focused on the load case for each time interval and its corresponding frequency content, rather than the number of vehicles entering the bridge in the given time interval.

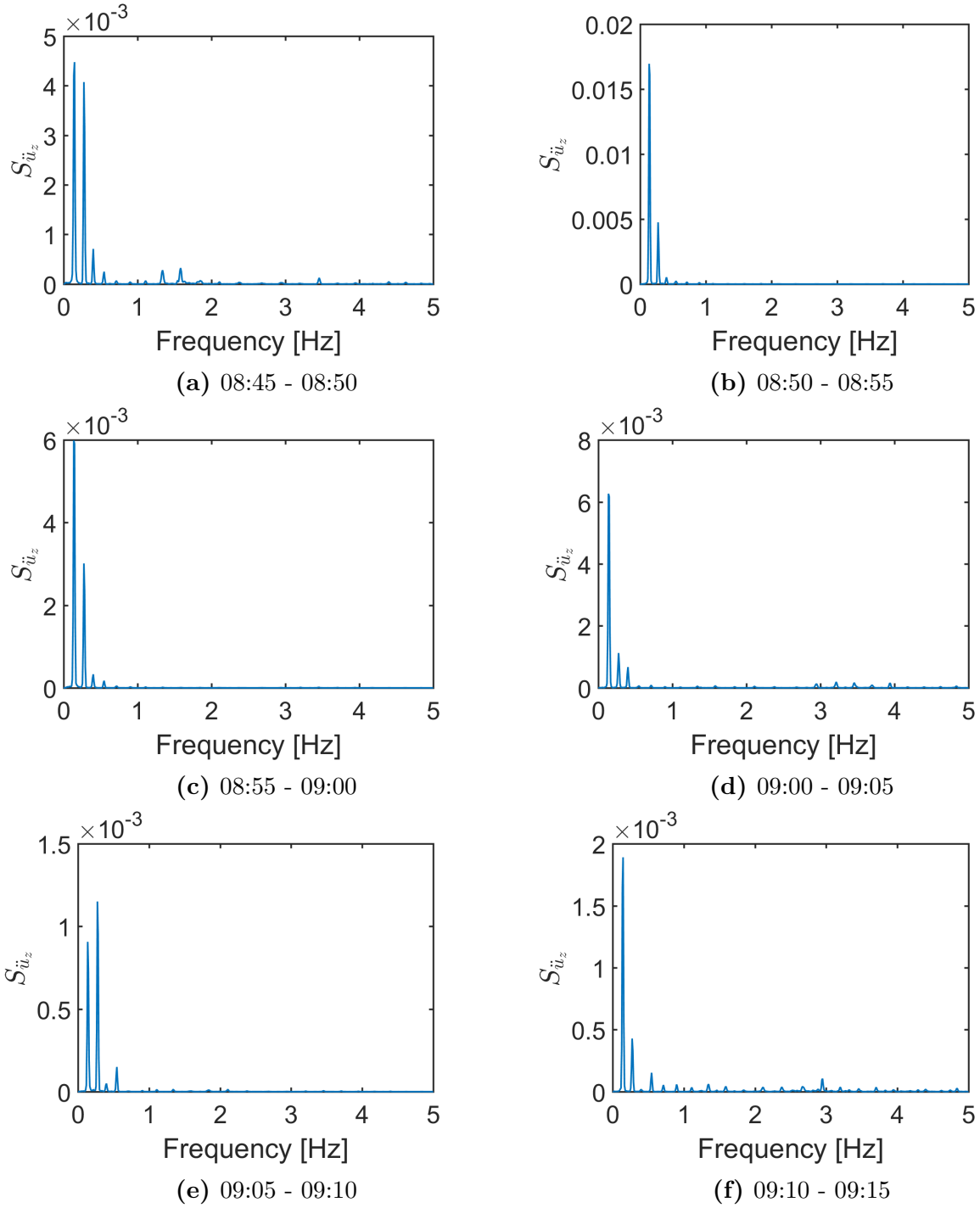

(a) 08:45 - 08:50

(b) 08:50 - 08:55

(c) 08:55 - 09:00

(d) 09:00 - 09:05

(e) 09:05 - 09:10

(f) 09:10 - 09:15

Figure 5.27: Power Spectral Density, Section H5

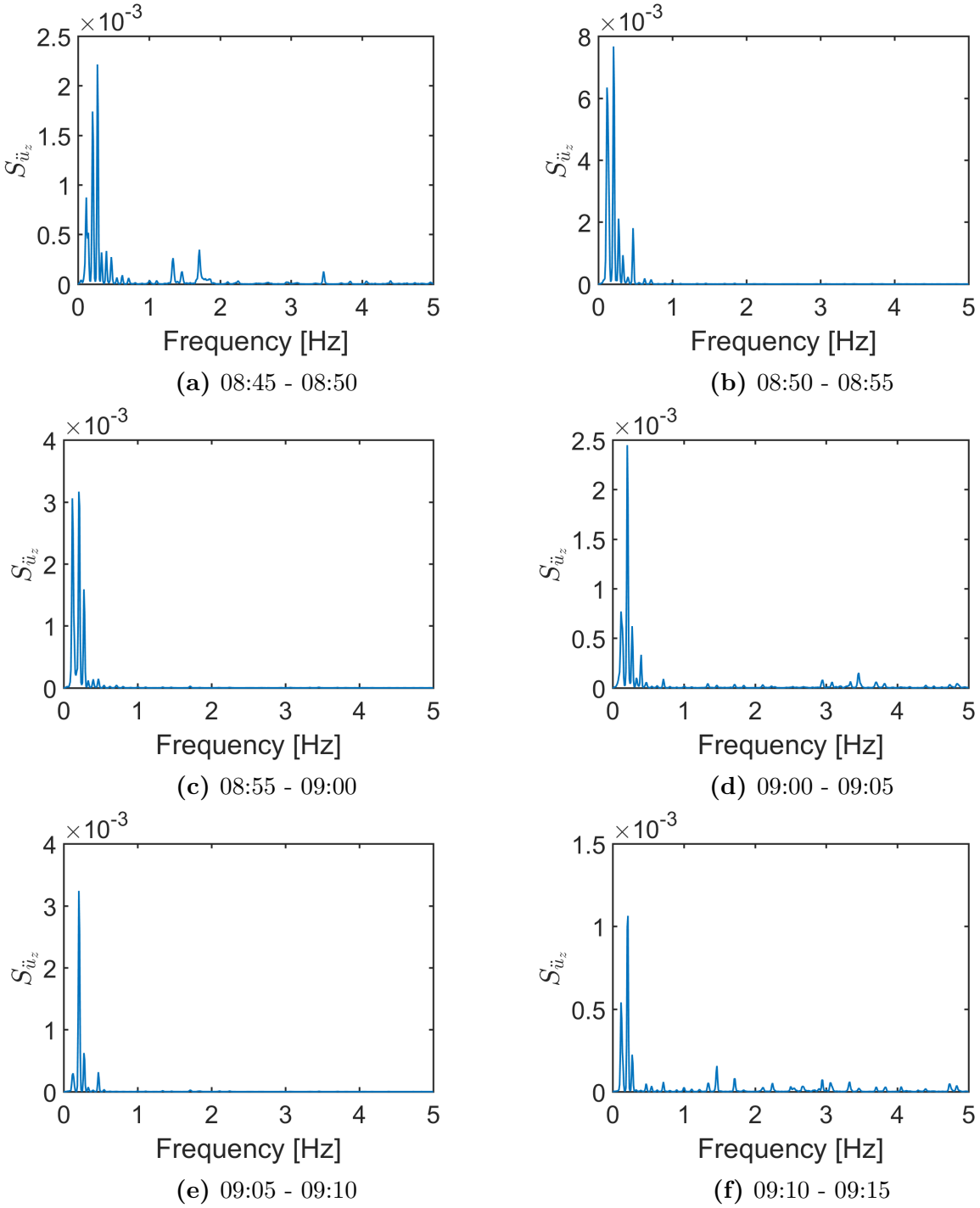

(a) 08:45 - 08:50

(b) 08:50 - 08:55

(c) 08:55 - 09:00

(d) 09:00 - 09:05

(e) 09:05 - 09:10

(f) 09:10 - 09:15

Figure 5.28: Power Spectral Density, Section H7

From the results in Figure 5.27 and Figure 5.28, it can be seen that the time intervals where only cars has been observed in Figure 5.27(b),(c),(e) and Figure 5.28(b),(c),(e), the frequency content of the vertical acceleration response remains below 1 hertz. For the time intervals where trucks has been observed in Figure 5.27(a),(d),(f) and Figure 5.28(a),(d),(f), the power spectral density estimations indicate that the response contains frequencies mostly below 1 hertz, but also contributions to eigenmodes with frequencies above 1 hertz. As stated in Section 4.1, wind induced response is assumed to remain in the frequency domain of 0 - 1 hertz, whereas traffic induced vibrations from heavy vehicles appear in the frequency domain of 1.5 - 4 hertz [3, 15]. These assumptions appear to be consistent with the results in Figures 5.27 and 5.28. Even so, the contribution to the eigenmodes in the frequency domain above 1 hertz is very small compared to the first three eigenmodes. Thus, it appears that the response due to traffic induced vibrations excites motions both in the low and high frequency domains. This will be further analysed in the following section.

In the time interval 08:50-08:55, the vertical acceleration response increases considerably, as stated in section 5.3.2. From the observations in the traffic log, and the wind conditions in Section 5.3.1, it was assumed that the increase in the vertical acceleration response could be the result of four cars passing the Hardanger Bridge at almost the same time, and with a horizontal wind velocity of 10 metres per second. Figures 5.27b and 5.28b shows that no modes with eigenfrequencies above 1 hertz are excited in the power spectral density for this time period. This observation may indicate that the previous assumption stating that wind induced response mostly excite modes below 1 hertz is valid. It is interesting that observations from Section 5.3.2 and observations from the power spectral density in Figures 5.27 and 5.28 could indicate that the induced response from passenger cars excite mostly modes with eigenfrequencies below 1 hertz.

In Table 5.2, the eigenfrequencies acquired from the power spectral density estimations for sections H5 and H7 are presented. Here, only the first six eigenfrequencies are shown for each section. As can be observed from Table 5.2, different modes are excited for sections H5 and H7. The results agree well with the previous statement in Section 5.1.2.

Table 5.2: Eigenfrequencies from power spectral density

(a) Section H5

Mode	**Frequency [Hz]**
1	0.1416
2	0.2734
3	0.4004
4	0.5469
5	0.7129
6	0.8984

(b) Section H7

Mode	**Frequency [Hz]**
1	0.1172
2	0.2051
3	0.2734
4	0.3320
5	0.4004
6	0.4688

5.3.5 Response filtering

For the script *trafficFilter*, the vertical acceleration response for sections H5 and H7 has been filtered using a FIR filter. For this analysis, two filters are designed: a high-pass filter and a low-pass filter. In order to separate the responses at 1 hertz, and provide a narrow transition band, the transition between the stopband and the passband is chosen for frequencies equal to 0.95 and 1.05 hertz. The results from using the designed FIR filters are shown in Figure 5.29 and 5.30.

As can be observed in Figures 5.29 and 5.30, the filtered vertical acceleration response with frequencies above 1 hertz shows large amplitudes close to the time for the observations of trucks entering the bridge. The results agree well with the observations of larger frequencies in the acceleration response due to heavy vehicles elaborated upon in Section 5.3.2.

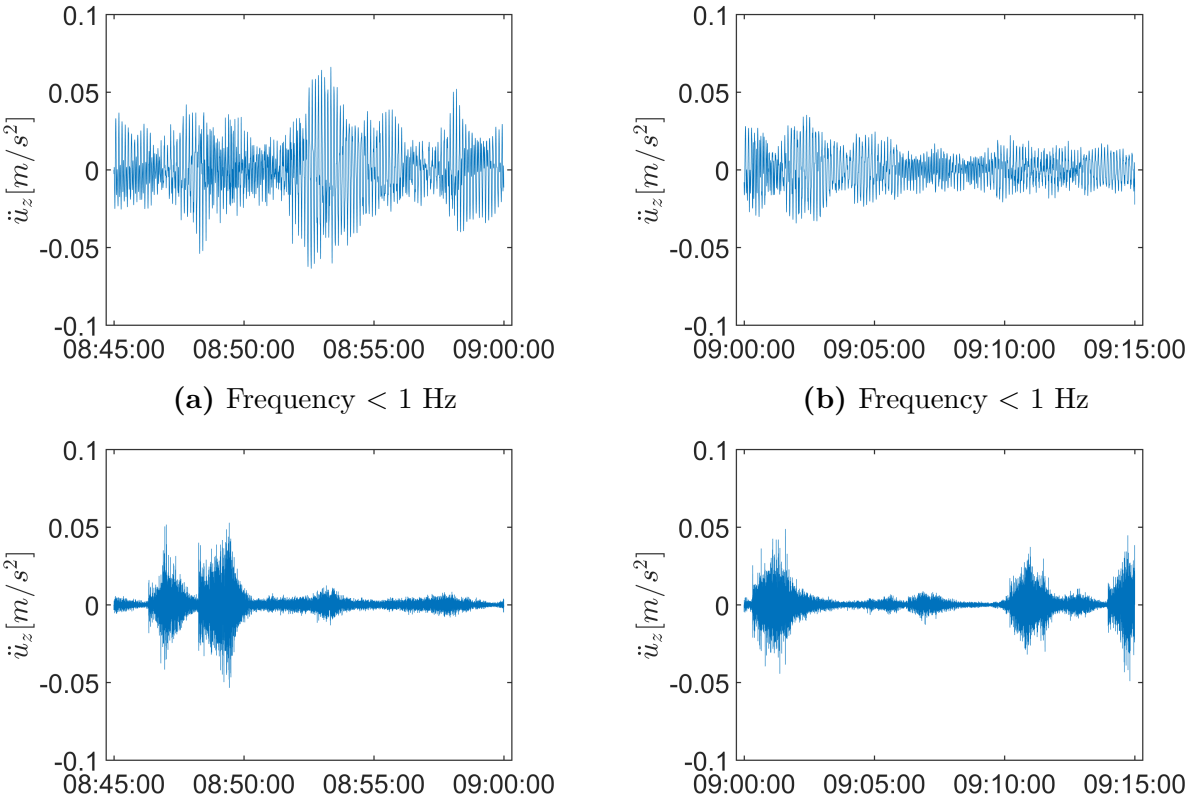

(a) Frequency $<$ 1 Hz

(b) Frequency $<$ 1 Hz

(c) Frequency $>$ 1 Hz

(d) Frequency $>$ 1 Hz

Figure 5.29: Filtered vertical acceleration response for Section H5

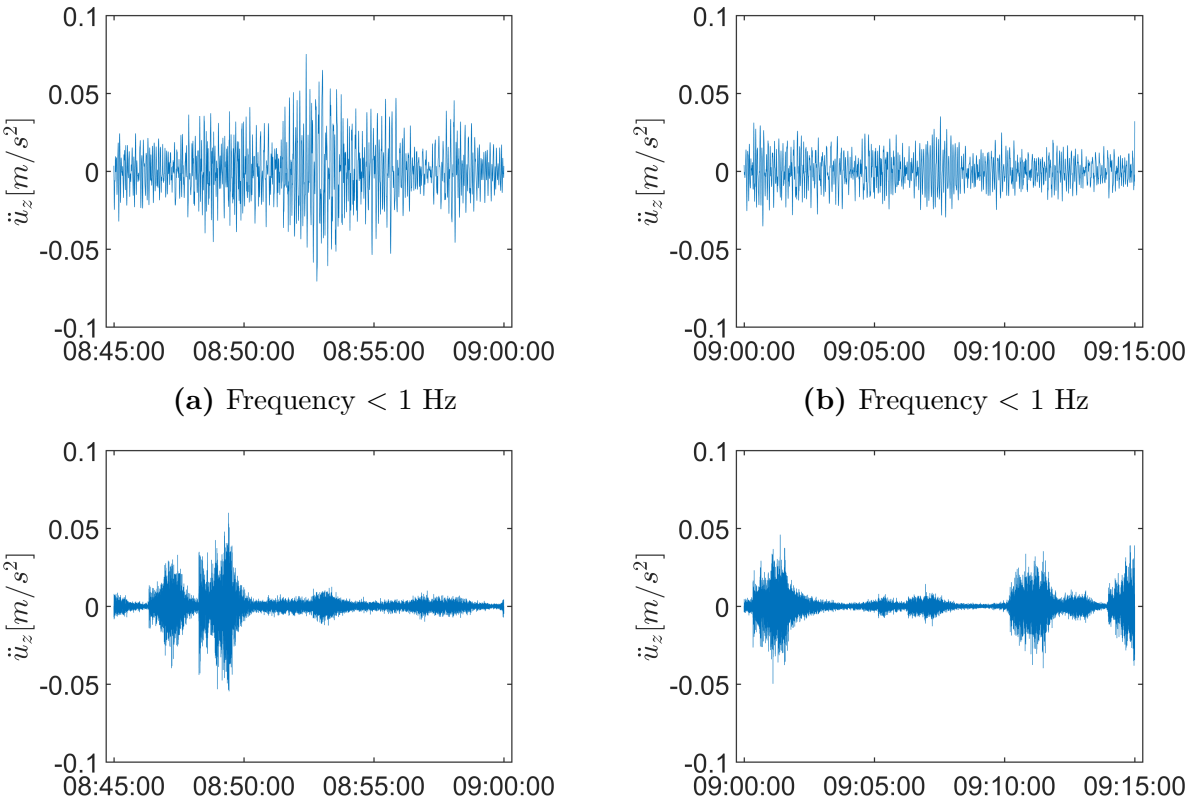

(a) Frequency < 1 Hz

(b) Frequency < 1 Hz

(c) Frequency > 1 Hz

(d) Frequency > 1 Hz

Figure 5.30: Filtered vertical acceleration response for Section H7

In order to evaluate if the acceleration response can be filtered directly by high-passing and low-passing, the filtered response should be further investigated. In the article by Cheynet et al [4], a study was conducted to analyse the vertical acceleration response for wind- and traffic induced vibrations. The study was carried out by separating the measured acceleration response from wind and traffic induced vibrations, based on which recordings were measured at night-time and daytime respectively. The analysis applied a plotting of the estimated standard deviation of the acceleration response against the mean wind velocity to compare the two responses.

A similar procedure is introduced to compare the filtered responses for section H5 and H7. Due to limited data from the traffic logging, a recording with longer duration has been chosen for this analysis. By considering a recording for a total of 24 hours, with high-passed and low-passed acceleration responses, an analysis for calculating the correlation of the standard deviation of the acceleration response with the mean wind velocity is carried out. The data for this analysis is gathered from 10 minute intervals of the recording of the Hardanger Bridge on January 15th 2016. The results from this analysis are given by Figure 5.31 and 5.32:

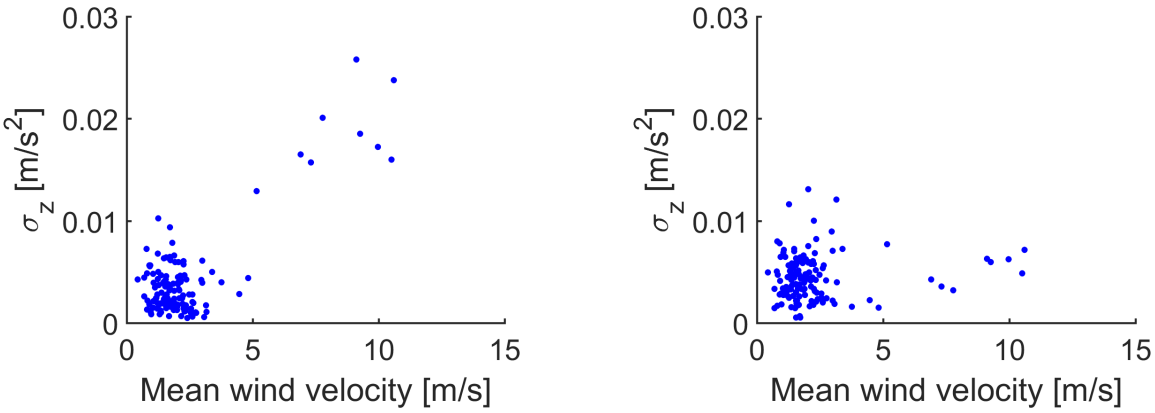

(a) Frequency < 1 Hz **(b)** Frequency > 1 Hz

Figure 5.31: Standard deviation for vertical acceleration response plotted against horizontal mean wind velocity, section H5

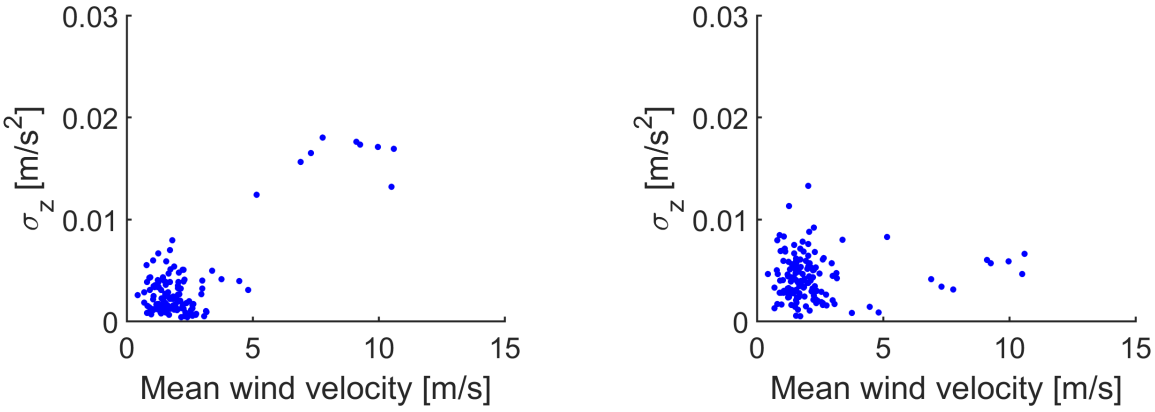

(a) Frequency < 1 Hz **(b)** Frequency > 1 Hz

Figure 5.32: Standard deviation for vertical acceleration response plotted against horizontal mean wind velocity, section H7

As can be observed from Figure 5.31 and Figure 5.32, the standard deviation of the response increases with respect to the mean wind velocity for the filtered response below one hertz, while this is not affected for responses with frequencies above one hertz.

5.3.6 Numerical integration

The script *calcDisplacement* is used to calculate the estimated displacements for the vertical acceleration response of section H5 and H7. The results from the use of the script are given in Figure 5.33 and 5.34:

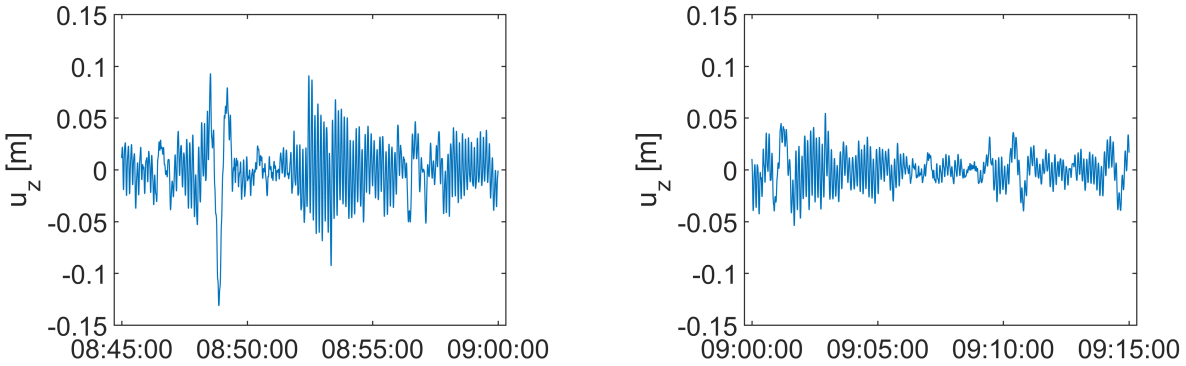

(a) 08:45 - 09:00 **(b)** 09:00 - 09:15

Figure 5.33: Estimated displacements by numerical integration, section H5

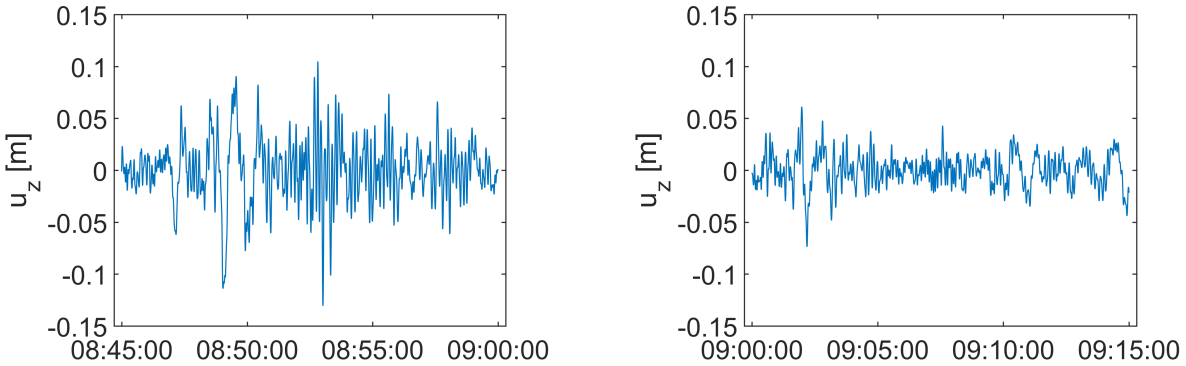

(a) 08:45 - 09:00 **(b)** 09:00 - 09:15

Figure 5.34: Estimated displacements by numerical integration, section H7

The estimated displacements will be used to compare the response with the displacements calculated from the FE model. In order to make use of the estimated displacements shown in Figures 5.33 and 5.34, the reliability of the displacements must be evaluated. As stated in Section 4.4, an evaluation of the estimated displacements provided by the script *acc2disp* can be carried out by comparing the power spectral density from the estimated displacements with the power spectral density estimated from the acceleration response and the transfer function $H_{\ddot{u}_z u_z}$. In this comparison, the power spectral density distribution is calculated using the Welch's method on both procedures. The analysis is performed for a 10 minute interval, and the results from the analysis are given in Figures 5.35 and 5.36. A comparison

between the eigenfrequencies and the corresponding power spectral densities for section H5 and H7 is given in Table 5.3 and Table 5.4, respectively.

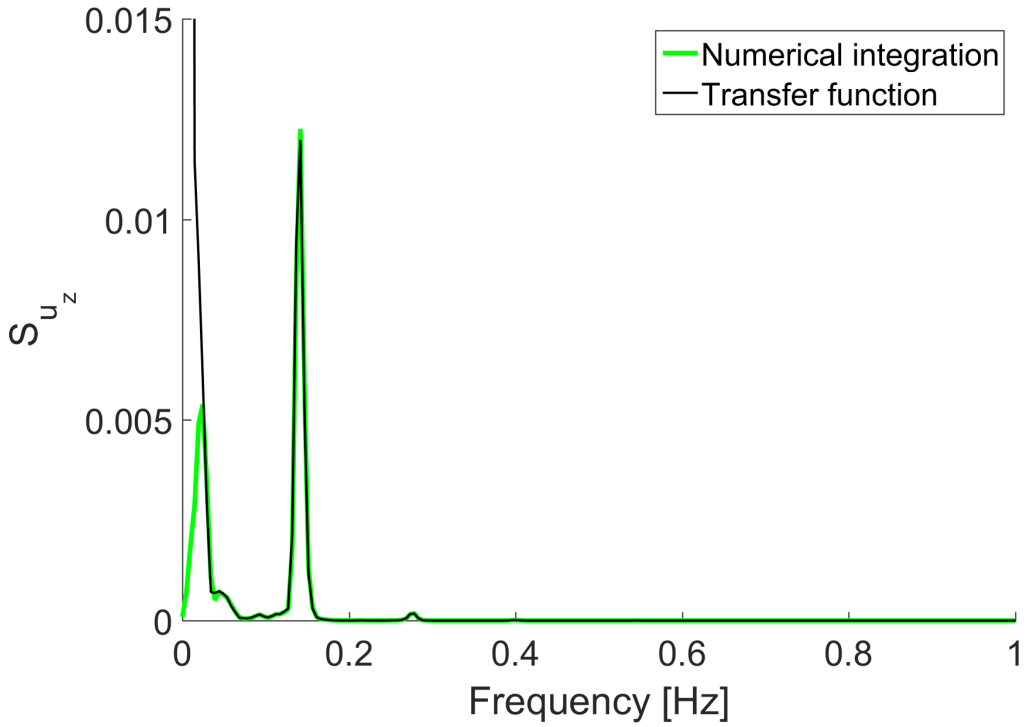

Figure 5.35: Power spectral density of displacements, section H5
Time: 09:00 - 09:10

Table 5.3: Power Spectral Density of displacements, Section H5

	Numerical integration		Transfer function		Deviation
Mode	f [Hz]	S_{u_z}	f [Hz]	S_{u_z}	$\lvert\Delta S_{u_z}\rvert$
1	0.02441	5.386E-03	-	-	-
2	0.14160	1.226E-02	0.14160	1.198E-02	2.28 %
3	0.27830	1.784E-04	0.27830	1.759E-04	1.40 %
4	0.40040	1.252E-05	0.40040	1.196E-05	4.47 %

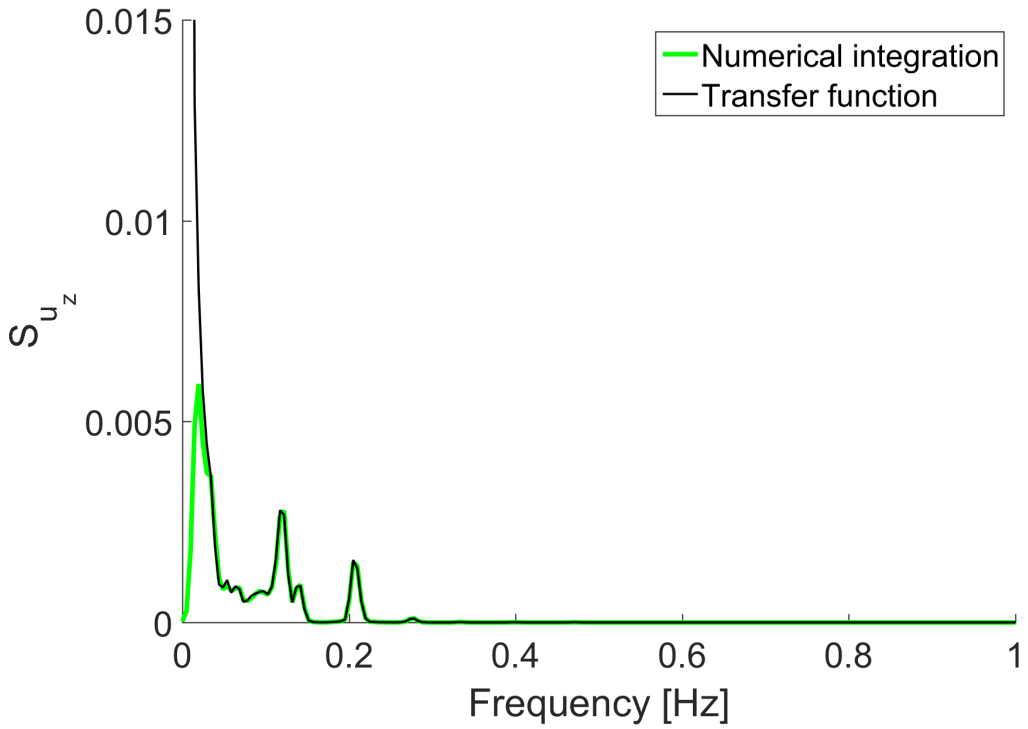

Figure 5.36: Power spectral density of displacements, section H7
Time: 09:00 - 09:10

Table 5.4: Power Spectral Density of displacements, Section H7

	Numerical integration		Transfer function		Deviation
Mode	f [Hz]	S_{u_z}	f [Hz]	S_{u_z}	$\lvert\Delta S_{u_z}\rvert$
1	0.01953	1.953E-02	-	-	-
2	0.11720	2.654E-03	0.11720	2.792E-03	5.20 %
3	0.14160	9.418E-04	0.14160	9.086E-04	3.53 %
4	0.20510	1.493E-03	0.20510	1.553E-03	4.02 %
5	0.27830	1.001E-04	0.27830	9.820E-05	1.90 %

As can be observed from Figures 5.35 and 5.36, the estimations of the power spectral density from the numerical integration and use of the transfer function produces closely the same result. This is also shown from the values given in Table 5.3 and Table 5.4. A discussion regarding these results will be carried out in Section 6.

5.4 Results from Abaqus

In this section, the results from the finite element analysis on the Hardanger Bridge model will be presented. The case study has addressed the eigenfrequencies of the system, the damping in the bridge and the moving load problem. In the moving load section, both the accelerations and deflections of the system has been investigated, and a parameter test was carried out investigating the influence of several constraints on the response of the model.

5.4.1 Eigenfrequencies

In the frequency step used to extract the theoretical eigenmodes and eigenfrequencies from the finite element model in Abaqus, only gravitational loads are subjected to the bridge. As the study of the Hardanger Bridge is done with regard to vertical displacements and accelerations, only the vertical eigenmodes are relevant when attempting to verfiy the validity of the FEA model using the results obtained from the measurement data. The Abaqus model does not distinguish between vertical, horizontal and rotational eigenmodes, but in the Abaqus data file, commonly referred to as the *dat-file* because of the file ending *.dat*, the participation factors for each mode is listed. Participation factors describe the interaction between the modes and the state variables of a system, and are nondimensional scalars [1]. By determining the dominant participation factor of a mode, it can be described as a vertical, horizontal or rotational eigenmode depending on the dominant state variable.

It should be noted that the directional property of the eigenmode only indicates the main direction of the mode, and that e.g. a horizontal mode may influence the vertical response in addition to the horizontal response. Some modes may also combine significant deflections in several directions. This is the case for, among other, mode 17 of the bridge model, which combines horizontal and torsional deflections. The directional property of the eigenmode can also be determined through visual evaluation of the mode shape in Abaqus. The mode shapes of the first 6 vertical eigenmodes will be shown in Figure 5.39.

When extracting the eigenmodes from Abaqus, pure pylon and cable modes are also included. These do not excite the bridge deck, and can be identified visually from the model or by finding the modes where all participation factors are close to zero.

The results from Section 5.3 shows that the vertical response is mainly from exciting modes with eigenfrequencies less than 1 hertz. The first 20 eigenmodes from the FE-model, all with frequencies below 1 hertz, are shown in Table 5.5.

Table 5.5: The first 20 eigenfrequencies of the Hardanger Bridge model in Abaqus

Mode	Eigenfrequency [Hz]	Main direction
1	0.050056	Horizontal
2	0.097990	Horizontal
3	0.110420	Vertical
4	0.140660	Vertical
5	0.168950	Horizontal
6	0.197220	Vertical
7	0.211010	Vertical
8	0.224980	Tower/Cable mode
9	0.232500	Tower/Cable mode
10	0.233570	Horizontal
11	0.244520	Torsional
12	0.272450	Vertical
13	0.292990	Horizontal
14	0.329230	Vertical
15	0.359700	Torsional
16	0.373530	Tower/Cable mode
17	0.392090	Horizontal/Torsional
18	0.393950	Vertical
19	0.405960	Horizontal
20	0.407740	Tower/Cable mode

The measured eigenfrequencies of the bridge are identified by taking the spectral density of the measured acceleration data at a sensor, and finding the coordinates of the peaks along the frequency axis. As can be seen in Figure 5.37 and Figure 5.38, which shows the power spectra from sensors at respectively the midspan of the bridge and three fifths of the bridge length from the Vallavik side, the exciting of certain modes may not be experienced at all positions. This is especially true at the midspan, as Figure 5.37 shows. At the mid of the bridge, mode 3, mode 6, mode 7 and mode 14 are not recorded. The mode shapes displayed in Figure 5.39 supports this result, as all of the above mentioned modes seems to have no deflection at the midspan. Mode 6 is not recorded at any sensors, and possible explanations for this will be discussed further down in this chapter.

The examining of the power spectras from the different sensors showed that sensor H7, positioned 415 metres from the Vallavik end of the bridge, see Figure 5.4, contained all the eigenfrequencies below 0.4 Hz, and the last of the vertical eigenfrequencies among the 20 first eigenfrequencies from Abaqus is mode 18 with eigenfrequency 0.3940 Hz. Figure 5.38 shows the power spectra obtained from taking the spectral density at sensor H7, with the first 6 eigenfrequencies highlighted. As can be seen from both Figure 5.37 and Figure 5.38, the lowest eigenfrequencies has the highest peaks, which is plausible as the first modes are easiest to excite.

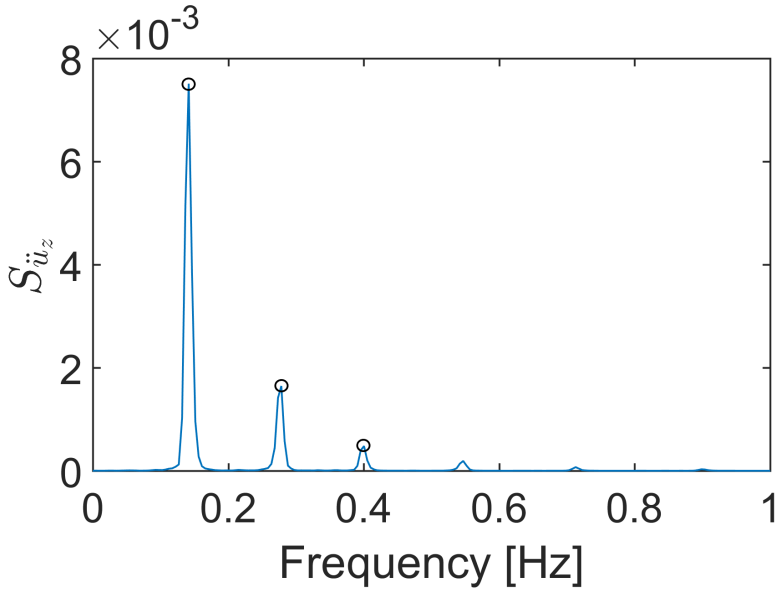

Mode	Frequency [Hz]
1	0.1416
2	0.2783
3	0.4004

Figure 5.37: The power spectra of the measured data from sensor H5 positioned 6 metres north of the midspan of the bridge

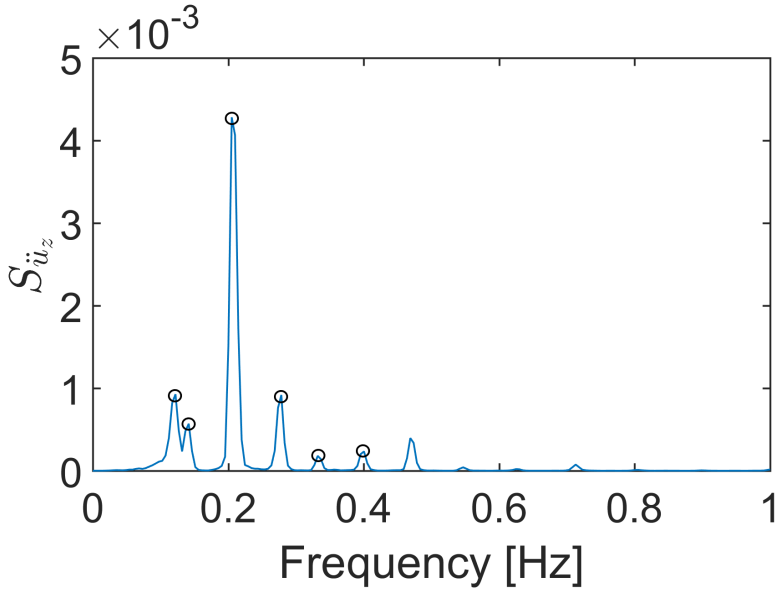

Mode	Frequency [Hz]
1	0.1172
2	0.1416
3	0.2051
4	0.2783
5	0.3320
6	0.4004

Figure 5.38: The power spectra of the measured data from sensor H7 positioned 415 metres from the southern end of the bridge

Of the first twenty eigenmodes from Abaqus, sixteen modes fully or partially excites the bridge deck, while four of the modes are pure pylon and/or cable modes. Seven of the modes are mainly vertical. In Table 5.6 the seven vertical eigenmodes from the first twenty modes in Abaqus are compared with the corresponding eigenmodes from the power spectra of the measured data. The pairing of the frequencies is based on a qualitative assessment where the FE eigenfrequency is paired with the closest measured eigenfrequency.

Table 5.6: Comparison of the first 7 vertical eigenfrequencies in Hz for the finite element model and the data measured at the Hardanger Bridge

Mode	Abaqus	Measured	Deviation
3	0.1104	0.1172	5.80 %
4	0.1407	0.1416	0.64 %
6	0.1972	-	-
7	0.2110	0.2051	2.80 %
12	0.2725	0.2783	2.13 %
14	0.3292	0.3320	0.84 %
18	0.3940	0.4004	1.60 %

The third vertical eigenmode from the Abaqus model, mode number 6, did not appear in the power spectra of the measured data from the Hardanger Bridge. Mode 6 and mode 7 are in very close proximity to each other along the frequency axis. The lack of eigenmode 6 in the power spectra might be due to the sensors not recording data at a high enough frequency to separate the two modes, and thus mode 6 being "swallowed" into mode 7. Another reason for the absence of the eigenmode may be because the sensors does not experience any response from the excitation of that specific frequency. Even though this is possible, e.g. how some modes are not present in the power spectra for the mid sensor as shown in Figure 5.37, it is deemed unlikely as the power spectra has been extracted from several sensors which should have been affected from the mode shape of the eigenmode, see Figure 5.39. A third possibility is the existence of environmental conditions like wind, and characteristics and properties of the bridge, which are not captured in the FE-model. This may e.g. be mistakes or improvised solutions during the construction of the bridge, that might influence the structure in a way that prohibits eigenmode 6. Thus, the bridge goes straight into mode 7, which is excited at a frequency very close to that of mode 6.

The comparison in Table 5.6 shows that the Abaqus model of the bridge estimates the eigenfrequencies of the Hardanger Bridge close to the actual eigenfrequncies. The deviation lies between 0.0009 hertz and 0.0068 hertz, and is deemed acceptable. Note that even though the deviation for mode 3 is almost 6 %, the discrepancy is only 0.0068 hertz. This is almost the same discrepancy as for mode 18, where the difference is 0.0064 hertz between the Abaqus value and the measured value, but as the value of the frequency is higher for mode 18 than mode 3, the deviation becomes only 1.60 %. The verification of the eigenmodes of the model is an important part of validating the model for further use in analyses of the moving load problem. The compliance between the results from the data and the Abaqus eigenfrequencies is plausible, and makes it reasonable to assume that the mode shapes of the model in Figure 5.39 are representative of the mode shapes of the actual bridge.

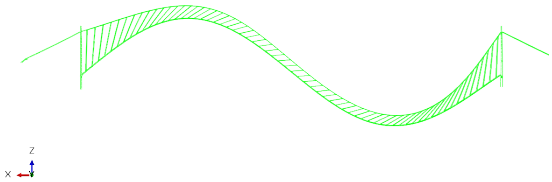

Eigenmode 3

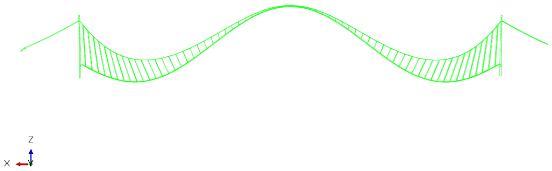

Eigenmode 4

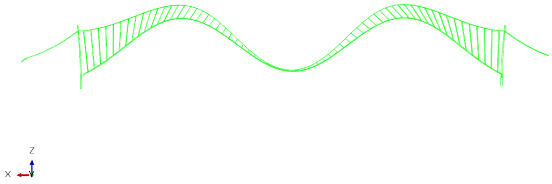

Eigenmode 6

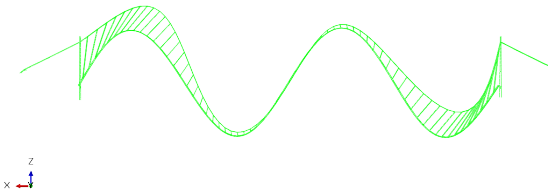

Eigenmode 7

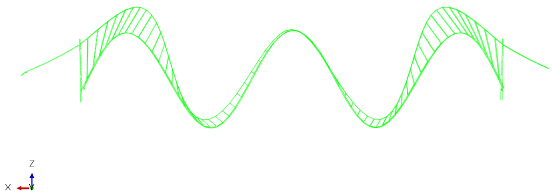

Eigenmode 12

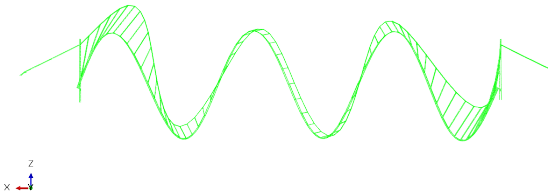

Eigenmode 14

Figure 5.39: The mode shapes of the first six vertical eigenmodes in the finite element model

5.4.2 Damping

To ensure a physical behaviour of the bridge model being used in the moving load simulation, the damping of the modes was further investigated. The complex eigenvalue problem for the model with implemented Rayleigh damping of $\xi_0 = 5\%$, see Section 5.2, yielded the real and the imaginary part of the eigenvalue for the eigenmodes of the system. From these, the damping ratio of each mode was obtained. In Table 5.7, the damping ratio for the seven first vertical eigenmodes of the Abaqus model are presented. The damping ratios of the first 50 eigenmodes are presented in Figure 5.40, where the stapled lines marks the applied range between ω_p and ω_r.

Table 5.7: The Rayleigh damping ratios and the modal damping ratios extracted from the complex eigenmodes of the Abaqus model for the seven first vertical eigenmodes of the Hardanger Bridge model

Mode	**Imaginary part of eigenvalue**	**Real part of eigenvalue**	**Eigenvalue**	**Modal damping ratio**	**Rayleigh damping ratio**
	$Im[\lambda]$	$Re[\lambda]$	λ	ξ_{Modal}	$\xi_{Rayleigh}$
3	0.693774	-0.003662	0.693784	0.69 %	3.23 %
4	0.885471	-0.015595	0.885608	0.84 %	3.12 %
6	1.235580	-0.076211	1.237928	1.76 %	3.29 %
7	1.325790	-0.012256	1.325847	0.50 %	3.36 %
12	1.710010	-0.035819	1.710385	0.72 %	3.80 %
14	2.067960	-0.051308	2.068596	0.77 %	4.28 %
18	2.478660	-0.036977	2.478936	1.07 %	4.87 %

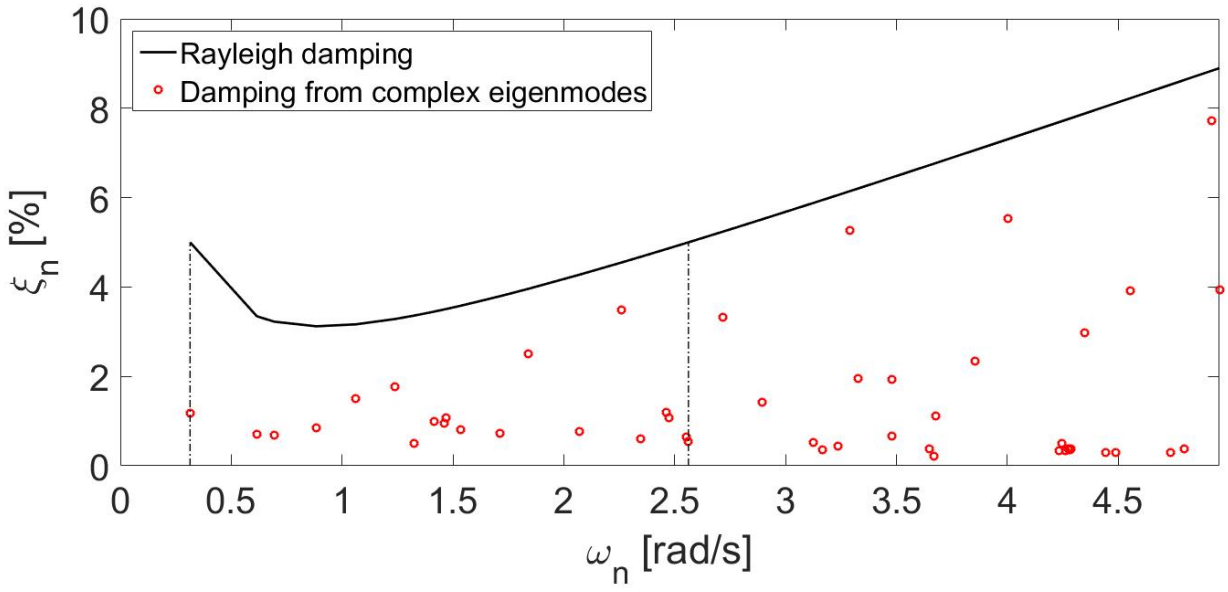

Figure 5.40: Rayleigh damping ratios compared to the effective modal damping ratios found from complex eigenmodes for the first 50 eigenmodes of the Hardanger Bridge. The stapled lines marks the applied range between ω_p and ω_r

The results show a significant overprediction of the damping of the bridge from the Rayleigh damping. From Figure 5.40, it can be seen that the Rayleigh damping ratios display the typical behaviour seen in Figure 2.1. The discrepancy between the theoretical Rayleigh damping and the actual damping in the model may partly be credited to geometric stiffness not being included in the Rayleigh damping in Abaqus. The discrepancy may also in some part be blamed on a too high estimation for the initial damping ratio ξ_0.

5.4.3 Acceleration response from the numerical simulation

The main case of the moving load model is a single force of 200 kilonewtons moving at 62 kilometres per hour, representing a truck weighing approximately 20 tonnes moving across the bridge from Bu to Vallavik in 76 seconds, in accordance with the data from the traffic logging, see Section 3.3. As stated in Section 5.3.1, there was much wind during the car logging, with horizontal wind speeds in the range of six to seven metres per second.

Implementing the main case onto the Hardanger Bridge model gave the acceleration response displayed in Figure 5.41. The results are for sensor H5, which is the sensor on the bridge closest to the midspan of the bridge, see Section 5.1.2 for the precise placement, and thus the most critical section of the bridge with regard to deflection. Figures 5.42 and 5.43 shows the acceleration from the Abaqus model at sensor H5 compared to the measured results. The accelerometers will give the acceleration response relative to the accelerations occurring prior to the beginning of the considered time series, and as such the measured acceleration response is adjusted to oscillate about the horizontal axis using the Matlab function *detrend*, see Section 5.3.4. The adjustment is done to make the recorded data comparable with the FE model, as the Abaqus accelerations begins in zero because the model starts at rest.

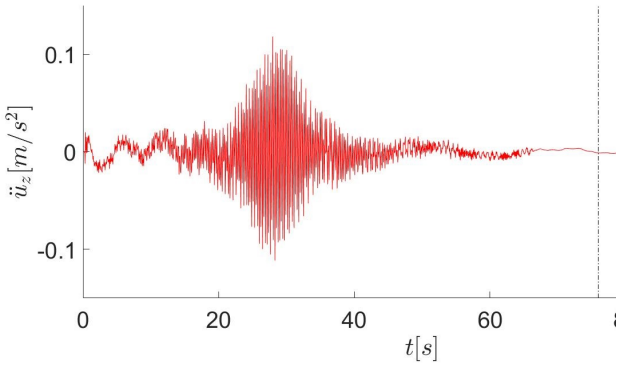

Trailer	
Axles	1
Weight	200 kN
Speed	62 km/h
Bridge	
Rayleigh damping	$\xi = 5$ %
Boundary condition	*Pinned*
Analysis	
Analysis type	*Dynamic*
Margin node moments	*Yes*

Figure 5.41: Acceleration at sensor H5 positioned 6 metres from midspan for the main case of the finite element moving load model. The dotted line marks where the car leaves the bridge

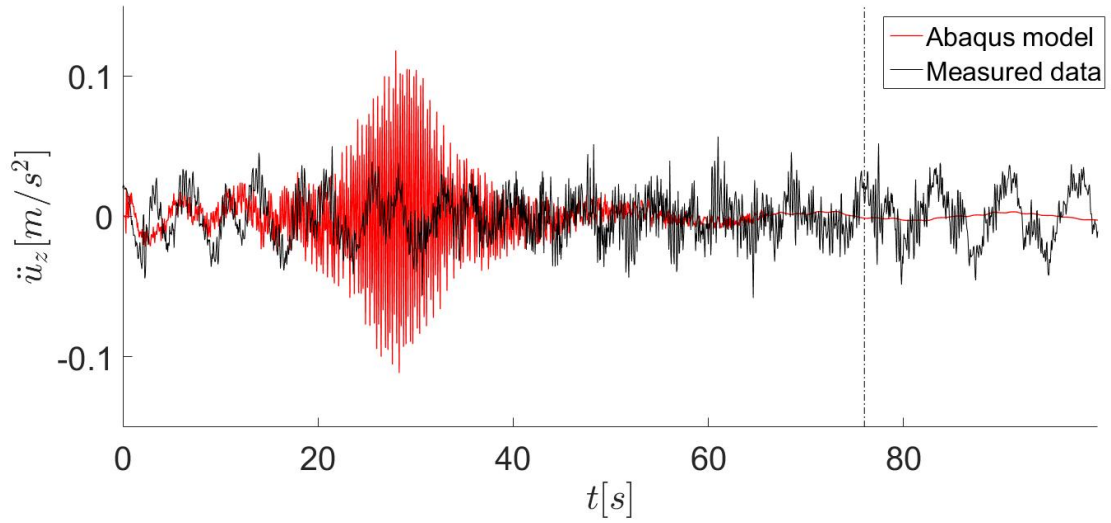

Figure 5.42: Comparison of the acceleration at sensor H5 for the Abaqus model and the measured data

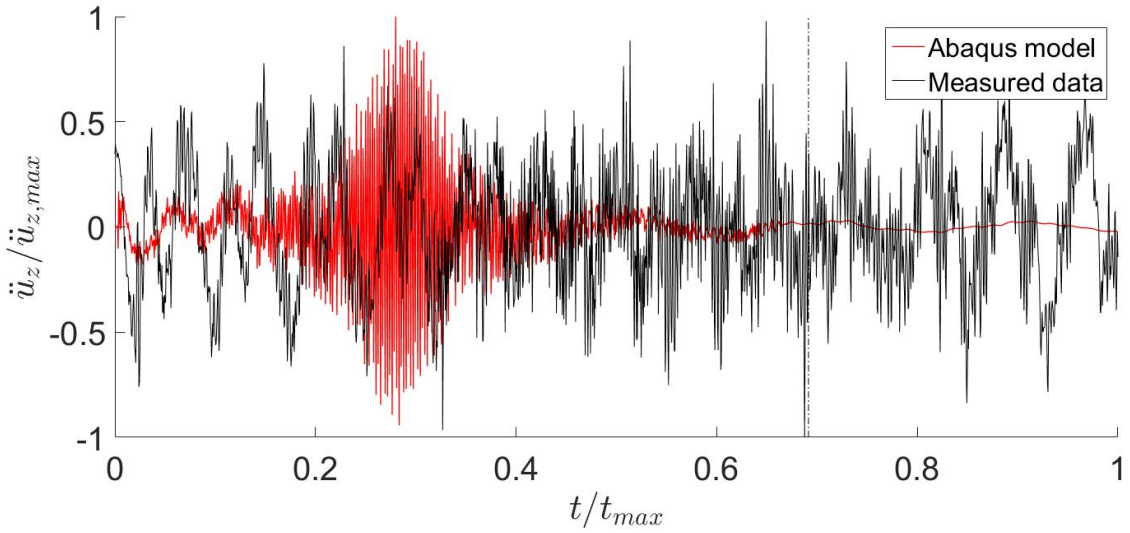

Figure 5.43: Comparison of the relative acceleration at sensor H5 for the Abaqus model and the measured data

As can be seen from Figures 5.42 and 5.43, the finite element model does not reproduce the measured results very accurately. The shapes of the two acceleration responses differ greatly. The amplitude of the measured accelerations remain about the same during the whole time series, and does not display the idealistic characteristics of a system subjected to a moving load seen in the Abaqus response. The frequency of the measured results seems to slightly increase after the the vehicle has driven past the sensor, a tendency also found in the finite element result. The acceleration response in Abaqus is overpredicted by a factor of 1.51, as the finite element model gives a maximal amplitude of 0.1181 m/s^2 and the measured maximal amplitude is 0.0782 m/s^2.

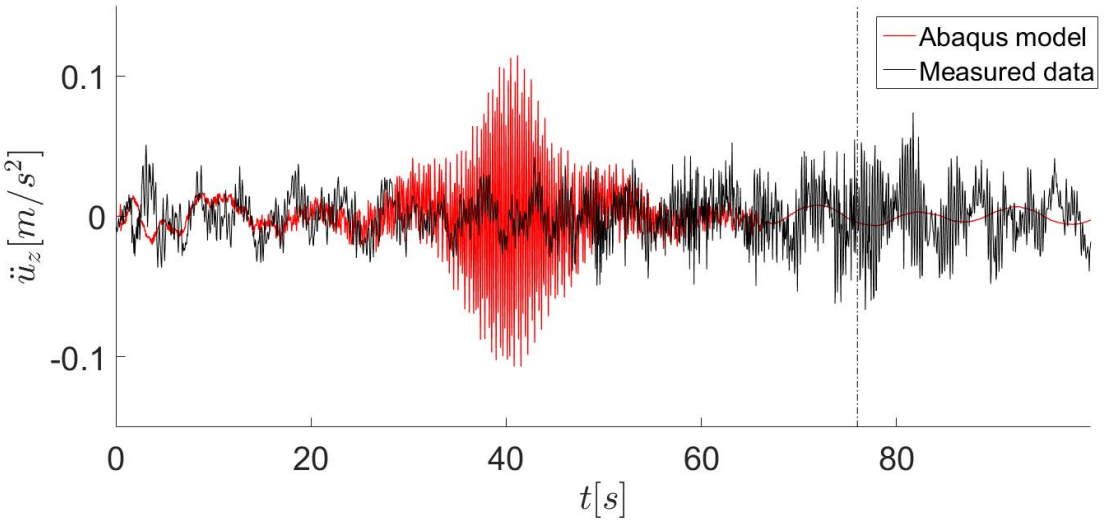

Figure 5.44: Comparison of the acceleration at sensor H7 for the Abaqus model and the measured data

Figure 5.44 shows that the model overpredicts the acceleration also at sensor H7, which is positioned 415 metres from the Vallavik side of the bridge, see Figure 5.4 in Section 5.1.2. At sensor H7, the maximal magnitude of the acceleration is overpredicted with a factor of 1.62. Note also how the frequency content in Table 5.8 shows that the FEA model excites very different eigenfrequencies compared to the recorded data at both sensors. There are some similar eigenfrequencies, e.g. 0.1565 hertz and 0.7040 hertz at sensor H5 and 0.3911 hertz at H7, but the general tendency is that the compliance is low. Note also that the most excited eigenfrequencies at both sensors are at 4.263 hertz and 4.381 hertz for the finite element model, whereas the recorded data excites the highest amplitudes for the eigenmodes at 0.1563 hertz and 0.2734 hertz at sensor H5 and 0.1953 hertz and 0.3906 hertz at sensor H7, as can be seen in Figures 5.45 and 5.46. Due to the short period of time used to compute the power spectra, the resolution becomes low. For a short time interval, the estimated power spectral density and the corresponding frequencies from the Welch's method will have too few data points to determine the eigenfrequencies. This is shown by comparing the eigenfrequencies in Table 5.8 with the estimated eigenfrequencies in Figure 5.37 and 5.38.

Table 5.8: The frequency content of the recorded accelerations and the Abaqus moving load model for the main case of a truck driving across the Hardanger Bridge

	Section H5		**Section H7**	
Mode	**Recorded [Hz]**	**FEA [Hz]**	**Recorded [Hz]**	**FEA [Hz]**
1	0.1563	0.0391	0.1953	0.0782
2	0.2734	0.1565	0.3906	0.2738
3	0.3906	0.4302	0.5469	0.3911
4	0.5469	0.5085	0.7031	0.7040
5	0.7039	0.7040	0.8203	0.9387
6	0.8984	1.1340	1.0940	1.0950

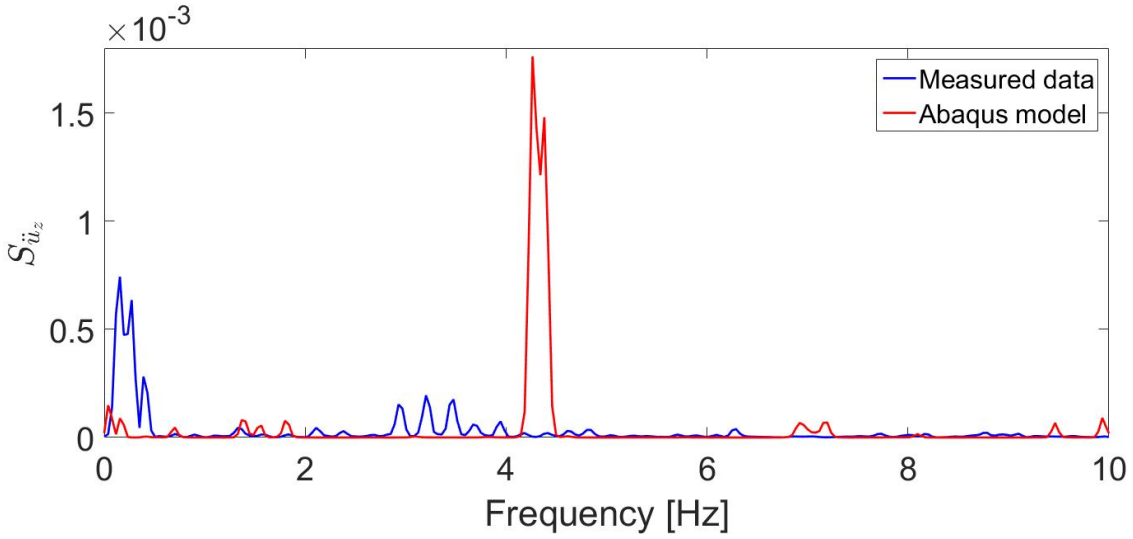

Figure 5.45: The power spectra for sensor H5 of the recorded accelerations and the Abaqus moving load model for the main case of a truck driving across the Hardanger Bridge

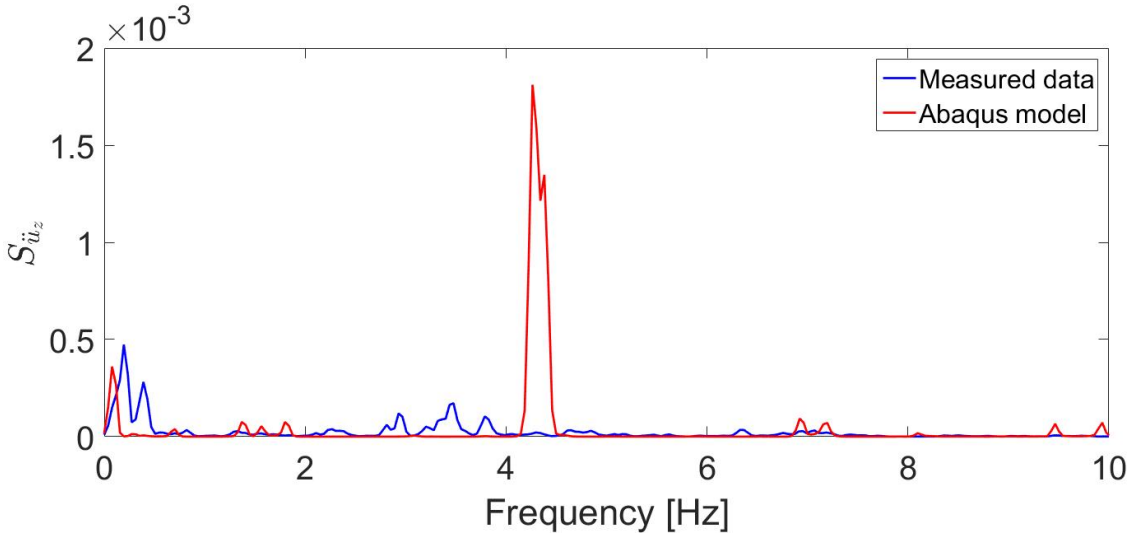

Figure 5.46: The power spectra for sensor H7 of the recorded accelerations and the Abaqus moving load model for the main case of a truck driving across the Hardanger Bridge

As the finite element result differ from the measured data at both sensor H5 and H7, the discrepancy between the model and the measured data does not seem to be caused by an error in one of the accelerometers. This inference is further encouraged by the results in Figure 5.47, which shows the recorded accelerations for all the sensors along the bridge for the time series of the single truck driving across the bridge. The results shows that all of the sensors experiences accelerations in approximately the same range of amplitudes, which indicates that there is no large errors in any of the sensors, as they in that case would have shown results that deviated from the other sensors. Another observation from Figure 5.47

is that, due to the high frequency of the fluctuations, it becomes difficult to distinguish patterns and particularities of each result and compare them with each other. Thus, the acceleration responses are not very well suited for comparison relative to each other, as they blend into each other in the figure.

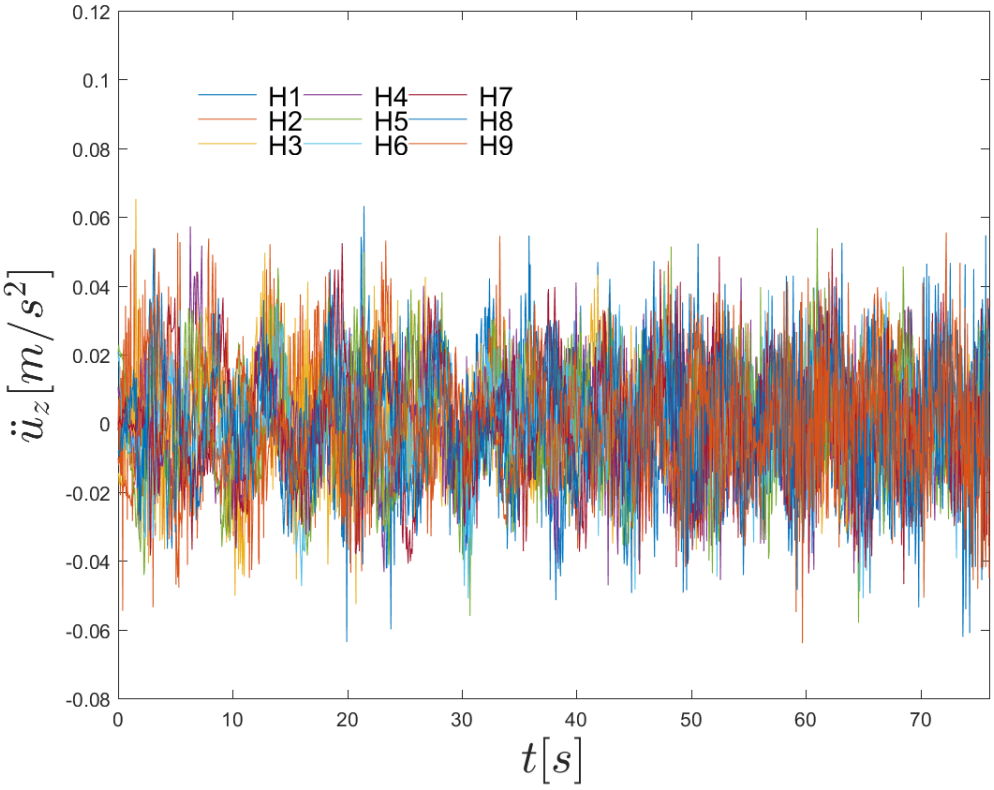

Figure 5.47: The measured acceleration at the sensors across the bridge for a single vehicle crossing the bridge

Some of the inaccuracy of the Abaqus model may be attributed to the effects of wind. Wind is considered one of the major components when studying the dynamic response of slender bridges, and as wind is the most influential force on the bridge, the perpetual oscillation of the measured acceleration response seen in Figures 5.42 and 5.44 may be explained by the accelerations from the wind cancelling out the effects from the vehicle. Wind is not included in the finite element model, as the purpose of the model is to find the effects of traffic alone. The measured data used in the comparison is done for a time series with large amounts of wind present, see Section 5.3.1. As presented in Section 5.3.5, the authors has not been successful in the attempt to filter out the effects of wind from the data. Thus, the interaction between wind forces and traffic forces might be significant and affect the data extensively.

During the time of the traffic logging, no time intervals without traffic over a long enough period for comparison was logged, but as discussed in Section 5.3.1, the effects of a passenger car on the response is negligible. Figures 5.48 and 5.48 shows the displacements for section H5 and H7 when the single truck drives across the bridge, compared to the situation of a single passenger car driving across the bridge. The passenger car arrives at the bridge at 08 : 55 : 50 and crosses the bridge in 60 seconds, marked by the dotted blue line, and thus moves at 78.6 kilometres per hour.

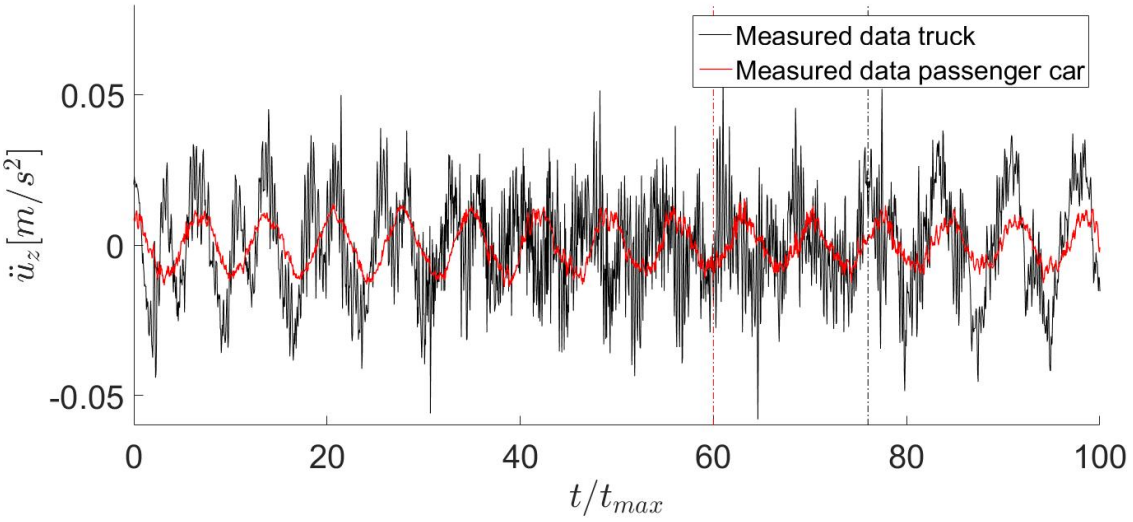

Figure 5.48: The measured acceleration at section H5 with and without a truck crossing the bridge

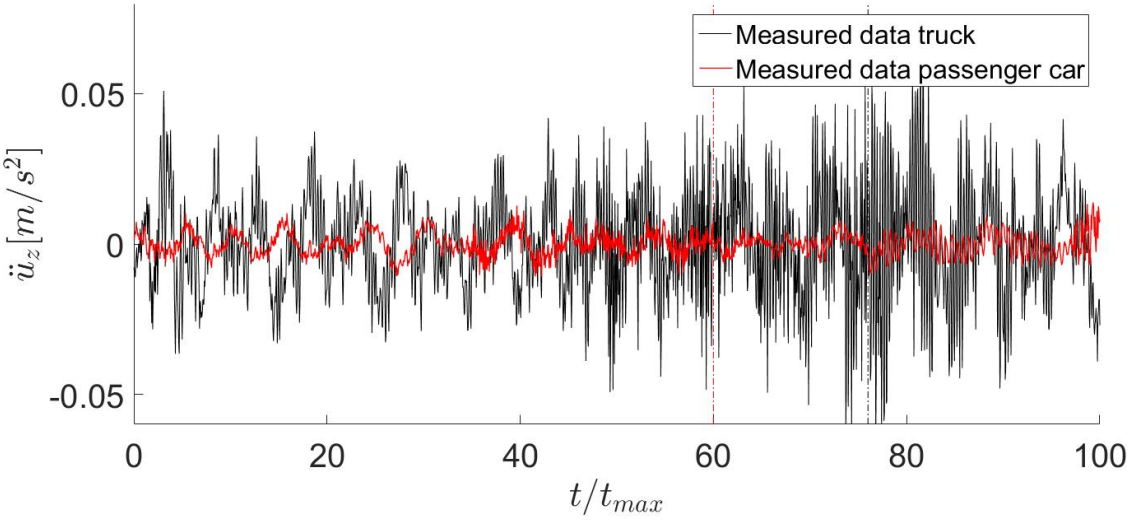

Figure 5.49: The measured acceleration at section H7 with and without a truck crossing the bridge

As can be seen from the figures, the response from a single passenger car on the bridge, which is considered as corresponding to a situation of pure wind, differs greatly from the situation with a truck on the bridge. The frequency and the amplitude of the oscillations increases when heavy vehicles are present. It can also be seen that the oscillations are more "messy", as opposed to the smoother curves of the time series without heavy vehicles, which indicates that more modes are excited when the vehicle drives across the bridge.

The wind speeds when the passenger cars crosses the bridge is in the range of six to seven metres per second, whereas the situation is four to five metres per second when the truck crosses the bridge. Hence, the wind situation seems to be even worse for the situation of no truck on the bridge than for the time period when the truck is on the bridge. Considering the increase in response when there are heavy vehicles on the bridge, the effects of wind on the response seems smaller than first assumed.

To examine the effects of different constrains on the finite element model, and investigate if other parameters than the interaction between wind and traffic may be responsible for some of the discrepancy between the finite element results and the measured results, the Abaqus model was subjected to a parameter test, as described in Section 5.2. Due to the difficulty of comparing acceleration responses with each other in a descriptive manner, and the influence of wind on the measured acceleration response giving deviations in the plotted shapes of the measured data and the FE results, the acceleration response is not seen as a suitable way of displaying the results from the parameter test. Thus, deflection from the integration of accelerations is chosen as the premise for the parameter test. The integrated accelerations will be further examined in Section 5.4.4. As the section at the midspan is the most critical, the deflection will be shown at section H5 since it is the closest section to the midspan of the bridge.

Even though deflection is chosen as the most suitable medium for displaying the results from the parameter test, some of the results from the parameter test turned out to have a significant effect on the acceleration response from the Abaqus model, and will be presented.

Number of moving loads

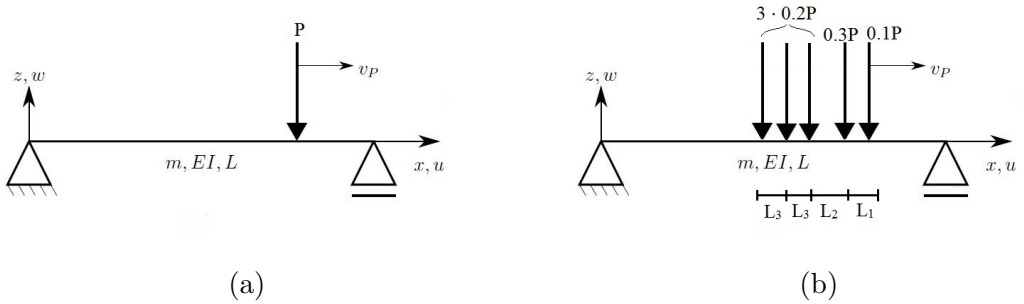

(a) (b)

Figure 5.50: The 1 axle moving load model (a) and the 5 axle moving load model (b) on a simply supported beam. For the 5 axle model, $L_1 = 3.7m$, $L_2 = 4.3m$ and $L_3 = 1.5m$. The figures are based on a figure from Frøseth's master thesis [12]

The accuracy of the moving load model may affect the response in the simulation of the vehicle travelling across the bridge. In Section 3.1 a moving force model was found as sufficient for modelling the moving load, but considering that a loaded truck often has five wheels, two on the tractor unit and three on the trailer, it was of interest to investigate the effect of modelling the moving load as five moving forces opposed to one moving force. The model consisting of five moving loads had a length of 11 metres in total, where the three wheels on the trailer had a centre to centre distance of 1.5 metres between each, and the distance between the centres of the wheels on the truck was 3.7 metres. Figure 5.50 (a) and Figure 5.50 (b) illustrates respectively the 1 axle moving load model and the 5 axle moving load model.

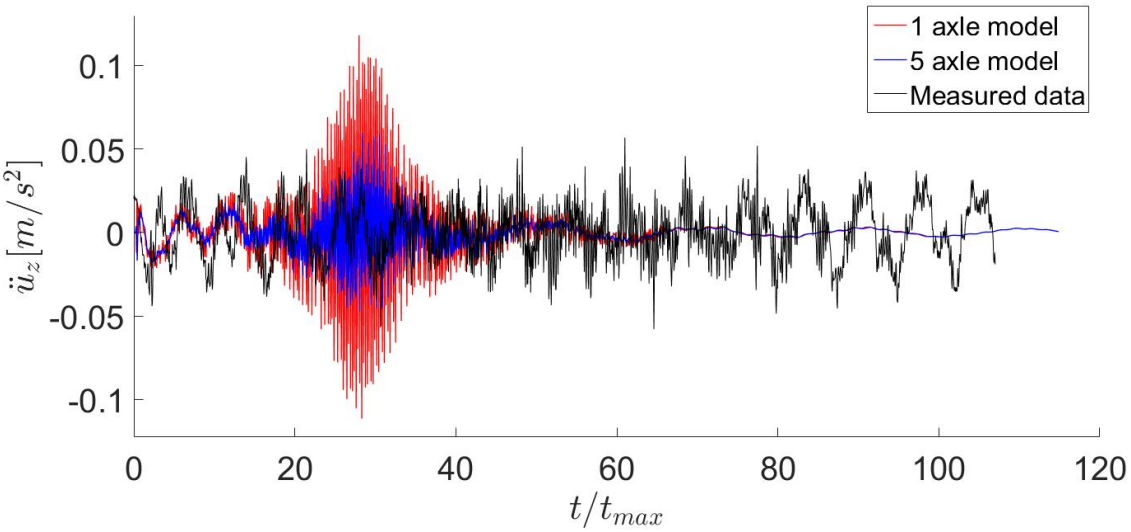

Figure 5.51: The acceleration at section H5 for a 1 axle moving load model and a 5 axle moving load model travelling across the bridge

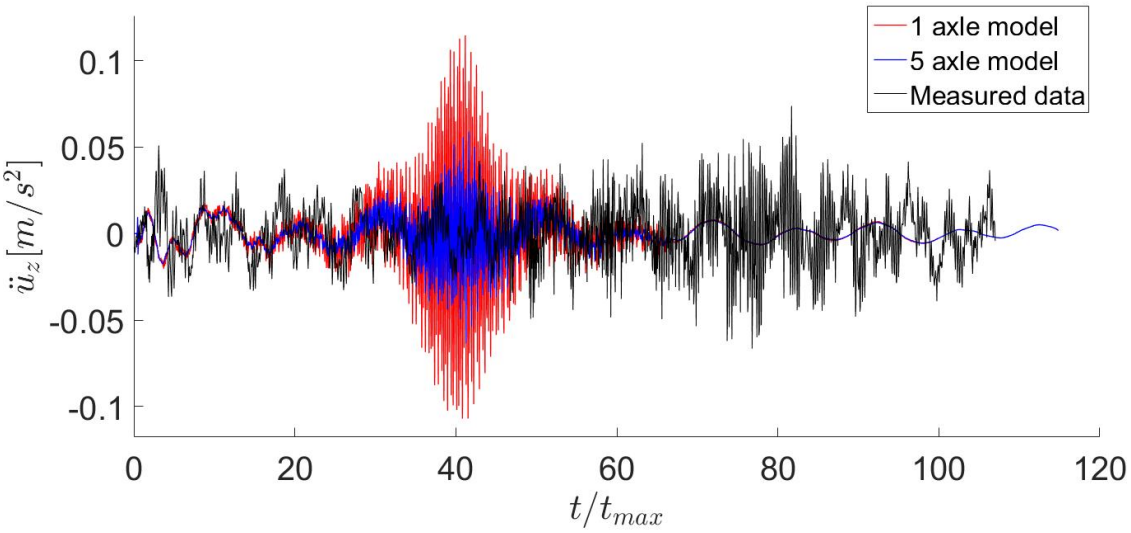

Figure 5.52: The acceleration at section H7 for a 1 axle moving load model and a 5 axle moving load model travelling across the bridge

The acceleration response in Figure 5.51 and Figure 5.52 shows that there there is a clear distinction between the two models. The 5 axle model seems to reduce a lot of the high frequency noise. This is further evidenced in Figure 5.53 which shows the spectral density of the 1 axle model and the 5 axle model. It can be seen that the eigenfrequencies higher than 7.2 hertz disappears, and that the amplitudes of the excited eigenfrequencies higher than 4.4 hertz are reduced to almost nothing. Also, the amplitudes of the first two excited eigenfrequencies at both sections remains the same for the 1 axle model and the 5 axle model, but the amplitudes of the rest of the excited eigenfrequencies is reduced significantly, or vanished, for both section H5 and section H7 when using the 5 axle model. The magnitude of the maximum acceleration at section H5 is reduced to a half, from 0.1181 m/s^2 to 0.0597 m/s^2, and at section H7 the magnitude is reduced by a factor of 0.55 as it goes from 0.1146 m/s^2 to 0.0635 m/s^2. The maximum amplitude of the measured acceleration at H5 is 0.0580 m/s^2, and 0.0621 m/s^2 at H7. Thus, the 5 axle model may be a more correct model of the moving vehicle, as it estimates the maximal of the acceleration magnitude with 97 % accuracy at section H5 and 98 % accuracy at section H7.

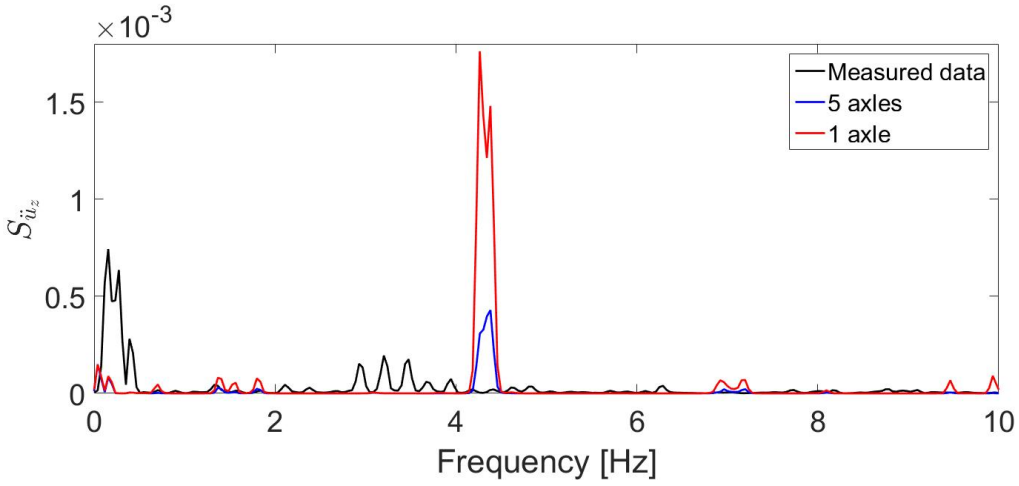

H5

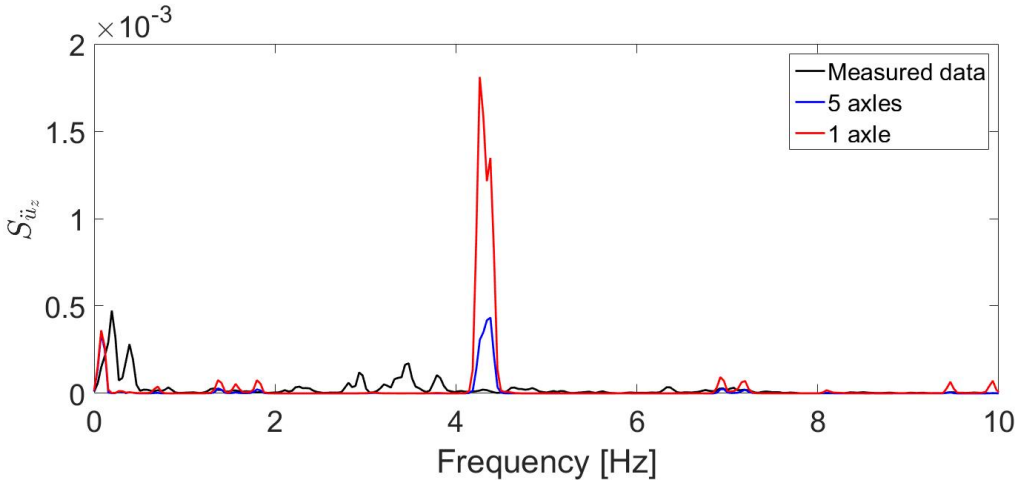

H7

Figure 5.53: The spectral density at section H5 for a 1 axle moving load model and a 5 axle moving load model travelling across the bridge

Damping

In a dynamic analysis, effects from oscillations in the structure may amount for a significant amount of the response. For a completely undamped system, the structure will experience free vibrations and the amplitude of the oscillations will not be reduced over time. Free vibration is a simplification only used theoretically, and will not be the case in an actual structure. Instead the oscillations will be damped out. As explained in Section 2.1.2, the Rayleigh damping is based on a guess of the damping ratio for two eigenmodes of the structure, ξ_0. In the Abaqus model, the value $\xi_0 = 5\%$ was chosen as appropriate, see Section 5.4.1. To investigate the effect of the damping, and the accuracy of the estimation of the damping ratio ξ_0, implementation of different damping ratios were introduced in the moving load model.

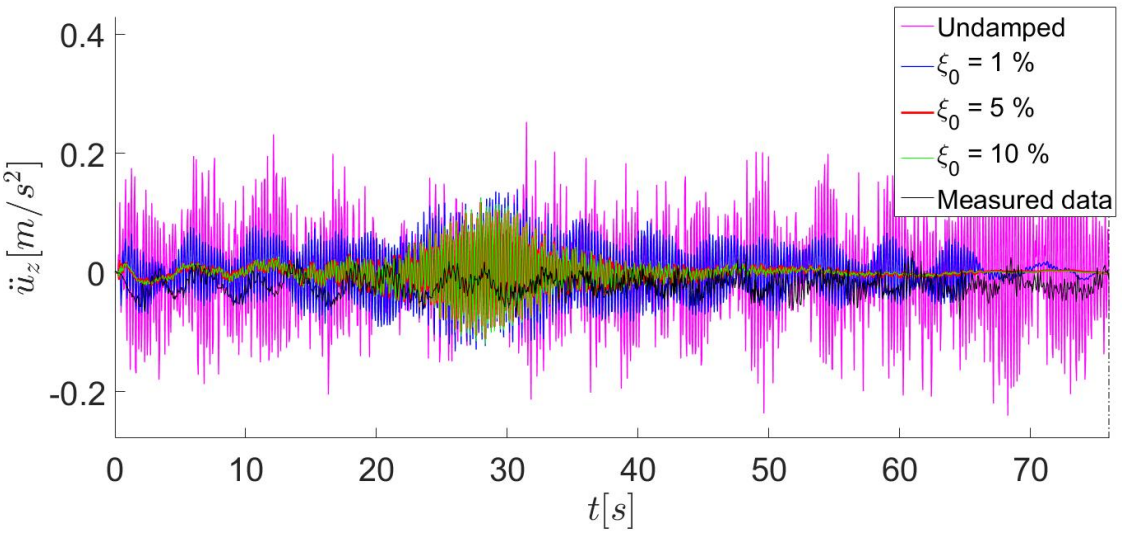

Figure 5.54: The acceleration at section H5 for different properties of damping in the structure

As can be seen from Figure 5.54, the introduction of damping has a big influence on the acceleration response of the system. The discrepancy between the undamped model and the model with 1 % Rayleigh damping, is evident. The same goes for the model with moderately high damping, $\xi_0 = 5$ %, and the model with low damping, $\xi_0 = 1$ %. The difference between implementing 5 % and 10 % Rayleigh damping to the structure seems almost non-existent, as the two graphs almost completely overlaps. Upon close inspection, it can be seen that when the vehicle is not at the midspan of the bridge, the higher damped model experiences a little bit less oscillations compared to the model with $\xi_0 = 5$ %, but the difference is so small it can be considered negligible. The results from Table 5.9, shows that the maximum acceleration is higher for the highly damped model than the moderately damped model. When looking at the magnitude of the maximum accelerations, the difference between the damped models is small, and the most significant result is the reduction in magnitude when introducing damping compared to the undamped model. The main model is seen to experience a maximum acceleration 53.3 % lower than the undamped model.

Table 5.9: Maximum deflection at section H5 for varying damping properties

Rayleigh damping ratio ξ_0	Undamped	1 %	5 %	10 %
Max acceleration $[\mathbf{m/s^2}]$	0.2528	0.1388	0.1181	0.1262

In Figure 5.55 it is shown how the damping influences the excitement of the eigenfrequencies. The plot shows that a change in damping ratio does not change which frequencies are excited, but rather to what degree they are excited. The magnitude of the peaks of the model with $\xi_0 = 1$ % is significantly larger than the peaks in the higher damped models, and it seems that a change from $\xi_0 = 5$ % to $\xi_0 = 10$ % influences the response very little. These results correlates well with the results from the examination in time domain.

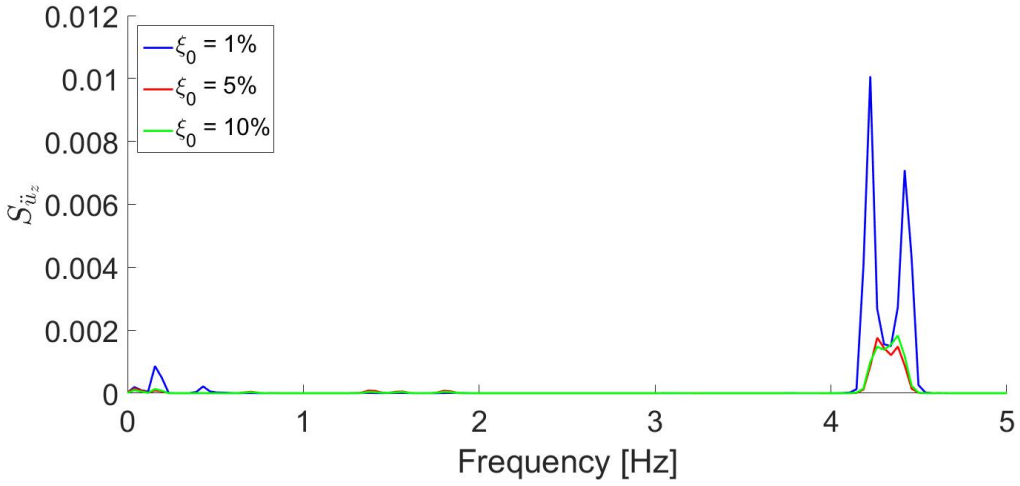

H5

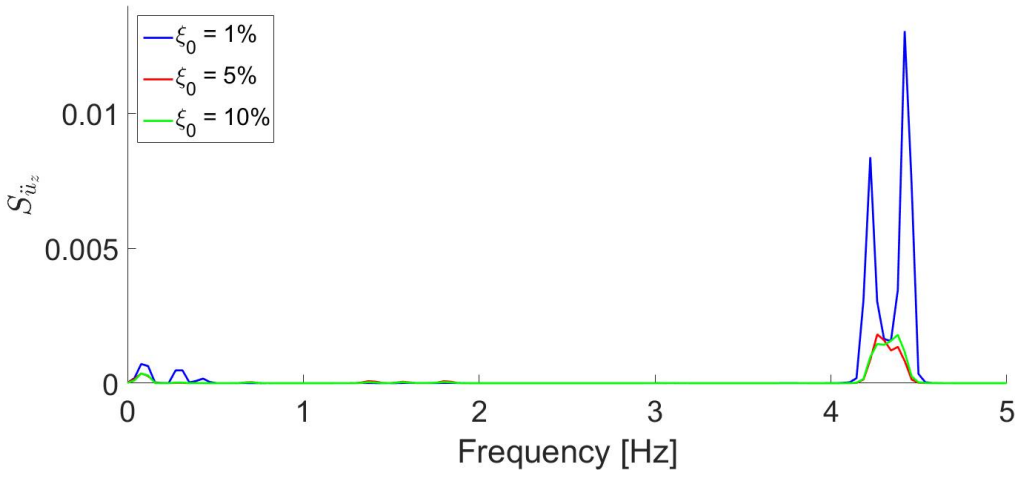

H7

Figure 5.55: The power spectra of the Abaqus model with different damping properties

5.4.4 Displacements from the numerical simulation

As discussed in Section 5.4.3, the frequency of the oscillations in the acceleration response is so high it becomes difficult to distinguish patterns and particularities of each result and compare them with each other. The results from the main moving load model in Figures 5.58 and 5.62 shows that the deflections are a more convenient way of displaying the response when comparing results. Hence the results from the parameter test will be presented as deflections. As the section at the midspan is the most critical, the deflection will be shown at section H5 due to it being the closest section to the midspan of the bridge.

The displacements of the measured data is obtained from numerical integration of the recorded accelerations. The integration is executed by a Matlab script provided by NTNU, and can be found in the digital appendix. When obtaining displacements from numerical integration of accelerations, there are some uncertainties present. Thus the accuracy of the displacements used in the comparison between the finite element model and the measured results is uncertain. The results from the investigation of the spectral density in Section 5.3.6 indicate that the method for obtaining displacements provides results of sufficient accuracy. As such, the displacements obtained from the measured results are deemed to be of acceptable accuracy for further use in the thesis.

Table 5.10: Comparison of the first seven vertical eigenfrequencies in Hz for the finite element model and from the recorded accelerations and integrated accelerations for the Hardanger Bridge

Mode	Abaqus	Accelerations	Deflections
NA	-	-	0.0195
NA	-	-	0.0244
3	0.1104	0.1172	0.1172
4	0.1407	0.1416	0.1416
6	0.1972	-	-
7	0.2110	0.2051	0.2051
12	0.2725	0.2783	0.2783
14	0.3292	0.3320	0.3320
18	0.3940	0.4004	0.4004

Table 5.10 shows the first eigenfrequencies for the integrated accelerations together with the frequencies from the Abaqus model and from the recorded accelerations. As can be seen, the results from the integrated accelerations and the other two methods corresponds strikingly well. The integrated accelerations displays low eigenfrequencies that are not present in either the finite element model or the recorded accelerations. The exciting of these eigenfrequencies is considered a source of error for the displacements from the recorded data, as it may instigate unhpysical response.

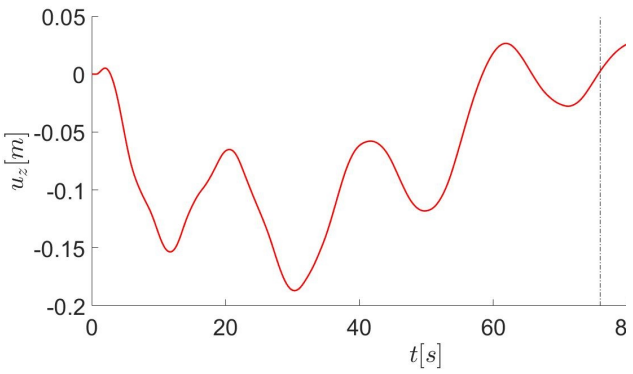

Trailer	
Axles	1
Weight	200 kN
Speed	62 km/h
Bridge	
Rayleigh damping	$\xi_0 = 5$ %
Boundary condition	*Pinned*
Analysis	
Analysis type	*Dynamic*
Margin node moments	*Yes*

Figure 5.56: Deflection at section H5 positioned six metres from midspan for the main case of the finite element moving load model. The dotted line marks where the car leaves the bridge

The moving load model implemented onto the Hardanger Bridge model gave the deflection results shown in Figure 5.56 with the parameters stated in the same figure. It is used as an estimation of the recorded data of a semi-trailer weighing approximately 20 tonnes moving across the bridge in 76 seconds, with horizontal wind speeds in the range $6 - 7$ metres per second.

Figure 5.57 shows a comparison between the main model and the moving load model without enforced moments in the nodes margining the moving load.

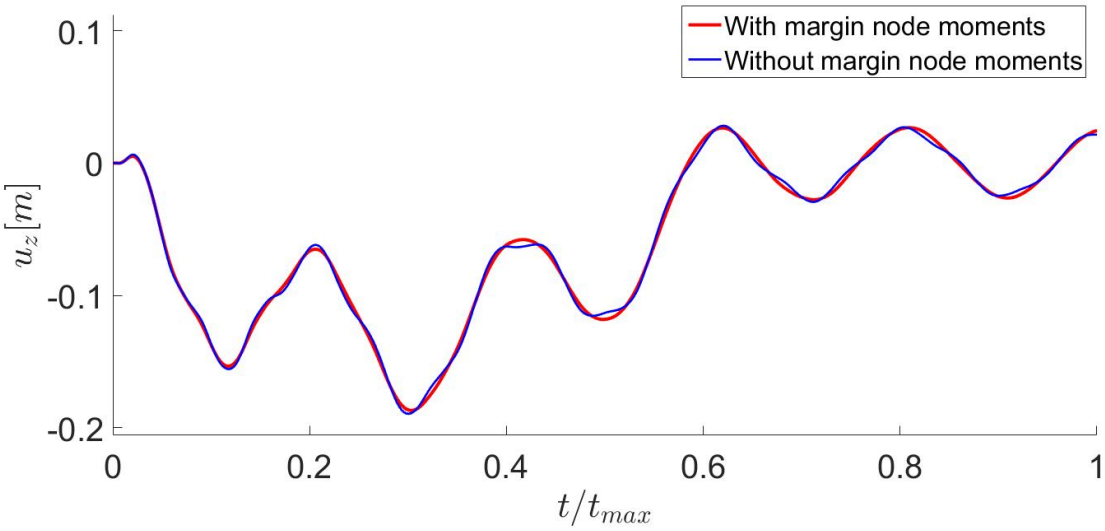

Figure 5.57: The deflection at midspan for the main moving load model and a moving load model without enforced moments in the margin nodes

As seen in Section 3.3, the solution with enforced moments in margin nodes and the solution without moments in those nodes showed high compliance when the mesh was fine enough for convergence towards the analytical solution. Figure 5.57 shows that the main model and the model without enforced moments in the nodes margining the moving load yields close to the

same solution. Hence, the size of the elements in the finite element model of the Hardanger Bridge seems to be sufficiently small.

In Figures 5.58 and 5.59 the deflection from the Abaqus model at section H5 is compared to the measured results. The moving load in Abaqus enters a bridge in resting position, whereas the measured data shows vehicles entering a bridge already in motion, and thus with initial deflection. Hence, the measured data is adjusted to start in zero on the y-axis, to show the effects from when the truck enters the bridge in a way that makes it easily comparable with respect to the finite element model.

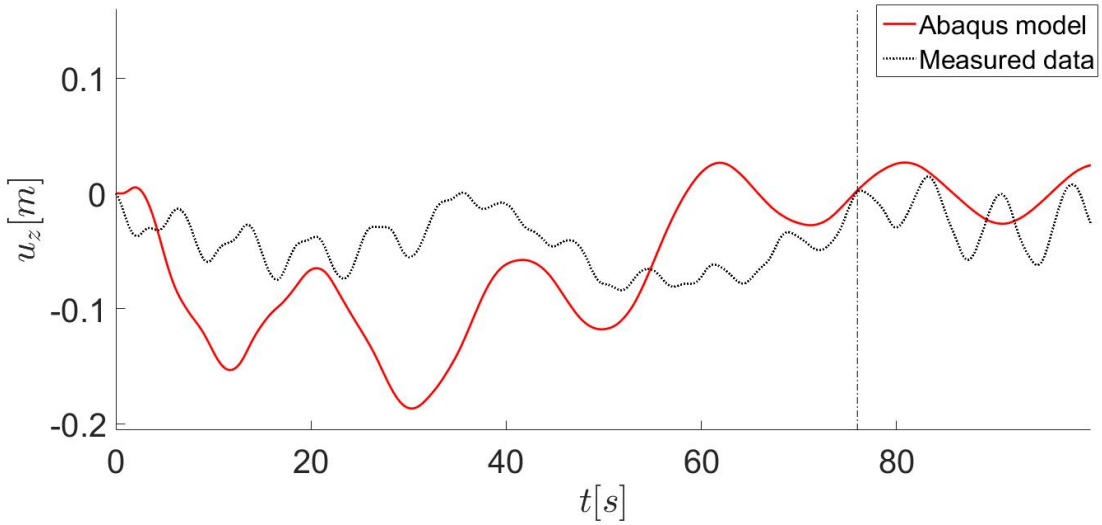

Figure 5.58: Comparison of the deflection at section H5 for the Abaqus model and the measured data

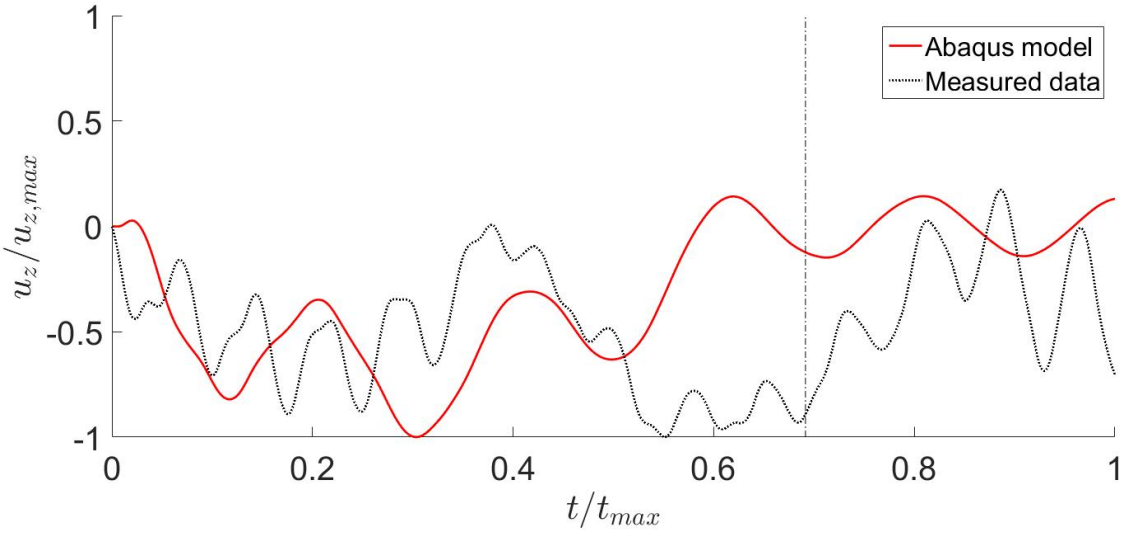

Figure 5.59: Comparison of the relative deflection at section H5 for the Abaqus model and the measured data

As can be seen from Figures 5.58 and 5.59, the finite element model does not reproduce the measured results very accurately. The maximum deflection of the Abaqus model is 186.9 millimetres, whereas the maximum deflection of the measured data is 84.2 millimetres. This means that the model predicts a deflection at the midspan 2.22 times larger than the real deflection. The comparison of the acceleration response shows that also the accelerations are overpredicted in the finite element model compared to the measured results, see Section 5.4.3. Hence, the overprediction of the displacements is plausible.

Table 5.11 shows that the FEA model excites very different eigenfrequencies for most of the modes compared to the recorded data at both section H5 and H7. It is interesting, however, that the most excited eigenfrequency at both sections are at 0.0391 hertz for both the finite element model and the recorded data, as can be seen in Figures 5.45 and 5.46. Note that the eigenfrequencies in the Abaqus model obtained from using Welch's method on the displacements does not correspond with the eigenfrequencies of the Abaqus model calculated from the eigenvalues, see Table 5.10.

Table 5.11: The frequency content of the recorded displacements and the Abaqus moving load model for the main case of a truck driving across the Hardanger Bridge

	Section H5		**Section H7**	
Mode	**Recorded [Hz]**	**FEA [Hz]**	**Recorded [Hz]**	**FEA [Hz]**
1	0.0391	0.0391	0.0391	0.0391
2	0.3906	0.3520	0.3906	0.3129
3	0.5469	0.4302	0.7422	0.4302
4	0.6250	0.5867	0.8984	0.7040
5	0.7422	0.7040	1.0160	1.0170
6	0.8594	1.0170	1.2890	1.2910

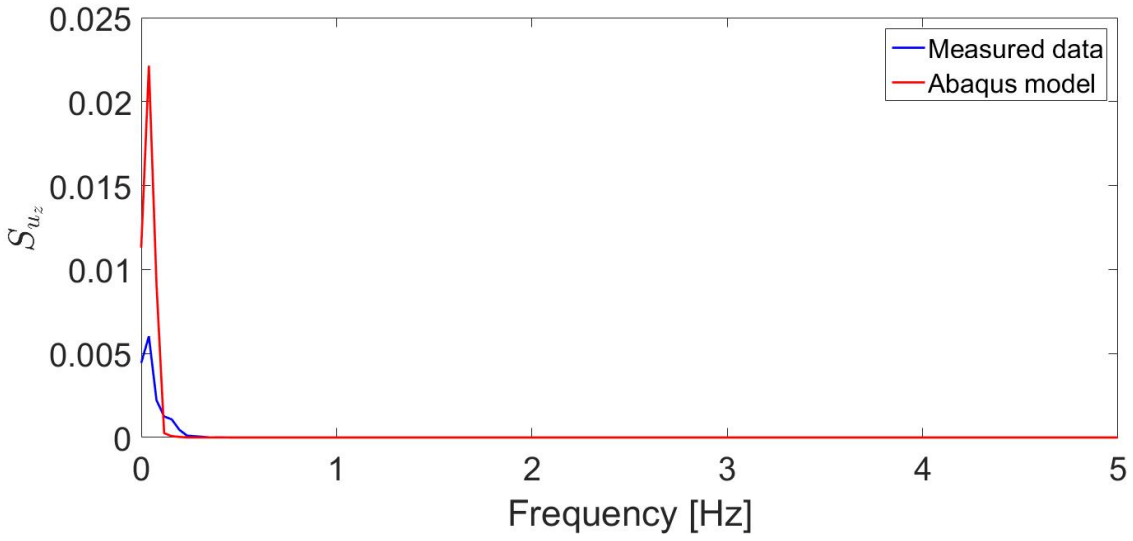

Figure 5.60: The power spectra for section H5 of the recorded displacements and the Abaqus moving load model for the main case of a truck driving across the Hardanger Bridge

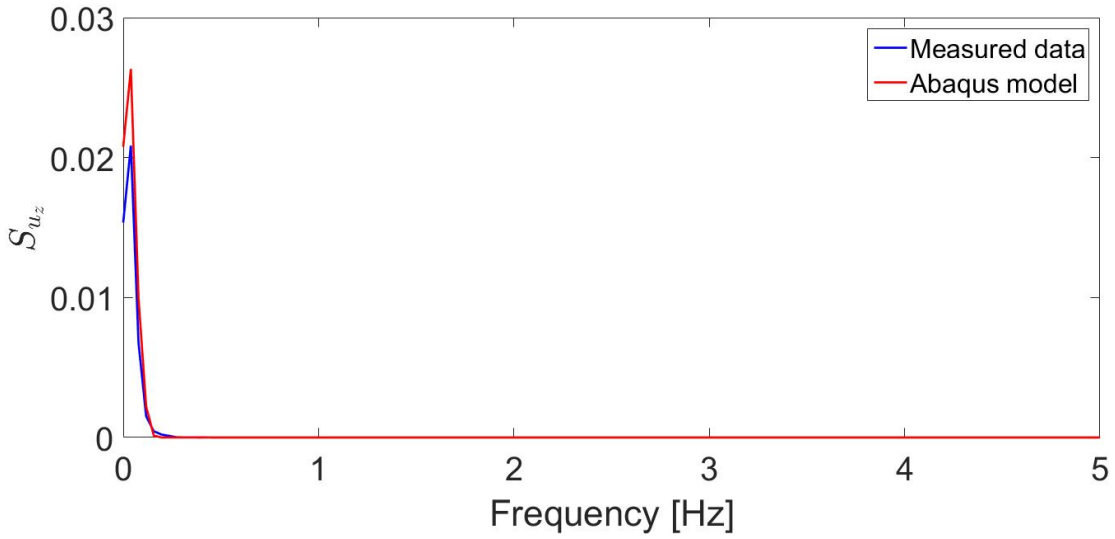

Figure 5.61: The power spectra for section H7 of the recorded displacements and the Abaqus moving load model for the main case of a truck driving across the Hardanger Bridge

As can be seen in Figure 5.62, the model also overpredicts the deflection at section H7. At section H7, the maximum deflection is overpredicted by a factor of 1.67, as the measured maximum deflection is 109.0 millimetres and the maximum deflection of the Abaqus model is 182.5 millimetres. This is less than the overprediction at section H5, but as can be seen in Figure 5.62, the maximum deflection of the measured data at section H7 is positive on the vertical axis, whereas the displacements for the finite element model is mainly negative.

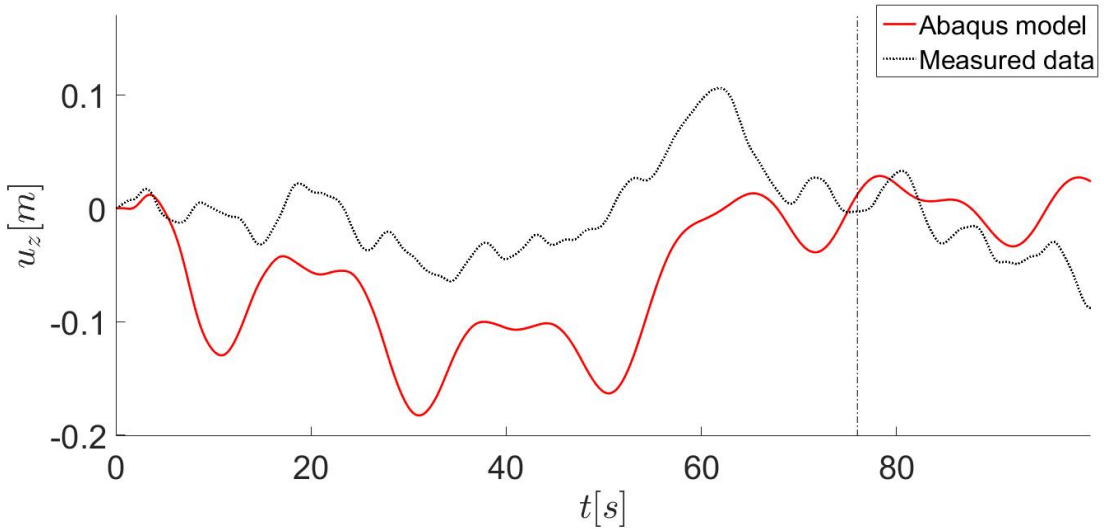

Figure 5.62: Comparison of the deflection at section H7 for the Abaqus model and the measured data

As the finite element model shows an overprediction of the displacements for both section H5 and H7, the discrepancy between the model and the measured data does not seem to be caused by an error in one of the accelerometers. This inference is further encouraged by the results in Figure 5.63, which shows the deflection for all of the sections along the bridge for the time series of the single truck driving across the bridge. The results shows that all of the sections' show deflections in approximately the same range of amplitudes, which indicates that there is no large errors in any of the sections, as they in that case would have shown results that deviated from the other sections. This is the same tendency seen for the acceleration response in Section 5.4.3, and thus supports the verdict that there is no error in the accelerometers. The use of section H5 for the study of the response in the system is, because of the discussion above, deemed acceptable for the continuation of the thesis.

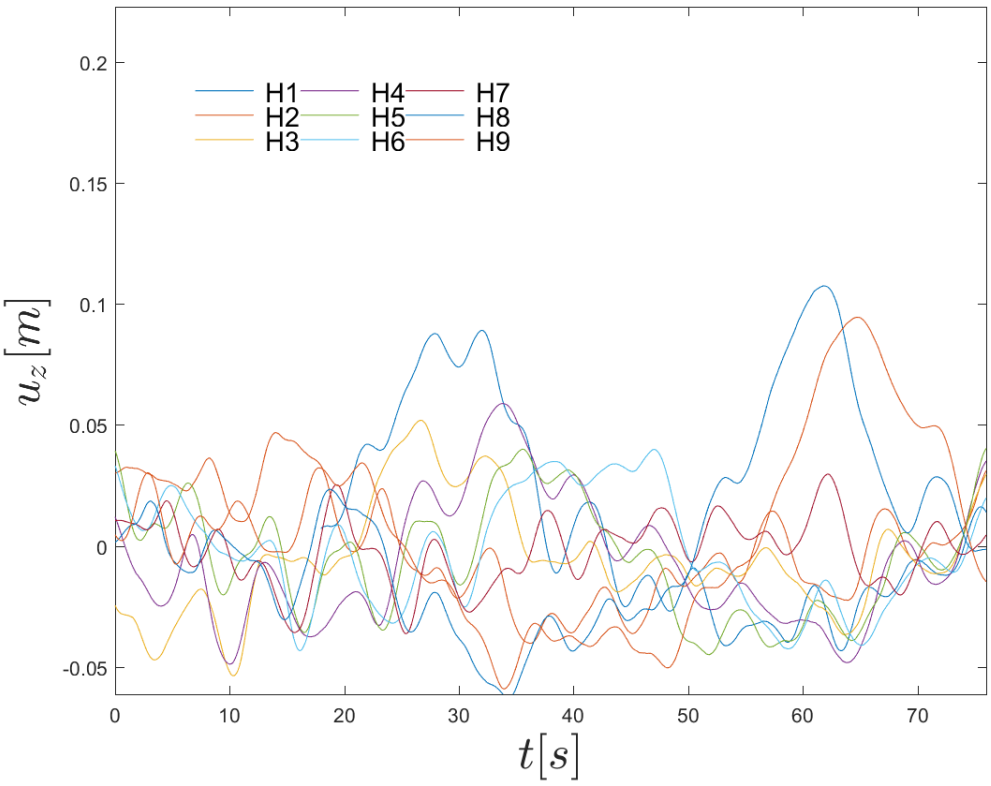

Figure 5.63: The measured displacement at the sections across the bridge for a single vehicle crossing the bridge

As discussed in Section 5.4.3, some of the discrepancy between the finite element model and the measured data may be attributed to the high wind speeds at the time of the car logging, and the effect of interaction between wind forces and traffic forces. During the time of the traffic logging, no time intervals without traffic over a long enough period for comparison was logged, but as discussed in Section 5.3.2, the effects of a passenger car on the response is negligible. Figures 5.64 and 5.65 shows the displacements for section H5 and H7 respectively, when the single truck drives across the bridge compared to the situation of a single passenger car driving across the bridge. The passenger car arrives at the bridge at 08:55:50 and crosses the bridge in 60 seconds, and thus moves at 78.6 kilometres per hour.

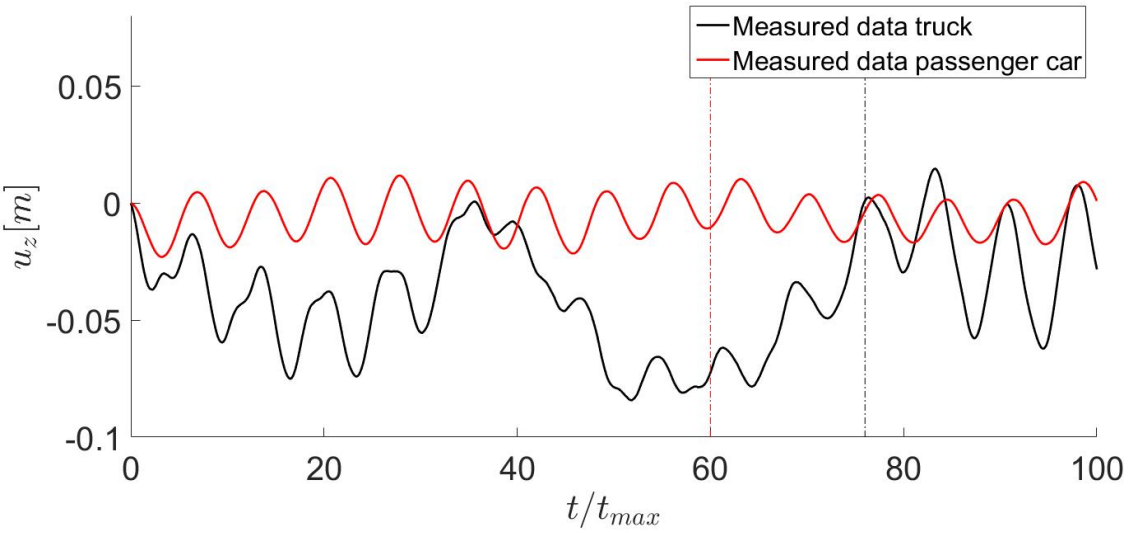

Figure 5.64: The measured displacement at section H5 with and without a truck crossing the bridge

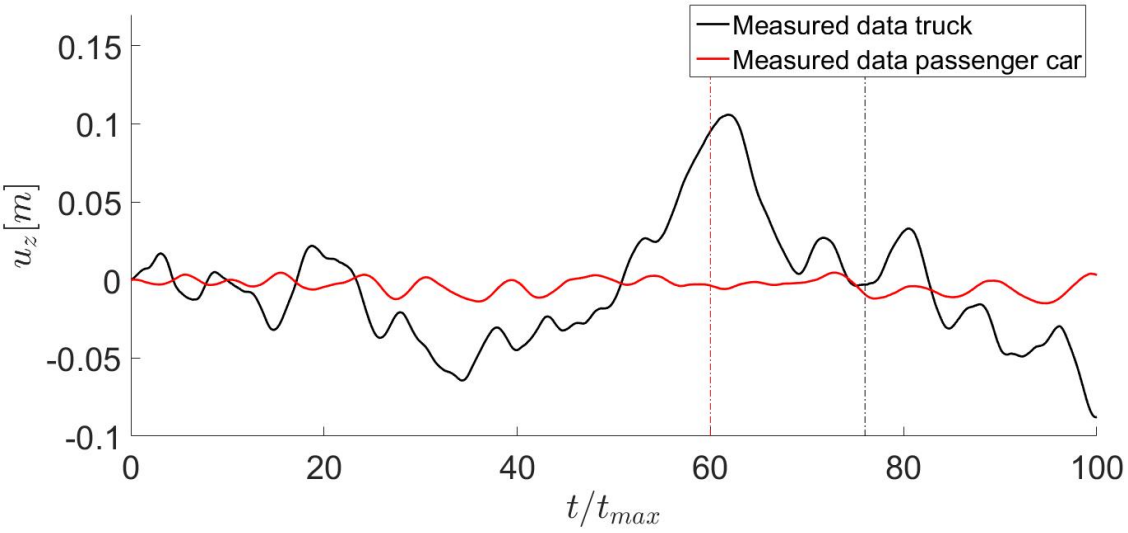

Figure 5.65: The measured displacement at section H7 with and without a truck crossing the bridge

As can be seen from the figures, the situation for a single passenger car on the bridge, which is considered as corresponding to a situation of pure wind, differ much from the situation with a truck on the bridge. At section H5, without the heavy traffic present on the bridge, the displacement varies constant in the same range of deflection and behaves like a harmonic oscillation, whereas the introduction of a truck on the bridge instigates larger deflections. Note how the bridge seems to continue to vibrate with the same oscillation as for the situation with no heavy traffic, along the deflection path instigated by the truck. At section H7 the effect of only wind is very small, and it is difficult to tell whether the deflection path of the large displacements, caused by the truck, vibrates with the preceding oscillations. The horizontal wind speeds when the passenger car crosses the bridge is in the range six to seven metres per second, whereas the situation is four to five metres per second when the truck crosses the bridge. The vertical wind fluctuates between minus one and one metres per second at both time intervals. Hence, for the situation of no truck on the bridge, the wind situation seems to be even worse than for the time period when the truck is on the bridge. Considering the increase in response when there is heavy vehicles are present on the bridge, the notion that most of the response of the bridge is due to wind can be dismissed.

To examine the effects of different constraints on the FE model, and investigate if other parameters than interaction between wind and traffic may be responsible for some of the discrepancy between the finite element results and the measured results, the Abaqus model was subjected to a parameter test. The constraints to be studied are given in Section 3.3, but for the convenience of the reader, the contents of the parameter test is presented here as well:

- The weight of the vehicle
- The speed of the vehicle
- The number of axles on the vehicle
- Static or dynamic analysis
- The boundary conditions of the connection between the bridge deck and the pylons
- The inclusion of damping in the bridge model

Weight and speed of the vehicle

The results from the parameter tests for the weight and speed of the vehicle are presented in respectively Figure 5.66 and Figure 5.67. The maximum deflection for the simulations with varying weight and speed are shown in respectively Table 5.12 and Table 5.13.

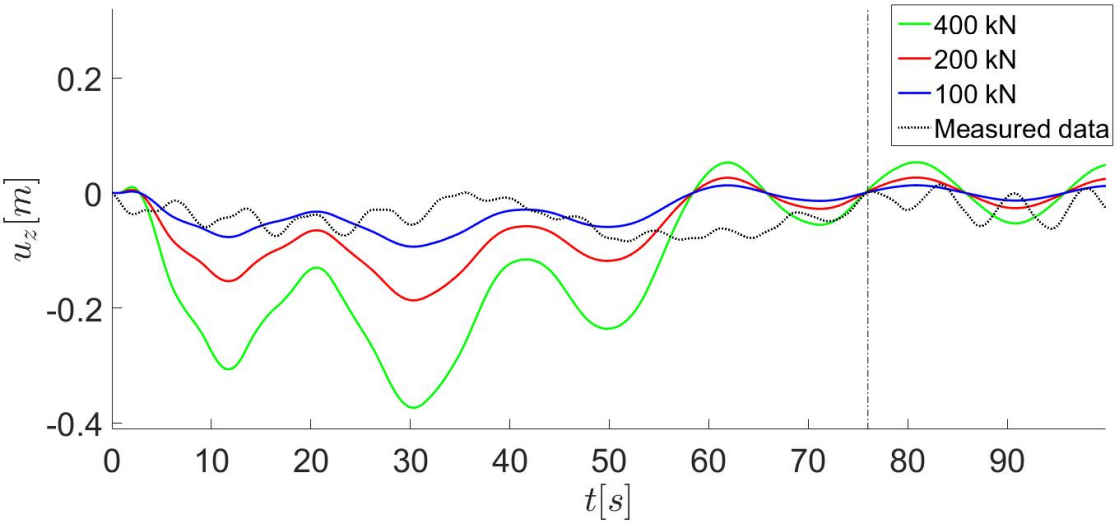

Figure 5.66: Comparison of the deflection at section H5 when varying the weight of the vehicle driving across the bridge

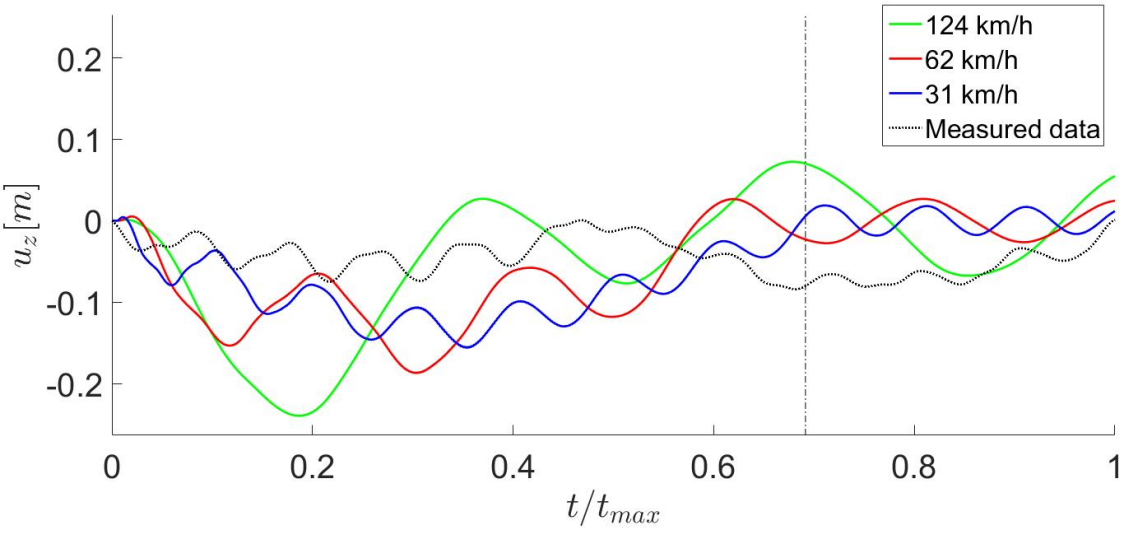

Figure 5.67: Comparison of the deflection at section H5 when varying the speed of the vehicl driving across the bridge

It can be seen that when the weight is reduced to a half of the original weight, from 200 kilonewtons to 100 kilonewtons, the maximum deflection is reduced to half of the value for the main model. When the weight is doubled, from 200 kilonewtons to 400 kilonewtons, the magnitude of the maximum deflection is also doubled, see Table 5.12.

Table 5.13 shows that when the speed is reduced to half of the original speed, from 62 kilometers per hour to 31 kilometers per hour, the maximum deflection is reduced by a factor of 0.83 compared to the original maximum deflection. When the velocity is increased by a factor of 2, from 62 kilometers per hour to 124 kilometers per hour, the magnitude of the maximum deflection increases by a factor of 1.28.

Table 5.12: Maximum deflection at section H5 for varying vehicle weight

Weight [kN]	**Max deflection [mm]**	**Relative max deflection versus main model**
100	93.37	0.4997
200	186.9	1.0000
400	373.3	1.9973

Table 5.13: Maximum deflection at section H5 for varying vehicle speed

Speed [km/h]	**Max deflection [mm]**	**Relative deflection versus main model**
31	156.0	0.8341
62	186.9	1.0000
124	239.7	1.2818

Considering how the response of the bridge is shown to behave linearly with the weight of the vehicle, it is deemed not likely that the discrepancy between the measured data and the model is single-handedly due to the assumed weight of the vehicle. The truck driving across the bridge at the time series which are used in this investigation, was photographed during the logging of traffic at the Hardanger Bridge, see Figure 5.22. Data for similar vehicles indicates a weight of approximately 200 kilonewtons [34, 42]. It is unlikely that the error in the estimation of the weight exceeds 5 tonnes, or approximately 50 kilonewtons, considering the size of the vehicle. Thus, given the relations found between weight of the vehicle and deflection, the error in the deflection of the moving load model due to the modelled vehicle being to heavy, may possibly account for up to approximately 45 millimetres.

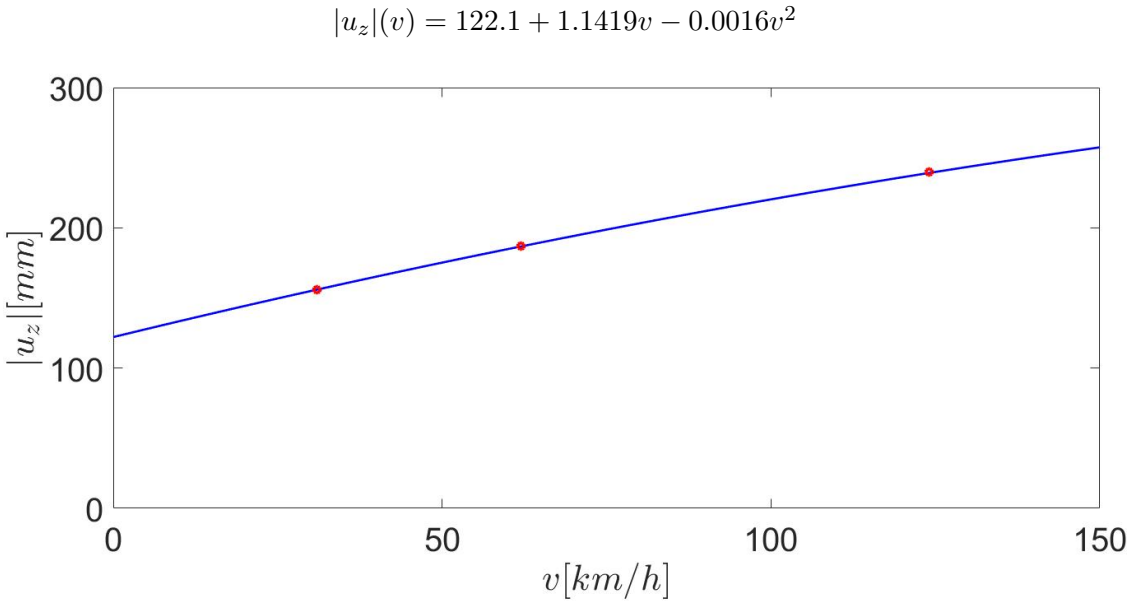

Figure 5.68: The relationship between speed and deflection for the moving load model

The speed of the vehicle was acquired from the traffic log done at the Hardanger Bridge, see Appendix A.2, and found to be 62 kilometers per hour. There may be some error in the time log due to human error. A trendline adaptation of the results in Table 5.13 gives the relation between speed and deflection as $|u_z|(v) = 122.1 + 1.1419v - 0.0016v^2$, see Figure 5.68, where u is deflection and v is speed. An error in time logging of five seconds thus gives at most 4 mm in error in deflection. As the error in the time logging is being considered as small, probably less than five seconds, the error in deflection due to error in the estimation of speed is thus deemed to be negligible.

Number of moving loads

The motivation behind modelling the moving load as multiple forces rather than one single force is explained in Section 5.4.3, but to avoid inconvenience for the reader, it is repeated in the following.

The accuracy of the moving load model may affect the response in the simulation of the vehicle travelling across the bridge. In Section 3.1, a moving force model was found sufficient for modelling the moving load. Considering that a loaded truck will have several axles, often in the form of two on the tractor unit and three on the trailer, it was of interest to investigate the effect of modelling the moving load as five moving forces opposed to one moving force. The model consisting of five moving loads had a length of 11 metres in total, where the three wheels on the trailer had a centre to centre distance of 1.5 metres between each, and the distance between the centres of the wheels on the truck was 3.7 metres. Figure 5.50 (a) and Figure 5.50 (b) in Section 5.4.3 illustrates respectively the 1 axle moving load model and the 5 axle moving load model.

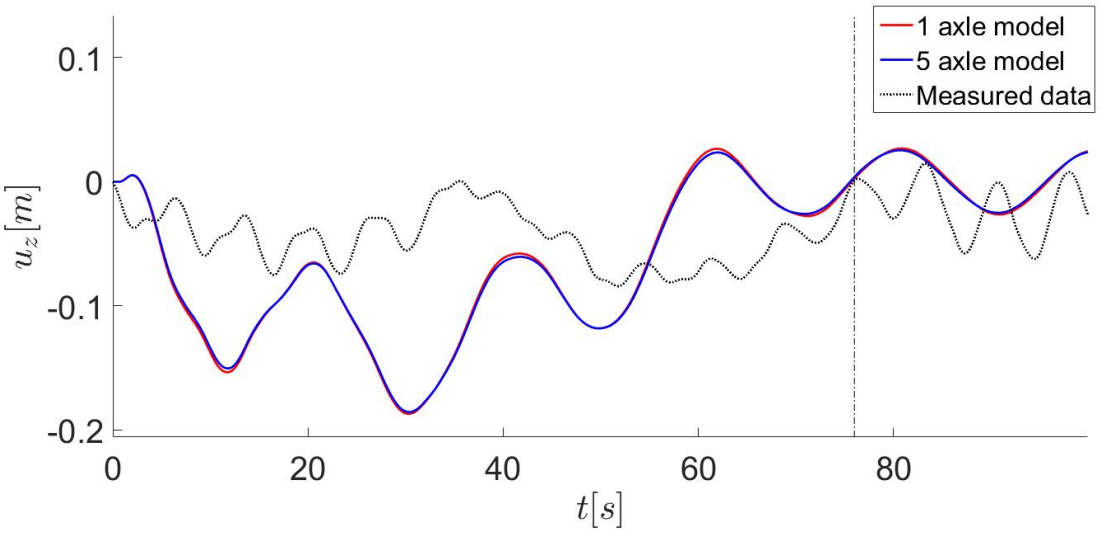

Figure 5.69: The deflection at section H5 for a 1 axle moving load model and a 5 axle moving load model travelling across the bridge

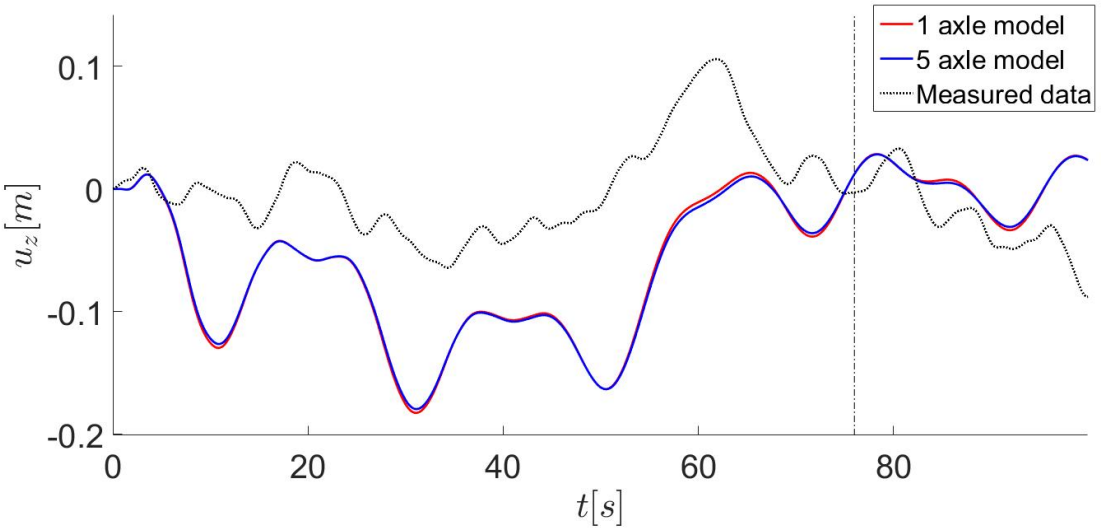

Figure 5.70: The deflection at section H7 for a 1 axle moving load model and a 5 axle moving load model travelling across the bridge

As can be seen in Figures 5.69 and 5.70, the difference in response between the two vehicle representations, consisting of one and five moving loads, is almost imperceptible. Because the deviation between the maximum deflection for the 1 axle moving load model and the 5 axle moving load model is 0.81 % at section H5 and 1.72 % at section H7, the difference between the two models is considered negligible when examining deflections.

These findings differ extensively from the results when examining the acceleration response in Section 5.4.3, where the modelling with multiple axles had a profound effect on the response.

Analysis method

As the response of the bridge has been shown to vary with the speed of the moving load, see Figure 5.67, the behaviour of the bridge is clearly dynamic. Even so, it was of interest to study the difference in the response for a static and a dynamic analysis of the moving load problem. Figure 5.71 shows a comparison between the main case of the moving load problem, a static analysis of the moving load problem, and a dynamic analysis of the moving load problem at very low speed.

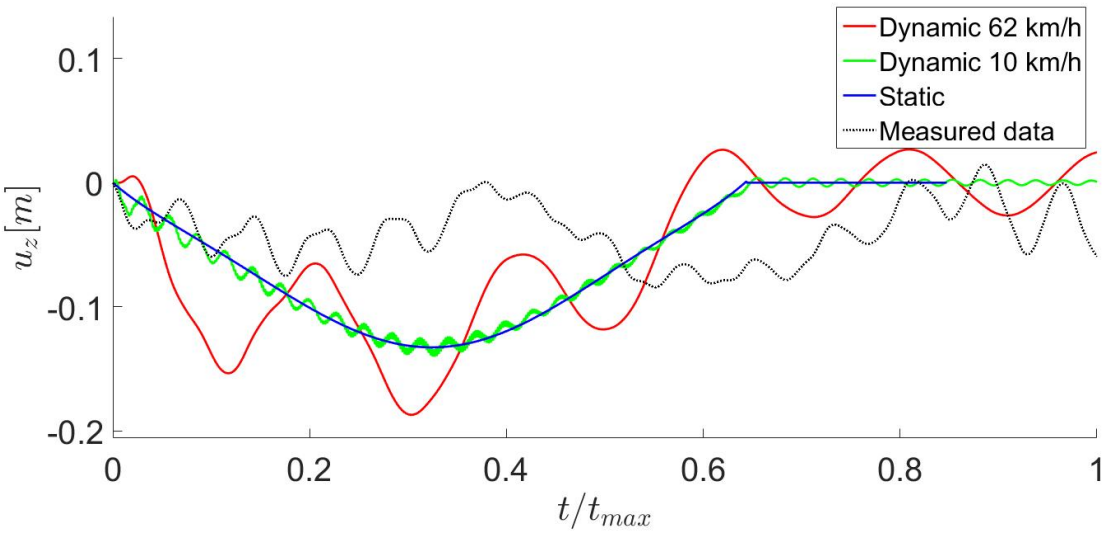

Figure 5.71: The deflection at section H5 for a dynamic analysis at 62 km/h, a dynamic analysis at 10 km/h and a static analysis

Figure 5.71 shows that the static analysis underestimates the maximum deflection of the bridge relatively to the moving load model used in the analyses. The maximum deflection of the static model is 132.6 millimetres, whereas the main model gives a maximum deflection of 186.9 millimetres, making the static analysis predicting only 71 % of the deflection from the dynamic analysis. This yields a dynamic amplification factor of 1.41 when the vehicle speed is 62 kilometres per hour. The curve of the deflection for the static analysis is almost sinusoidal in its form, as opposed to the dynamic deflection curve which fluctuates. This is because the static model does not consider the dynamic effects from wave propagation and the oscillations created by the vehicle moving at high speed. In Section 2.1, it was stated that the dynamic response should be close to the static response when the loading frequency is 1/4 of the lowest natural frequency of the structure. As seen in Table 5.5, the lowest natural frequency of the Hardanger Bridge is 0.050 hertz. Thus, for a 1310 metres long bridge, a loading frequency of 4.55 kilometres per hour should give equal results for the dynamic and the static analysis. These findings are supported by the results from Figure 5.71, which shows that for low speeds of the moving load, the dynamic analysis and the static analysis initiates approximately the same response in the bridge.

It should be remarked that the shape of the deflections from the recorded data shows few similarities to the static solution. The results above indicates that the static component of the displacements is not captured by the accelerometers. Note that this conclusion cannot be drawn upon just this one result, and hence should be the focus of further studies.

The frequency content of the dynamic response shows similarities to that of the static response, with the exception of a high frequency mode, see Figure 5.72. The dynamic analyses only have one large peak each, at 0.0049 hertz for the model going 10 kilometres per hour, and at 0.0391 hertz for the model going 62 kilometres per hour. The static analysis also excites a low frequency, 0.0244 hertz, with a high amplitude, but in addition has a peak at 4.322 hertz. Figure 5.72 shows that the slow dynamic analysis yields a higher amplitude in the power spectra than the other analyses, but this can be explained by the time series on which the spectral density function has been applied is much larger for the slow analysis than the other two.

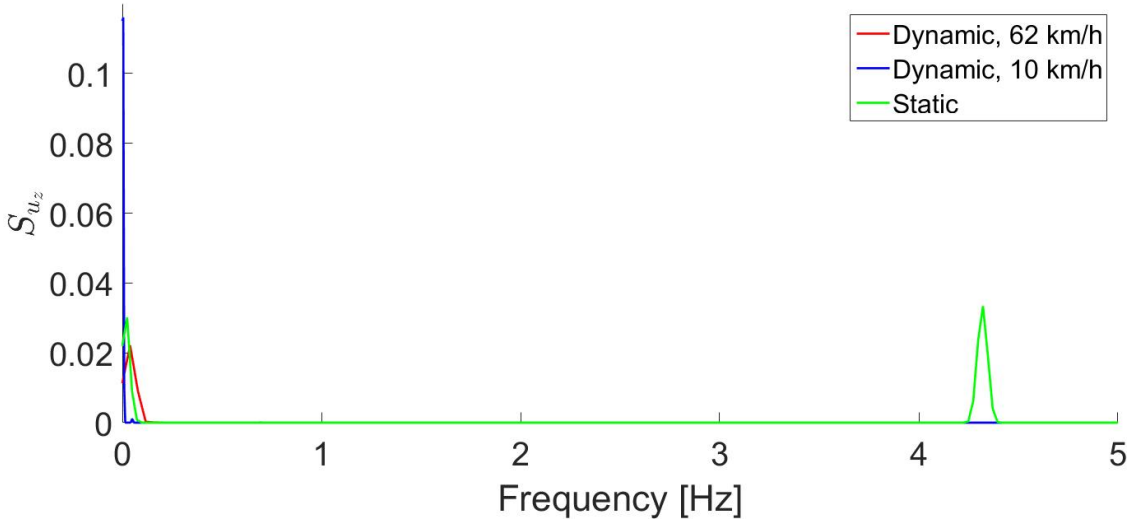

Figure 5.72: The power spectra for section H5 of the recorded displacements and the Abaqus moving load model for dynamic and static analysis

Boundary conditions

The bridge deck of the Hardanger Bridge is supported on the bottom transverse girders of the pylons at the end, see Appendix A.1.1. The bridge deck lies on top of these girders and goes on further until it reaches the ground, where it transitions into the highway. The Abaqus model of the bridge models the bridge deck as simply supported at the pylons, and the side spans are not included in the model. As the boundary conditions used in analyses are idealizations, and actual structures are most likely connected in a way that does not give perfectly idealized boundary conditions, the effect of different connection criteria between the bridge deck and the pylons was investigated for the finite element model.

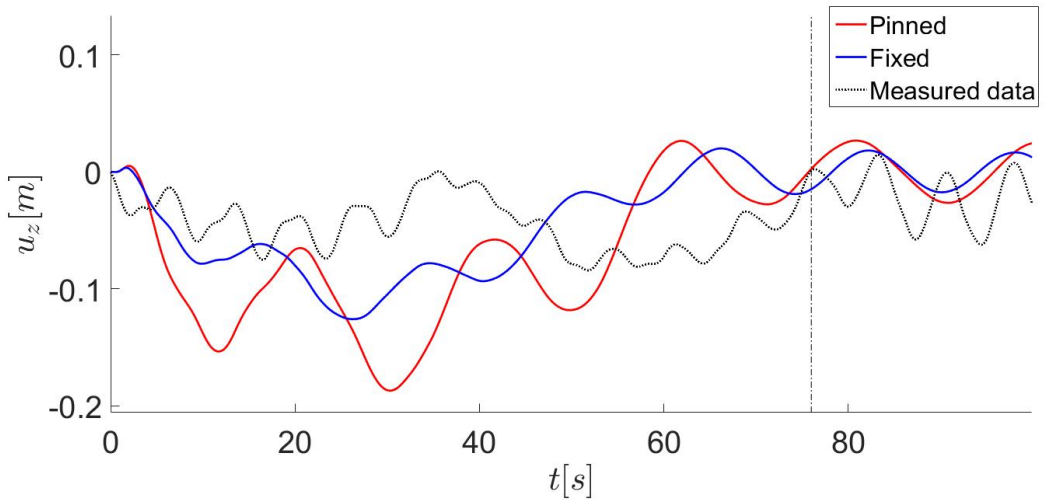

Figure 5.73: The deflection at section H5 for pinned and fixed boundary conditions at the connection between the bridge deck and the pylon

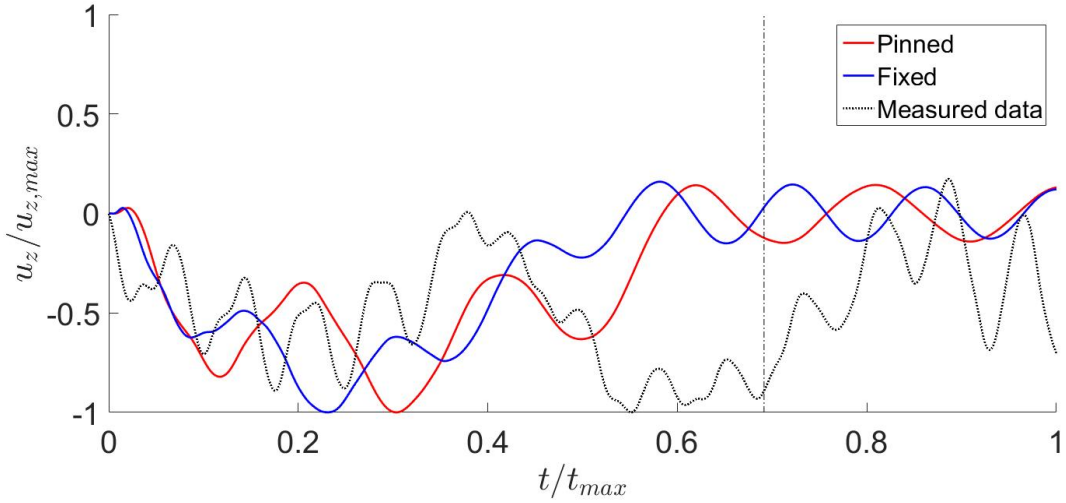

Figure 5.74: The relative deflection at section H5 for pinned and fixed boundary conditions at the connection between the bridge deck and the pylon

As can be seen from Figure 5.73 and Figure 5.74, the change of boundary conditions at the connection between the bridge deck and the pylon gives approximately the same shape of the displacements as the main model does, but with reduced deflections. The change of boundary conditions gave a reduction in maximum deflection from 186.9 millimetres to 125.9 millimetres, effectively reducing the maximum deflections to 67 % of its original value. Considering the overestimation of deflections in the moving load model compared to the measured results, the boundary conditions for the Abaqus model may therefore be worth looking into. It should be noted that the change of boundary conditions does not seem to correct the deviation in the shape between the deflections from the finite element model and the recorded data.

Damping

The Rayleigh damping is based on a guess of the initial damping ratio of the structure, ξ_0. In the Abaqus model, the value $\xi_0 = 5\%$ was chosen as appropriate, see Section 5.4.1. To investigate the effect on the model from the damping, and the accuracy of the estimation of the damping ratio ξ_0, a study for different damping ratios was carried out.

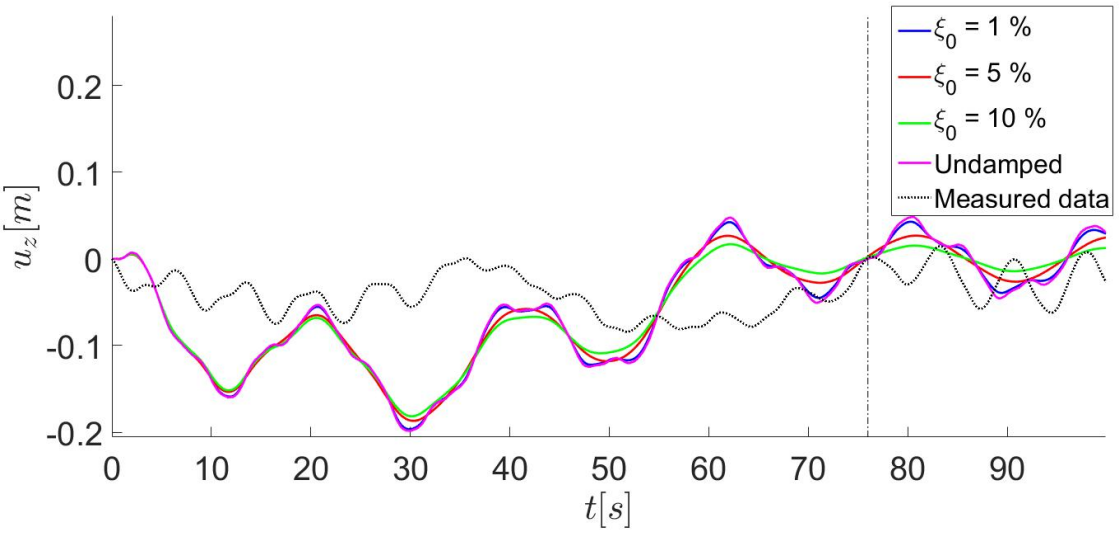

Figure 5.75: The deflection at section H5 for different damping properties in the structure

As evident in Figure 5.75, when increasing the damping of the structure, the shape of the deflection plot will remain approximately the same, but the peaks get smoothed out, and the displacements will be reduced. Table 5.14 shows that the difference in displacements when increasing the damping is relatively small, but still significant. For the main moving load model with $\xi_0 = 5$ %, the maximum displacement is 11.6 millimetres smaller than for the undamped case, yielding a reduction in maximum deflection of 5.8 %. Hence, as expected, when regarding the results from Section 5.4.3 it can be seen that the damping has a bigger influence on the acceleration response of the structure than the displacements.

Table 5.14: Maximum deflection at section H5 for varying damping properties

Rayleigh damping ratio ξ_0	Undamped	1 %	5 %	10 %
Maximum deflection [mm]	198.5	196.7	186.9	181.7

Improved model

The findings from the parametric study suggests that an improved model of the moving load can be achieved. This will be discussed in greater detail in Section 6.

6 Discussion

In this section a discussion on the results from the case study will be presented, and the methods used will be reviewed in regard to theory and previous studies on the subject.

Discussion of numerical methods for data processing

The analysis done to identify traffic induced loading described in section 5.3.2, showed that response due to traffic induced vibrations could be identified in the vertical acceleration response. The acceleration response due to traffic induced vibrations may be identified as oscillations in the acceleration response with a sudden rise in frequency. One disadvantage with this procedure is that it is highly dependent on observations in order to identify the sudden change in the acceleration response. In addition, this method is dependent on the quality of the recorded acceleration response, which may contain high frequency noise for certain time periods. It should be noted that the presence of passenger cars on the bridge does not seem to affect the acceleration response in a way consequent enough to draw any conclusions regarding the identification of passenger cars. Therefore, identification of traffic induced vibrations is more suited to be carried out by analysing the frequency domain of the acceleration response.

The numerical method for analysing the power spectral density of an acceleration response is more suited for analysing a chosen time series than the procedure for investigating the acceleration response in time domain. By analysing the frequency content of an acceleration response, rather than analysing the response directly, an evaluation of its content can be executed more efficiently. The examination of the power spectra only analyses a chosen time interval for the frequency content of the acceleration response, and does not consider when the load case enters the bridge. Thus, it may be necessary to analyse the acceleration response in order to detect the time when a heavy vehicle enters the bridge. This is essential for selecting the correct time interval to compare the estimated displacements from the numerical integration with the displacements from the finite element model.

The analysis of moving traffic in Section 5.3.3, examining the cross-covariance distribution for the acceleration response, gave indistinct results. The recorded acceleration response consists of several independent signals being processed as one signal. From the analysis of the output in Figure 5.24, 5.25 and 5.26, it proved to be difficult to interpret and specify a time lag for the acceleration response between section H5 and H7. This could presumably be a result of vibrations excited by heavy vehicles on the bridge deck with velocities larger than the vehicle itself. In Section 5.3.1, it was stated that the wind data recorded at different anemometers differed from each other. This deviation in the wind field may affect the cross-covariance and the time lag for the acceleration response. From these observations and considerations, the calculation of the cross-covariance, and a corresponding time lag, is not seen as suited for analysing moving traffic due to the complexity of the acceleration response.

As stated in Section 4.3.2, in order to evaluate the possibility of separating the responses from wind- and traffic induced vibrations, two filters are applied to the acceleration response.

From the analysis done on filtering the acceleration response in Section 5.3.5, the results in Figure 5.29 and 5.30 showed that the high frequency response for both sections indicated traffic induced vibrations, and were in accordance with the traffic log. In order to evaluate whether this method is valid or not, an analysis regarding how the acceleration response varies with the mean wind velocity was deemed as necessary.

From the results in Section 5.3.5, it can be observed that for situations with low mean wind velocity at section H5, there are small differences for the standard deviation of the filtered acceleration responses. In Figure 5.32, the standard deviation of the filtered acceleration response with frequencies above 1 hertz shows a larger difference for a low mean wind velocity. For a higher mean wind velocity, both Figure 5.31 and 5.32 shows that the filtered response for frequencies below 1 hertz has bigger standard deviation than the filtered response with frequencies above 1 hertz. These results indicates that the standard deviation of the wind induced response increases with an increase in mean wind velocity, and that the traffic induced response becomes negligible for large wind velocities. Even so, for low wind velocities there are little difference in the standard deviation for the filtered responses, as shown in Figure 5.31 and 5.32. In cases with low wind velocities, one would assume that wind induced vibrations would cause the high frequency response to vary more than the low frequency response. From the figures it can be observed that this is not the case. This indicates that traffic induced vibrations also excites modes with frequencies lower than 1 hertz. This agrees well with the theory from basic dynamics stating that the lowest eigenmodes are easiest to excite. Thus, from these observations, it can be seen that direct separation of wind- and traffic induced vibrations is difficult due to the frequency content of the acceleration response induced by traffic.

For the numerical integration presented in Section 4.4, an estimate of the displacements from section H5 and H7 was carried out using the script *calcDisplacement*, see Figure 5.33 and 5.34. In order to evaluate the reliability of the estimated displacements, the frequency content of the displacement response was analysed. By comparing the eigenfrequencies from the numerically integrated displacements with the frequencies estimated through the transfer function, the accuracy of the displacements could be analysed. As shown in Figure 5.35 and 5.36, there is a large similarity for the power spectral density estimations for both procedures. On the other hand, the estimated power spectral density calculated with the transfer function shows that when $f \to 0 \Rightarrow S_{u_z} \to \infty$. Due to this divergence issue, it is impossible to compare the power spectral density of the first vertical eigenmode for both procedures.

Table 5.3 and 5.4 shows that the estimated eigenfrequencies for each mode is identical for both procedures. The tables also show little deviation in the estimation for the power spectral density, which indicate that the power spectral density of the displacements for both procedures provide approximately the same results. Even so, comparing the power spectral density and the eigenfrequencies from these estimations may not be sufficient in evaluating the reliability for the estimated displacements. In addition, the eigenfrequencies from the numerically integrated displacements should also be compared with the eigenfrequencies from the vertical acceleration response. This is shown in Table 6.1 and 6.2.

Table 6.1: Comparison of eigenfrequencies, Section H5

Mode	**Numerical integration f [Hz]**	**Acceleration response f [Hz]**
1	0.02441	-
2	0.14160	0.14160
3	0.27830	0.27830
4	0.40040	0.40040

Table 6.2: Comparison of eigenfrequencies, Section H7

Mode	**Numerical integration f [Hz]**	**Acceleration response f [Hz]**
1	0.01953	-
2	0.11720	0.11720
3	0.20510	0.20510
4	0.33200	0.33200
5	0.40040	0.40040

From the tables above, it is shown that most of the eigenfrequencies from the numerically integrated displacements and the vertical acceleration response are identical. Note that the first estimated eigenfrequency from the numerical integration for both section H5 and H7 does not appear in the vertical acceleration response. The reason why these eigenfrequencies occur in the power spectral density for the numerically integrated displacements is unclear. These frequencies might be a result of an error in the numerical integration, and represent an incompatible eigenmode. The eigenfrequencies from both the vertical acceleration response and the numerically integrated displacements will be further discussed with regard to the results from the FE model.

Discussion of the finite element model of the moving load

In Section 5.4.1, the eigenvalues of the finite element model of the Hardanger Bridge was investigated. The simulated eigenfrequencies seemed to coincide well with the vertical eigenfrequencies of the Hardanger Bridge obtained from the spectral density of the acceleration spectra. As seen in Table 5.6, only one of the simulated eigenfrequencies did not appear in the spectral density plots, and that one was so close to another mode that it is reasonable to assume it exists in the physical bridge as well, but gets "swallowed" into the adjacent mode in the spectral density plot. The rest of the eigenfrequencies deviates by at most 0.0068 hertz, and as such the results correspond well. It should be noted that the eigenfrequencies were matched using a qualitative approach, comparing each FEA eigenfrequency with the closest measured eigenfrequency, but the agreement is so good that the approach seems to be accurate. This also implies that it is reasonable to assume the mode shapes in Figure 5.39 are representative for the actual bridge.

The results shows the importance of taking care when identifying the eigenfrequencies from measured data, as not all eigenmodes will be excited everywhere along the bridge. This can be seen in Figure 5.37 and Figure 5.38. The midnode in particular should be avoided being used alone for this purpose.

The eigenfrequency results implies that the Abaqus model of the bridge is correct, and is adequate for use in simulations. This was expected considering that the model was built by the Norwegian Public Roads Administration (NPRA). The model acquired from the NPRA did not implement damping, and thus Rayleigh damping was implemented. As Table 5.7 and Figure 5.40 shows, the modal damping ratios extracted from the complex eigenmodes of the model deviates noticeably from the damping ratios calculated using Rayleigh damping. This may be because Rayleigh damping in Abaqus does not consider geometrical stiffness, but can also be attributed to a bad guess of ξ_0. As Figures 5.54 and 5.75 shows, a change in the implemented Rayleigh damping ratio does not yield drastic differences in the response. Hence, it is reasonable to assume that the guessed value of the initial Rayleigh damping ratio is not solely the problem, but to some degree also the omitting of the geometric stiffness contribution.

From Section 5.4.3 and Section 5.4.4, it was found low compliance between response from the finite element model and the recorded data from the accelerometers. The shape of the plotted accelerations and displacements were not the same for the model and the data, and the amplitudes were overestimated. At the midspan of the bridge, the estimated maximum displacements were more than twice the size of the maximum displacements acquired from the measured data. To examine which parameters influenced the response of the model, and thus see if the model could be improved, a parameter test was conducted.

From the investigation of the moving load model, as well as the examining of the recorded data by means of numerical methods, five parameters emerged as possible sources of the discrepancy:

- Wind-traffic interaction
- The compliance between eigenmodes in the model and the recorded data
- The estimated weight of the vehicle
- The modelled boundary conditions at the ends of the bridge deck
- The omitting of the static component in the recorded data

In addition to these, the neglecting of the geometric stiffness in the implementation of the damping in the model may also influence the results significantly.

The car loggings upon which basis the case study has been conducted, were taken at a time of high wind speeds in the horizontal direction and high fluctuations in the vertical direction. As the attempt to filter away the wind response did not emerge successful, the response spectra used in the comparison with the FE model will be influenced by wind. The examination of the power spectra for the recorded data showed that the traffic response is highest in the low frequencies, with some high frequency response as well. Wind response is primarily lower than 1 hertz, hence wind and traffic response will interact and thus impact each other. As such, a superpositioning of the responses is not applicable.

As Figures 5.48, 5.49, 5.64 and 5.65 show, the vertical response from wind is small compared to the vertical response when heavy vehicles are present. This implies that the deviation of the measured response and the simulated response is presumably not due to wind and traffic response cancelling each other out and reducing the deflection. A more likely effect of the wind is that it inflicts oscillations on the bridge, both vertically and horizontally, which influences the stiffness of the bridge. If the bridge becomes stiffer due to wind effects, it will also be harder to deform, and this may explain some of the discrepancy in the magnitudes of the response, as well as the different shapes of the plotted response for the recorded data and the simulated response.

It would be of interest to establish a FE model which incorporates the effects of wind. To avoid having to model wind forces, and thus making the model more computationally expensive, implementing pre-applied oscillations in the model may be a possibility. This method might comply well with the recorded acceleration response, as the response seems to indicate almost a harmonic oscillation of the bridge also when traffic is present. If solely deflections is of interest, applying a reduction factor to the loading which is dependent on the wind speeds might be a computiationally inexpensive solution. Estimating a reduction factor based on wind speeds will demand the analysis of several recordings with different wind speeds, and as such may be a big undertaking. Another way to account for the effects of wind would be to increase the stiffness of the model. Changing the stiffness affects the eigenfrequencies of the model, and may as such lead to a less realistic behaviour. Because of this, the modification of the stiffness matrix is considered an inferior method.

In Section 5.3.6, numerical integration of recorded accelerations was performed in order to get displacements. Both methods to obtain the power spectra of the deflections yielded a very low eigenfrequency which was present neither in the Abaqus model nor the power spectra of the accelerations. Due to the high amplitudes of these new modes, see Figure **??**, there may be an error in the deflections obtained from the recorded data, as the excitement of these non-existing eigenmodes might be influential.

The deflection of the midspan of the bridge was seen to behave linearly with the weight of the vehicle by a factor of 0.94 millimetres per kilonewton. The investigation shows this relation to be valid in the examined range $100 - 400$ kilonewtons, but the relation might not hold true for values outside that range. Most heavy traffic is expected to be approximately in this interval, the limit for what can be counted as a light commercial vehicle and not a truck is 3500 kilograms [33] or 34 kilonewtons, and a truck can be expected to be noticeably larger than a large passenger car. The maximum accepted vehicle weight in Norway is 50 tonnes [32] or 490 kilonewtons. Thus, all vehicles relevant for this study is assumed to be in the aforementioned range, and the relation is applicable for this discussion.

This means that the weight of the modelled vehicle proves to be significant, and an error in the estimation of the mass of the vehicle of 5 tonnes, a reasonable error as the gross weight of trucks varies quite much between models, may lead to an error of 46 millimetres in the estimated deflection. Hence, care should be taken when modelling the traffic on the bridge in the finite element model.

The boundary conditions at the ends of the bridge deck has a significant influence on the response. In the case study, the maximum deflection was reduced to 67 % of the original value when changing the connection from simply supported to fully constrained. As the bridge deck of the actual bridge continues beyond the pylons and onto the road on the other side, modelling it as supported at the pylon, but not continuing beyond the pylon, probably reduces the bending resistance of the bridge significantly. An encastre connection is not a good estimation of the support, considering the details of the support seen in Appendix A.1.1, but it seems that neither is a pure, pinned connection. Modelling the connection as simply supported, with a spring to add bending resistance in the joint, might be a solution. Hence, boundary conditions should be considered in further work.

The results from the study on analysis methods indicates that the static component of displacements due to the moving load is omitted in the recorded data. If the accelerometers are not able to pick up and record the static component of responses, the deflections obtained from recorded data will be inaccurate.

It should be noted that even though the modelling of the vehicle as multiple moving forces, rather than a single moving force, did not influence the deflection response of the model significantly, it seems to improve the acceleration response as it removes much of the high frequency noise. As such, a model representing the actual number of axles seems to show behaviour superior to the one axle model in a finite element analysis.

When performing the static analysis for the moving load, a dynamic amplification factor (DAF) of 1.41 was found for the main case. This is a high value, but not unrealistic. In his doctorate thesis, Karoumi [19] found DAF's up to 1.39 for his studies of the moving load model of a single moving vehicle on cable-stayed bridge models using finite element analysis. Karoumi observed in his thesis that the finite element dynamic moving load model on bridges provided accurate results from an engineering viewpoint.

It would be of interest to perform a study of the moving load problem for more load models than just the moving force. Karoumi [19] found that the moving force model may in some cases overestimate the dynamic amplification. A sprung mass model might be able to give a less conservative estimation, as the sprung mass may absorb some vibrations.

Considering the findings in this thesis, a finite element moving load model can be used to conservatively estimate the effect of traffic loading on a cable-supported bridge. Care should be taken when modelling the bridge structure, particularly when considering the damping of the structure and the boundary conditions, as these parameters seems to influence the bridge noticeably. The vehicle should be modelled with one moving force representing each axle, and it should be noted that the weight of the car influences the response in a way that demands great care when estimating vehicle weight.

The wind-traffic interaction is presumed to be considerable for the structure, but as it only seems to stiffen the structure, neglecting the effects of wind-traffic interaction only leads to a conservative estimation of the response. The traffic loading might be most critical for the bridge in time series with low wind, as the wind appears to mostly act as a stiffener when considering vertical response. As such, the existing model may be a good estimate for the worst case scenario. Therefore, it is recommended to obtain traffic loggings from time periods with low wind and compare to the high wind situation, as well as the FE model, before making further conclusions regarding the applicability of the Abaqus model.

7 Conclusion and further work

7.1 Conclusions

In this thesis, methods for analysing traffic induced response on cable-supported bridges have been proposed and reviewed. Numerical methods for examining recorded data from existing structures have been derived and implemented in Matlab, and used for the identification of traffic and the characteristics of the response invoked by said traffic. In a case study, the investigation of the recorded data from the Hardanger Bridge was done in both the time domain and the frequency domain. A finite element model of the moving load problem has been established in Abaqus, and is used for the simulation of traffic induced response in bridge structures.

An increase in the frequency, and amplitudes, of the oscillations in the acceleration response may be used as means of identifying heavy vehicles. The presence of passenger cars has not been found identifiable in the time domain, as they inhibit no consistent influence on the acceleration response. The cross-covariance function has not proven useful when analyzing traffic induced vibrations. The research done in this thesis has not been able to identify the characteristics of traffic on the bridge from analyses in the time domain.

The investigation in the frequency domain indicates that wind and traffic induced response interacts significantly on slender bridges. The response of wind induced vibrations was found to be in the range below one hertz, and the same was the case for passenger cars. The majority of the response from heavy vehicles also appear in the frequency domain below one hertz, but heavy vehicles may also excite some higher frequencies. The frequency content of vibrations can be identified from the power spectral density obtained by the use of Welch's method. Due to wind and traffic both appearing in the same range in the frequency domain, the application of finite impulse response (FIR) filtering has not proven successful as a means of separating wind and traffic induced response.

The application of numerical integration as a method of obtaining displacements has proven successful, but with some uncertainties. The power spectra of the displacements includes the fairly large excitement of a very low frequency mode which is present in neither the power spectra of the accelerations nor the Abaqus model. As such, the integrated accelerations may excite an non-physical shape, which may lead to an error. The eigenfrequency may also just be noise, and thus not impact the response. The rest of the eigenfrequencies of the displacements correspond well with the eigenfrequencies of the accelerations, as well as the Abaqus model, and both a transfer function and the spectral density of the displacements directly yields the same power spectra. Thus, the integrated accelerations appear to be of sufficient accuracy for estimations, but the uncertainties make the method unfit for use as an exact representation of the deflections.

For the finite element model, the following parameters were found to significantly influence the results:

- Interaction between wind and traffic. This effect may possibly be accounted for by a reduction factor, pre-applied oscillations on the bridge model, or by increasing the stiffness of the model.
- The implementation of damping in the model. Abaqus neglects geometric stiffness in the implementation of Rayleigh damping. This might instigate non-physical behaviour in the structure.
- The boundary conditions modelled for the connection at the ends of the bridge deck.
- The estimated weight of the vehicle.
- The number of moving forces used in modelling the moving load

By taking care when establishing the model and taking these parameters into account, it seems the moving load model can be improved compared to the main model used in the parametric study. For the time series of the traffic loggings used in this thesis, the finite element model of the moving load provides a conservative estimate of the response in the bridge. It is believed that this is due to an increase in the stiffness due to the wind, which is not considered in this thesis. Thus, the model may serve as an estimate of the worst case scenario of no wind present. Further study and comparisons for recordings and car loggings from a period with low wind is recommended.

7.2 Further work

Due to the limitations of this thesis, some of the following topics may be of interest for further work:

- In the case study, only a 30 minute interval of recorded data with a corresponding traffic logging was available. In order to gain more knowledge regarding the response from traffic induced vibrations, analyses for longer time intervals and lower wind conditions should be carried out.
- In the case study, the analysis of the vertical acceleration response were only carried out for two sections containing accelerometers. In further work, it would be interesting to analyse the responses for other accelerometers along the main span of the Hardanger Bridge.
- To limit the scope of this thesis, only vertical acceleration response has been analysed. Therefore, it would be interesting to investigate the effects from horizontal and torsional accelerations from traffic induced vibrations as well.
- The use of other load models than the moving force. For instance, implementation of sprung mass model may provide better results due to its functionality of absorbing vibrations.
- The acceleration response from the simulations in the finite element model showed an idealised result. This result differed greatly from the acceleration response for the measurements. A further work could include a modified analysis, where the the effects of wind induced motions is considered in the model used in the case study, either implementing a reduction factor based on recorded data, or having the bridge being excited by a harmonic motion representing wind when the simulated vehicle moves across the bridge.
- Results from the study indicates that the static component of the displacements is not captured by the accelerometers along the Hardanger Bridge. Further studies to see if this is the case, and how the static component may be accounted for, is seen to be of interest.

Bibliography

[1] Eyad H. Abed, David Lindsay, and Wael A. Hashlamoun. On participation factors for linear systems. *Automatica*, 36(10):1489–1496, 2000.

[2] Geir Brekke. Informasjonsbrosjyre hardangerbrua. `http://www.vegvesen.no/_attachment/219596/binary/418198?fast_title=Informasjonsbrosjyre+Hardangerbrua.pdf`, 2011.

[3] J.M.W. Brownjohn, M. Bocciolone, A. Curami, M. Falco, and A. Zasso. Humber bridge full-scale measurement campaigns 1990-1991. *Journal of Wind Engineering and Industrial Aerodynamics*, 52:185–218, 1994.

[4] Etienne Cheynet, Jasna Bogunović Jakobsen, and Jónas Þór Snæbjörnsson. Full scale monitoring of wind and traffic induced response of a suspension bridge. *MATEC Web of Conferences*, 24, 2015.

[5] Ray W. Clough and Joseph Penzien. *Dynamics of structures*. McGraw-Hill, New York, 2 edition, 1993.

[6] Robert D. Cook, David S. Malkus, and Michael E. Plesha. *Concepts and applications of finite element analysis*. Wiley, New York, 4 edition, 2002.

[7] Roy R. Craig and Andrew J. Kurdila. *Fundamentals of structural dynamics*. Wiley, Hoboken, N.J, 2 edition, 2006.

[8] Alvaro Cunha. *Topics in Dynamics of Bridges, Volume 3 : Proceedings of the 31st IMAC, A Conference on Structural Dynamics*. Springer New York, New York, 2013.

[9] Richard C. Dorf. *The Engineering Handbook, Second Edition*. Taylor and Francis, Hoboken, 2 edition, 2012.

[10] André Filiatrault, Robert Tremblay, Constantin Christopoulos, Bryan Folz, and Didier Pettinga. *Elements of earthquake engineering and structural dynamics*. Presses internationales Polytechnique, Québec, 3 edition, 2013.

[11] Ladislav Frýba. *Dynamics of railway bridges*. Thomas Telford, London, 1996.

[12] Gunnstein Thomas Frøseth. Numerical analysis of the dynamic response of existing railway bridges. Master's thesis, Norwegian University of Science and Technology, Trondheim, 2014.

[13] Henri P. Gavin. Classical damping, non-classical damping and complex modes. `http://people.duke.edu/~hpgavin/cee541/ComplexModes.pdf`, 2016.

[14] Arturo Gonzàlez, Eugene J. OBrien, Daniel Cantero, Yingyan Li, Jason Dowling, and Ales Žnidaric. Critical speed for the dynamics of truck events on bridges with a smooth road surface. *Journal of Sound and Vibration*, 329(11):2127–2146, 2010.

[15] Mark F. Green, David Cebon, and David J. Cole. Effects of vehicle suspension design on dynamics of highway bridges. *Journal of Structural Engineering*, 121:272–282, 1995.

[16] Fredric J. Harris. On the use of windows for harmonic analysis with the discrete fourier transform. *Proceedings of the IEEE*, 66(1):51–83, 1978.

[17] Gerhard Heinzel, Albrecht Rüdiger, and R. Schilling. Spectrum and spectral density estimation by the Discrete Fourier transform (DFT), including a comprehensive list of window functions and some new flat-top windows, 2002.

[18] Ole Øiseth. Measurements of dynamic response and wind velocities at the hardanger bridge november 2013 - december 20xx. unpublished, 2015.

[19] Raid Karoumi. *Response of cable-stayed and suspension bridges to moving vehicles*. PhD thesis, Royal institute of technology, Stockholm, 1999.

[20] Erwin Kreyszig. *Advanced Engineering Mathematics*. Wiley, 10 edition, 2011.

[21] Knut Andreas Kvåle. Assessment of the dynamic response of the bergsøysund bridge in the frequency domain. Master's thesis, Norwegian University of Science and Technology, 2013.

[22] Siu-Seong Law and Xin-Qun Zhu. *Moving Loads – Dynamic Analysis and Identification Techniques*. CRC Press, Hoboken, 2011.

[23] Y.-H. Lin and M.W. Trethewey. Finite element analysis of elastic beams subjected to moving dynamic loads. *Journal of Sound and Vibration*, 136(2):323–342, 1990.

[24] K. Liu, G. De Roeck, and G. Lombaert. The effect of dynamic train–bridge interaction on the bridge response during a train passage. *Journal of Sound and Vibration*, 325(1-2):240–251, 2009.

[25] Kjell Magne Mathisen. Lecture 9: Solution of the nonlinear dynamic equilibrium equations, 2015.

[26] Matlab. Cumulative trapezoidal numerical integration - matlab cumtrapz - mathworks nordic. `http://se.mathworks.com/help/matlab/ref/cumtrapz.html`.

[27] Patrick J. McGetrick, Chul-Woo Kim, Arturo Gonzalez, and Eugene J. Obrien. Dynamic axle force and road profile identification using a moving vehicle. *International Journal of Architecture, Engineering and Construction*, pages 1–16, 2013.

[28] Leonard Meirovitch. *Computational methods in structural dynamics*. Sijthoff and Noordhoff, Alphen aan den Rijn, 1980.

[29] Olav Kristoffer Mork and Kenth Daniel Solheim. Sammenligning av predikert og målt vindindusert dynamisk respons av hardangerbrua. Master's thesis, Norwegian University of Science and Technology, 2014.

[30] Arvid Naess. *An introduction to random vibrations*. Centre for Ships and Ocean Structures Department of Structural Engineering Norwegian University of Science and Technology, 2011.

[31] A.V. Pesterev, L.A. Bergman, C.A. Tan, T.-C. Tsao, and B. Yang. On asymptotics

of the solution of the moving oscillator problem. *Journal of Sound and Vibration*, 260(3):519–536, 2003.

[32] Samferdselsdepartementet. Forskrift om bruk av kjøretøy, for-1990-01-25-92. https://lovdata.no/dokument/SF/forskrift/1990-01-25-92, 1990.

[33] Samferdselsdepartementet. Forskrift om krav til kjøretøy, for-1990-01-25-91. https://lovdata.no/dokument/SF/forskrift/1990-01-25-91, 1990.

[34] Scania. Specifications on the scania r730. http://www.scania.co.uk/Images/SL5451274-R730LA4x2MNA_tcm48-231884.pdf.

[35] Steven W. Smith. The scientist and engineer's guide to digital signal processing, 1997.

[36] Petre Stoica and Randolph Moses. *Spectral Analysis of Signals*. Prentice Hall, 2004.

[37] Dassault Systémes. *Abaqus Analysis User's Guide*. Providence, RI, USA, 6.14 edition, 2014.

[38] Petre P. Teodorescu. *Treatise on Classical Elasticity : Theory and Related Problems*. Springer Netherlands, Dordrecht, 2013.

[39] Statens Vegvesen. Drawing of the bridge. http://www.vegvesen.no/_attachment/64048/binary/21512?fast_title=Drawing+of+the+bridge.

[40] Statens Vegvesen. Hardangerbrua illustrasjoner. http://www.vegvesen.no/vegprosjekter/Hardangerbrua/Illustrasjoner.

[41] Statens Vegvesen. Hardangerbrua teknisk brosjyre. http://www.vegvesen.no/_attachment/113342/binary/206605?fast_title=Technical+Brochure+Hardanger+Bridge+%28pdf%29.

[42] Volvo. Specifications on the volvo fl. http://www.volvotrucks.com/trucks/UAE-market/en-ae/trucks/volvo-fl-euro3/chassis/Pages/chassis.aspx.

[43] Randolph E. Walpole, Raymond H. Myers, Sharon L. Myers, and Keying Ye. *Probability and Statistics for Engineers and Scientists*. Prentice Hall, 9 edition, 2012.

[44] Peter D. Welch. The use of fast fourier transform for the estimation of power spectra: A method based on time averaging over short, modified periodograms. *IEEE Transactions on Audio and Electroacoustics*, AU-15:70–73, 1967.

[45] Jia-Jang Wu, A.R. Whittaker, and M.P. Cartmell. The use of finite element techniques for calculating the dynamic response of structures to moving loads. *Computers and Structures*, 78(6):789–799, 2000.

[46] Y.B. Yang. *Vehicle-bridge Interaction Dynamics : With Applications To High-speed Railways*. World Scientific Publishing Company, Singapore, 2004.

A Additional information to the case study

A.1 Comprehensive information on the Hardanger Bridge

A.1.1 Structure

Bridge deck

The bridge deck between the pylons is made of steel box girders. The steel sections used in the bridge deck are 60 metres long, made by welding five sections of 12 metres length together. The bridge was assembled by connecting these 60 metre sections, 23 in total weighing in at 400 tonnes each, to the hangers along the cables [2]. There are hanger clamps attached to the bridge deck every 20 metres in the longitudinal direction. For every four metres of the girder, there is installed a transverse bulkhead. At the bottom of the girder there is a guide vane at each side to stabilize against aerodynamic loads. The outside of the girder is spray-galvanized and painted, with the exception of the carriageway [41].

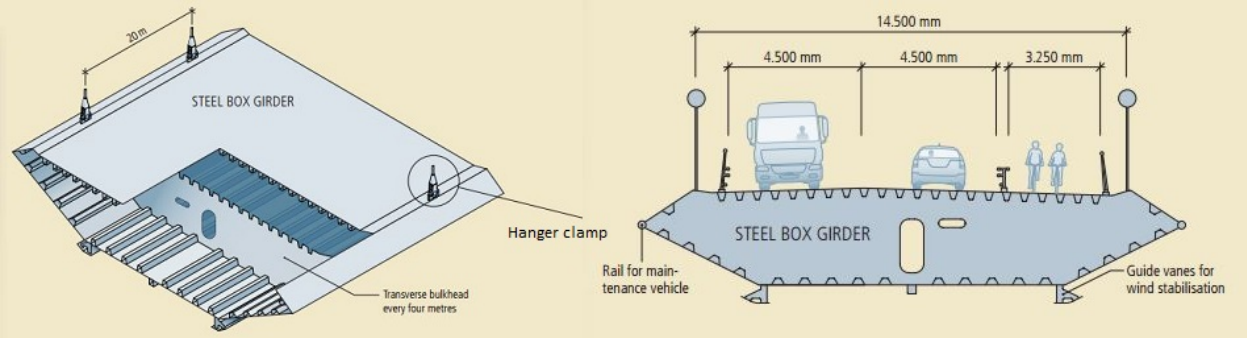

Figure A.1: Steel box girder used for the bridge deck [41]

Pylons

The pylons are raging 201.5 metres into the sky at Bu and 193.5 metres high at Vallavik, since the foundation base lies 8 metres higher at Vallavik. Each pylon is anchored in foundations of 900 m^3 of concrete at the bottom of each column [2]. The cross section of each pylon is made of two rectangular columns with rounded corners, connected by three transverse girders. The base of the columns has a cross section $8.6 \cdot 7.0$ metres at the bottom, and then narrowing into a cross section of $4.5 \cdot 4.5$ metres at the top. The pylons are made of B45 concrete, with wall thickness 600 millimetres in the columns, and up to 800 millimetres wall thickness in the transverse girders. The saddles where the suspension cables rests are located on top of the tower columns surrounded by protective concrete housing [41]. The bridge deck is supported on the bottom transverse girder at each pylon.

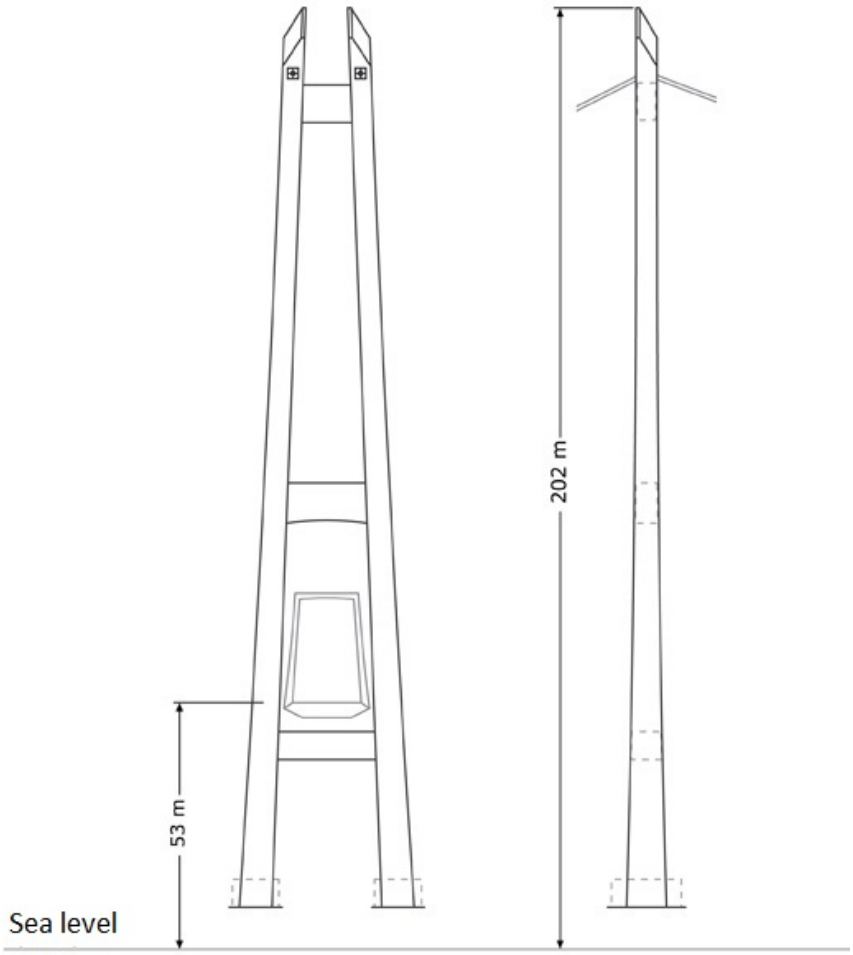

Figure A.2: Pylon [40]

Cables and hangers

The bridge is held up by 65 hanger pairs, 130 hangers in total. The hangers are connected to the bridge every 20 meters, and are at the other side connected to a steel cable. The placement of the clamps connecting the hangers to the bridge deck can be seen in Figure A.1. The suspension cable consists of 10032 galvanized steel wires with a 5.3 millimetre diameter. This is done by compressing 19 strands, each consisting of 528 wires with a tensile strength of 1570 megapascals, into a circular cross section with the use of a hydraulic press. The cable has a breaking load of 342 kilonewtons [41]. The bending stiffness of the cables is negligible, and hence all transferring of loads will occur in the form of axial strain.

Similarly to the cables, the hangers will only transfer loads as axial strain. The hangers are connected to the cable and the girder box through hanger clamps, see Figure A.3. The connection between the hangers and the clamps are made with bolts with a diameter 160 millimetres. The hangers vary in length from 2.04 metres to 127.6 metres, and the five shortest hangers are not made of cables and is instead made as one piece of cast steel. The rest of the hangers are comprised of a cable with a cast steel socket at each end. The hanger cables are locked coil cables consisting of seven layers of wires, the outer three are Z-shaped wires. To anchor the hanger cables into the steel sockets, a conically shaped zinc block is cast around the cable wires [41].

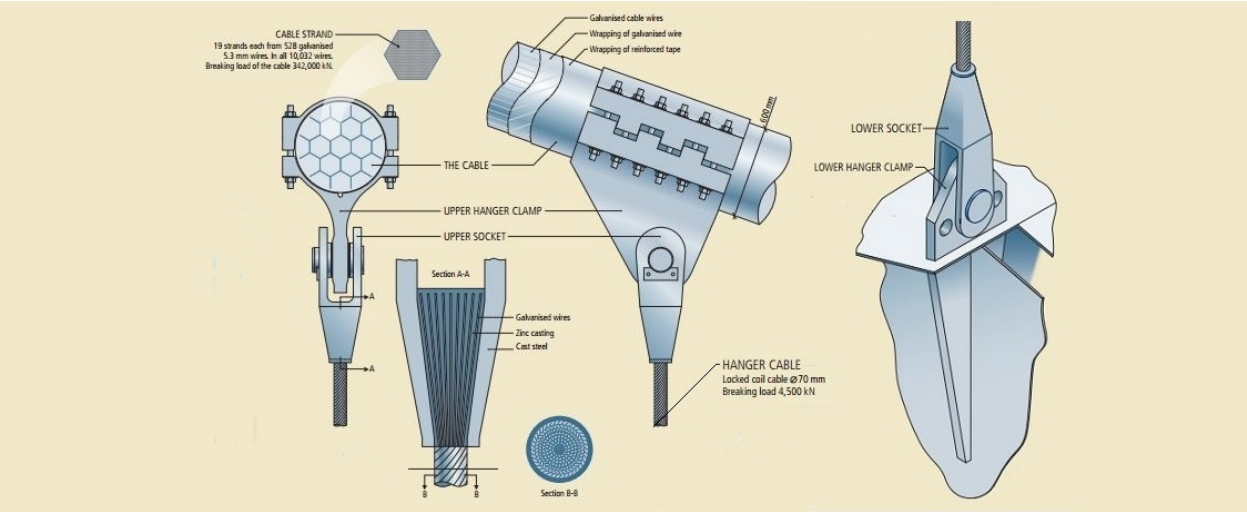

Figure A.3: Hanger and hanger clamps [41]

Cable anchorage

To secure the bridge, the cables are anchored in solid rock on both sides of the bridge, and the anchorage plates on both sides lies in rock caverns [2]. To anchor the cables, there are two splay chambers and one anchorage chamber on each side of the bridge. The design of the splay chambers is done in a way that makes only the top of the chamber visible, and at Vallavik the splay chambers are constructed inside the mountain and only the front wall is visible.

The suspension cables are supported on splay saddles inside splay chambers. Inside the chamber the cables are split into 19 individual strands which are then fixed to strand shoes. Through anchorage units, the strand shoes are connected to an anchorage block. These anchorage blocks are furthermore connected by 76 prestressing cables to anchorage plates made of concrete, which are located in the anchorage chamber. The anchorage chambers lies inside the mountains, and are 15 metres deep and 40 metres long [41].

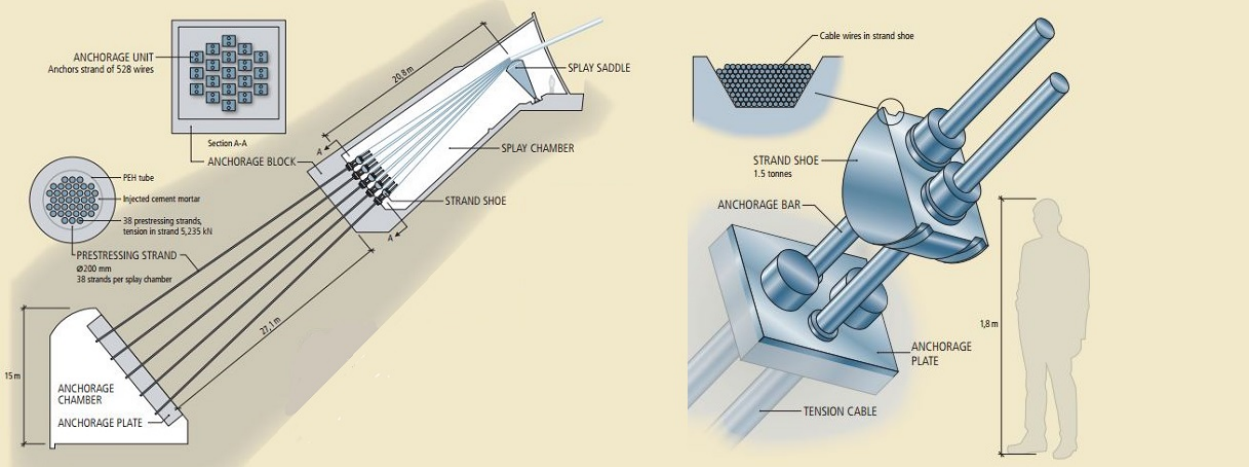

Figure A.4: The anhorage system for securing the suspension cables [41]

A.1.2 Recorder position

Channel	Name	X-coordinate [m]	Y-coordinate [m]	Z-coordinate [m]
1	H1 East	480	6.33	8.38
2	H1 Vest	480	-6.64	-8.38
3	H2 Vest	360	-6.64	-6.41
4	H3 East	240	6.33	-4.45
5	H3 Vest	240	-6.64	-4.45
6	H4 East	120	6.33	-2.48
7	H4 Vest	120	-6.64	-2.48
8	H5 East	-7	6.33	-0.40
9	H5 Vest	-7	-6.64	-0.40
10	H6 East	-120	6.33	-2.25
11	H6 Vest	-120	-6.64	-2.25
12	H7 East	-240	6.33	-4.22
13	H7 Vest	-240	-6.64	-4.22
14	H8 East	-360	6.33	-6.18
15	H9 East	-480	6.33	-8.15
16	H9 Vest	-480	-6.64	-8.15
17	H10 East	-655	4.50	120.50
18	H10 Vest	-655	-4.50	120.50
19	H11 East	655	4.50	120.50
20	H11 Vest	655	-4.50	120.50
21	A1	460	7.25	0.30
22	A2	280	7.25	0.30
23	A3	240	7.25	3.90
24	A4	200	7.25	4.56
25	A5	180	7.25	4.89
26	A6	-10	-7.25	8.00
27	A7	-180	7.25	5.22
28	A8	-420	7.25	1.28
29	A9	-655	4.50	140.00

A.2 Traffic log

Date	Enter Time	Exit Time	Load case	Lane/direction	Direction
31.03.2016	08:44:02	08:45:03	Car	NS	South
	08:44:05	08:45:06	Car	NS	South
	08:44:15	08:45:22	Car	SN	North
	08:44:22	08:45:27	Car	SN	North
	08:46:19	08:47:32	Truck	SN	North
	08:48:14	08:49:25	Truck	SN	North
	08:50:36	08:51:31	Car	SN	North
	08:52:39	08:53:43	Car	NS	South
	08:52:54	08:53:54	Car	NS	South
	08:52:57	08:53:57	Car	NS	South
	08:52:59	08:53:59	Car	NS	South
	08:55:50	08:56:50	Car	SN	North
	08:56:45	08:57:43	Car	NS	South
	08:57:14	08:58:14	Car	NS	South
	08:59:56	09:01:04	Car	NS	South
	09:00:18	09:01:34	Truck	SN	North
	09:01:45	09:02:45	Car	NS	South
	09:01:48	09:02:48	Car	NS	South
	09:04:18	09:05:20	Car	SN	North
	09:05:09	09:06:00	Car	NS	South
	09:06:12	09:07:04	Car	NS	South
	09:06:16	09:07:13	Car	NS	South
	09:06:18	09:07:15	Car	NS	South
	09:06:55	09:07:50	Car	NS	South
	09:09:31	09:10:35	Car	SN	North
	09:10:04	09:11:21	Car	SN	North
	09:10:11	09:11:29	Car	SN	North
	09:10:20	09:11:56	Car	NS	South
	09:10:24	09:12:02	Car	NS	South
	09:10:52	09:12:19	Car	NS	South
	09:12:17	09:13:08	Camper van	NS	South
	09:13:56	09:15:15	Truck + 3 cars	SN	North
	09:14:10	09:15:28	Car	SN	North
	09:14:50	09:15:51	Car	NS	South
	09:16:38	09:17:40	Truck	NS	South

B Supplementary Plots

B.1 Plots from the formulation of the moving load model

B.1.1 Damping for the moving load on a SSB

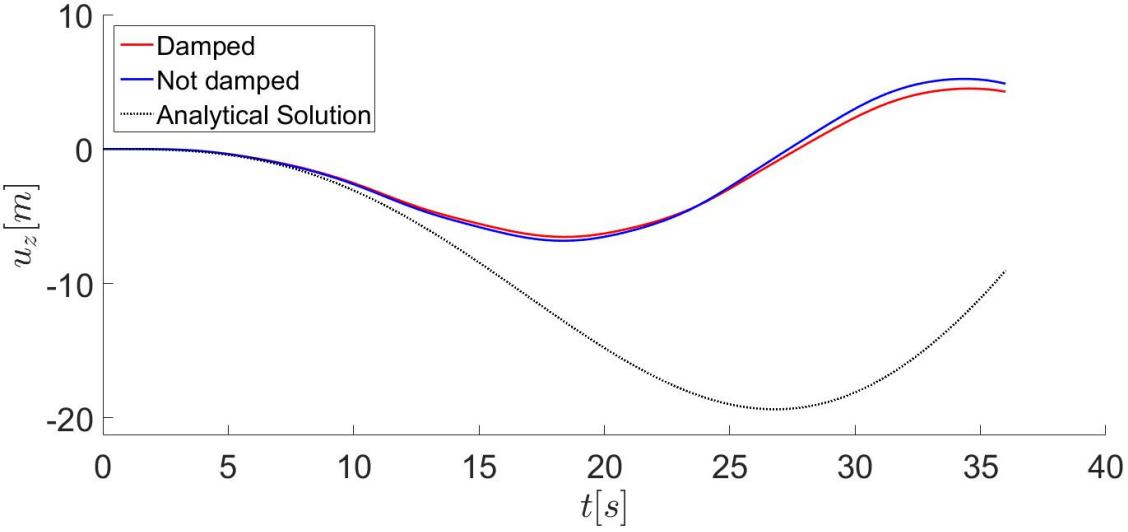

Figure B.1: Displacement at midspan for beam discretized into 4 elements with and without Rayleigh damping of $\xi_0 = 5\%$

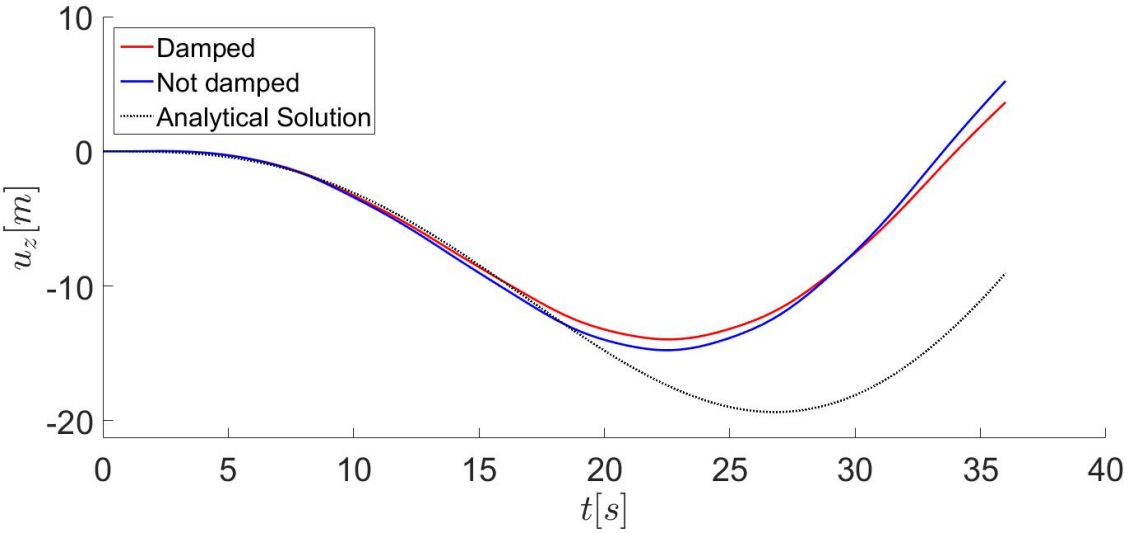

Figure B.2: Displacement at midspan for beam discretized into 10 elements with and without Rayleigh damping of $\xi_0 = 5\%$

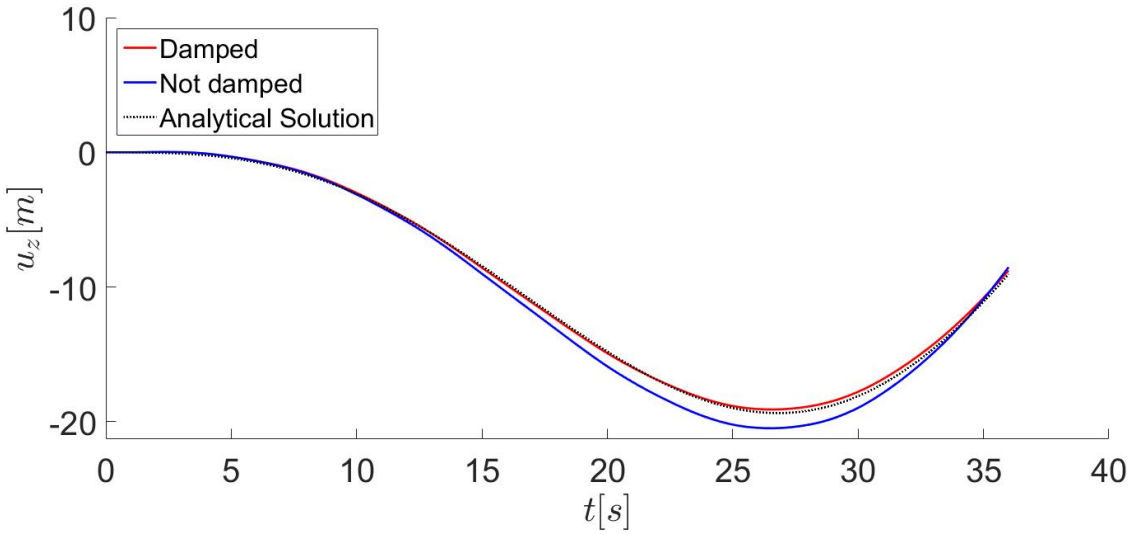

Figure B.3: Displacement at midspan for beam discretized into 500 elements with and without Rayleigh damping of $\xi_0 = 5\%$

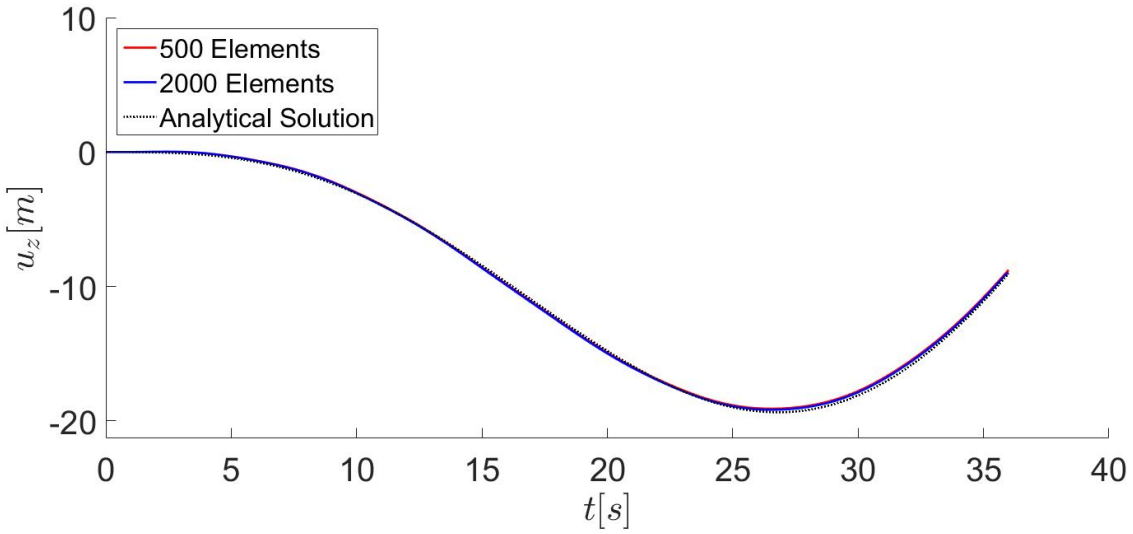

Figure B.4: The displacement at midspan for a simply supported beam with Rayleigh damping of $\xi_0 = 5\%$, discretized into 500 and 2000 elements compared to the analytical solution

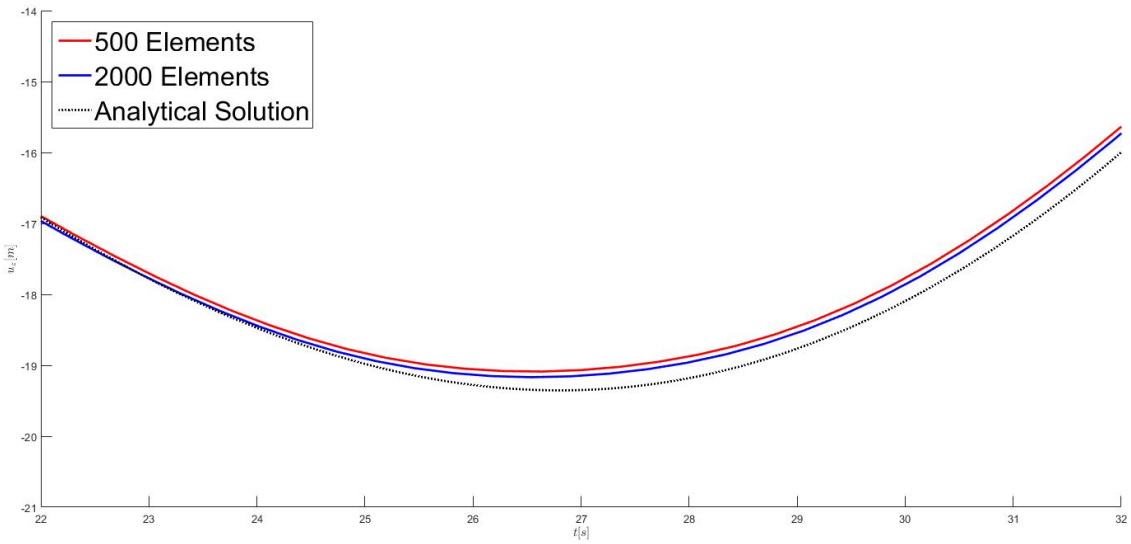

Figure B.5: Zoomed in section at maximum deflection at midspan for the simply supported beam with Rayleigh damping of $\xi_0 = 5\%$, discretized into 500 and 2000 elements compared to the analytical solution

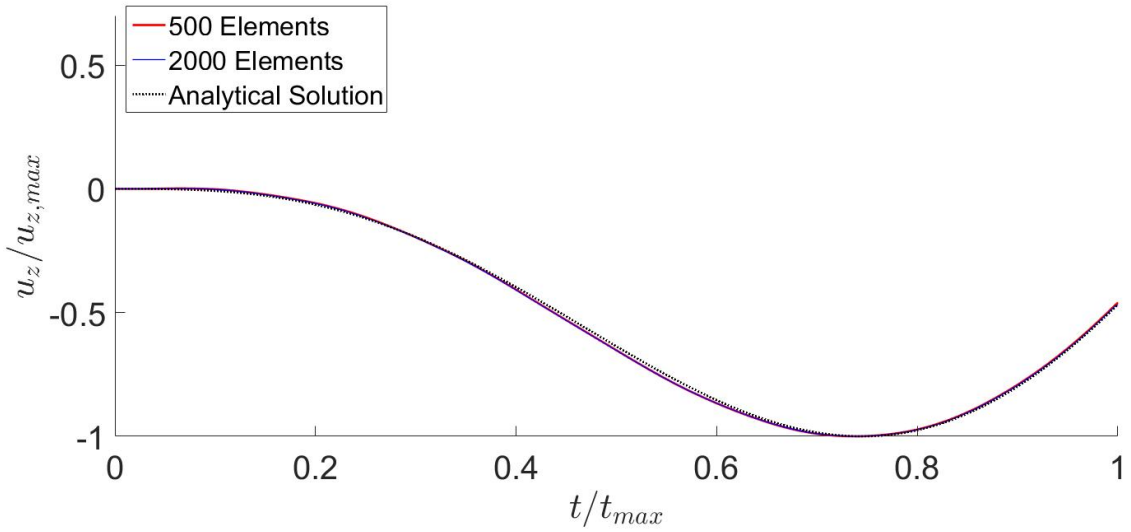

Figure B.6: The relative displacement at midspan for a simply supported beam with Rayleigh damping of $\xi_0 = 5\%$, discretized into 500 and 2000 elements compared to the analytical solution

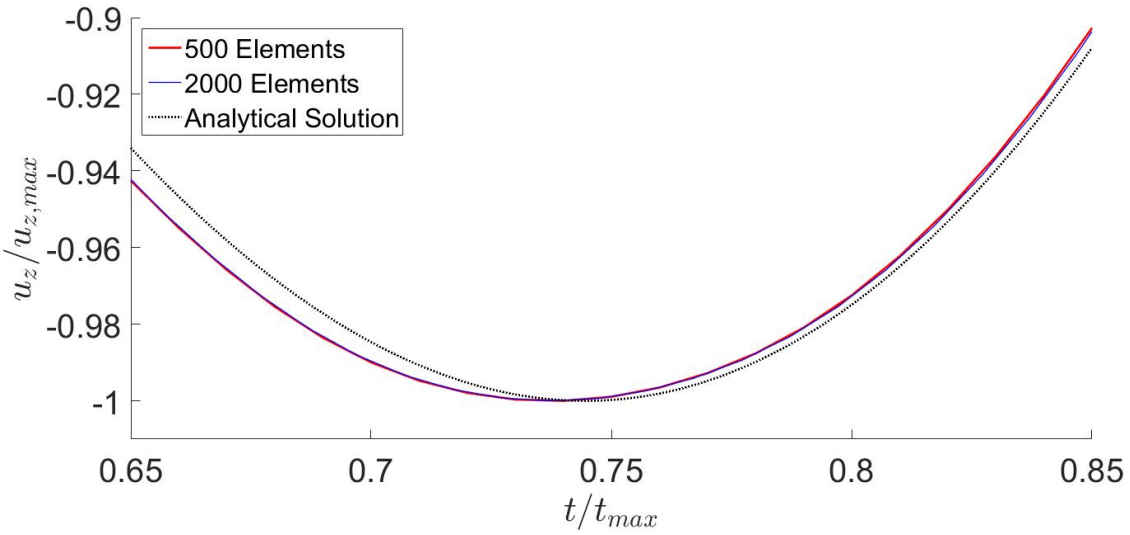

Figure B.7: Zoomed in section at maximum relative deflection at midspan for the simply supported beam with Rayleigh damping of $\xi_0 = 5\%$, discretized into 500 and 2000 elements compared to the analytical solution

B.1.2 Moments in margin nodes for the moving load on a SSB

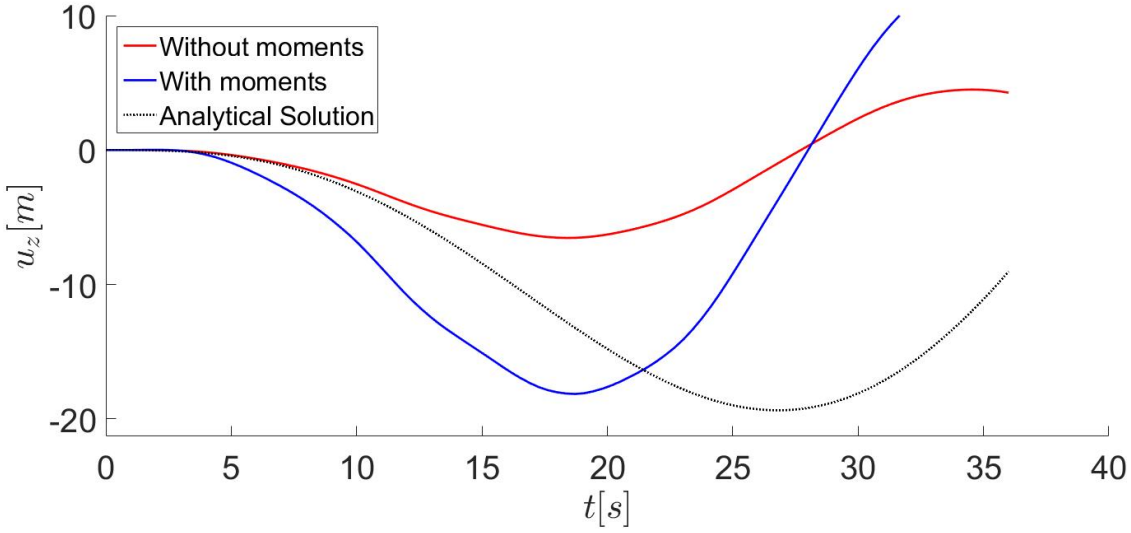

Figure B.8: Displacement at midspan for beam discretized into 4 elements with enforced moments at bounding nodes

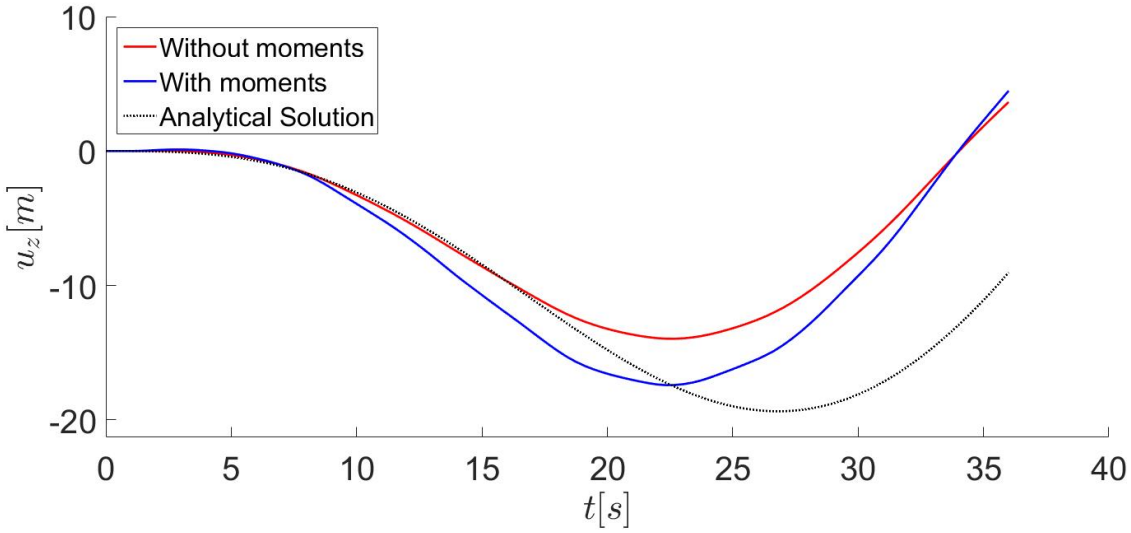

Figure B.9: Displacement at midspan for beam discretized into 10 elements with enforced moments at bounding nodes

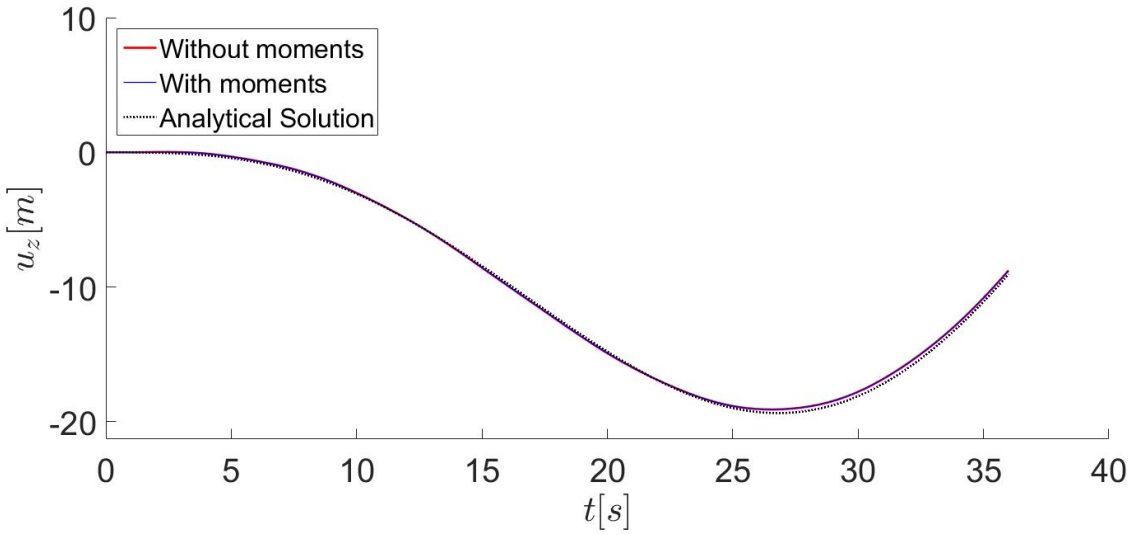

Figure B.10: Displacement at midspan for beam discretized into 500 elements with enforced moments at bounding nodes

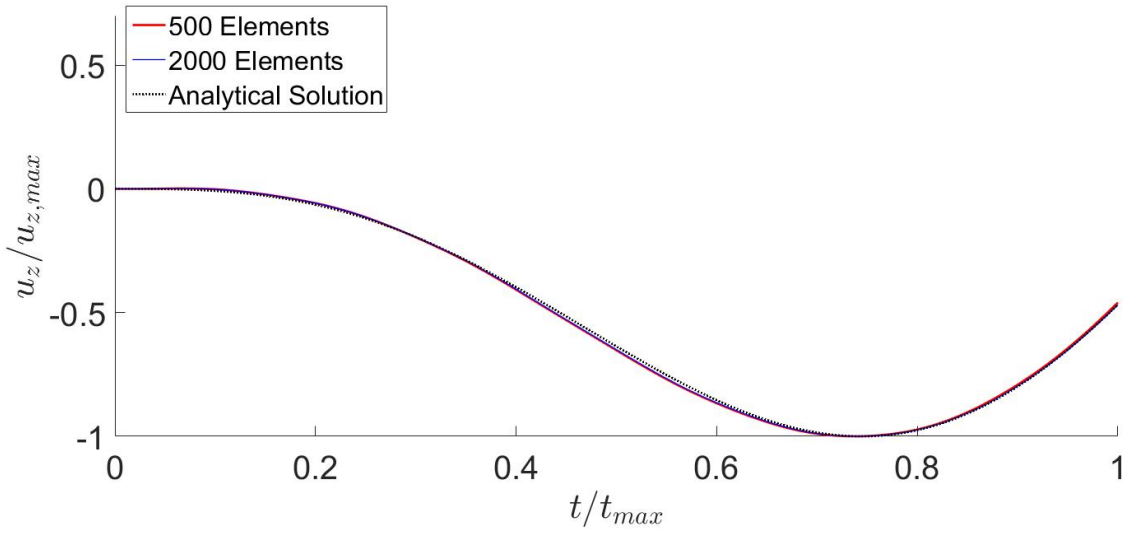

Figure B.11: Relative displacement for beam discretized into 500 elements and 2000 elements with enforced moments at nodes

B.2 Measurements from Hardanger Bridge

B.2.1 Wind measurements

Sensor A1

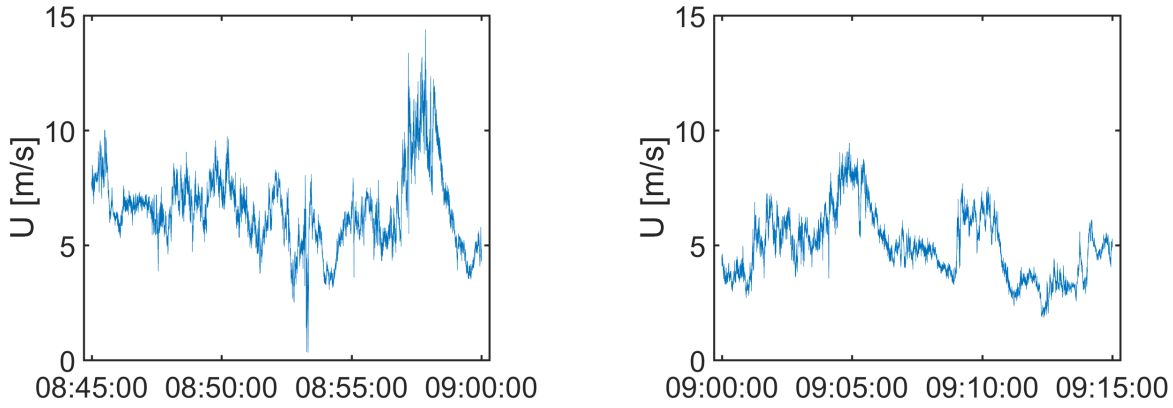

Figure B.12: Horizontal wind velocity, sensor A1

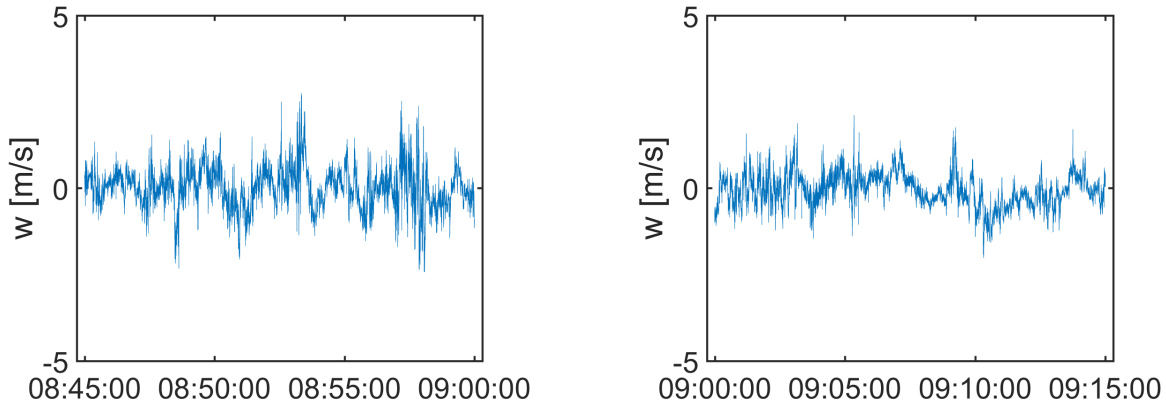

Figure B.13: Vertical wind velocity, sensor A1

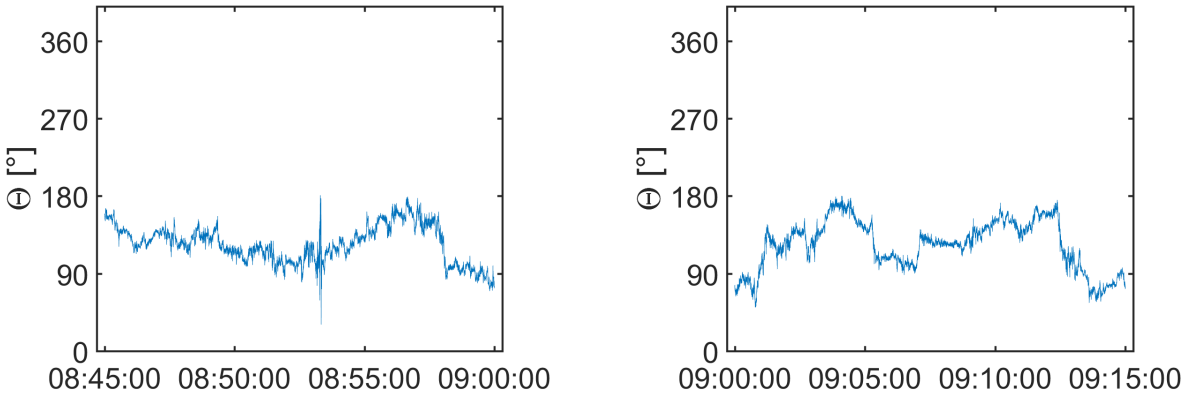

Figure B.14: Angle for horizontal wind, sensor A1

Sensor A2

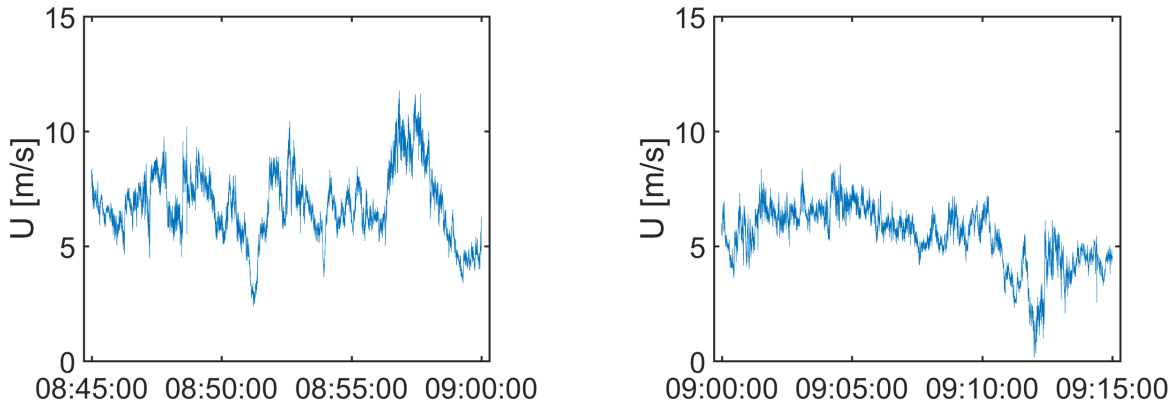

Figure B.15: Horizontal wind velocity, sensor A2

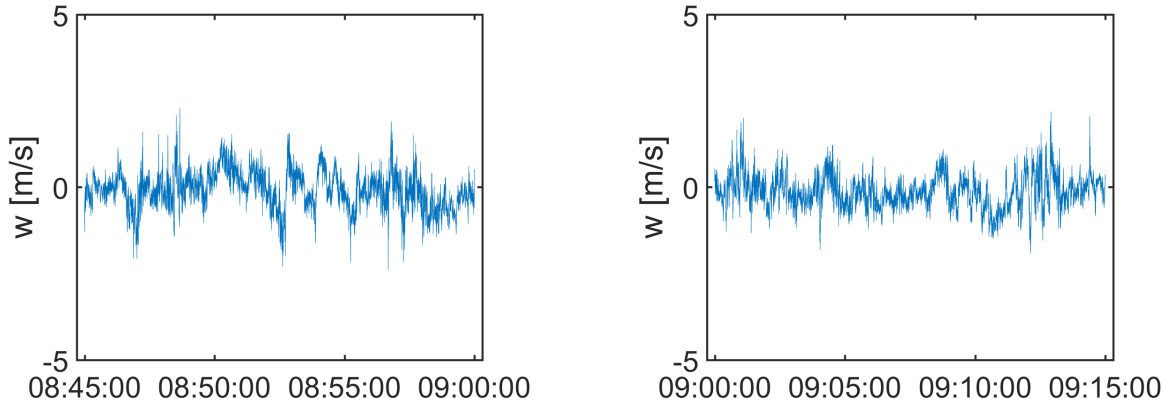

Figure B.16: Vertical wind velocity, sensor A2

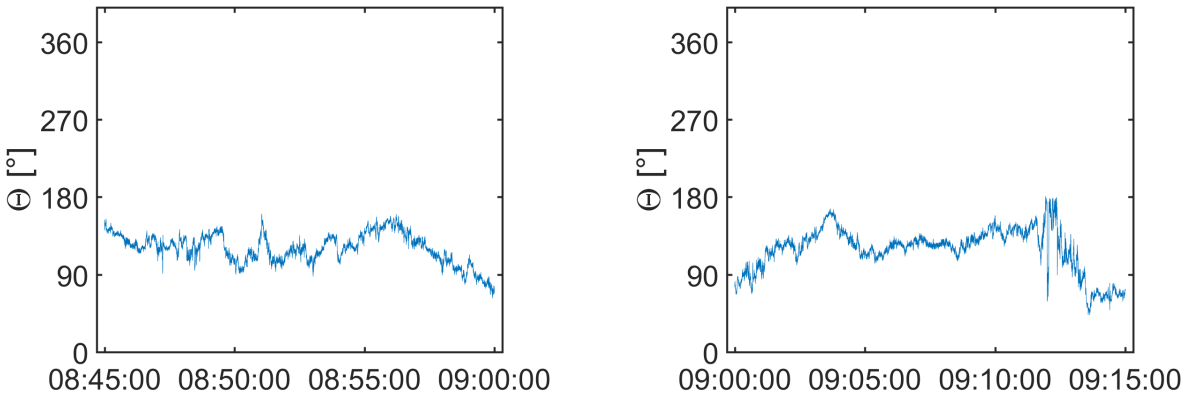

Figure B.17: Angle for horizontal wind, sensor A2

Sensor A3

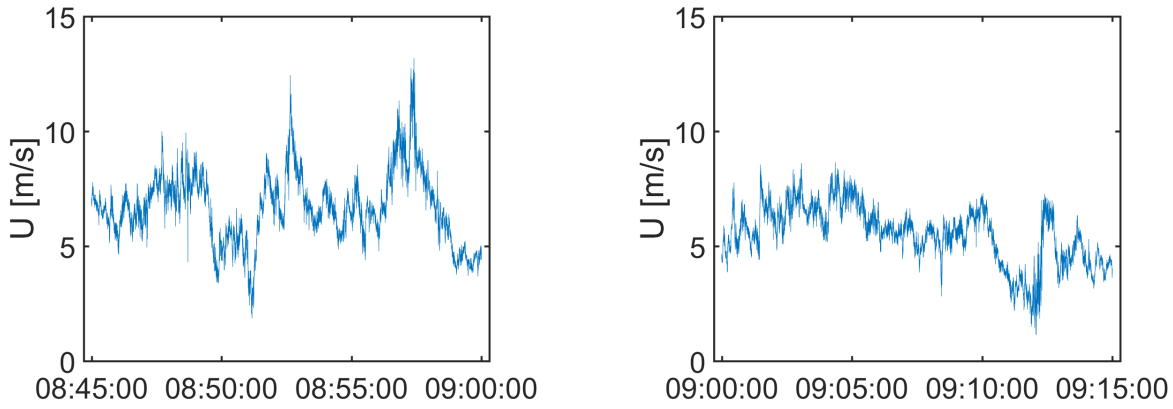

Figure B.18: Horizontal wind velocity, sensor A3

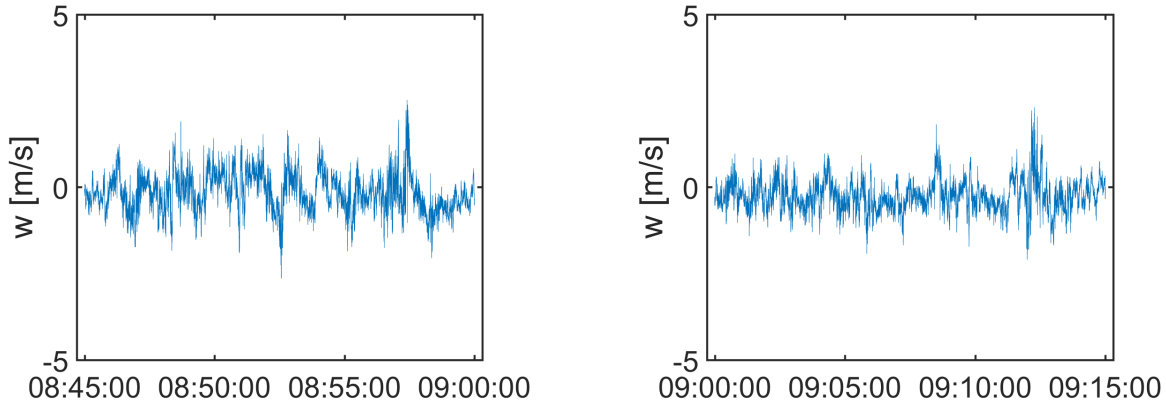

Figure B.19: Vertical wind velocity, sensor A3

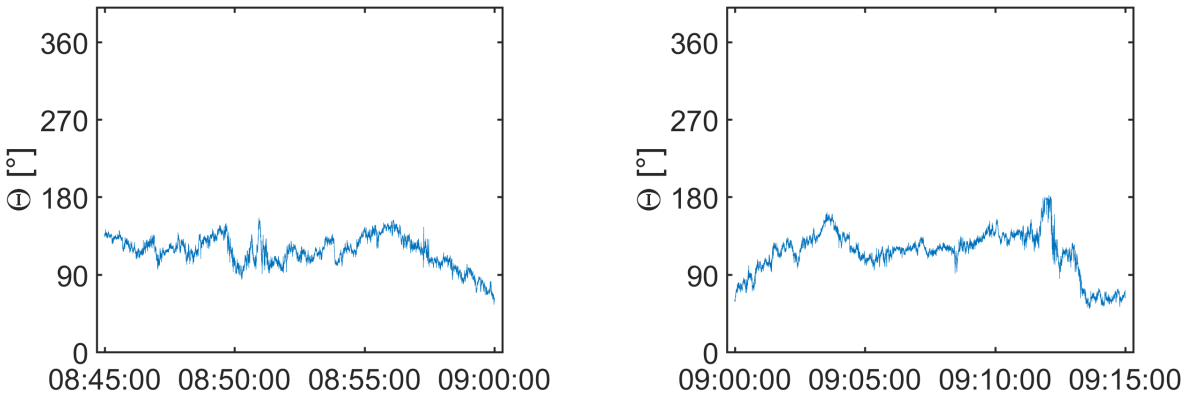

Figure B.20: Angle for horizontal wind, sensor A3

Sensor A4

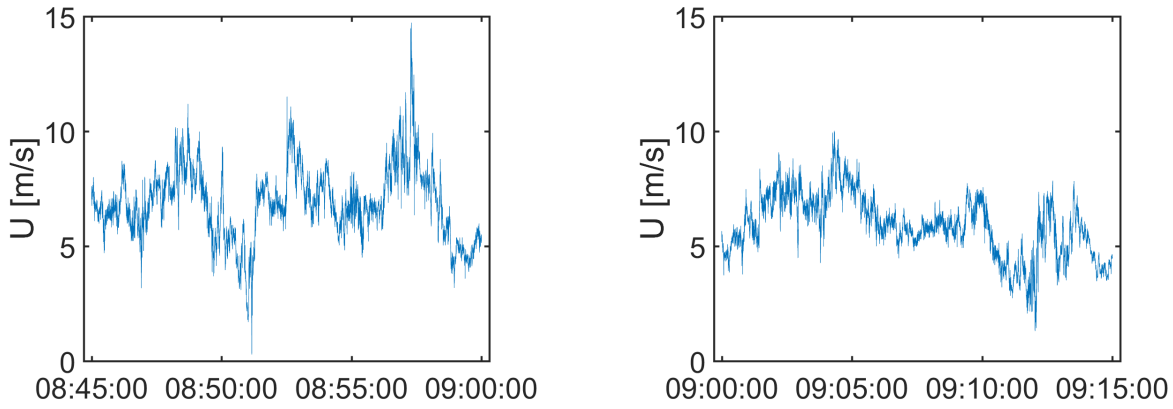

Figure B.21: Horizontal wind velocity, sensor A4

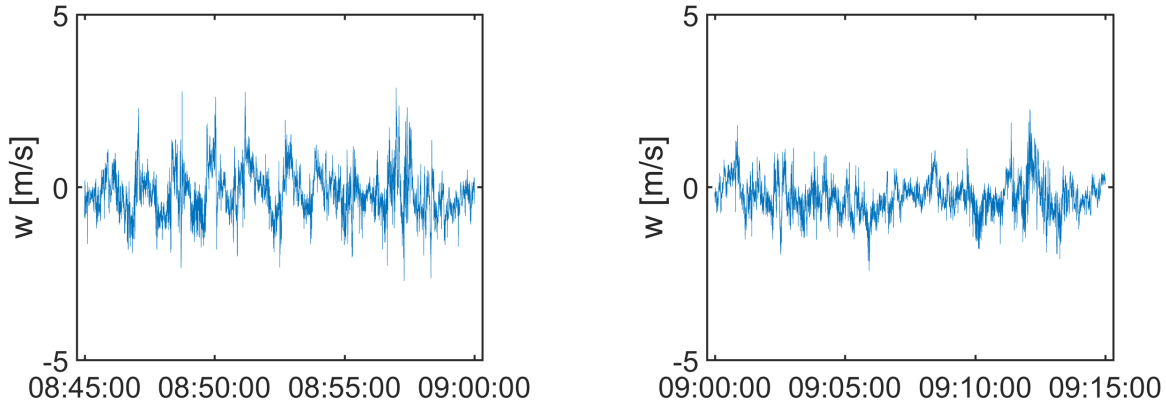

Figure B.22: Vertical wind velocity, sensor A4

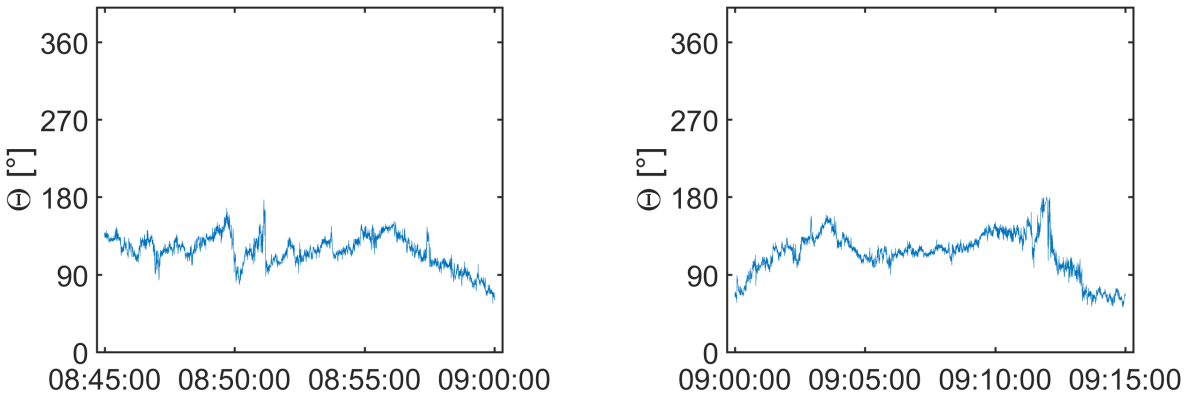

Figure B.23: Angle for horizontal wind, sensor A4

Sensor A5

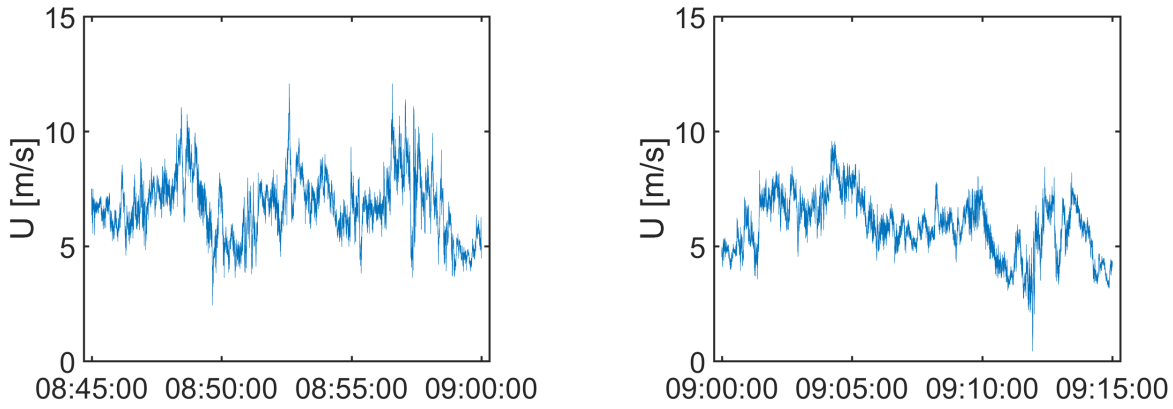

Figure B.24: Horizontal wind velocity, sensor A5

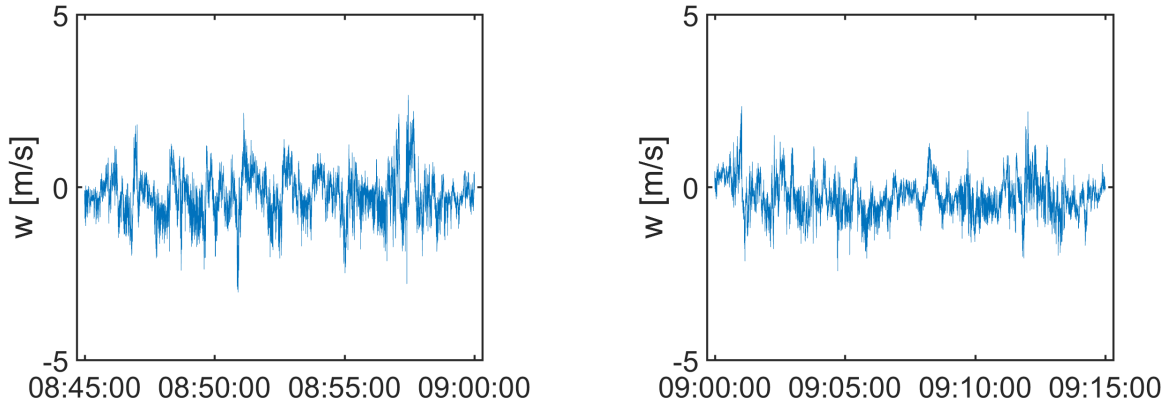

Figure B.25: Vertical wind velocity, sensor A5

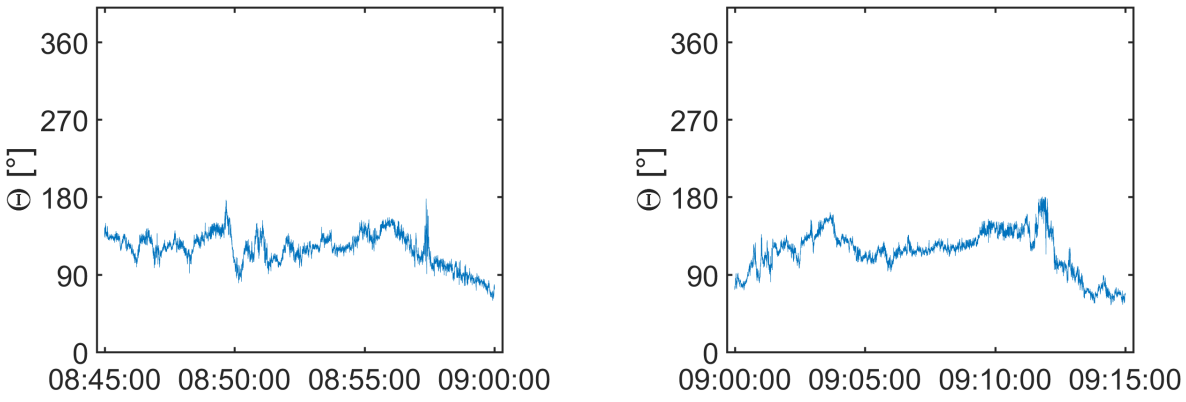

Figure B.26: Angle for horizontal wind, sensor A5

Sensor A6

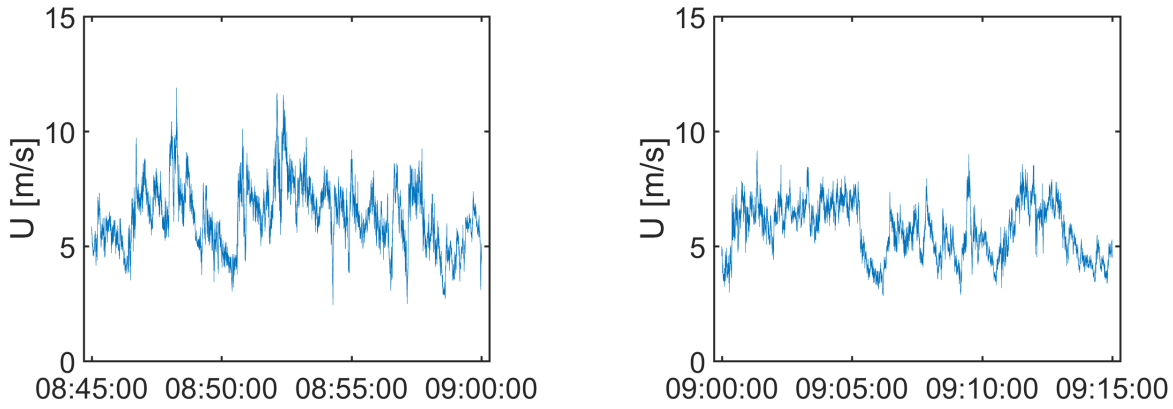

Figure B.27: Horizontal wind velocity, sensor A6

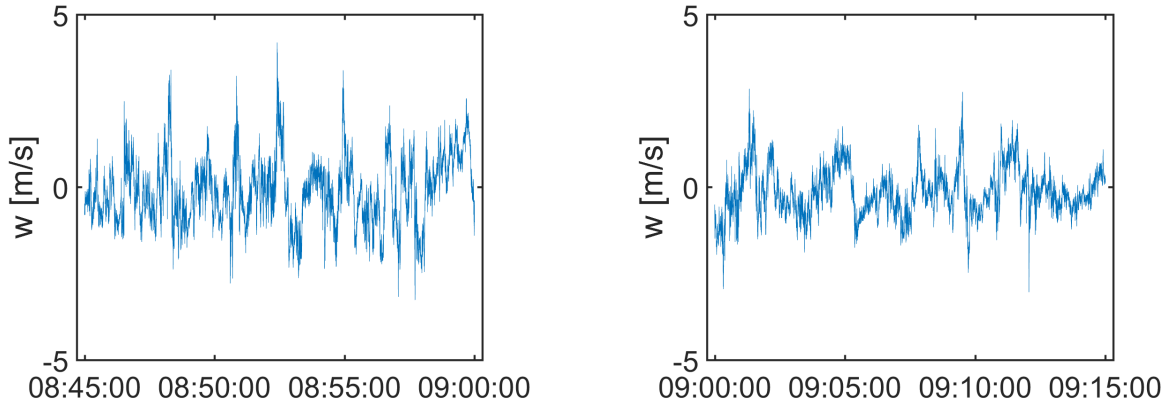

Figure B.28: Vertical wind velocity, sensor A6

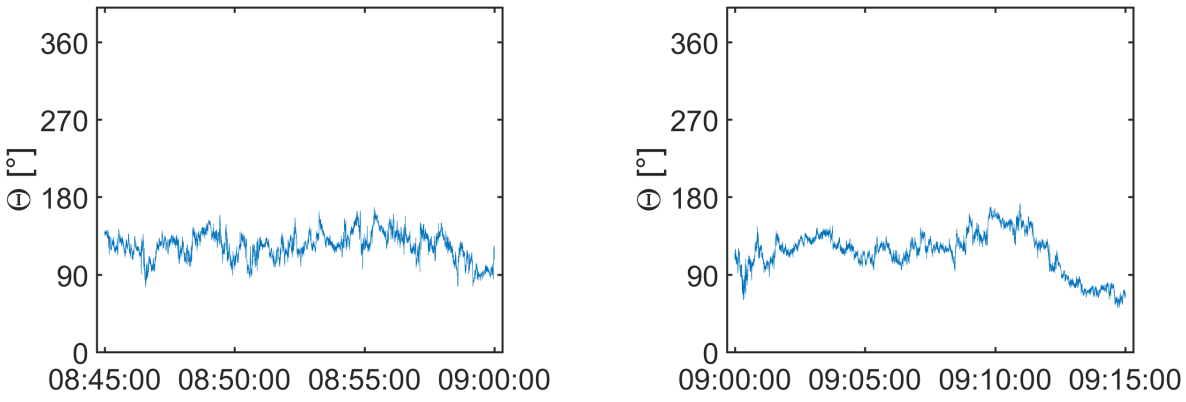

Figure B.29: Angle for horizontal wind, sensor A6

Sensor A7

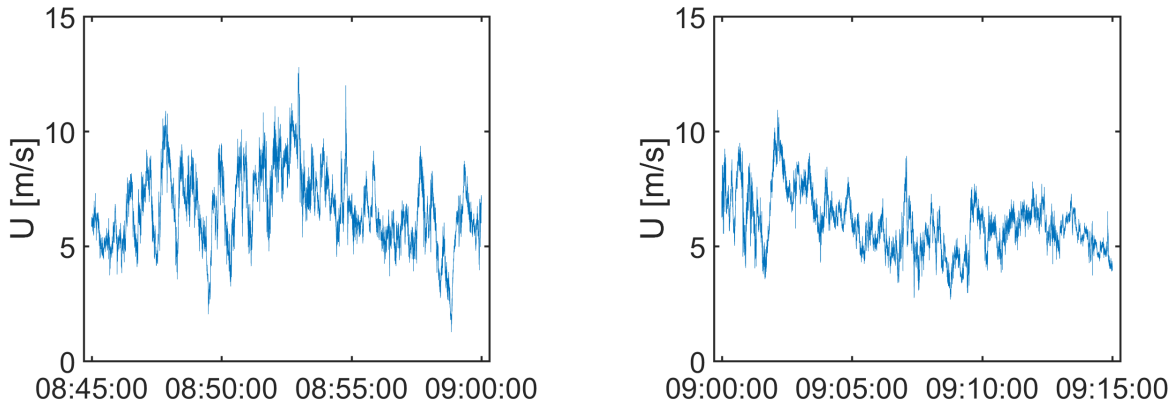

Figure B.30: Horizontal wind velocity, sensor A7

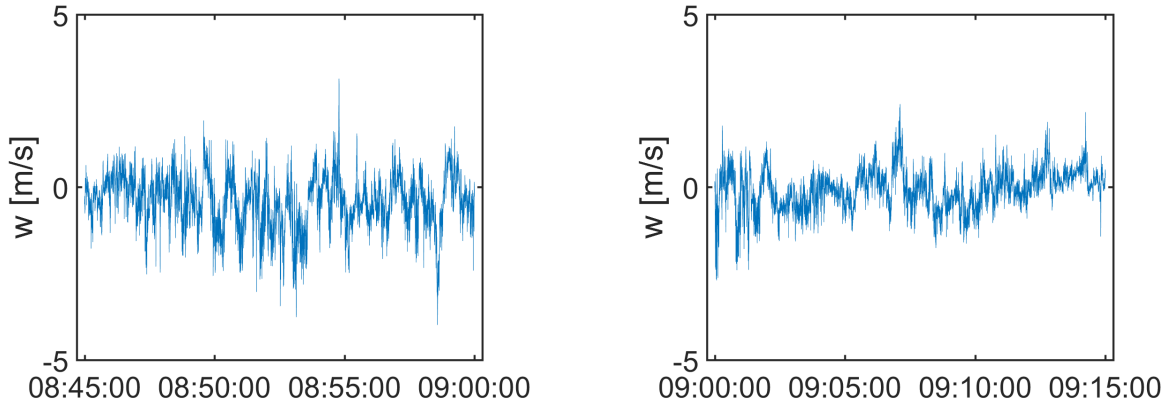

Figure B.31: Vertical wind velocity, sensor A7

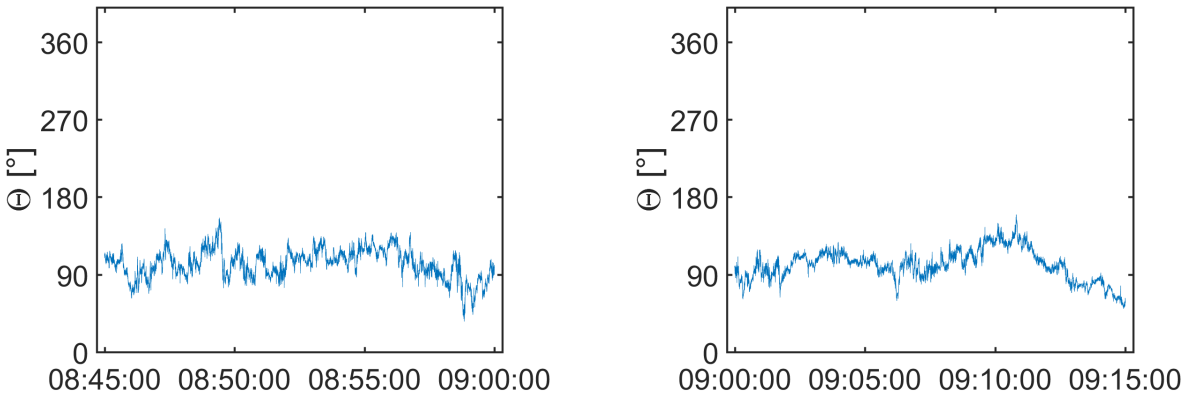

Figure B.32: Angle for horizontal wind, sensor A7

Sensor A8

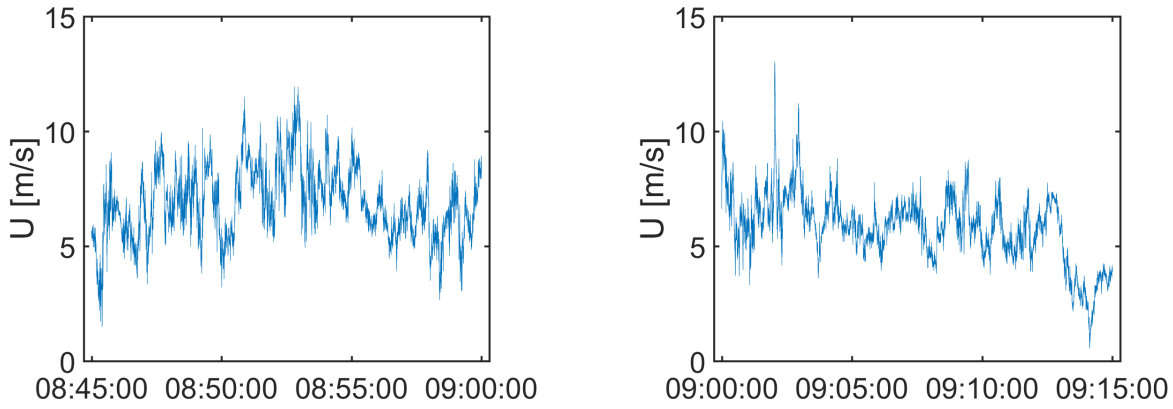

Figure B.33: Horizontal wind velocity, sensor A8

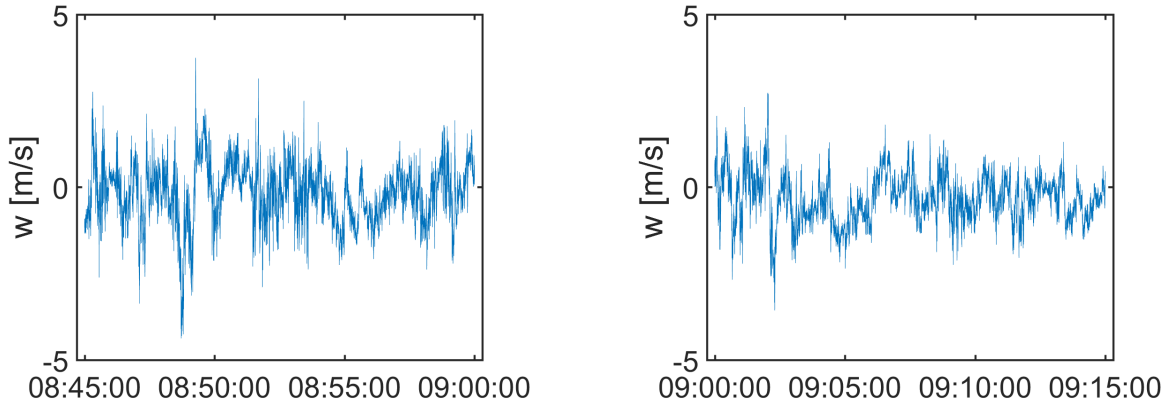

Figure B.34: Vertical wind velocity, sensor A8

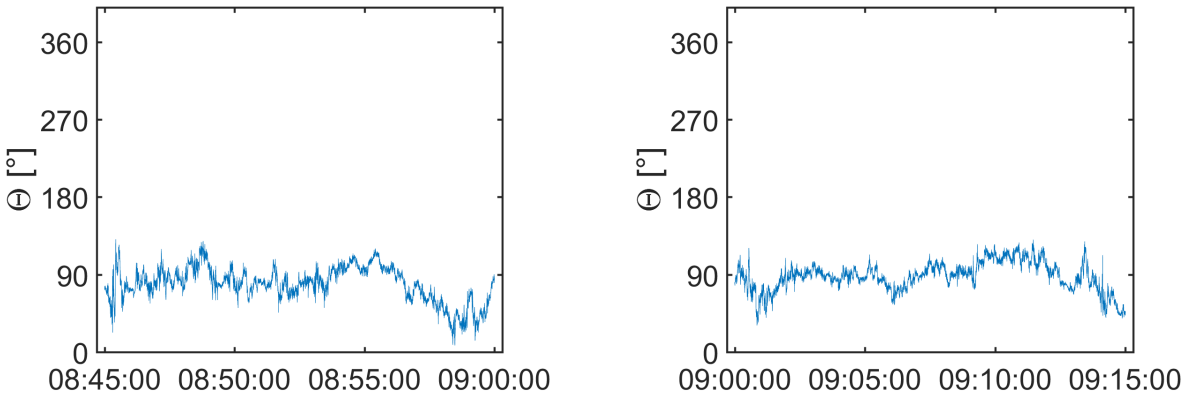

Figure B.35: Angle for horizontal wind, sensor A8

Sensor A9

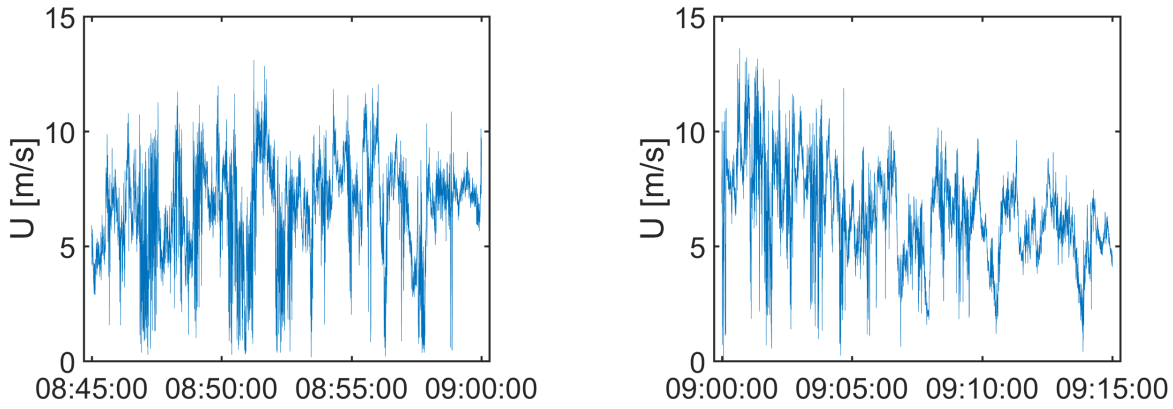

Figure B.36: Horizontal wind velocity, sensor A9

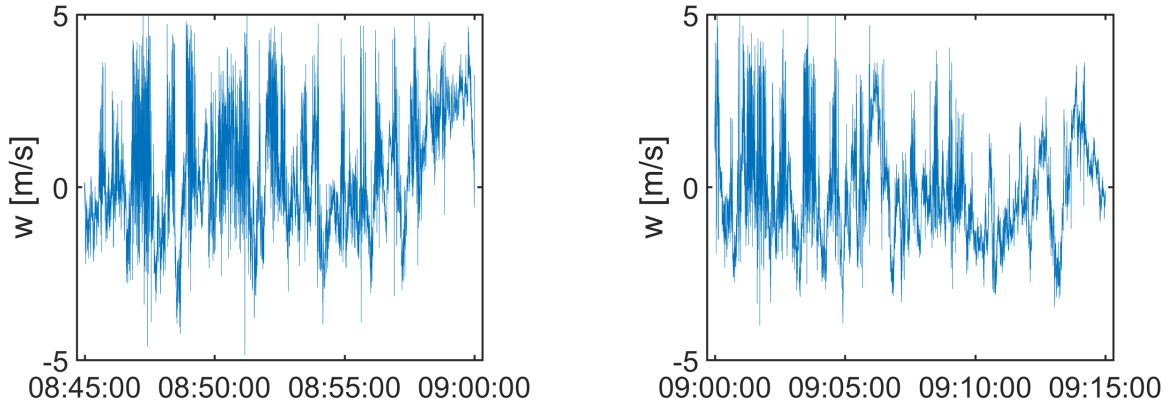

Figure B.37: Vertical wind velocity, sensor A9

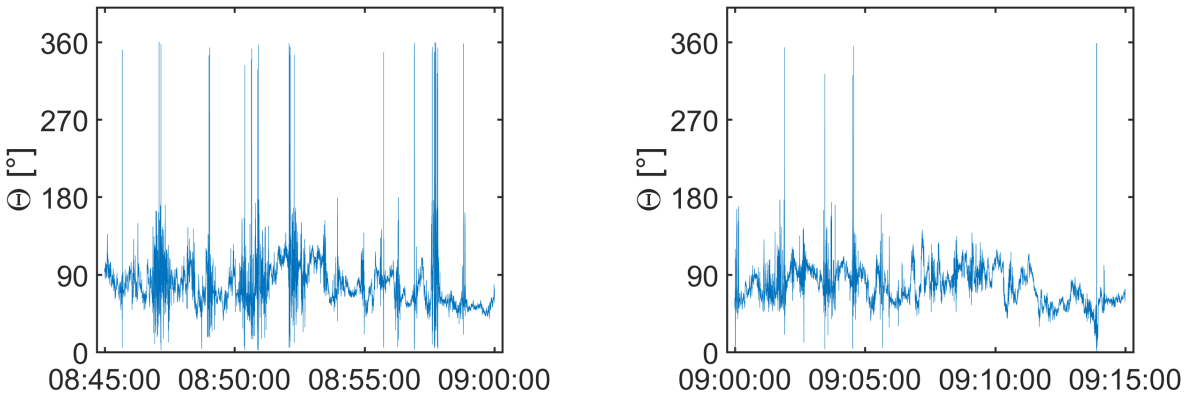

Figure B.38: Angle for horizontal wind, sensor A9

B.2.2 Vertical acceleration response

Section H1

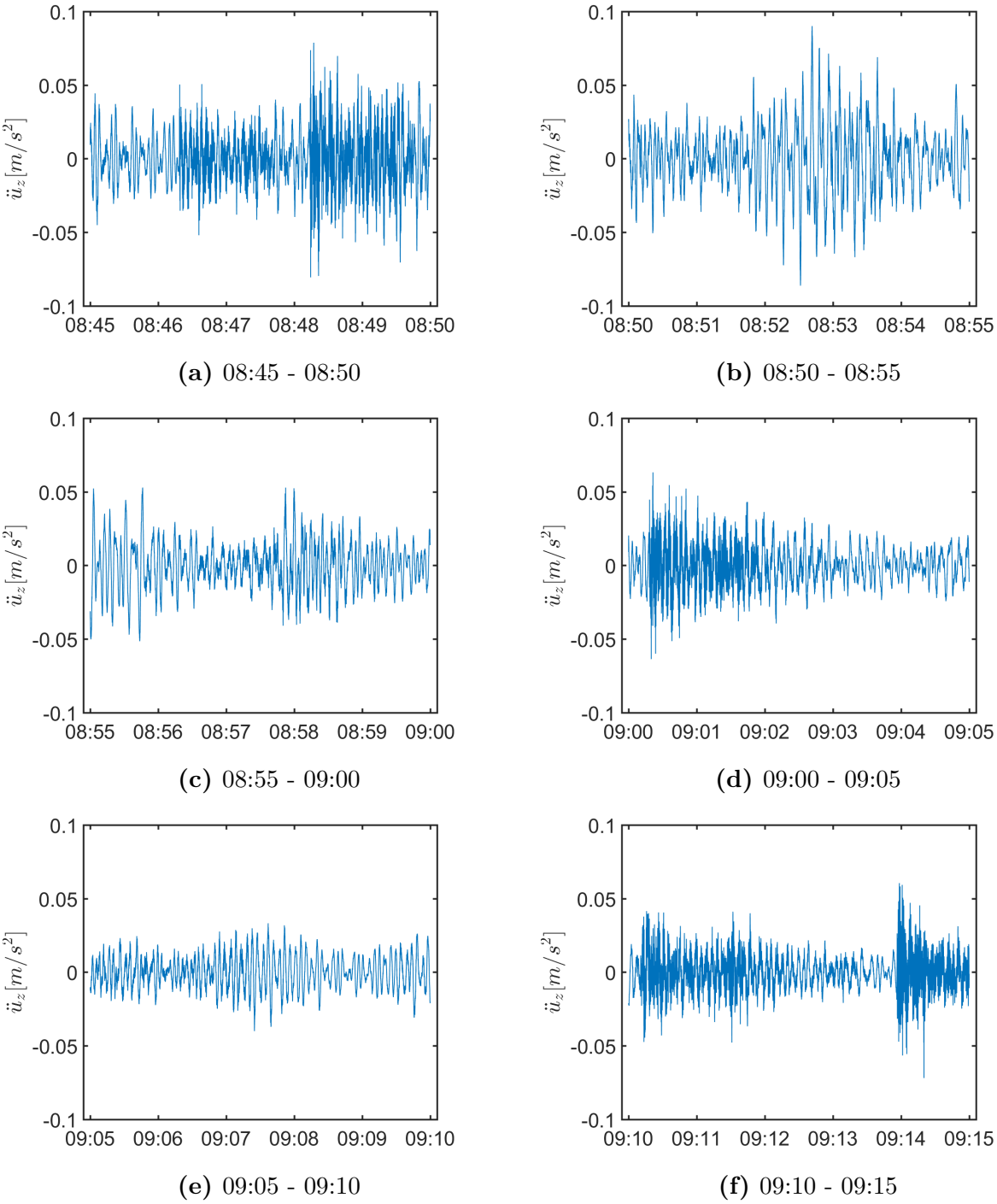

(a) 08:45 - 08:50

(b) 08:50 - 08:55

(c) 08:55 - 09:00

(d) 09:00 - 09:05

(e) 09:05 - 09:10

(f) 09:10 - 09:15

Figure B.39: Vertical acceleration response, Section H1

Section H2

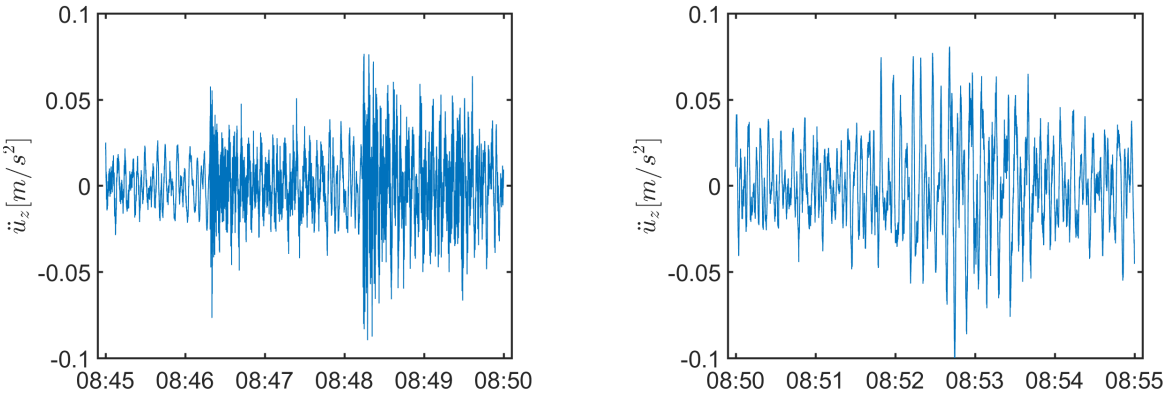

(a) 08:45 - 08:50

(b) 08:50 - 08:55

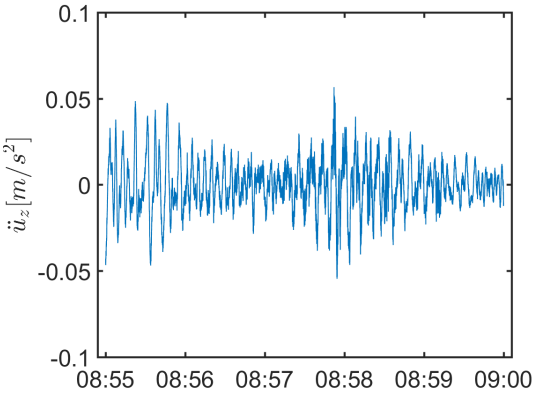

(c) 08:55 - 09:00

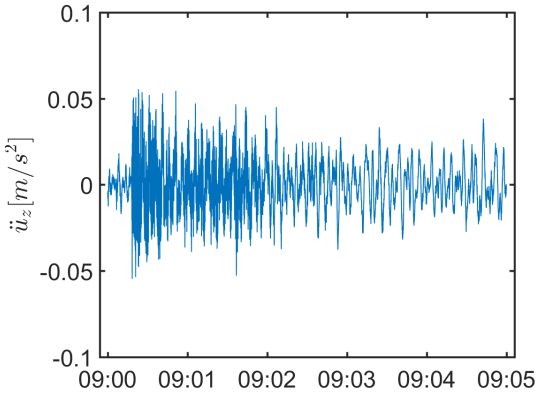

(d) 09:00 - 09:05

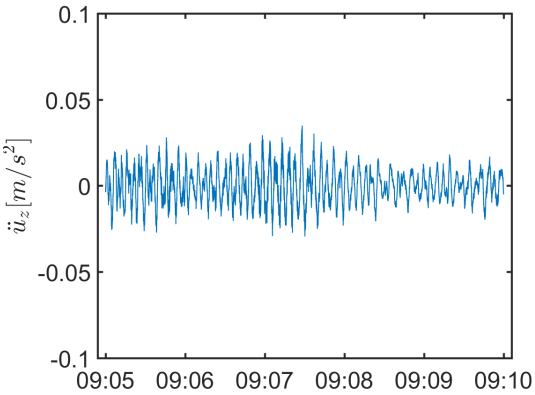

(e) 09:05 - 09:10

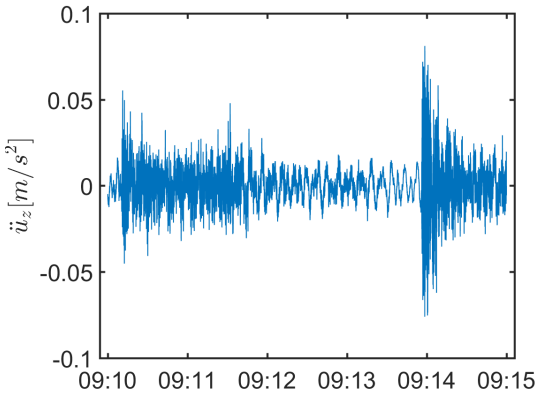

(f) 09:10 - 09:15

Figure B.40: Vertical acceleration response, Section H2

Section H3

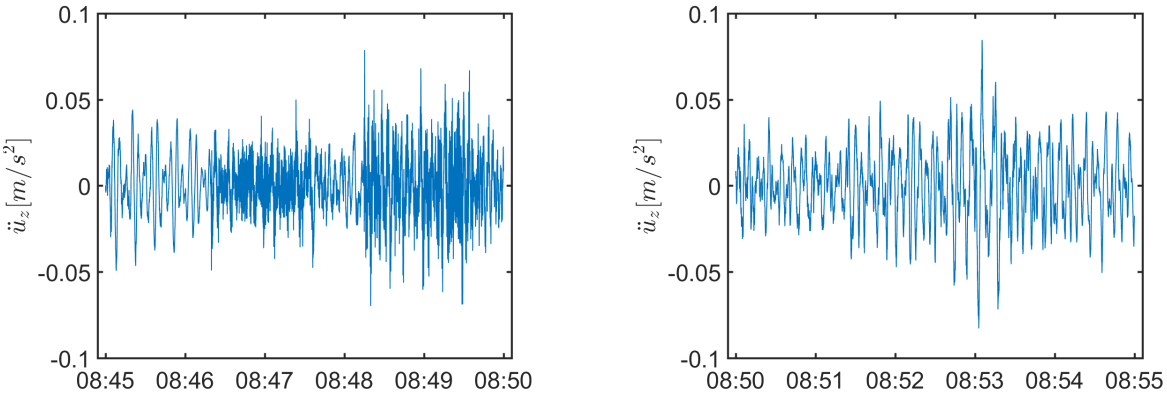

(a) 08:45 - 08:50

(b) 08:50 - 08:55

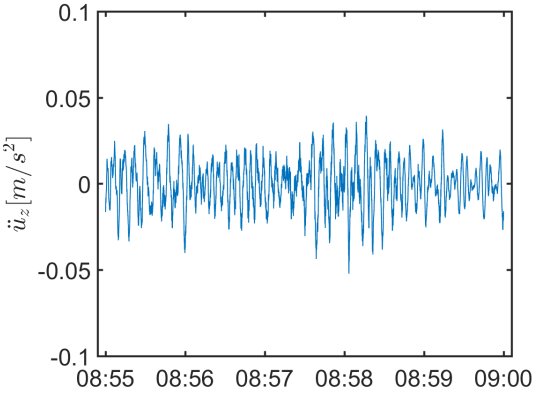

(c) 08:55 - 09:00

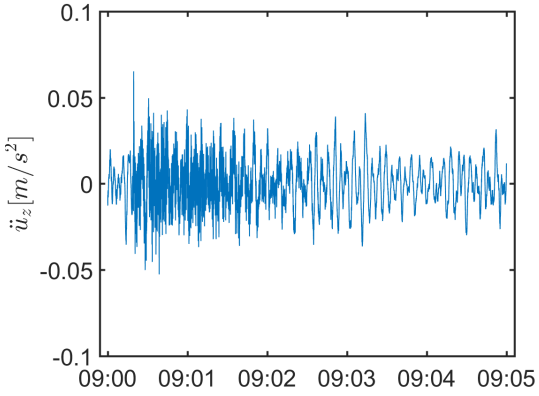

(d) 09:00 - 09:05

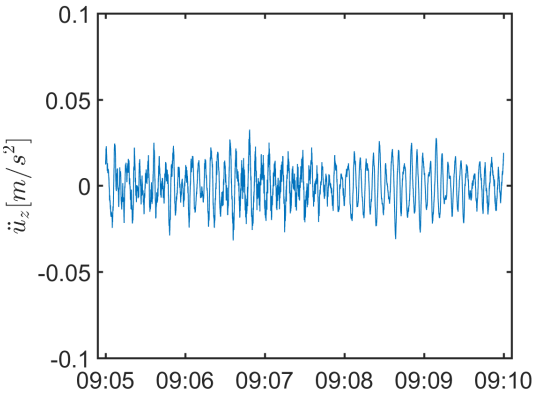

(e) 09:05 - 09:10

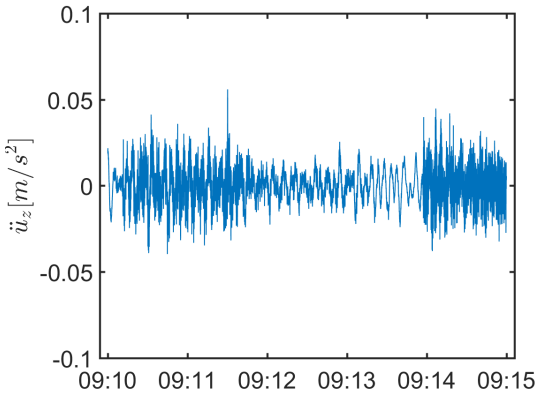

(f) 09:10 - 09:15

Figure B.41: Vertical acceleration response, Section H3

Section H4

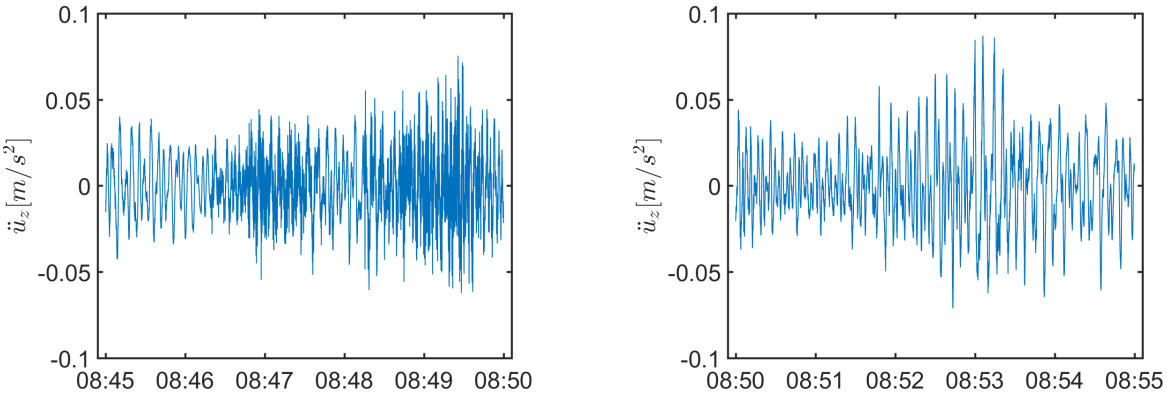

(a) 08:45 - 08:50

(b) 08:50 - 08:55

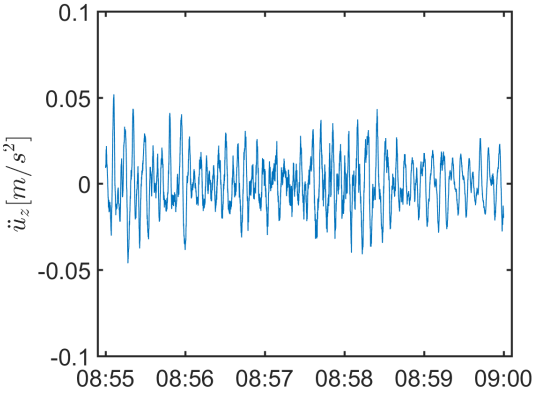

(c) 08:55 - 09:00

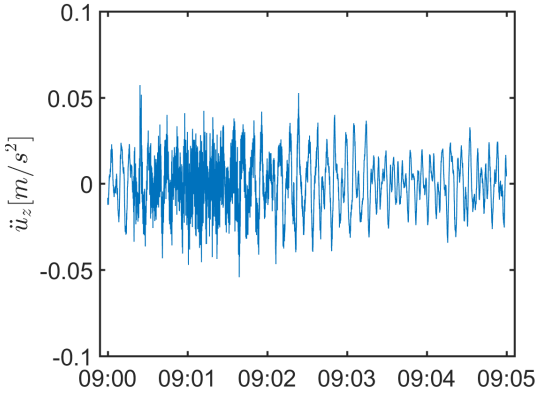

(d) 09:00 - 09:05

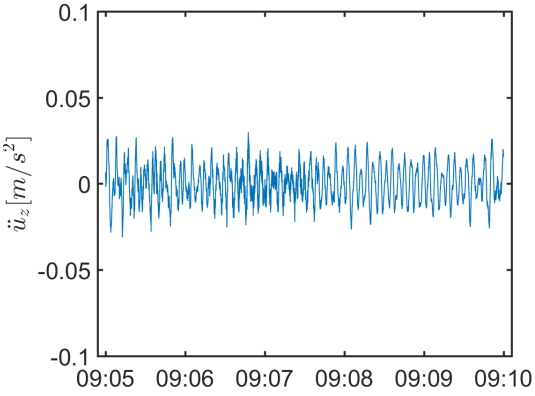

(e) 09:05 - 09:10

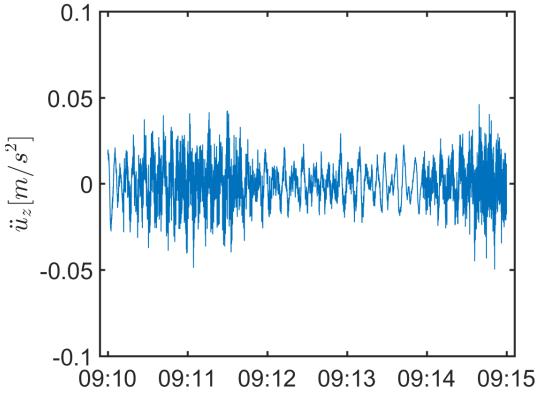

(f) 09:10 - 09:15

Figure B.42: Vertical acceleration response, Section H4

Section H5

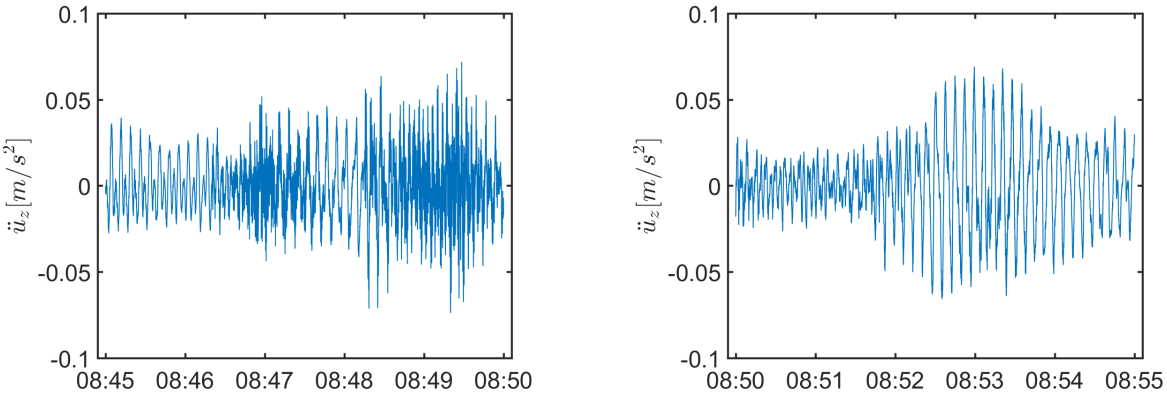

(a) 08:45 - 08:50

(b) 08:50 - 08:55

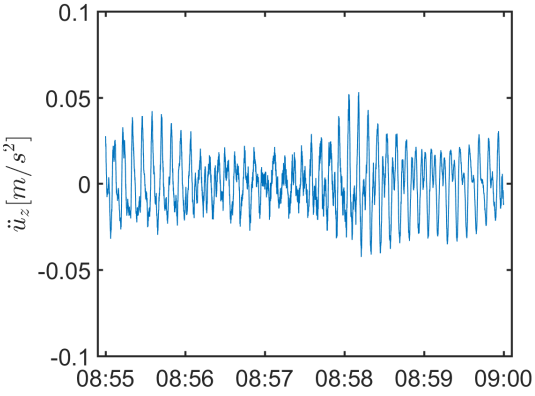

(c) 08:55 - 09:00

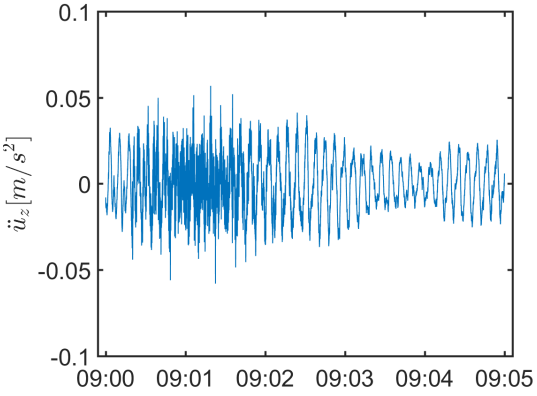

(d) 09:00 - 09:05

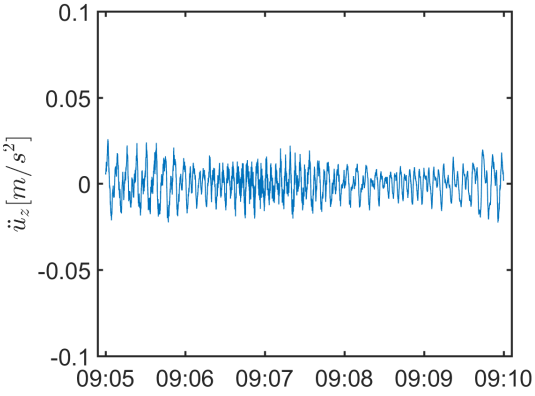

(e) 09:05 - 09:10

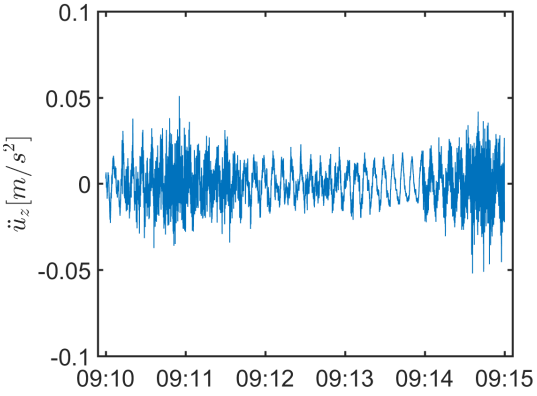

(f) 09:10 - 09:15

Figure B.43: Vertical acceleration response, Section H5

Section H6

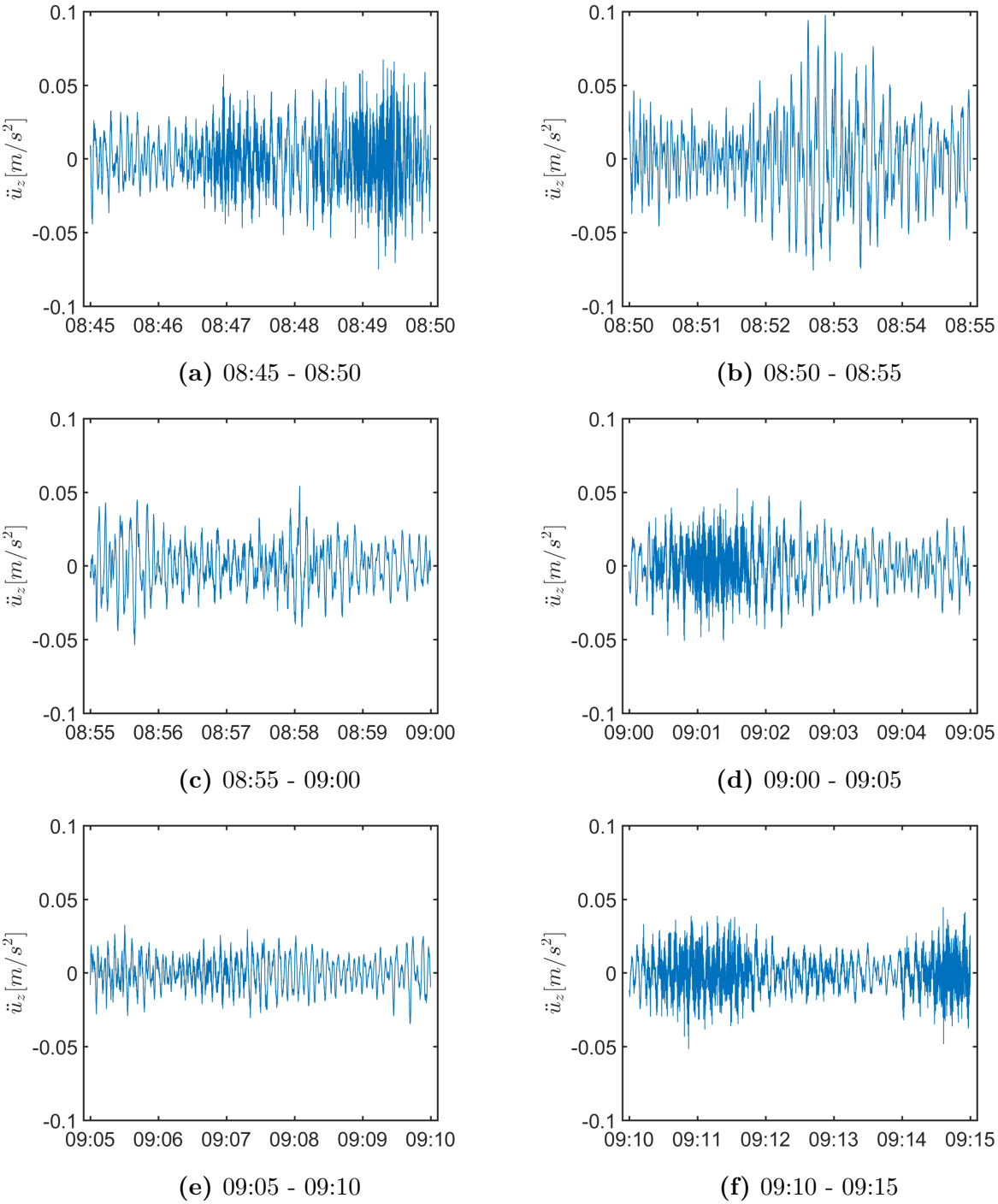

(a) 08:45 - 08:50

(b) 08:50 - 08:55

(c) 08:55 - 09:00

(d) 09:00 - 09:05

(e) 09:05 - 09:10

(f) 09:10 - 09:15

Figure B.44: Vertical acceleration response, Section H6

Section H7

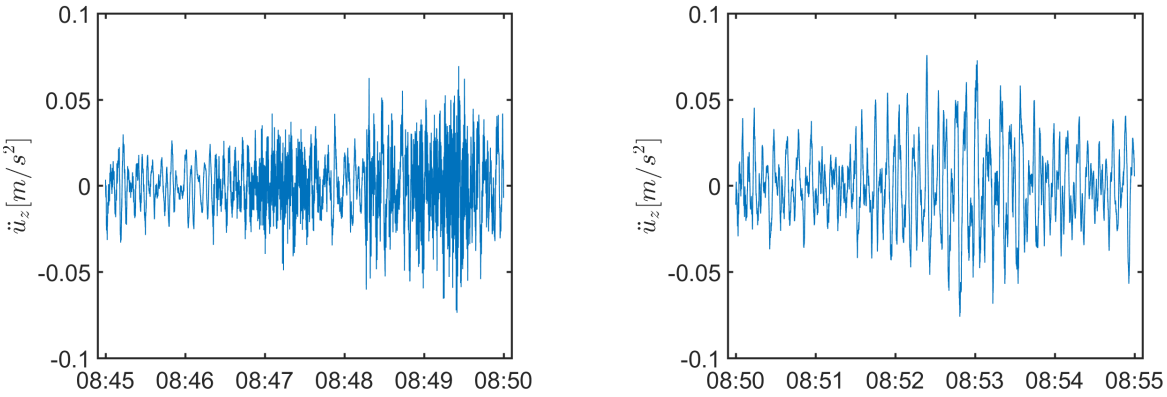

(a) 08:45 - 08:50

(b) 08:50 - 08:55

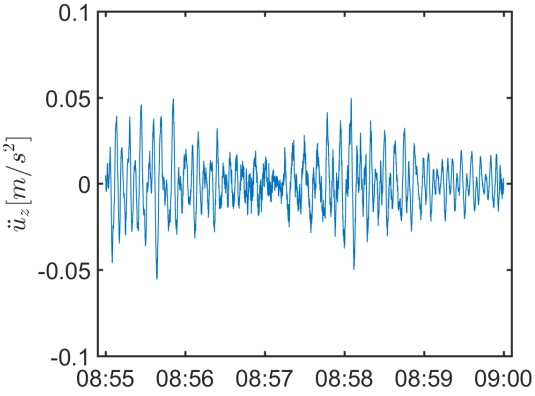

(c) 08:55 - 09:00

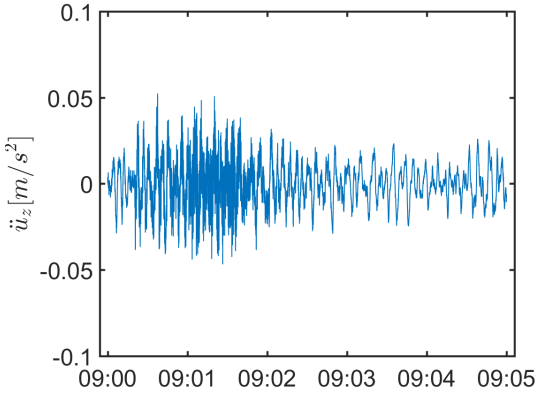

(d) 09:00 - 09:05

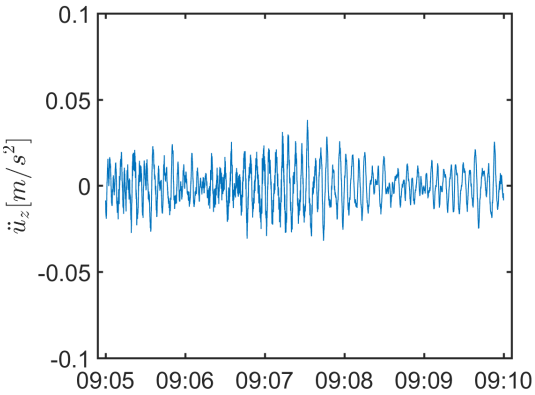

(e) 09:05 - 09:10

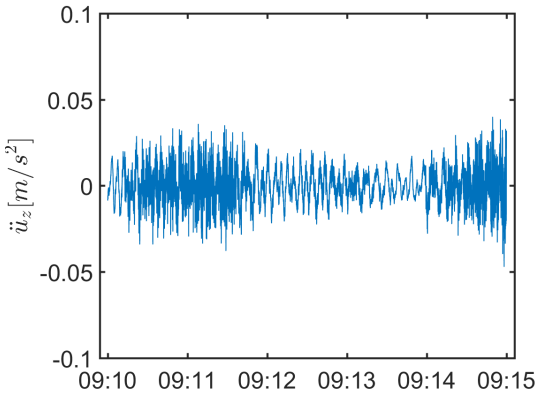

(f) 09:10 - 09:15

Figure B.45: Vertical acceleration response, Section H7

Section H8

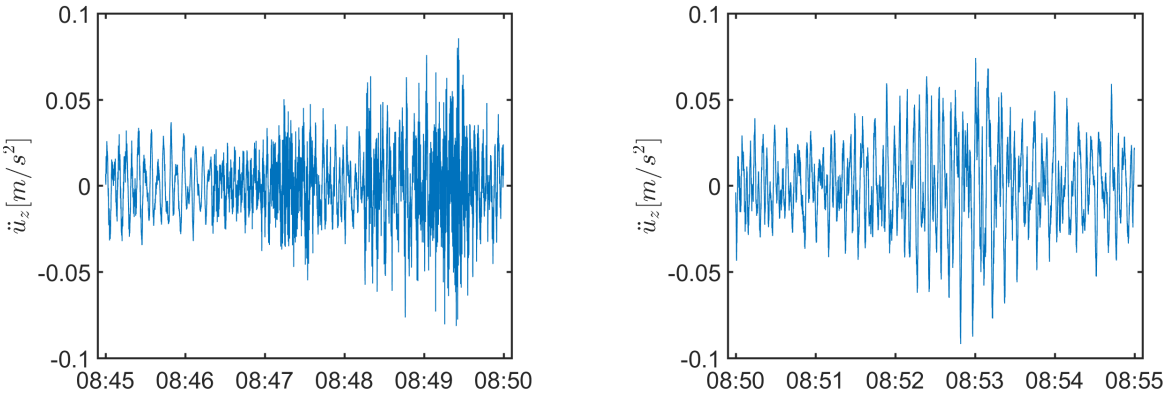

(a) 08:45 - 08:50

(b) 08:50 - 08:55

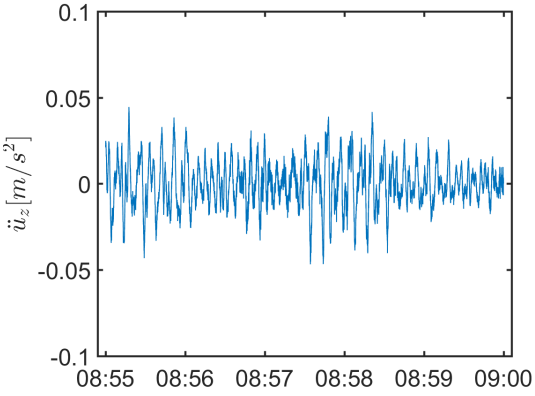

(c) 08:55 - 09:00

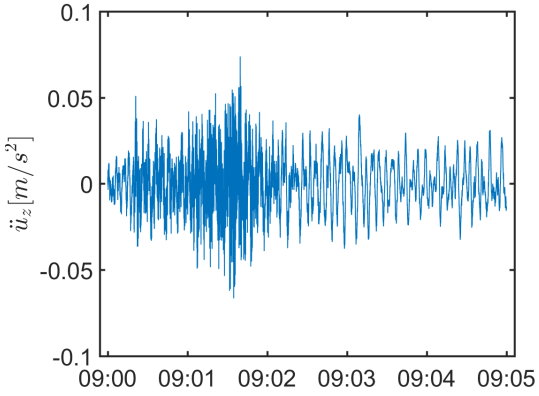

(d) 09:00 - 09:05

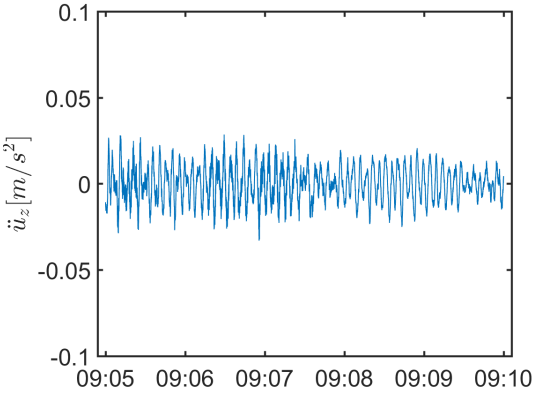

(e) 09:05 - 09:10

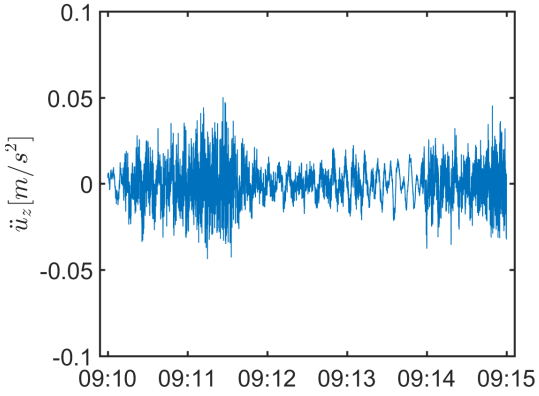

(f) 09:10 - 09:15

Figure B.46: Vertical acceleration response, Section H8

Section H9

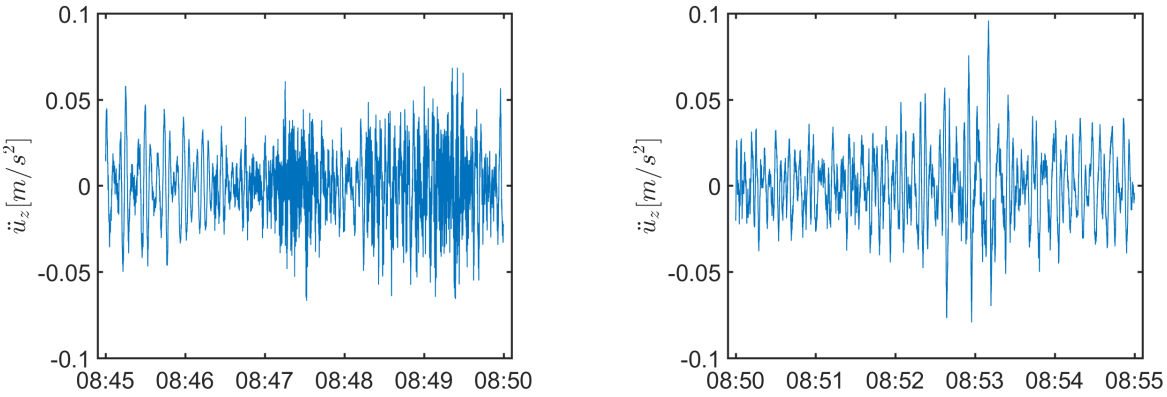

(a) 08:45 - 08:50

(b) 08:50 - 08:55

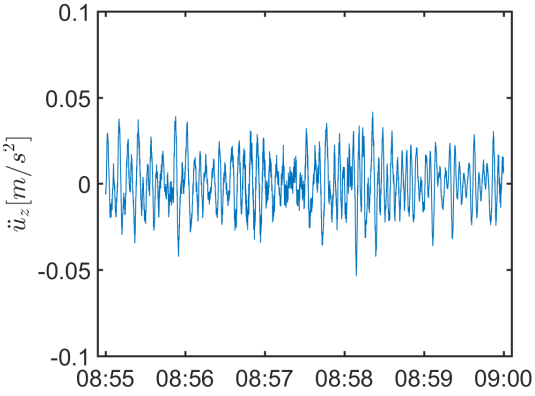

(c) 08:55 - 09:00

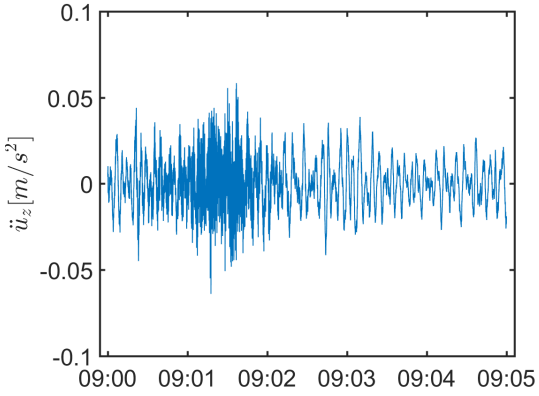

(d) 09:00 - 09:05

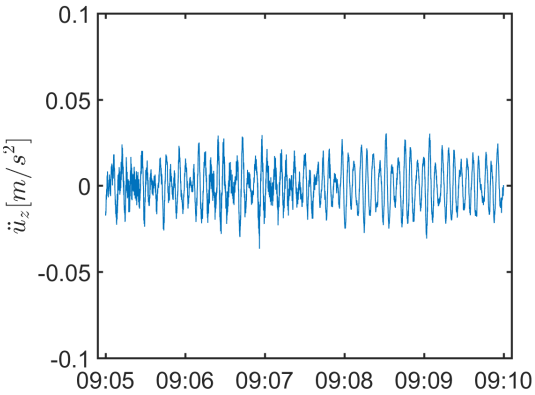

(e) 09:05 - 09:10

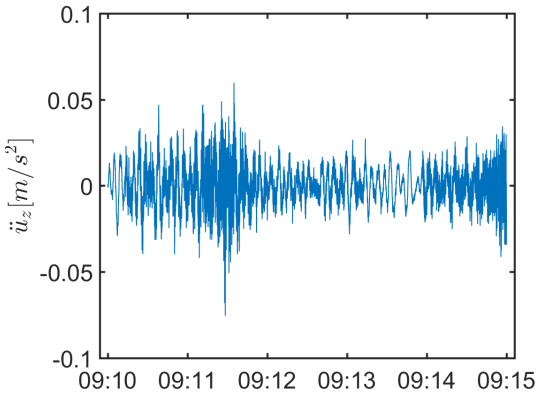

(f) 09:10 - 09:15

Figure B.47: Vertical acceleration response, Section H9

B.2.3 Power spectral density

Section H1

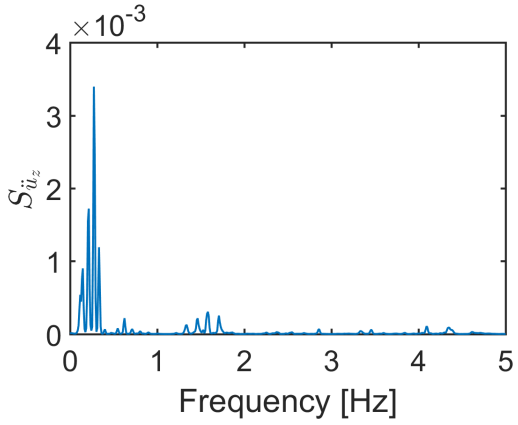

(a) 08:45 - 08:50

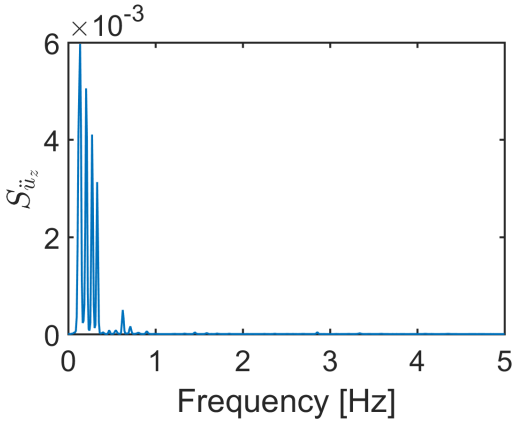

(b) 08:50 - 08:55

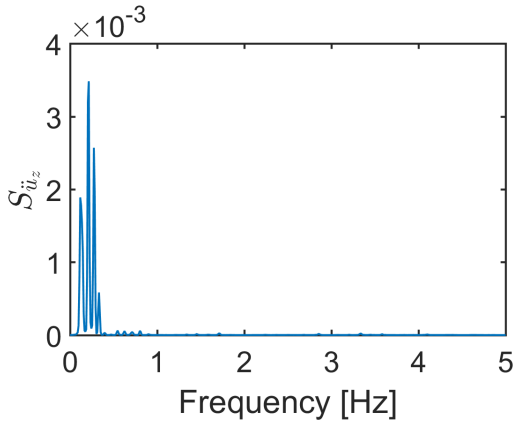

Figure B.48: 08:55 - 09:00

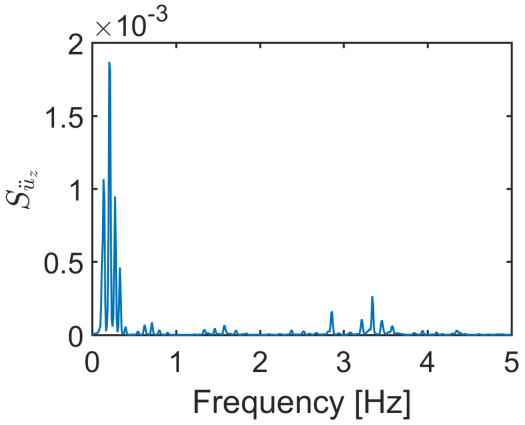

(a) 09:00 - 09:05

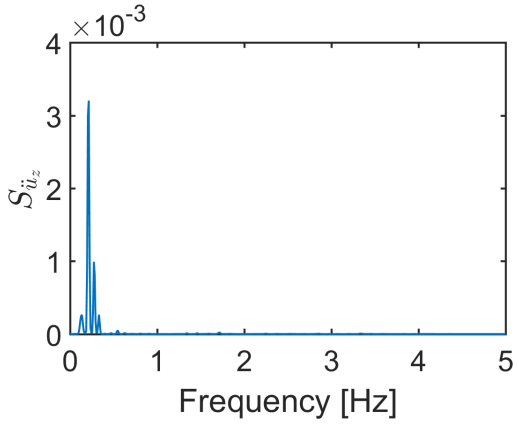

(b) 09:05 - 09:10

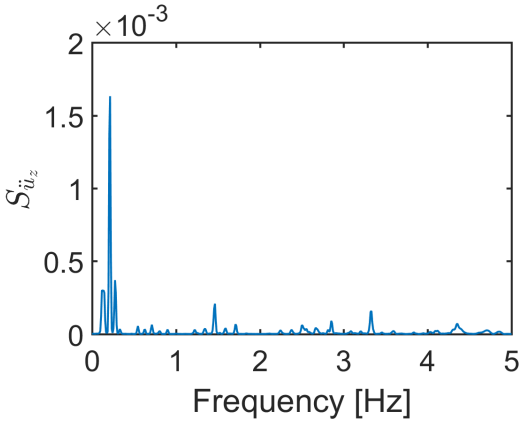

(c) 09:10 - 09:15

Figure B.49: Power Spectral Density, Section H1

Section H2

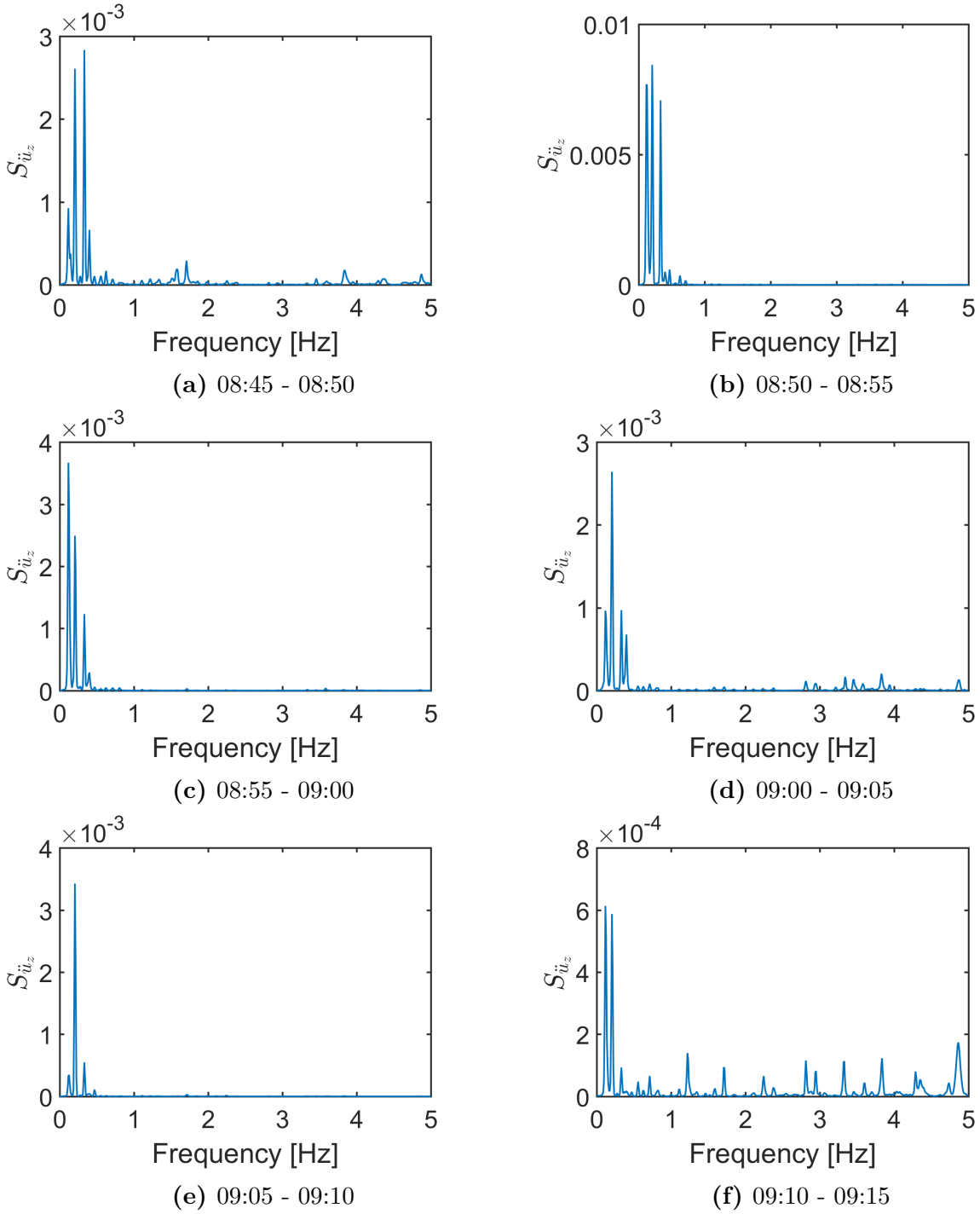

(a) 08:45 - 08:50

(b) 08:50 - 08:55

(c) 08:55 - 09:00

(d) 09:00 - 09:05

(e) 09:05 - 09:10

(f) 09:10 - 09:15

Figure B.50: Power Spectral Density, Section H2

Section H3

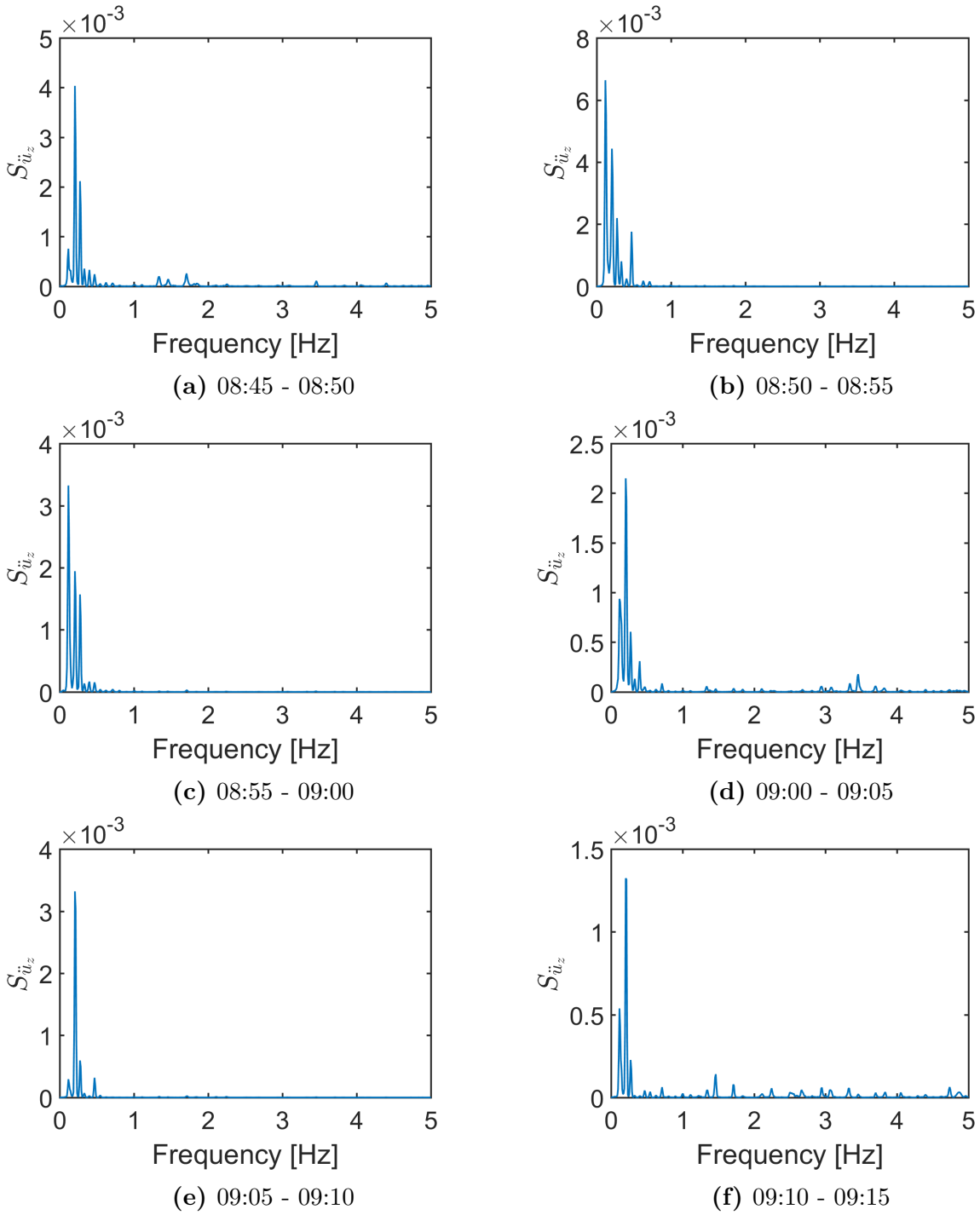

(a) 08:45 - 08:50

(b) 08:50 - 08:55

(c) 08:55 - 09:00

(d) 09:00 - 09:05

(e) 09:05 - 09:10

(f) 09:10 - 09:15

Figure B.51: Power Spectral Density, Section H3

Section H4

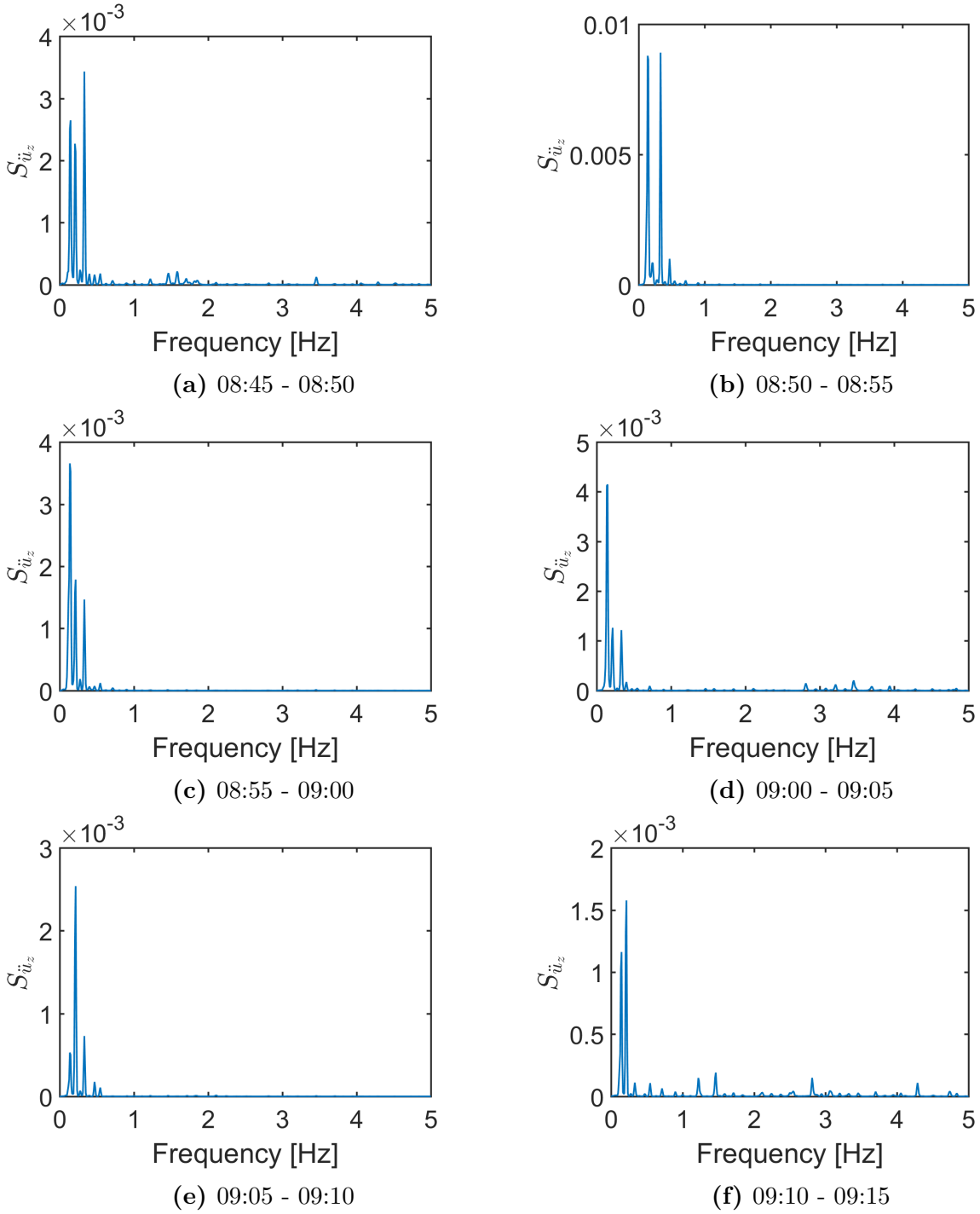

(a) 08:45 - 08:50

(b) 08:50 - 08:55

(c) 08:55 - 09:00

(d) 09:00 - 09:05

(e) 09:05 - 09:10

(f) 09:10 - 09:15

Figure B.52: Power Spectral Density, Section H4

Section H5

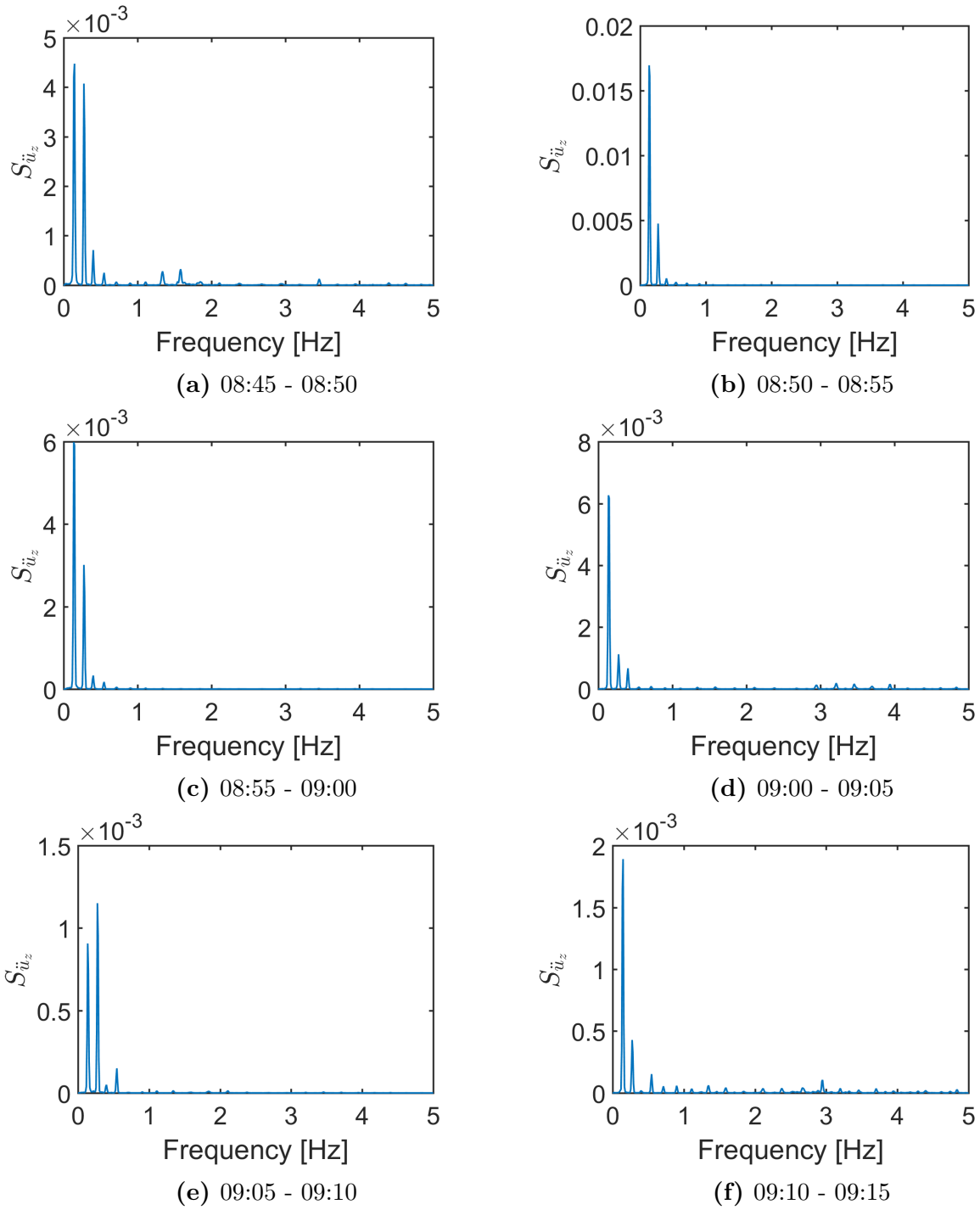

(a) 08:45 - 08:50

(b) 08:50 - 08:55

(c) 08:55 - 09:00

(d) 09:00 - 09:05

(e) 09:05 - 09:10

(f) 09:10 - 09:15

Figure B.53: Power Spectral Density, Section H5

Section H6

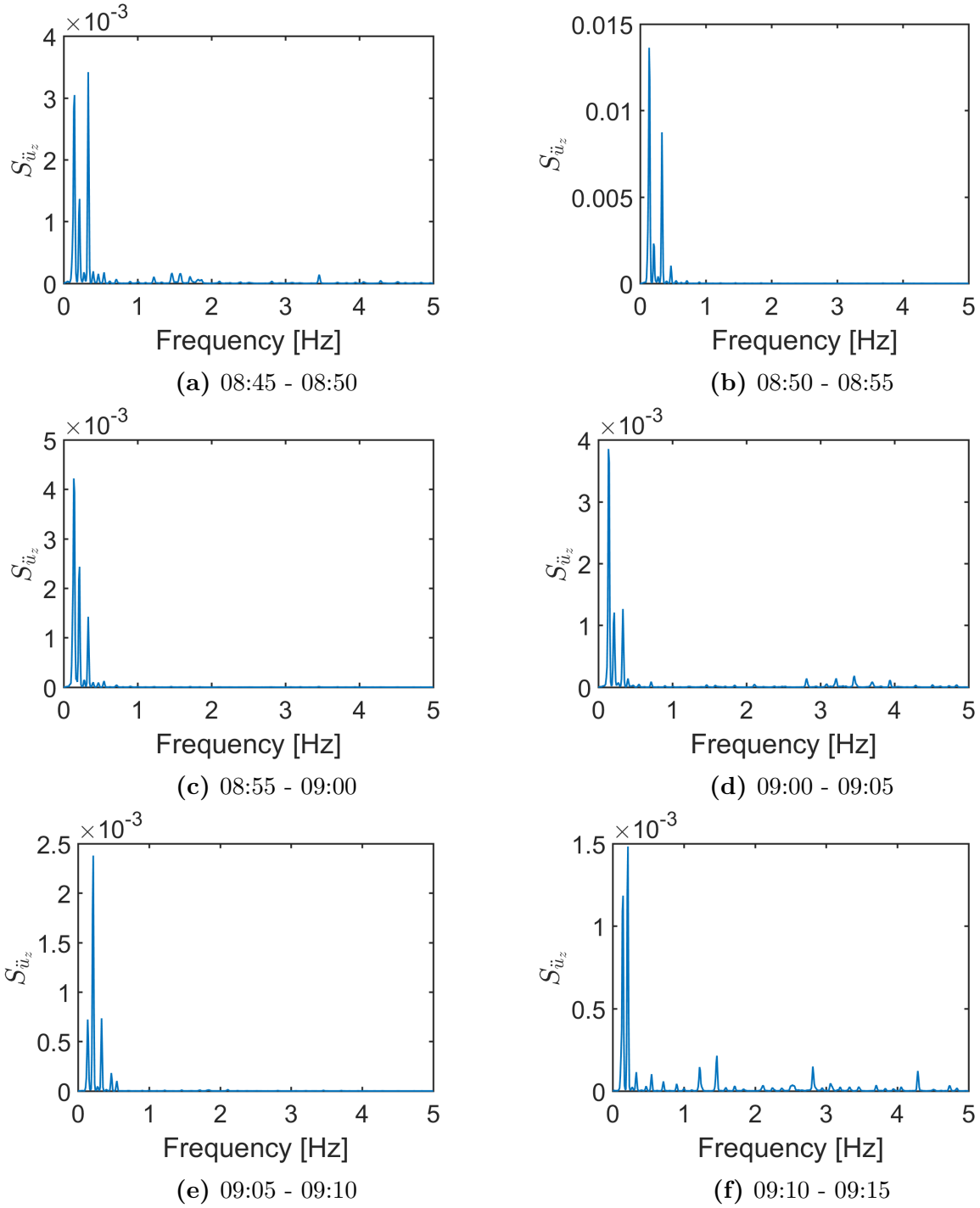

(a) 08:45 - 08:50

(b) 08:50 - 08:55

(c) 08:55 - 09:00

(d) 09:00 - 09:05

(e) 09:05 - 09:10

(f) 09:10 - 09:15

Figure B.54: Power Spectral Density, Section H6

Section H7

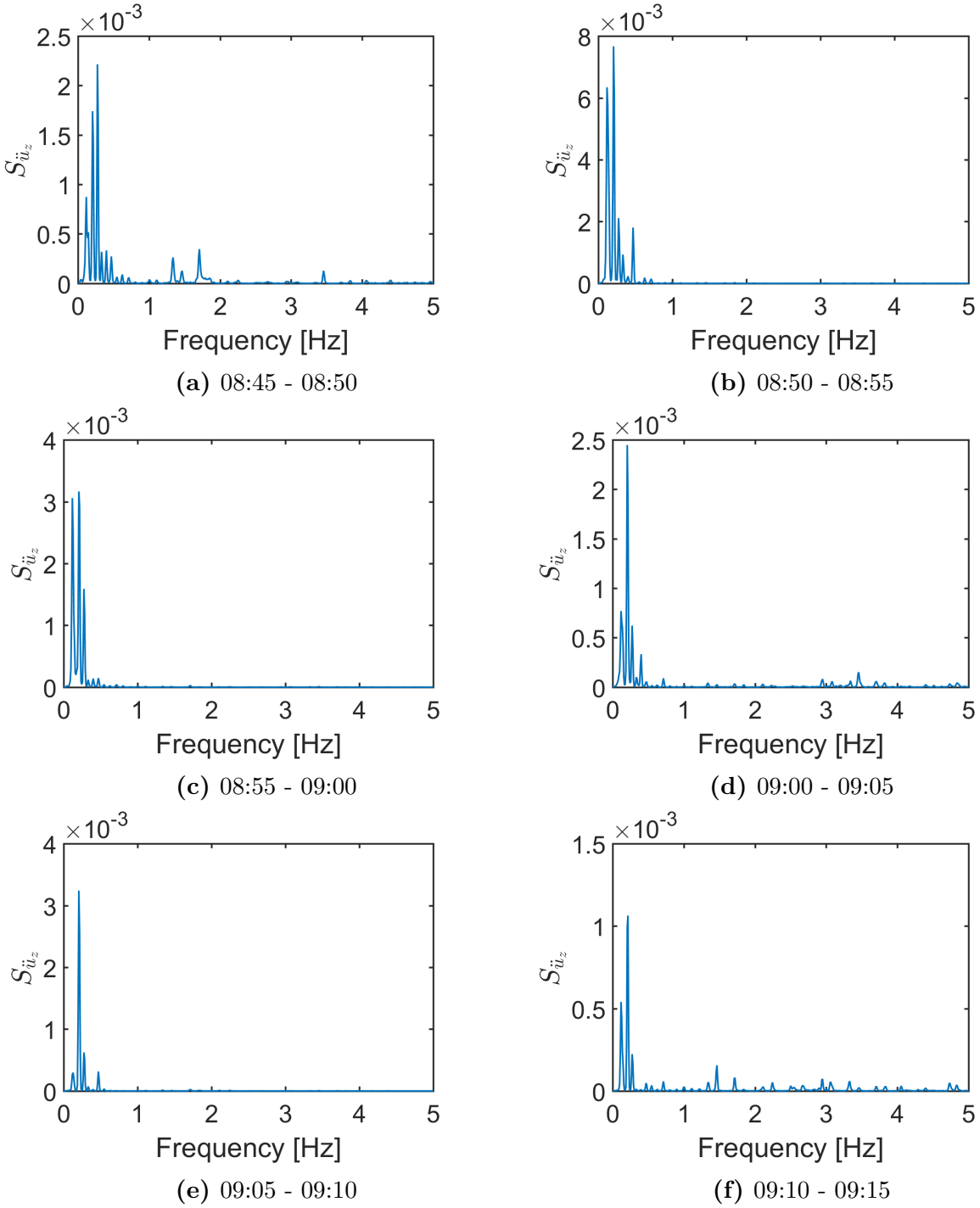

(a) 08:45 - 08:50

(b) 08:50 - 08:55

(c) 08:55 - 09:00

(d) 09:00 - 09:05

(e) 09:05 - 09:10

(f) 09:10 - 09:15

Figure B.55: Power Spectral Density, Section H7

Section H8

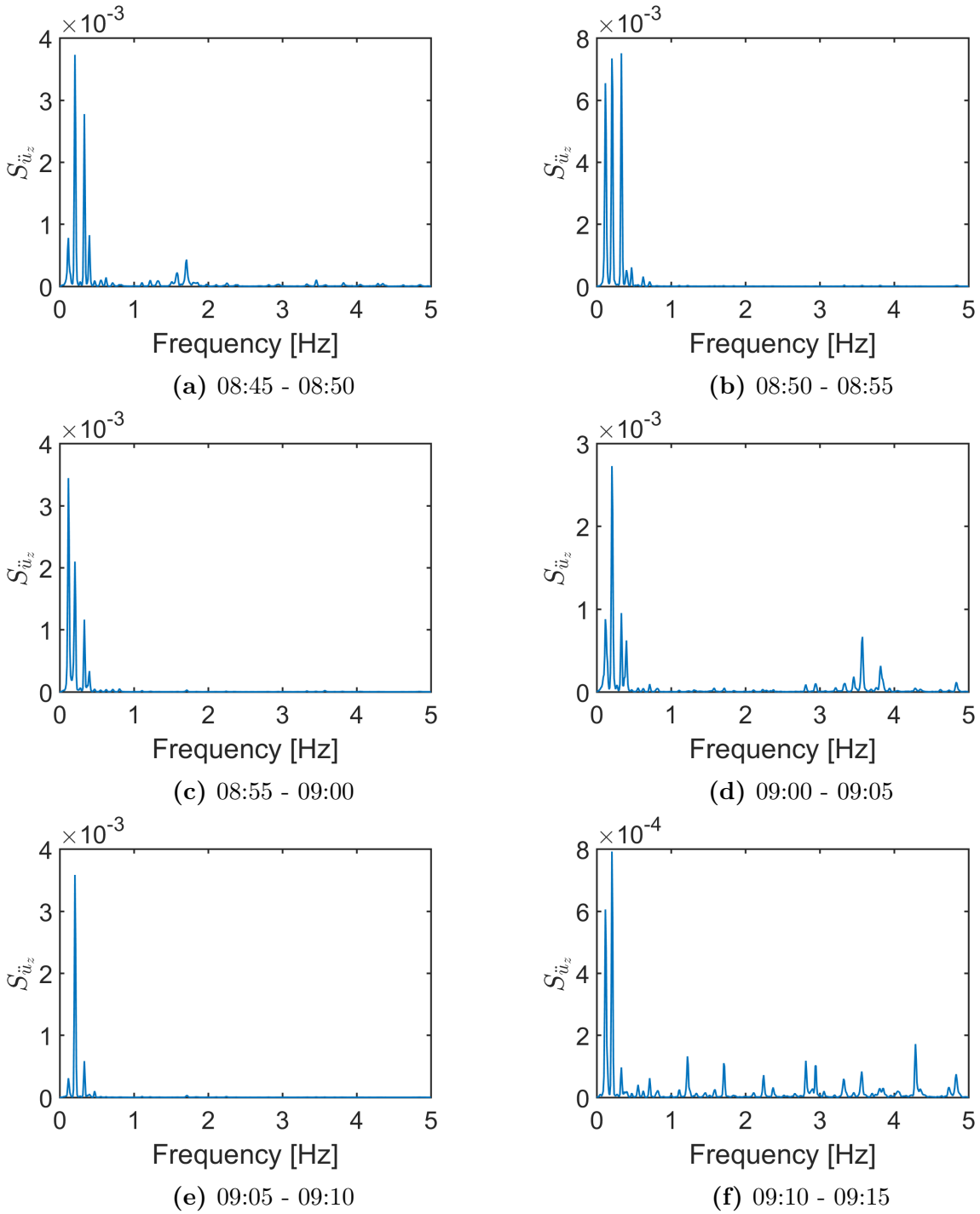

(a) 08:45 - 08:50 **(b)** 08:50 - 08:55

(c) 08:55 - 09:00 **(d)** 09:00 - 09:05

(e) 09:05 - 09:10 **(f)** 09:10 - 09:15

Figure B.56: Power Spectral Density, Section H8

Section H9

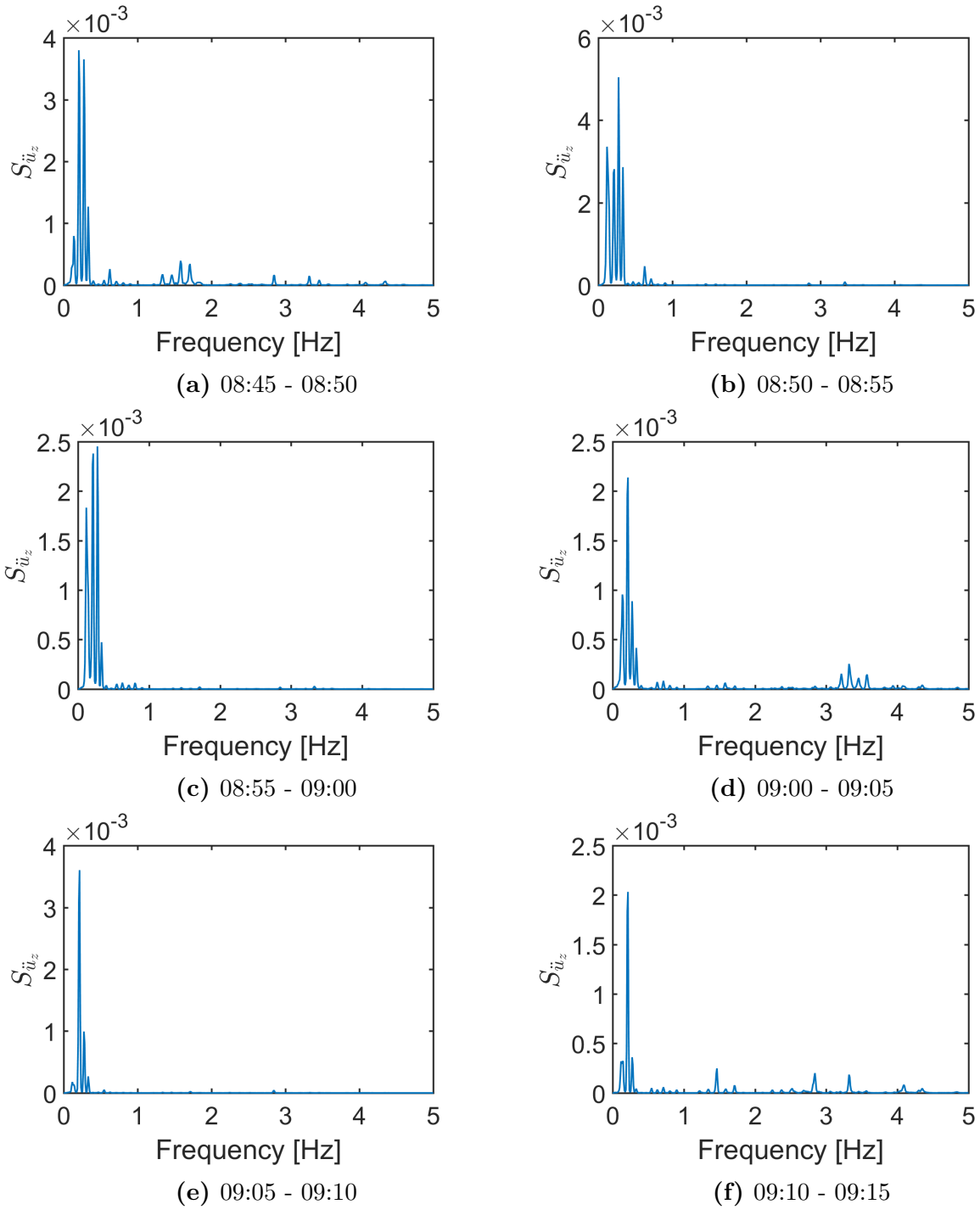

(a) 08:45 - 08:50

(b) 08:50 - 08:55

(c) 08:55 - 09:00

(d) 09:00 - 09:05

(e) 09:05 - 09:10

(f) 09:10 - 09:15

Figure B.57: Power Spectral Density, Section H9